Comparison of Peripheral Quantitative Computed Tomography and Magnetic Resonance Imaging for Tissue Characterisation in the Gastrocnemius Muscle

Thesis submitted to Cardiff University for the degree of Doctor of Philosophy

By

Fahad Al Gohani

Cardiff University

Ph.D. Thesis

April, 2017

Abstract

Rupture of the medial head of the gastrocnemius muscle (GM) is a common injury of the calf muscles. Magnetic resonance imaging (MRI) and ultrasound (US) are the medical imaging modalities that are usually used to assess such injuries.

Texture analysis is a digital image processing technique that quantifies the relationship between pixel intensities (grey levels) and pixel positions. Texture can reveal valuable information that cannot be perceived by the naked eye. Dedicated image processing software is required to extract texture parameters. Texture analysis has been implemented for medical imaging modalities such as MRI, US and computed tomography (CT) for the evaluation sports muscle injury.

Peripheral quantitative tomography (pQCT) is an adaptation of conventional CT. In this project, texture analysis was implemented on MRI and pQCT images of the gastrocnemius muscle (GM). MRI is an expensive technique that requires specialised facilities. Conversely, pQCT utilises a small-bore, low-dose X-ray scanner, which is portable and less costly than MRI. It has traditionally been used mainly for bone analysis. The aim of this study was to assess the suitability of pQCT for GM tissue characterisation using texture analysis compared with MRI. The study is novel in that it is the first to apply texture analysis to GM images using pQCT

Texture analysis was done on image data acquired from MRI (GE, 1.5T) and pQCT (Stratec XCT 2000) in a group of healthy human subjects and an injured subject. A water phantom was also scanned with pQCT. An existing standard imaging protocol was observed for MRI acquisition, while pQCT image acquisition parameters were explored and optimised to yield a standard protocol.

The pQCT scanner was shown to be capable of acquiring calf muscle images and distinguishing calf muscle boundaries. Texture parameters (grey level, variance, skewness, kurtosis, co-occurrence matrix, run length matrix, gradient, autoregressive (AR) model and wavelet transform) were extracted from the acquired images. The repeatability of these quantities for pQCT in a healthy human subject and a water phantom was assessed by calculating the coefficient of variation (%CV). The effect of pQCT parameters (scan speed and pixel size) was tested using multiple variate

analysis of variance (MANOVA). The effect of region of interest (ROI) area and anatomical position were evaluated using simple linear regression.

The t-test was used to compare the mean values of the texture features in the right and left leg for both MRI and pQCT in a group of healthy human subjects. Neither MRI nor pQCT showed significant differences between the two legs for any of the texture features. In addition, there was no significant difference between the two modalities for the AR model and wavelet transform texture parameters. Reference ranges for the medial head of the GM were defined for both modalities. A study of a single injured subject revealed that the values of the AR model texture parameter fell outside the reference ranges for both MRI and pQCT, and so the AR model was identified as the most sensitive texture parameter for distinguishing injured from uninjured GM.

The principal conclusion from this work is that pQCT has the potential to be used for imaging the gastrocnemius muscle and that GM images from both MRI and pQCT scanners can be objectively characterised by texture analysis. In addition, the auto-regressive model texture parameter may be the most appropriate for muscle characterisation.

Acknowledgments

First and foremost, I would like to thank almighty Allah (God), for giving me the opportunity to curry out this research.

I offer my deep and sincere thanks to my supervisors: Professor Len Nokes and Professor Wil Evans for their supports, encouragement and guidance. I could not wish for better supervisors.

I offer my kind regards to the staff at Clinical Engineering and Medical Physics and School of Engineering Research Office for their directly and indirectly extending their help during the work.

Finally, I would like to acknowledge the most important person in my life- my wife Hana, for her support and encouragement in my life.

Fahad

Table of Contents

List of Tables

List of Figures

Abbreviations

ANOVA	Analysis of variance
AR	Auto-regressive
BMD	Bone mineral density
BMP	Bit map
CSV	Comma separated values
CT	Computed tomography
CV	Coefficient of variation
CSF	Cerebrospinal fluid
DICOM	Digital imaging and communication in medicine
DMOS	Delayed onset muscle
EBT	Electron beam tomography
ECG	Electrocardiogram
FBP	Filtered back-projection
FID	Free induction decay
FWHM	Full width at half maximum
GL	Grey level
HU	Hounsfield unit
ICC	Intra-Class Correlation
MDA	Multiple rows of detector array scanner
MANOVA	Multiple variate analysis of variance
MDCT	Multi-detector computed tomography
MG	Medial gastrocnemius
MSCT	Multi-slice computed tomography
MRI	Magnetic Resonance Imaging
MHz/T	Megahertz/tesla
POM	Polyoxymethylene
PTFE	Polytetrafluorethylene
pQCT	Peripheral quantitative computed tomography
PVC	Polyvinylchloride
PVDF	Polyvinylfluoride
QA	Quality assurance
QCT	Quantitative computed tomography
RF	Radio frequency
ROI	Region of interest
SD	Standard deviation
SNR	Signal-to-noise ratio
TE	Time of echo
TLD	Thermo-luminescent dosimetry
TP	Texture parameter
TR	Time of repetition
US	Ultrasound

Chapter 1 Introduction

1.1 Introduction

Muscle injuries are the most common type of injuries and often occur during sport or training activity. This is particularly important for élite athletes where decisions regarding a return to activity have significant financial and/or strategic consequences for both the player and the team (Armfield *et al.,* 2006, Blankenbaker and Tuite, 2010). These injuries are prevalent in sports such as football and rugby. Moreover, in football they constitute 31% of all injuries (Mueller-Wohlfahrt *et al*. 2012) . The most common muscle injuries occur within the lower extremities including: the quadriceps, the hamstring, and the calf muscle, specifically the gastrocnemius muscle (Blankenbaker and Tuite, 2010). In a specific sports activity, like football, muscle injuries present as a heterogeneous group of muscle disorders; 92% of injuries affect the lower limbs with 37% in the hamstring, 23% in the adductors, 19% in the quadriceps, and 13% in calf muscles. Furthermore, 96% of the injuries result from non-contact situations (Mueller-Wohlfahrt *et al.*, 2012). The chance of re-occurrence of injuries in football, for example, is 16%, and this is associated with a 30% longer time before a return to competition compared with the return time after the original injury (Mueller-Wohlfahrt *et al.,* 2012). This emphasises the importance of a correct diagnosis, and the assessment of progress for healing.

Muscle injury diagnosis starts by clinical examination and is followed by the RICE principle (Rest, Ice, Compression and Elevation). Particularly, this is used as first aid to stop injury-induced bleeding into the muscle tissue in order to minimise the extent of the injury. However, if a more detailed characterisation is needed, medical imaging modalities can be used (Jarvinen *et al.,* 2007).

The modalities that are most commonly used for the assessment of muscle injury are Magnetic Resonance Imaging (MRI) and Ultrasound (US) imaging (Nsitem, 2013; Crema *et al.,* 2015). MRI uses a very strong magnet field to align the nuclei of hydrogen atoms inside the body, and a variable magnetic field that causes the atoms to resonate, while US uses high frequency sound waves and their echoes. However,

each technique has its benefits and drawbacks, which can have a bearing on both quality and cost of the diagnosis of muscle injury. In general, both modalities are non-invasive and painless.

Another imaging technology that may overcome some of the disadvantages of MRI (cost, scan time) and US (operator dependence, image quality) is Computed Tomography (CT) and its variant, peripheral Quantitative Computed Tomography (pQCT). The CT scanner uses x-rays to produce cross sectional layers that display detailed images of the inner body in a quick and painless procedure. It can be used for primary diagnosis and to examine whether a previously treated illness has recurred. In a situation, where, for instance, patients have implanted medical devices, a CT scan is a good alternative to MRI for imaging of the lower limbs. A pQCT scanner is a dedicated CT scanner for limbs. It has a lower radiation dose than conventional CT and may become an alternative to conventional CT and MRI for the investigation of muscle injury and the assessment of the muscle healing process.

In recent years, there has been considerable interest in developing objective quantitative methods for medical diagnosis, rather than relying on subjective methods. Subjective methods relate to visual identification of specific tissue. The possibility of human error is always present (Chan and Mccarty, 1990). Moreover, Giger et. al. (2008) have shown that there are limitations in the human eye-brain visual system: distraction, reader fatigue and the presence of overlapping structures that camouflage abnormality in images. These may lead to detection and interpretation errors.

In medical imaging, quantitation is based on the analysis of digital images using a variety of computational approaches. Such images consist of individual picture elements (pixels) with assigned brightness values, which can be evaluated objectively. For example, digital images analysis is the core of computer-aided diagnosis (CAD), which has become one of the major research subjects in medical imaging and diagnostic radiology. At present, the concept of CAD is to provide a valuable second opinion to assist image interpretation made by radiologists and thus to improve the accuracy of radiological diagnosis and reduce image reading time.

Possible methods for quantitative image evaluation include texture analysis, shape analysis and parametric mapping analysis (Kim *et.al,* 2011). The texture analysis method will be the standard method in this project. Image texture analysis is a technique to evaluate the spatial relationships (position and intensity) between image pixels to provide an objective approach to image property quantification. The spatial information of any material is a description of the material's internal structure (texture). Any changes in the material texture can therefore be numerically computed and may be used as a measure of changes. Similarly, changes in internal tissue texture, due to the development of disease for example, change the texture of tissue images. Hence, numerical texture analysis can be implemented to detect tissue abnormality (disease) and for the assessment of the size of the tissue region affected by the disease. Tissue texture analysis can improve the accuracy and objectivity of medical diagnosis (Hajek *et al.,* 2006).

Previous studies have investigated the use of quantitative texture analysis for the characterisation of muscle tissue using US (Nielsen *et al.*, 2000; Nielsen *et al.*, 2006; Pillen *et al.,* 2009; Alqahtani *et al.,* 2010) and MRI (Herlidou *et al.,*1999; Skoch *et al.,* 2004). It is possible that the same approach could be used to enhance the diagnosis of muscle injury with pQCT.

Following a review of the literature, it is hypothesised that a pQCT scanner is capable of acquiring soft tissue images, and that the application of texture analysis techniques provides information which can aid the detection of changes in muscle during the early stages of injury. Furthermore, the availability, cost-effectiveness, operator independence and time saving of pQCT, may make it superior to MRI and CT for following up muscle injuries and for the assessment of muscle healing.

1.2 The General Objective

The general objective is to investigate whether pQCT offers an alternative to MRI, which is used as the current standard method of imaging muscle injury in elite sports people, for tissue characterisation of the gastrocnemius muscle.

1.3 Specific Objectives

1. To investigate the suitability of pQCT for imaging normal and injured muscles.
2. To investigate the suitability of pQCT in monitoring the healing process of soft tissue injury over time.
3. To evaluate the accuracy of a texture analysis technique of pQCT muscle images.
4. To characterise and quantify gastrocnemius muscle tissue texture for two different imaging modalities (MRI and pQCT).
5. To employ descriptive statistics, linear regression and correlation to compare texture features between the two modalities.
6. To investigate the influence of the size of a muscle region of interest (ROI) on textural features.
7. To compare texture features between the left and right legs in MRI and pQCT images.
8. To acquire images in a pathological case of muscle injury and compare them with normal case images.

As this work involved human participants, approval was sought and obtained from the Ethics Committee of the Cardiff University School of Engineering. The first application was for the scanning of healthy subjects, using MRI and pQCT. The second application was for the scanning of a pathological muscle injury case using pQCT.

1.4 Thesis Structure

To demonstrate the importance and significance of the research carried out, this thesis has been arranged as follows (Figure 1.1):

Chapter 1: Introduction, including general and specific objectives of this thesis, research methodology and the thesis structure.

Chapter 2: Literature review, including muscle anatomy, muscle injury and healing, imaging and diagnosis of muscle injury with MRI, ultrasound and CT, texture analysis techniques and their applications in medical imaging, and the potential of pQCT.

Chapter 3: Investigation of the influence of pQCT scan setting parameters on extracted texture parameters in a water phantom and a single healthy subject, testing pQCT repeatability, defining ROI cut-off area, demonstrating a standard pQCT image acquisition protocol and studying the influence of image transformation on extracted texture parameters.

Chapter 4: Acquiring images of recruited healthy subjects using MRI and pQCT modalities, comparing muscle texture in the right leg to that in the left leg, comparing MRI and pQCT using linear regression and obtaining reference ranges of normal muscle.

Chapter 5: Imaging in an Injured Subject.

Chapter 6: Summary and conclusion.

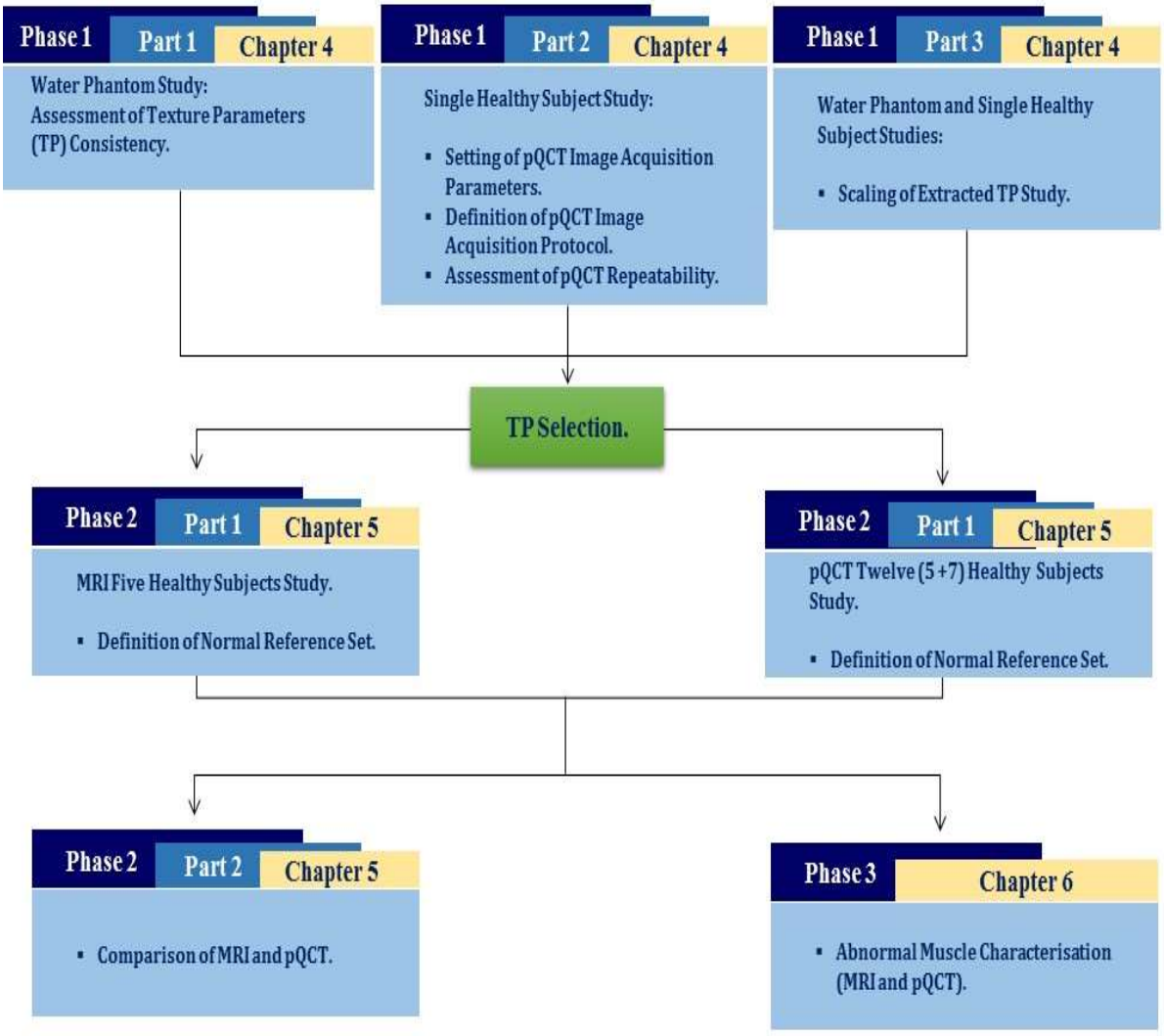

Figure 1.1: Methodology Diagram.

Chapter 2 Literature Review

2.1 Muscle Structure and Function

The muscular system of the human body is made up of three different types of muscle tissue: skeletal, smooth and cardiac. The most common type is skeletal muscle, which comprises striated and voluntary muscles (Erik *et al*. 2008). The whole human body mass is comprised of about 40% to 50% skeletal muscle (Joe *et al*. 2007, Roel *et al*. 2011); it is the largest single tissue in the human body (El-Khoury *et al*., 1996). Most skeletal muscles cross at least one joint, but many cross two joints (Blankenbaker *et al*. 2004). Muscles generate force that leads to body motion. In addition, during the body's inactive phase, deep muscles are responsible for body posture and joint stability and the generation of body heat (Joe & Derrickson 2007).

Skeletal muscle consists of various components working together to function efficiently (Erik *et al.* 2008). Muscle tissue is composed of thousands of elongated, cylindrical cells that are known as muscle fibres. The muscle fibres are aligned in bundles called fascicles (Kawakami, *et al*., 1998), each of which is surrounded by collagenous connective tissue called endomysium. Fascicles are enclosed in a stronger collagenous connective tissue which is known as epimysium. The two layers of connective tissue fuse together at each muscle end to form highly specialized connective tissue tendons, as shown in Figure 2.1 (Holsbeeck and Introcaso 2001, Fornage 1995, Peetrons 2002).

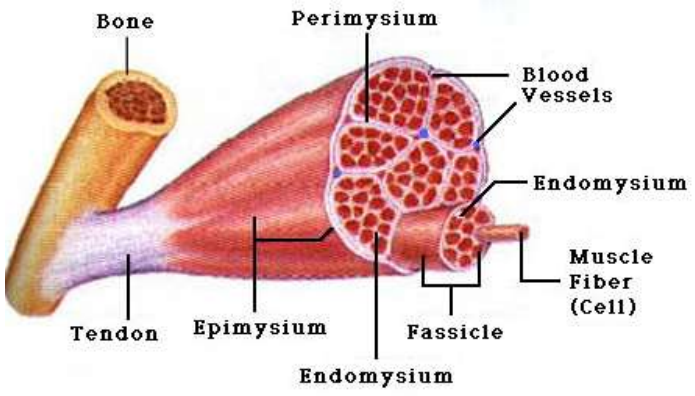

Figure 2.1:Composition of Muscle tissue (Joe & Derrickson 2007)

Muscle fibres are made up of myofibrils. The largest working units of the filaments of muscle fibre, myofibrils are cylindrical in shape and cover the entire length of the muscle fibre. They are composed of two types of protein filaments, called the thin filament and the thick filament(Joe & Derrickson 2007). Both filaments overlap in specific patterns and form compartments that are known as sarcomeres, which are aligned end to end. A sarcomere is the smallest functional unit in a muscle that can perform all the functions of muscle. The sarcomeres are separated from each other by a dense protein in a zig-zagging zone called the Z-discs. Furthermore, within each individual sarcomere there is a darker area called the A-band. At the centre of each A-band there is a zone called H, which contains the thick filament only. Moreover, at both ends of the A-band, overlapping of the thick and thin filaments takes place. The rest of the thin filament (with no overlapping portion) is called the I-band, which extends into two sarcomeres but is divided in half by the Z-disc as shown in Figure 2.2 (Joe and Derrickson 2007).

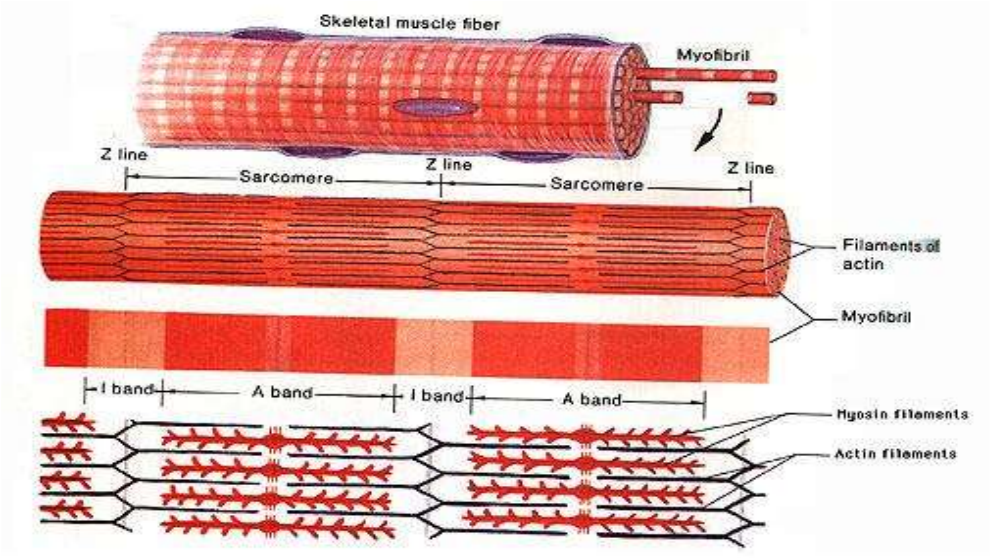

Figure 2.2: Muscle belly split into various component parts (https://home.comcast.net/~pegglestoncbsd/muscular.htm).

The shape of the thick filament (myosin) is like two golf clubs twisted together. The tails are arranged in parallel to each other, not unlikegolf club handles to form the shaft of the thick filament, and the head of the golf clubs projects outwards from the surface of the shaft and are called myosin heads (Joe & Derrickson 2007).

The thin filaments are attached to the Z discs. The main component of the thin filaments is the protein actin. Each actin molecule joins in a twisted helix shape to form an actin filament. Furthermore, each actin molecule includes a myosin-binding site, where a myosin head can attach. The thin filaments are composed of two other proteins, tropomyosin and troponin. During the muscle relaxation phase, myosin is blocked from binding to the actin as a result of strands of tropomyosin that cover the myosin-binding sites on the actin. The tropomyosin proteins are held in place by troponin molecules as shown in Figure 2.3 (Joe and Derrickson 2007).

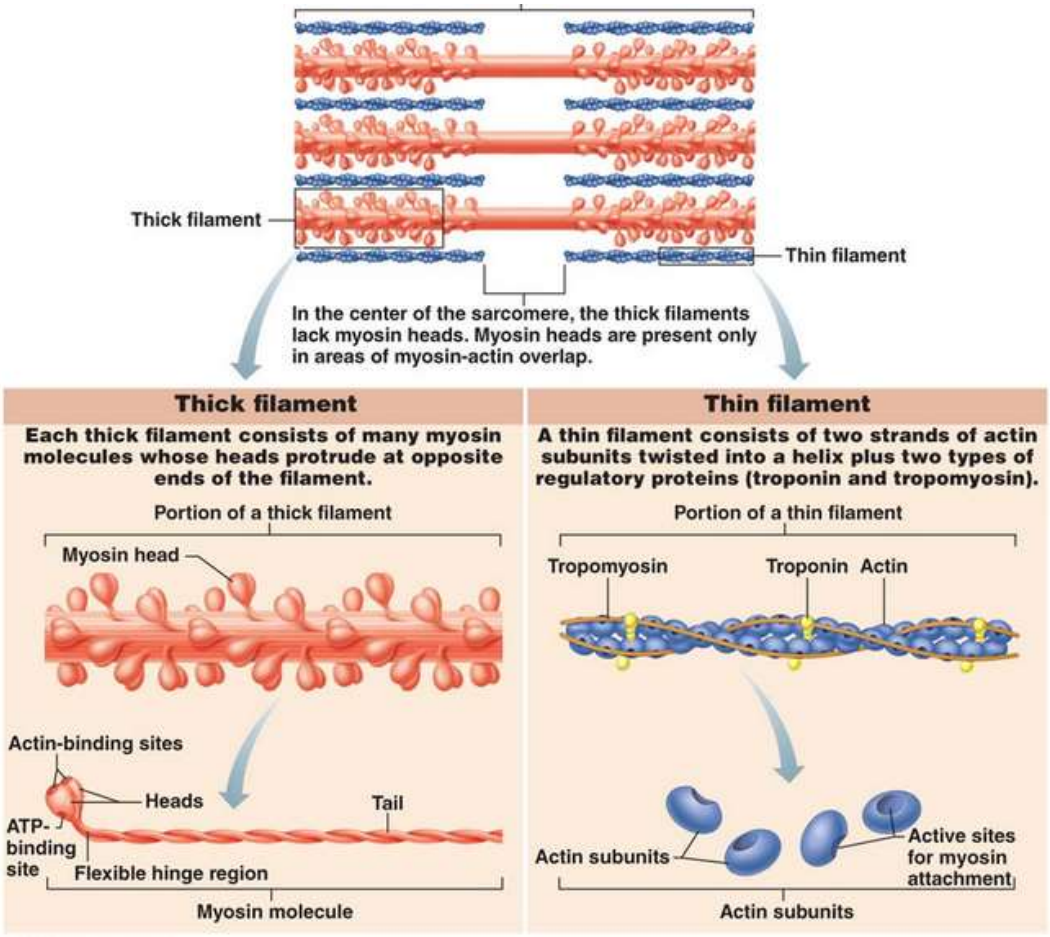

Figure 2.3:Longitudinal section of filaments within one sarcomere of a myofibril (http://classs.midlandstech.edu).

2.2 Types of Skeletal Muscle Fibres

Skeletal muscles contains three types of muscle fibres: type I (slow oxidative/slow-twitch), type IIA (fast oxidative-glycolytic/fast-twitch) and type IIB (fast glycolytic) (Joe & Derrickson 2007). All three types differ from each other according to their structural, metabolic, molecular and contractile properties (Schiaffino and Reggiani 1996). Table 2.1 illustrates some key characteristics of muscle fibres. Most skeletal muscles are composed of a mixture of all three types of fibres. For example, leg muscles have large numbers of both slow oxidative and fast oxidative-glycolytic fibres.

Table 2.1: Characteristics of muscle fibres, adapted from Staron (1997).

	Type I (slow oxidative)	Type IIA (fast oxidative-glycolytic)	Type IIB (fast glycolytic)
Diameter	Small	Intermediate	Large
Myoglobin content	High	Intermediate	Low
Speed of contraction	Slow	Fast	Fast
Rate of fatigue	Slow	Intermediate	Fast
Muscle colour	Red	Red	White

2.3 Anatomy of the Lower Leg

The lower leg is mainly divided into three groups of muscles. The first group comprises the anterior compartment, at the front of the leg, which includes the following muscles: tibialis anterior, extensor halluces longus, and extensor digitorum longus as shown in Figure 2.4. These muscles play a role in upward movement (dorsiflexion) of the foot, raising the foot at the ankle during walking (Agur and Dalley 2005).

The second group comprises the lateral compartment, on the outer side of the leg, which includes the following muscles: peroneus brevis and peroneus longus. These muscles attach to the fibula at the top and run down the leg, passing through tendon

sheaths at the ankle and joining the fifth metatarsal of the foot. These muscles provide plantar flexion and the eversion movement of the foot (Agur and Dalley 2005).

The third group is located at the back of the leg. This posterior compartment is divided into two sections: the superficial posterior compartment and the deep posterior compartment. The superficial posterior compartment includes the gastrocnemius, soleus and plantaris, whereas the deep posterior compartment includes the following muscles: flexor halluces longus, flexor digitorum longus, tibialis posterior and popliteus. The muscles of the superficial posterior compartment are responsible for the plantar flexion of the ankle, lowering the foot at the ankle joint. The muscles of the deep posterior compartment enable the foot to push off from the ground (Agur and Dalley 2005).

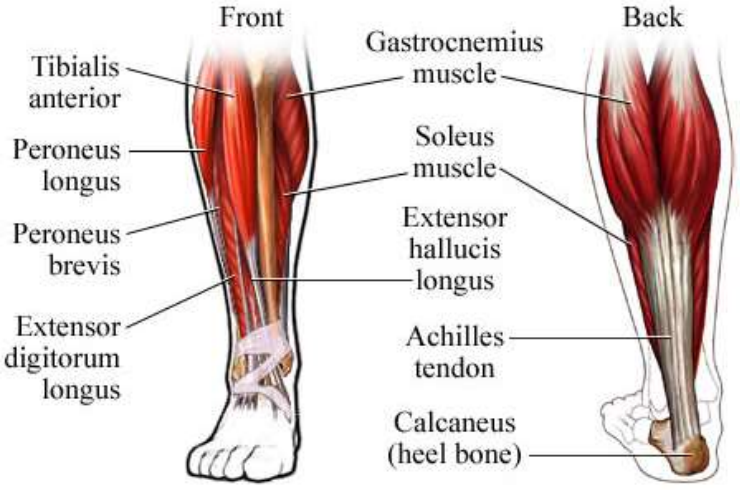

Figure 2.4: Anatomy of the lower leg (http://media.omedix.com?healthwise/nr55552069.jpg).

2.4 Anatomy of the Gastrocnemius Muscle

The gastrocnemius muscle is located at the posterior part of the lower leg. With the soleus muscle, it forms the calf muscle and it is the most superficial part of the calf muscle. It attaches to the heel via the Achilles tendon and runs behind the knee to the femur, crossing two joints. The gastrocnemius muscle is composed of two heads, the lateral and medial heads, as shown in Figure 2.5. The lateral head is smaller than the

medial head and rises from the lateral condyle of the femur, whereas the medial head originates from the medial condyle of the femur. The two heads of the gastrocnemius join and merge with the soleus muscle-tendon complex to form the Achilles tendon, which is inserted into the calcaneus posterior surface (Dark *et al.* 2009). It contributes to standing, walking, running and jumping. It induces plantar flexion of the foot at the ankle joint, flexing of the leg at the knee and plays an important role in the gait cycle (Dark *et al.* 2009).

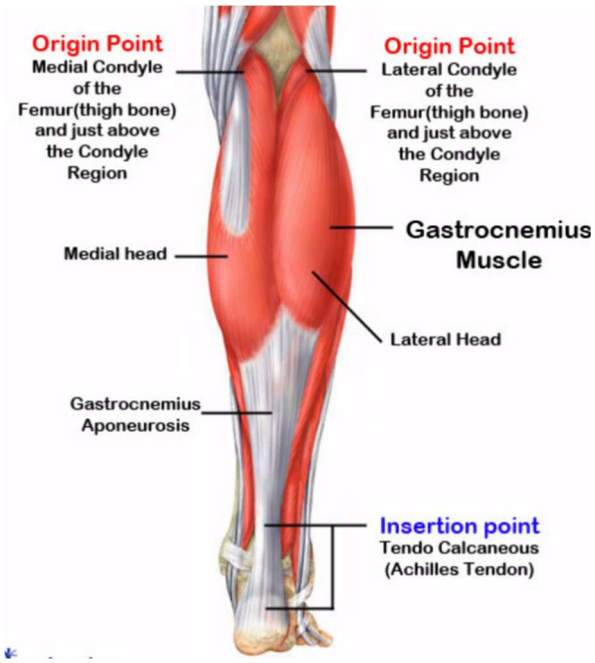

Figure 2.5: Anatomy of gastrocnemius muscle (http://www.droualb.faculty.mjc.edu).

The gastrocnemius is composed of a high proportion of type 2 fast-twitch muscle fibres to produce quick strong movements (Herzog *et al*. 1993). The soleus muscle is composed of twice as many type 1 slow-twitch fibres (slow oxidative) as type 2 fibres. Its function is the same as that of the gastrocnemius, i.e. to raise the heel, except that it works in a different position with the knee bent. During physical exercise the volume of the gastrocnemius muscle is modified, which may also lead to variation in the size and density of the fibres. Furthermore, blood flow increases to five or six times more than that of a muscle at rest (Basset *et al.* 1994). This can hamper methods of diagnosis that focus on swelling as an indicator of injury, immediately following exercise.

2.5 Muscle injuries

Muscle injuries are one of the most common sports injuries among athletes. Fuller et al (2006) defined sports injury as "any physical complaint sustained by an athlete that results from a match, competition or training, irrespective of the need for medical attention or time loss from sportive activities" Muscle injuries may have different causes, such as strain, contusion or laceration (Jarvinen 2005, 2007). Of these, strains and contusions are the most common muscle lesions, accounting for more than 90% of all sports-related injuries (Umile 2012). The most frequently injured muscles are in the lower extremities, particularly the hamstring, adductor, rectus femoris, biceps femoris, semitendinosis and the medial head of the gastrocnemius (El-Khory *et al.* 1996, Garrett 1996, Steinbach *et al.*,1997, De Smet and Best 2000, Varela *et al.*,2000, Blankenbaker and De Smet 2004, Ehman and Berquist 1986).

Muscle injuries can be assigned into two classes: direct injuries and indirect injuries (Jarvinen *et al.*, 2007). Direct injuries are caused by external force. They include contusion, haematoma and laceration (uncommon in sports-related injuries, as mentioned earlier), while indirect injuries do not result from direct contact but can result from the actions of the performer, such as a lack of fitness or poor technique. They include muscle strain and delayed onset muscle soreness (excessive muscle stretching) (Blankenbaker and De Smet 2004, Wong 2005).

There are two types of muscles in respect to the way they cross joints. Most muscles cross one joint, but many muscles cross two. Muscles crossing two joints are strained and perform eccentric contraction; examples include the calf, the hamstring and the quadriceps. If the resisting force is greater than the force generated by the muscle, this is known as eccentric contraction, whereas concentric contraction occurs if the resisting force is less than the force generated by the muscle. Muscles that cross two joints are the most susceptible to injury (Blankenbaker and De Smet 2004).

Muscle fibre type has a significant influence on muscle injury. As shown earlier, in Table 2.1, most muscles are composed of both type one and type two muscle fibres.

Type one muscle fibres are more resistant to muscle fatigue because they have slower contraction (slow twitch fibres). Type two fibres, on the other hand, have a fast contraction time (fast twitch fibres), and thus this type of muscle is more prone to injury (Blankenbaker and De Smet 2004, Wong 2005). Other factors that lead to muscle injuries include the following: insufficient stretching before exercise and warm-up, lack of flexibility, abnormal muscle contraction during running, awkward running style, and a return to sports after incomplete rehabilitation programme (Blankenbaker and De Smet 2004). The latter factor demonstrates the importance of the ability to adequately diagnose and monitor the healing of muscle injuries.

2.5.1 Muscle strain

Muscle strain results from indirect stretch-induced injury. It is common among athletes who are involved in activities that depend on high-speed running, such as football, rugby and basketball. Muscle strain is the rupture of muscle fibres as a result of overstretching. Muscle strain occurs mostly at the myotendinous junction (Blankenbaker 2004, Wong 2005).

Strain injuries are classified into the three following categories: grade one, two and three strain, or mild, moderate and severe, respectively (Peetrons 2002,Wong 2005, Jarvinen 2007). Grade one (mild) strain occurs when the muscle is extended beyond its elastic capability, leading to a tear in a few muscle fibres, typically less than 5%. Other symptoms include minor swelling and discomfort, with no or only limited loss of muscle strength and restriction of movement. The pain is intense, but there will be rapid recovery after conservative treatment (Wong 2005, Jarvinen 2007).

Grade two (moderate) strain involves greater (partial) rupture to the muscle with a clear loss of contraction. There will be acute pain accompanied by swelling. Furthermore, there will be partial detachment of muscle from the adjacent fascia or aponeurosis. Haematoma formation at the myotendinous junction occurs very often (Palmer *et al.*,1999). An example of grade two strain is the detachment of the medial gastrocnemius muscle from its common aponeurosis with the soleus muscle (tennis leg) (Wong 2005, Jarvinen 2007).

Grade three (severe) strain involves complete rupture of the entire muscle cross-section and complete loss of muscle function (Jarvinen 2007). It is usually associated with spasm, retraction and shortening of the muscle (Blankenbaker 2004).

2.5.2 Delayed Onset Muscle Soreness

Delayed onset muscle soreness (DOMS) is a muscular pain, soreness and swelling, that appears several hours or days after unaccustomed or strenuous exercise, such as the commencement or resumption of sports activity in athletes after a period of time without training. It is also called muscle fever (Wong 2005, Kubo *et al.* 2012). Delayed onset muscle soreness is characterised by tenderness and movement pain. In addition, the severity of damage depends on several factors, e.g. exercise intensity, familiarity with exercise, muscle stiffness, the angle of contraction and the velocity of contraction. DOMS is most frequent with eccentric exercise, like downhill running. The nature of the injury is mechanical disruption to the sarcomeres (Connolly *et al.,* 2003, Warren *et al.,* 1993). Injury follows a sequential event pattern, typically: mechanical damage, inflammation and swelling and free radical proliferation. Figure 2.6 depicts this sequence (Declan *et al.,* 2003).

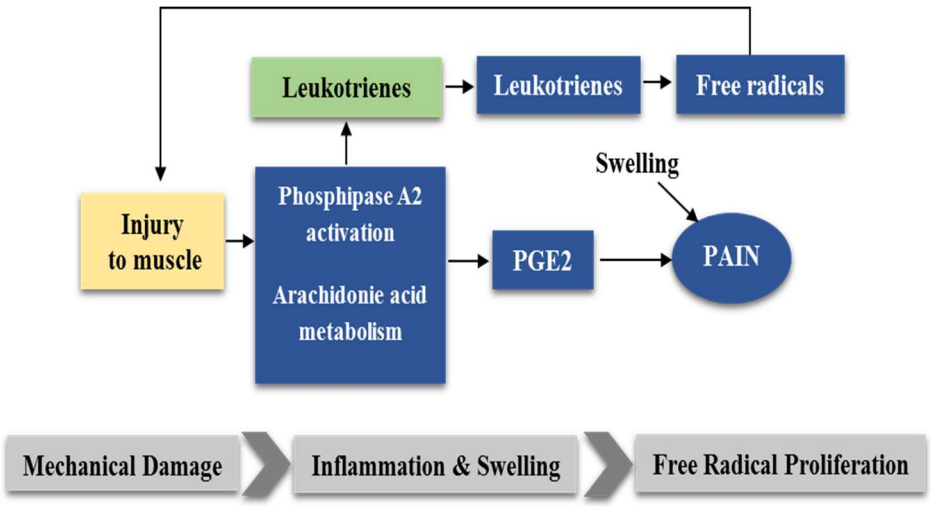

Figure 2.6: Schematic diagram showing possible sequence of injury and delayed onset muscle soreness, adapted from Declan et al. (2003).

2.5.3 Haematoma

Haematoma is the accumulation of blood within a limited space in soft tissue, following direct or indirect injury. In soft tissue, haematoma has two injury mechanisms: following direct contusion, or following a tear in the muscle fibres (indirect) (Klein et al. 1990, Blankenbaker 2004). Contusion can be classified into mild, moderate and severe (Beiner and Jokl 2001; Kary 2010). Injury may lead to damage to the tissue capillaries at the level of the skin or the subcutaneous muscle tissue, resulting in blood leakage. Haematomas very frequently occur among athletes incurring sports related injuries (Nozaki et al. 2008). Furthermore, haematomas are most common in direct contact sports, such as football and rugby (Smith *et al.* 2006). In sports-related injuries, haematoma is common and very frequently involves the quadriceps and gastrocnemius muscles, as shown in Figure 2.7 (Kneeland 1997). Haematoma is a key sign of a muscle tear (Peetrons 2002), and thus an ability to image haematoma is very useful in making a diagnosis of a number of muscle injuries.

Figure 2.7: Injured tissue showing haematoma (Adapted from http://www.essentialoilspedia.com/wp-content/uploads/bruise.jpg).

Haematoma is classified according to its location, the types are intramuscular and inter-muscular haematoma. In intramuscular haematoma, the muscle sheath and the

fascia remain intact, which results in an increase in intramuscular pressure. The symptoms include pain and tenderness, a decrease in muscle function, and swelling after 48 hours. The second type of haematoma, inter-muscular haematoma, results from a torn fascia and sheath. Blood will thus seep between the muscle and the fascia; the symptoms include severe bruising and swelling (Smith et al. 2006).

A recent study carried out by Mueller-Wohlfahrt et al (2014) presented a new and comprehensive classification system for athletic muscle injuries. The research group proposed the term 'tear' for structural injuries of muscle fibres, instead of 'strain'. The group concluded that the previous grading systems have a lack of sub-classification within the grades or types. Furthermore, the group classified indirect muscle injuries into functional muscle disorder and structural muscle injury. Functional muscle disorder is defined as "acute indirect muscle disorder without macroscopic evidence (in MRI or ultrasound) of muscular tear". Structural muscle injury is defined as "any acute indirect muscle injury with macroscopic evidence (in MRI or ultrasound) of muscle tear" (Mueller-Wohlfahrt et al. 2012). The new classification is represented in Table 2.2.

Table 2.2: New suggested muscle injury classification (Mueller-Wohlfahrt et al. 2012).

	Type	Sub-type	
Indirect muscle injury	Functional muscle disorder	1:Over-exertion muscle disorder	A: Fatigue-induced muscle disorder.
			B: Delayed-onset muscle soreness (DOMS).
		2:Neuromuscular disorder	A: Spine-related neuromuscular Muscle disorder.
			B: Muscle-related neuromuscular Muscle disorder.
	Structural muscle injury	3: Partial muscle tear	A: Minor partial muscle tear.
			B: Moderate partial muscle tear.
		4: (Sub)total tear	Subtotal or complete muscle tear and tendinous avulsion
Direct muscle injury		Contusion & Laceration	

2.6 Mechanism of Skeletal Muscle Healing

It is very important to understand the mechanism of skeletal muscle cellular healing process, in order to achieve successful treatment and healing monitoring. Skeletal muscle reacts to injury in a constant pattern, irrespective of the cause of the injury. The healing process is a repair mechanism which consists of three distinct phases: degeneration and inflammation, regeneration, and fibrosis (Fukushima *et al.* 2001, Garrett et al. 1989, Garrett et al. 1990, Kasemkijwattana et al. 2000, Jarvinen 2007). The first phase starts a few days after trauma and is characterised by local swelling and haematoma formation to fill the gap in the stump of the myofibres. Necrosis takes

place at both ends of the ruptured myofibres. The degeneration and inflammation response starts with the infiltration of activated macrophages from the torn blood vessels (Honda *et al*., 1990, Hurme *et al*., 1991).

The regeneration phase starts five to ten days after trauma and is characterized by phagocytosis of the damaged tissue and the regeneration of the injured muscle. The release of numerous growth factors has been noticed (Alameddine *et al*. 1989, Carlson and Faulkner 1983).

The final phase, fibrosis, normally starts two to three weeks post-injury and it is characterized by the formation of scars as the final product of muscle repair (Li *et al.,* 2004, Li and Huard 2002). However, partial tears normally heal completely without fibrosis, whereas moderate partial tears can result in a fibrous scar (Mueller-Wohlfahrt *et al.* 2012).

2.7 Injury to the Gastrocnemius Muscle

The first reported case of injury to the gastrocnemius muscle was presented by Powel in 1883 in a patient who had a sudden sharp pain during tennis activity (Powel 1883). Much later, Froimson described injury to the gastrocnemius following a tennis serve, during the push-off movement, as a painful condition of parital tearing of the medial belly, resulting from the overstretching of the muscle by concomitant ankle dorsiflexion and full knee extension (Froimson 1969). Injury to the gastrocnemius muscle most commonly occurs in the medial head (Bryan 2009). Rupture of the medial head of the gastrocnemius muscle, also known as tennis leg, is common in sports activities, e.g. hill running, tennis and jumping (Bianchi *et al.* 1998, Delgado *et al.* 2002).

The gastrocnemius is susceptible to a high risk of injury because it crosses the knee and ankle (two joints) and is composed of a high density of type two fast twitch muscle fibres (DeLee *et al.* 2003, Garrett 1996, Armfield 2006, Simon *et al.* 2006, Nsitem 2013).

Gastrocnemius muscle injury results from the application of an eccentric force during knee extension (flexion). Gastrocnemius muscle injury occurs near the musculotendinous junction, where the muscle attaches to the fascia leading to the Achilles tendon. Patients usually describe the injury as a 'pop' in the calf, and they suffer severe pain and swelling during the first 24 hours (Delgado *et al.* 2002).

2.8 Clinical Assessment of Muscle Injury

Clinical examination consists of inspection and palpation of the injured muscles. Furthermore, testing the function of the muscles involved, with and without external resistance, is also carried out. The diagnosis is relatively easy if a typical history of muscle contusion or strain is accompanied by an obvious swelling, whereas if there is deep haematoma within the muscle belly, clinical diagnosis becomes more difficult (Jarvinen *et al.,* 2007).

Studies by different research groups have suggested that muscle injury assessment should start with taking a precise history of the occurrence and circumstances of the injury, the patient's symptoms and any previous relevant history. This should be followed by a careful clinical examination with inspection, palpation of the injured area, comparison with the uninjured side and the testing of muscle function (Askling *et al.,* 2007; Askling e*t al.*, 2008).

The clinical assessment of muscle injury can be divided into two categories: subjective and objective, as presented in detail in the flow charts below (Tables 2.3 and 2.4) (Porter 2013).

The purpose of subjective assessment is to collect all relevant information about the injury, such as its site, nature and behavior, and also information about the onset of symptoms. Furthermore, it includes reviewing the patient's history, such as general health, medication and social issues. In this system of classification, subjective assessment also includes a review of past imaging and laboratory investigations. Imaging might include planar radiography, ultrasound, x-ray computed tomography or magnetic resonance imaging. One of the main components of laboratory testing is the measurement of creatinine kinase (CK) concentration in blood to help detect

muscle damage. CK is a skeletal muscle enzyme and its blood concentration is used as a marker of the functional status of muscle tissue. An increase in blood levels of this enzyme might indicate cellular necrosis or tissue damage following acute and chronic muscular injuries (Brancaccio *et al.,* 2010). However, a single non-pathological cramp might also cause a substantial rise in CK levels (Brancaccio *et al.,* 2007).

The outcome of subjective assessment should lead to the next step in assessment. The aims of objective assessment are to find abnormalities of function by implementing different approaches, such as passive, active, resisted and neurological tests of the injured area. The goal of this task is to reproduce all or part of the patient's symptoms and to determine the range, resistance, pattern, and pain response for each movement. In addition, it includes trying to obtain signs of the disorder and monitoring the injury for a re-assessment of the effectiveness of the treatment.

Subjective and objective assessment flowcharts are presented in Tables 2.3 and 2.4 (Porter 2013).

Table 2.3: Flow chart of subjective clinical assessment of muscle injury (Porter 2013).

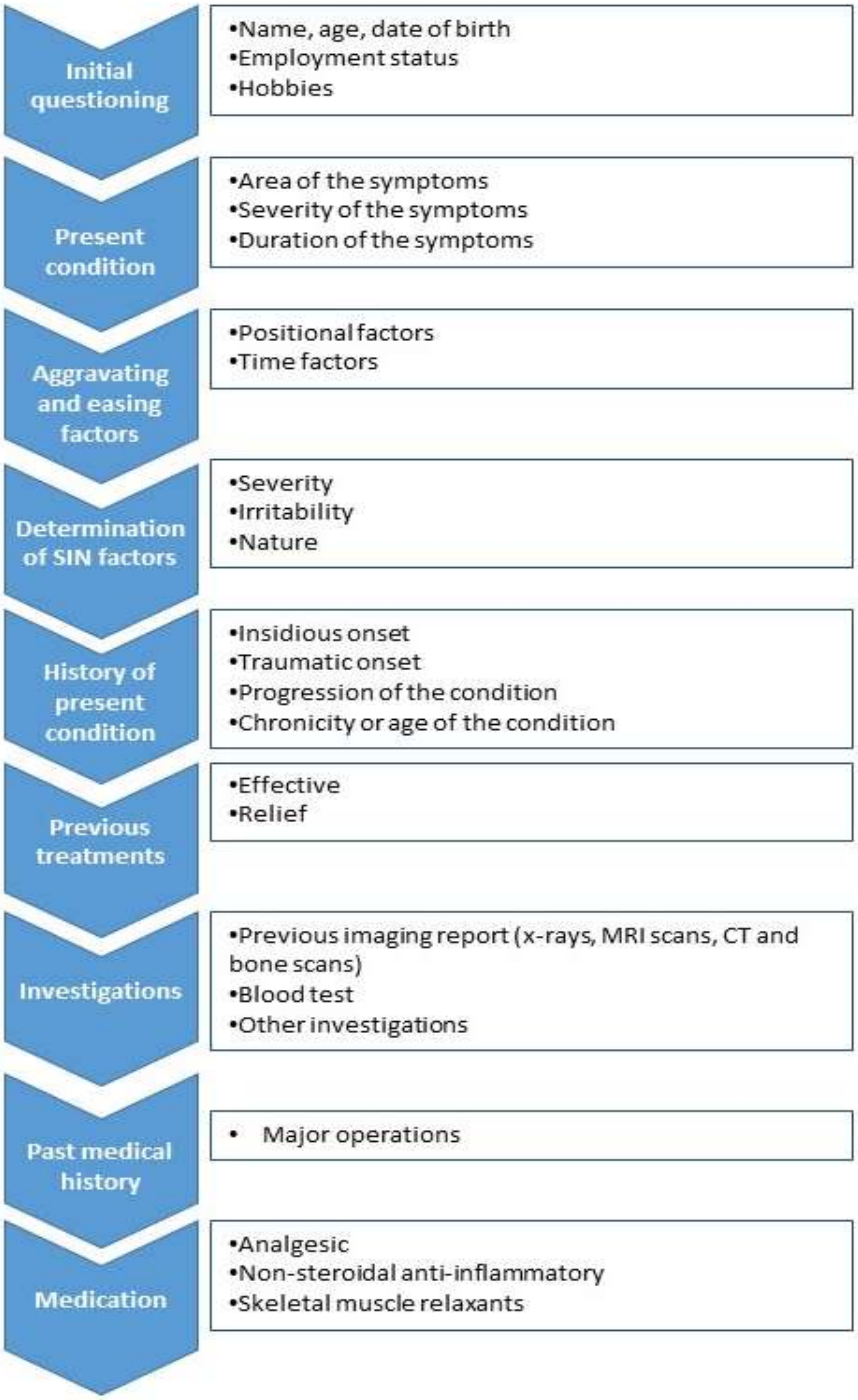

Table 2.4: Flow chart of objective clinical assessment of muscle injury (Porter 2013),

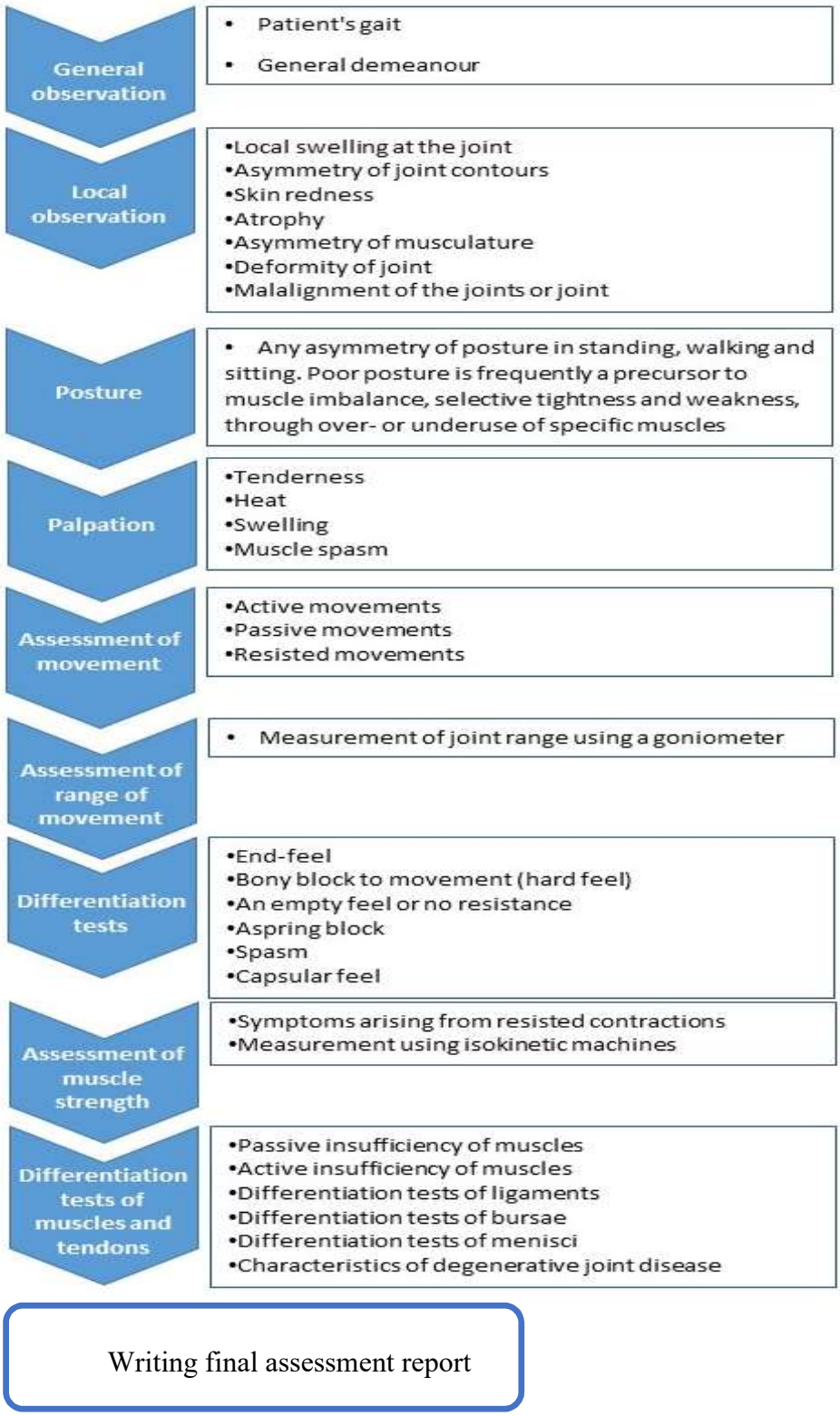

2.9 Imaging Muscle Injury

Investigation of muscle injury should always start with activities such as careful history taking, and physical examination such as inspection and palpation. It may also include muscle testing with and without resistance. However, information obtained about the nature and extent of the injury is often limited because of factors such as pain and swelling. In these circumstances, muscle imaging with modalities, such as ultrasound (US), magnetic resonance imaging (MRI) or x-ray computed tomography (CT) is useful to verify and characterize the injury. In particular, ultrasound and MRI have become widely adopted for the assessment of muscle injury (Jarvinen *et al.* 2007).

The modalities used for muscle imaging have their own technical characteristics and these are compared and contrasted in Table 2.5.

Table 2.5: Comparison of muscle imaging modalities, adapted from Clague et al. (1995).

	Ultrasound	**CT**	**MRI**
Availability	Readily available	Readily available	Increasingly available
Relative cost	Inexpensive	Expensive	Very expensive
Portability	Portable	Fixed	Fixed
Soft tissue contrast	Fair	Good	Excellent
Muscle visualisation	Fair	Good	Very good
Repeated investigation	Yes	Limited	Yes
Safety	Non-ionizing radiation	Ionizing radiation	Non-ionizing radiation

2.9.1 Muscle Imaging with MRI

2.9.1.1 Physical Basis of MRI

MRI is a very sophisticated medical imaging technology. It is based on the magnetic properties of hydrogen nuclei (protons) when placed in a strong external magnetic field. Within the human body, protons are abundant in water and in fat. Under the influence of the external field, they develop a net magnetization in the same direction as the field and they also precess about the field direction at a characteristic frequency. When a pulse of radio frequency (RF) radiation of the same frequency is applied, resonance occurs and the magnetization is deflected from the field direction. Immediately afterwards, relaxation occurs: longitudinal magnetization recovers along the external field direction with a characteristic time T_1 while transverse magnetization (in the plane normal to the external field) decays with a characteristic time T_2. Proton density (the number of protons per unit volume) and the relaxation times T_1 and T_2 vary between tissues and for a particular tissue, between its condition in health, disease and injury.

In magnetic resonance image acquisition, RF pulse sequences may be chosen such that the detected RF signal is weighted according to T_1, T_2 or proton density. This allows great flexibility in creating image contrast. In particular, MRI demonstrates much better natural contrast between soft tissues than other modalities; in some situations, contrast may be enhanced by the administration of agents that modify values of the relaxation times. More complex pulse sequences may be used to highlight or suppress fat or fluid.

Spatial localization of RF signal source within tissue is accomplished with the use of gradient magnetic fields, which may be applied along the external field or orthogonally to it. Gradients are applied to select slice position, orientation and thickness and to encode positional information using signal frequency and phase. Projection data are collected in such a way as to allow a set of tomographic slices to be reconstructed using two-dimensional Fourier transformation; in these slice images pixel values are related to detected RF signal amplitude. Appropriate combination of

gradient magnitude, signal sampling rate and reconstruction parameters yields images with very good spatial resolution. However, there is a trade-off between resolution (small pixel size and slice thickness) and noise. In addition, noise is relatively high in images whose weighting results in small signal amplitudes.

A more complete description of the physics and technology of MRI is given in Appendix A.

2.9.1.2 Advantages and Disadvantages of MRI

MRI has many advantages as a medical imaging technology; these include the following:

- There is no hazard from ionizing radiation;
- It may be applied to the diagnosis of a wide range of medical conditions;
- It is capable of producing direct coronal, transverse and sagittal slice images and, indeed, slices in any arbitrary direction;
- It does not produce artefacts at air-bone interfaces.

The disadvantages of MRI can be listed as follows:

- The imaging procedure is lengthy and noisy;
- In general, only static images are produced;
- The technology is very expensive and availability is still limited in some areas;
- A special site, remote from stray magnetic fields and RF radiation, is needed for operation of the MRI equipment;
- It cannot be used for patients with certain implanted medical devices;
- Patient movement over a prolonged image acquisition time may cause image artefacts and the need for a re-scan - in some cases, this may be overcome by sedating the patient but this causes drowsiness for the remainder of the day;
- Some patients experience discomfort, worry and stress because of claustrophobia induced by the tunnel-like scanner gantry;
- When required, the use of artificial contrast material may cause kidney problems or result in an allergic reaction at the injection site or elsewhere.

2.9.1.3 MRI of Muscle

MRI has gained widespread application for muscle imaging. One reason for this is that it is relatively less operator dependent (than ultrasound imaging for example), through the use of well-designed and standardized imaging protocols. It is also the case that magnetic resonance images can be interpreted globally.

MRI is very efficient in visualizing both deep and superficial muscles, with most studies being confined to the leg. It generates a set of contiguous thin tomographic slices, which means that it can provide panoramic views of the body. Therefore, it has the capability to assess deep muscle and detect lesions that may be missed by ultrasound. Congenital myopathies and congenital muscular dystrophies are both characterized by muscle weakness and wasting; MRI studies have shown that several of these conditions display specific patterns of muscle involvement, which can help in the differential diagnosis of these disorders (Jungbluth, 2004). Muscle MRI is able to detect and differentiate between fatty infiltration and oedema; the latter can be an early sign of inflammatory myopathy, a condition characterized by muscle inflammation and weakness. Thus MRI is of additional value in cases of suspected inflammatory myopathy when ultrasound findings are normal (Pillen 2011).

2.9.1.4 Application to Muscle Injury

Although all muscle injuries should have a clinical assessment, MRI is a useful tool to confirm clinical findings. Indeed, MRI is now considered essential for muscle injury assessment at most centres worldwide where the technology is available. It has application across the range of muscle injuries.

Contusion leads to oedema and interstitial haemorrhage, which cause muscle swelling. In the magnetic resonance fat suppressed image, the injured muscle shape is feather-like, as presented in Figure 2.8. In a T_1 weighted image, the presence of blood may result in a faint high signal, as presented in Figure 2.9. This finding is similar to that in a Grade 1 muscle strain injury, but it is easy to distinguish between the two cases by clinical assessment of the injury. The morphology of haematoma development follows the following pattern. At the beginning, there is an irregular muscle laceration

and after 48 hours, there is a clear fluid collection within the muscle. The muscle surrounding the haematoma usually remains as a high signal on fluid-sensitive magnetic resonance pulse sequences, as presented in Figure 2.10. The signal characteristics of haematoma vary with time, depending on the predominant blood product, as illustrated in Table 2.6. Moreover, there will be further haematoma healing phases: fibrosis (scar formation) and/or calcification. The fibrosis of the margins of the haematoma will contract the lesion over time, whereas calcification will lead to the development of a condition known as myositis ossificans (Lee *et al.* 2012).

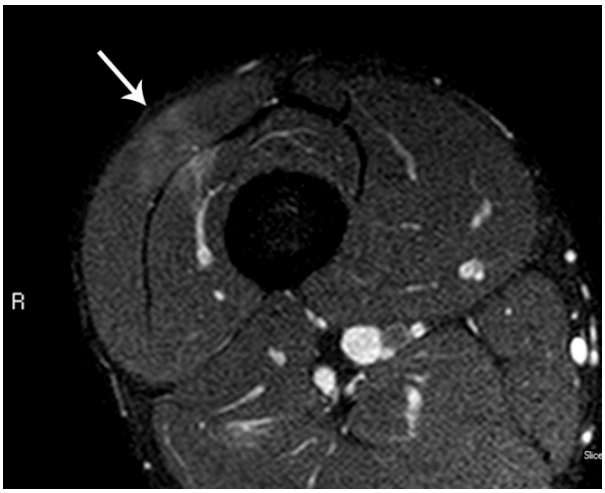

Figure 2.8: Transverse magnetic resonance fat suppressed image in a 26 year old professional male footballer with a minor thigh contusion. The arrow indicates the direction of the impact of the blow. Note the high signal within the vastus lateralis and vastus intermedius muscles in the line of the force vector (Lee et al. 2012).

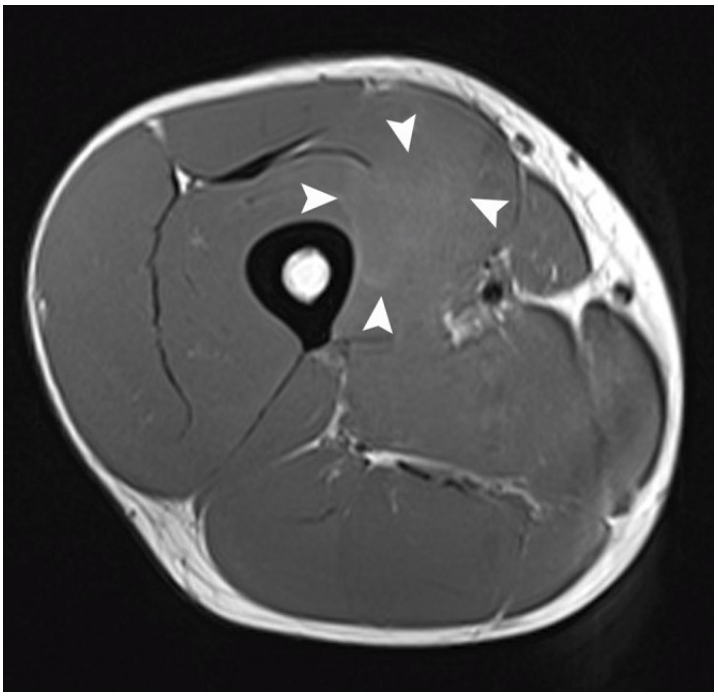

Figure 2.9: Transverse magnetic resonance image in a 32 year old professional footballer with a deep surface haematoma of the thigh. Note the faint high signal margins of the haematoma indicated by the white arrows (Lee et al. 2012).

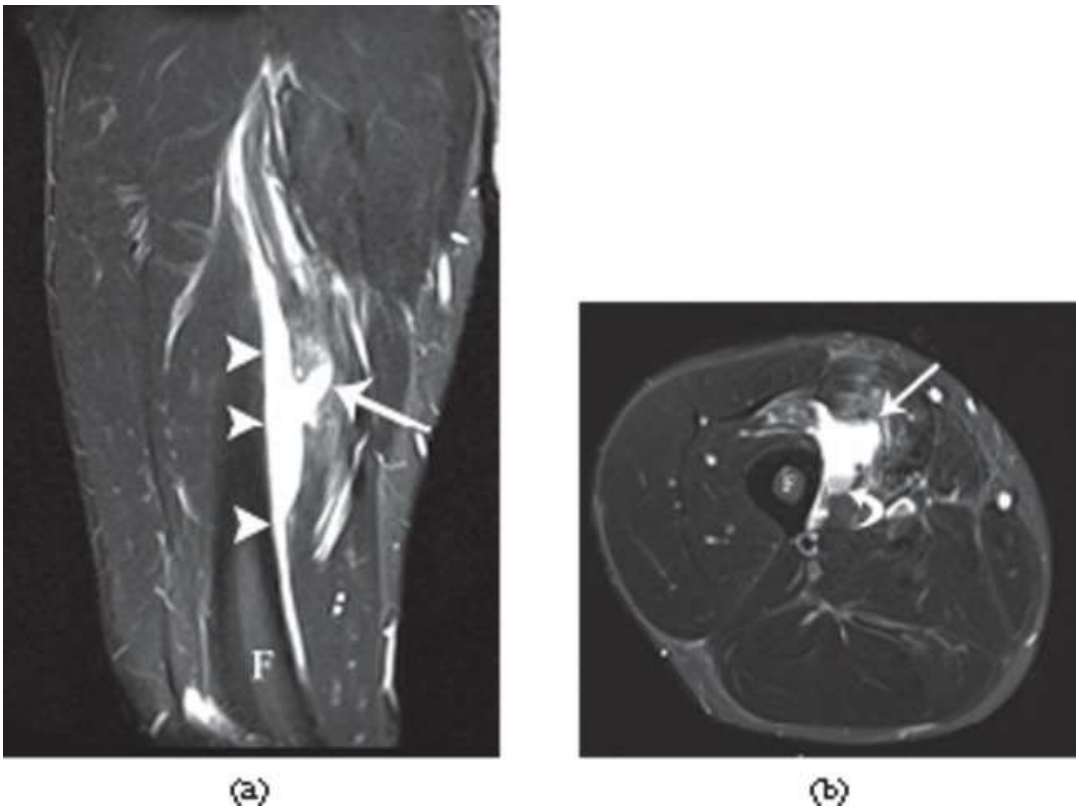

Figure 2.10: Magnetic resonance images in a 32 year old male professional footballer with a deep surface thigh haematoma: (a) coronal and (b) axial (transverse) images demonstrating a large haematoma deep to the vastus intermediate muscle (arrow heads) adjacent to the femoral cortex (F). Note the laceration into the muscle (arrow) and the layering of blood products on the axial image (curved arrow) (Lee et al. 2012).

Table 2.6: Changing magnetic resonance signal characteristics of a haematoma with time, dependent on the nature of the predominant blood product within (Lee et al. 2012).

Stage	Blood product	T_1 signal intensity	T_2 signal intensity
Hyperacute (< 4h)	Intracellular oxyhaemoglobin	Intermediate	Bright
Acute (4 - 6 h)	Extracellular oxyhaemoglobin	Intermediate	Dark
Early sub-acute (6 - 72 h)	Intracellular methaemoglobin	Bright	Dark
Late sub-acute (72 h - 4 weeks)	Extracellular methaemoglobin	Bright	Bright
Chronic (> 4 weeks)	Haemosiderin	Dark	Dark

MRI is capable of grading muscle injury although this ability depends on the magnetic field strength and RF pulse sequence, both of which influence image quality (Kujala *et al.,* 1997, Jarvinen *et al.,* 2007, Elliott *et al.,* 2008, Ekstrand *et al.,* 2012).

In a Grade 1 muscle strain, a high signal is expected at the injury site on fluid sensitive, fat suppressed magnetic resonance pulse sequences due to oedematous blood radiating from the musculotendinous junction along fascicles of the muscle. This leads to feather shaped region within the muscle image, as presented in Figure 2.11. Similarly to ultrasound, perifascial fluid may be observed on MRI in Grade 1 strain (Lee *et al.,* 2012).

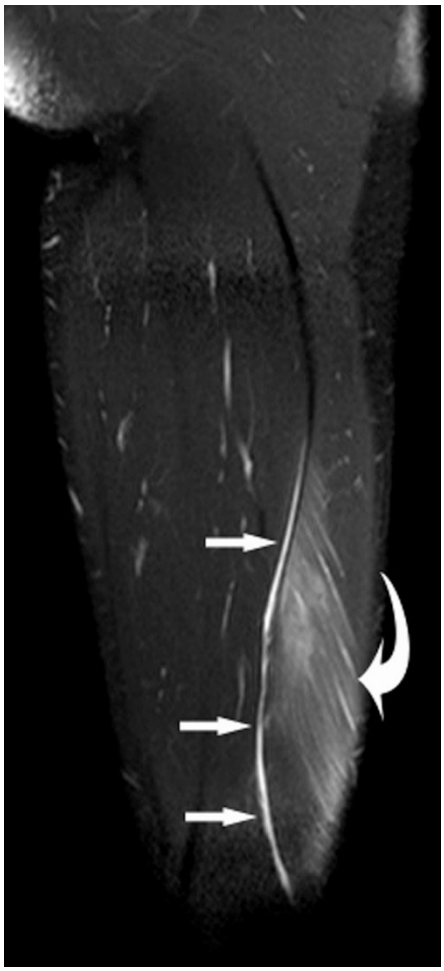

Figure 2.11: Sagittal MRI scan of a 28 year old male professional footballer with Grade 1 distal hamstring strain. Note the feathery high signal along the muscle fibres (curved arrow) and the small slither of fluid in the epifascial space (arrows)(Lee et al. 2012).

In a Grade 2 strain, the main finding is the distortion of the normal muscle architecture at the injury location, which leads to haematoma formation at the musculotendinous junction, as illustrated in Figure 2.12. The feather type shape of Grade 1 strain is also present. Furthermore, laxity of the central tendon may be noticed, as illustrated in Figure 2.13 (Lee *et al.,* 2012).

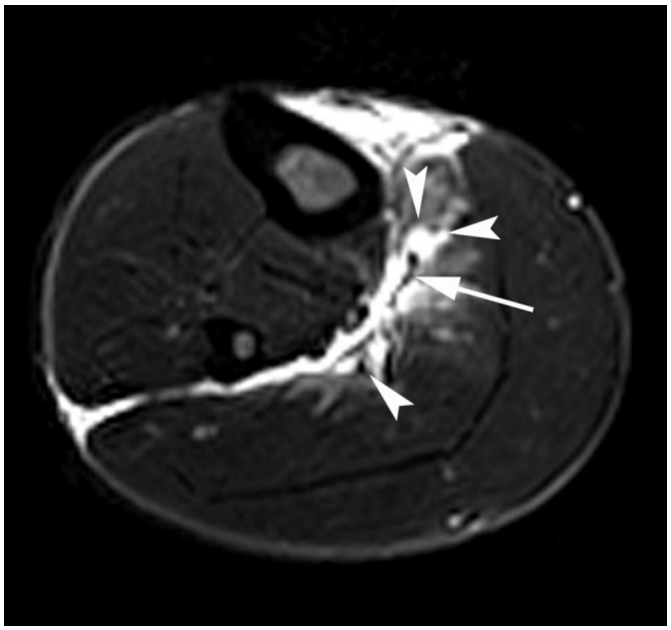

Figure 2.12: Transverse short tau inversion-recovery MRI scan of a 29 year old male professional footballer with Grade 2 calf strain. Note the separation of the muscle (arrow heads) away from the deep soleus tendon (arrow) and the prominent epifascial fluid on the deep medial and lateral surface of the muscle (Lee et al. 2012).

Figure 2.13: Coronal fat saturated proton density MRI scan of the calf of a 29 year old male professional footballer with Grade 2 calf strain. Note the laxity within the central tendon (arrows) at the epicentre of the muscle injury (Lee et al. 2012).

In Grade 3 muscle strain, there is complete disruption of the musculotendinous unit, with haematoma filling the space in between. When there is avulsion of the musculotendinous unit from the bony attachment, as illustrated in Figure 2.14, this is sometimes described as Grade 3B disorder. This is common in the calf, where muscle fibres stay normal and without rupture (Lee *et al.,* 2012; Peetrons 2002).

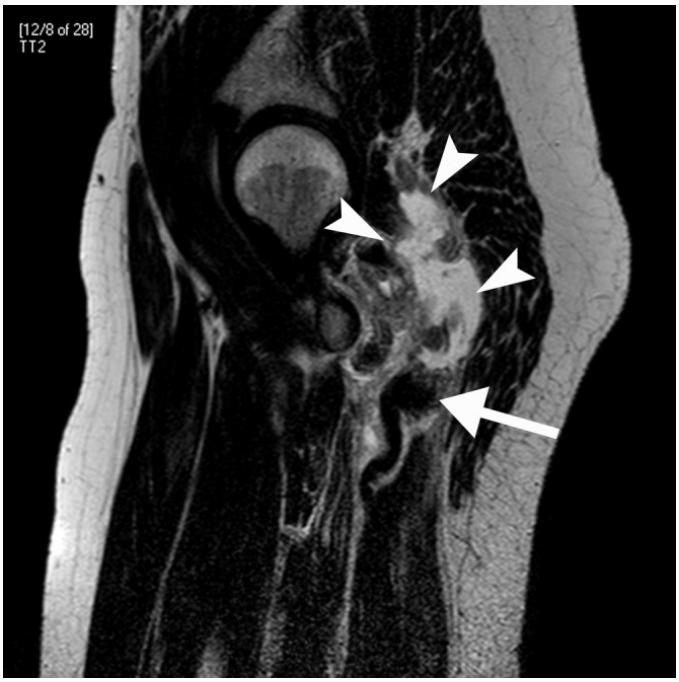

Figure 2.14: Sagittal MRI scan of a 38 year old female footballer with Grade 3 hamstring avulsion. The hamstring tendons have avulsed (arrow) and the tear gap is filled by a heterogeneous signal intensity haematoma (arrowheads) (Lee et al. 2012).

MRI also has a role in predicting recovery from muscle injury. For example, in a five-year study, Gibbs et al (2004) showed that injury lesion length and cross-sectional area measured with MRI could be used to predict recovery time from acute Grade 1 strains in Australian Rules football players. However, neither of these indices of size nor the recovery time were reliable indicators of the likelihood of recurrence of strain within the same sporting season.

2.9.2 Muscle Imaging with Ultrasound

2.9.2.1 Physical Basis of Ultrasound Imaging

Ultrasound imaging uses pulses of high-frequency sound (2-20 MHz) and their echoes to produce real-time images of body organs and tissues. This is called the pulse-echo technique. The pulses are produced by a multi-element transducer (probe), which operates on the piezoelectric principle. The probe is applied directly to the skin with good acoustic contact being ensured through the use of a coupling gel. The pulses are

transmitted from the transducer through the gel into the scanned body. The transducer also collects the echoes that return and these are processed by a computer to develop an image (Kremkau 2006).

Echoes are produced through reflection at tissue boundaries and scattering by small tissue structures as a result of differences in acoustic impedance. The time between the issue of a pulse and the detection of an echo is used to calculate the depth within tissue of the echo source, assuming a standard vale of the speed of sound (1540 m/s). The attenuation of ultrasound increases with the distance traversed in tissue. Time-gain compensation is used to overcome this phenomenon so that signals derived from scatters of equal strength are displayed with equal intensity irrespective of depth.

The image is generated by electronically sweeping the ultrasound beam through the tissue region of interest. The result is an image of a slab or slice of tissue, although this is not reconstructed from projections as is the case with MRI and CT. The beam is focused to improve lateral spatial resolution. Axial resolution is determined by spatial pulse length while slice thickness depends on transducer width. In general, the greater the ultrasound frequency, the better is the image quality, although depth of penetration in tissue is reduced since attenuation is proportional to frequency.

2.9.2.2 Advantages and Disadvantages of Ultrasound Imaging

The advantages of medical imaging with ultrasound include the following:

- It is non-invasive, safe and relatively painless;
- It uses no ionizing radiation;
- It does not usually require injection of a contrast medium;
- It may be used to diagnose a range of conditions in different parts of the body, such as the abdomen, pelvis, blood vessels, breast, kidneys, muscles, bones and joints;
- It can be used to assess the health and development of a baby during pregnancy.

The disadvantages of ultrasound imaging can be listed as follows:

- The quality and interpretation of the image is operator dependent;
- The image can be affected by the presence of air and calcified areas in the body (e.g. bones, plaques and hardened arteries), and by a person's body size.

2.9.2.3 Ultrasound imaging of Muscle

As a medical imaging modality, ultrasound has the advantages of availability, low cost, rapid image acquisition and ease of use during examination. The technology has improved dramatically over the past few years. For example, high frequency transducers provide excellent image spatial resolution of 200-450 μm in-plane 0.5-1.0 mm section thickness, which exceed the values obtainable with MRI (Lin *et al.*2008). However, high frequencies limit penetration depth in muscle and other tissue and are best suited for the assessment of superficial structures. Deeper muscles, are difficult to visualise, especially when overlying muscles are affected. To display deeper muscles, transducers that can emit ultrasound at lower frequencies have to be used (Pillen, 2010). New ultrasound developments have resulted in the ability to image a volume of tissue giving panoramic images, which make it possible to visualize several muscles in one particular plane.

Ultrasound may be used to image muscles in the arms as well as the legs; this can be of additional value when selective arm muscle involvement is present. The sonographic appearance of muscle is fairly distinct and it can easily be discriminated from surrounding structures such as subcutaneous fat, bone, nerves and blood vessels. Normal muscle is relatively black, i.e. has low echo intensity. In the transverse plane, perpendicular to its long axis, muscle has a speckled appearance because of reflections from perimysial connective tissue, which is moderately echogenic.

An important application of muscle ultrasound is screening for the presence of general neuromuscular abnormalities, especially in patients who cannot remain still. Neuromuscular disease is a very broad term that encompasses many conditions that impair the functioning of the muscles, either directly due to pathologies of the voluntary muscle, or indirectly due to pathologies of nerves or neuromuscular

junctions. Furthermore, ultrasound can be used for guidance in selecting the optimal site for muscle biopsy, or when nerves and vessels need to be avoided (Pillen 2011). However, the use of diagnostic ultrasound for the assessment of muscle disorders is limited by operator and patient dependent factors. In some situations, such as patients with large thighs, ultrasound imaging can miss deep lesions (Lee *et al.* 2012) due to attenuation of the acoustic signal. Under these circumstances, alternative imaging modalities (such as MRI and CT) that are not susceptible to depth effects are more effective.

A prospective pilot study of 33 patients with suspected neuromuscular disorder, followed by a larger study of 150 patients, showed that muscle ultrasound is a useful and reliable tool in the diagnostic evaluation of these patients. Muscle ultrasound was capable of detecting neuromuscular disorders with an overall positive predictive value of 91% and a negative predictive value of 86%. Above the age of 3 years, muscle ultrasound was very reliable with a negative predictive value of 95%. Below the age of 3 years, more false negative results were found giving a positive predictive value 75%. This was caused by the fact that often only few structural changes are present in early stages of a neuromuscular disorder, resulting in no or only slightly increased muscle echo intensity (Pillen 2011).

Figure 2.15 shows digital ultrasound images taken from two individuals of 3.5 years of age. The rectus femoris muscle is encircled. The distribution of echo intensity is shown in the frequency histograms below the images (on a scale in which black = 0 and white = 255). The rectus femoris of the DMD patient has increased muscle echo intensity, with the corresponding histogram being displaced to the right. The attenuation of the ultrasound beam with depth is clear, i.e. the echo intensity in deeper areas of the muscle is decreased compared to that in superficial areas.

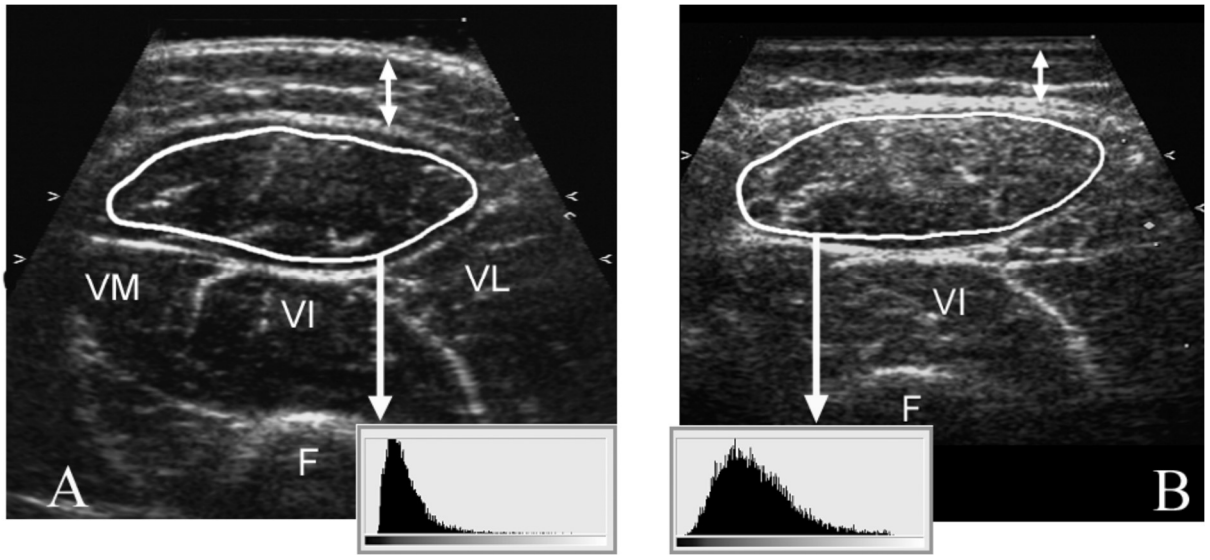

Figure 2.15: Transverse ultrasound images of a normal left quadriceps muscle (A) and of a patient with Duchenne muscular dystrophy (DMD) (B). Key: VM, vastus medialis; VL, vastus lateralis; VI, vastus intermedius; F, femur; double arrow, subcutaneous tissue.

However, visual evaluation of muscle ultrasound images gives a sensitivity of only 67 to 81% for the detection of neuromuscular disorders in children. This value of sensitivity is relatively low if the purpose of muscle ultrasound imaging is to serve as a screening tool for neuromuscular disorders.

Peetrons (2002) used linear-array transducers to visualise a large surface of muscle tissue within one slice of that muscle in order to identify deep as well as superficial lesions. With respect to muscle tumours, the study demonstrated limitations of the modality including lack of specificity and loss of sensitivity in the presence of tumour extension.

2.9.2.4 Application to Muscle Injury

Ultrasound imaging is a significant modality for the diagnosis of most types of muscle injury. It is becoming increasingly popular in elite sport and is frequently performed by radiologists and sports clinicians in the acute and hyper-acute injury setting (up to 7 days post injury). However, the ideal time to conduct the initial assessment is between 2 and 48 h after muscle trauma. It can be used for muscle injury grading and to assess the extent of haematoma. In this context, the high frame-rate capability of

ultrasound is important because it permits real-time dynamic imaging. Thus imaging can be done while mobilizing an injured limb, which increases the sensitivity of detection of muscle fibre disruption and assessment of muscle injury healing (Crema et al. 2015).

The earlier the diagnosis, the easier it is to monitor injury healing. Ultrasound may be used to in the follow-up of muscle injuries (5-7 weeks) to assess healing and it is a favourable modality for observing muscle injury complications such as cysts, hernias and ossification. In his study, Peetrons (2002) found that ultrasound was superior to MRI for following-up lesions and detecting problems such as fibrosis, cystic haematomas or myositis ossificans.

On an ultrasound image, a contusion is seen as an ill-defined area of hyper-echogenicity within the muscle that crosses fascial boundaries (Figure 2.16). In the hyper-acute situation, the injured muscle initially appears swollen and may be isoechoic with adjacent unaffected muscle. If the impact force is great enough, there will be significant rupture of muscle fibres and bleeding into a potential space, resulting in haematoma formation. In the first 24–48 h, the haematoma will appear as an irregularly outlined muscle laceration separated by hypoechoic fluid with marked increased reflectivity in the surrounding muscle (Figure 2.17). During this period, the haematoma may solidify and become hyper-echoic to the surrounding muscle. After 48–72 h, the haematoma develops into a clearly defined hypo-echoic fluid collection with an echogenic margin.

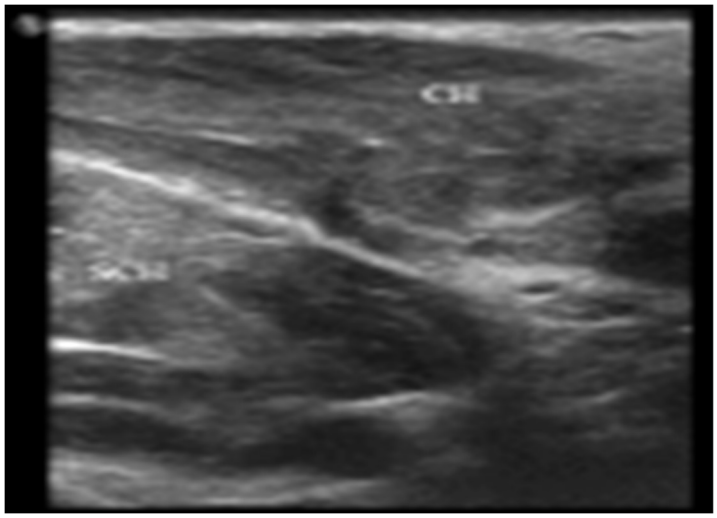

Figure 2.16: A 27-year-old male elite boxer presenting with pectoralis muscle contusion following punch injury to the chest. Note the generalised reflectivity within the clavicular (CH) and sternocostal (SCH) heads of the pectoralis major muscle.

This echogenic margin gradually enlarges and "fills in" the haematoma in a centripetal fashion (Figure 2.17). If the haematoma causes intense pain, exerts a local mass effect on adjacent neurovascular structures or places the limb at risk of compartment syndrome, evacuation of the clot may be necessary. This is usually performed under ultrasound guidance 10–14 days after the initial injury.

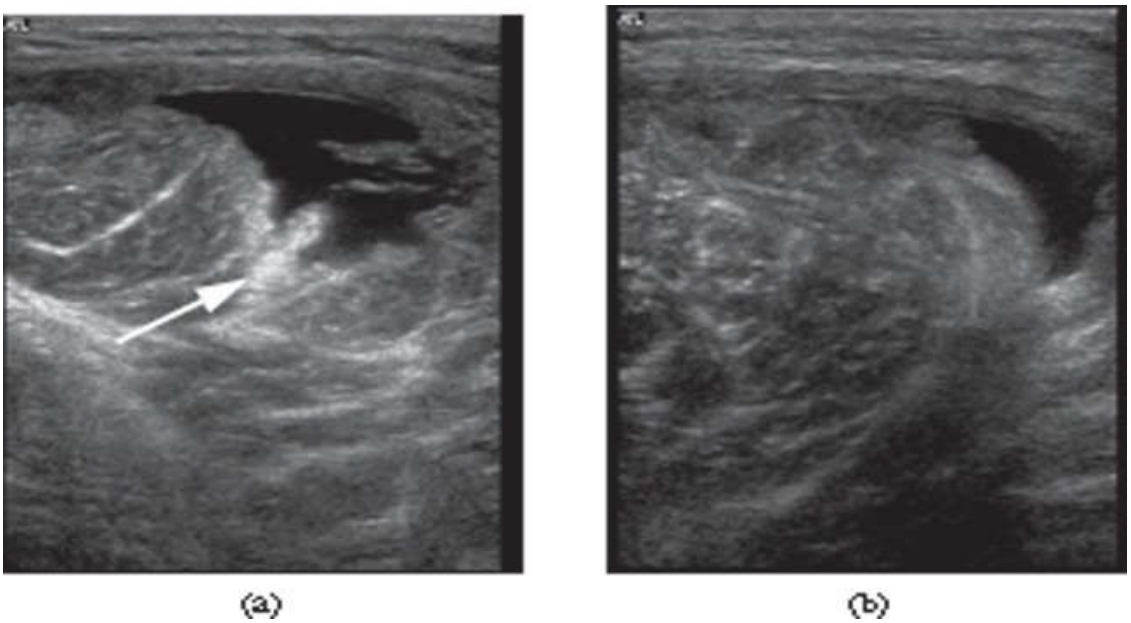

Figure 2.17: A 26-year-old male professional footballer with thigh haematoma. (a) Axial sonogram of the anterolateral thigh 2 days following a direct blow to the lateral side. Note the echogenic torn muscle tissue (arrow). (b) Axial sonogram taken 2 weeks later showing filling in of the haematoma.

2.9.3 Muscle Imaging with X-Ray CT

2.9.3.1 Physical Basis of CT

Like MRI, x-ray CT is a technology that reconstructs tomographic slice images of the body. An x-ray source (tube) and x-ray detectors are attached to a rigid gantry that rotates rapidly about the longitudinal axis of the patient. As it does so, x-ray attenuation is measured along multiple paths through the body and the imparting of radiation dose to the patient is an inevitable consequence of this process. The resulting projection data are reconstructed into transverse slices using filtered back-projection or iterative techniques. Pixel values represent tissue linear attenuation coefficients, although the latter are usually expressed relative to the attenuation coefficient of water as CT numbers. Linear attenuation coefficient is strongly dependent on tissue density.

In CT, there is high contrast between bone and soft tissue because of the large density difference and other factors. However, density does not vary much between different soft tissues and so soft tissue contrast is subtle, but it can be revealed by limiting noise and careful windowing of the digital images. As with MRI, small pixels and thin slices give the best spatial resolution at the cost of relatively high noise. Spatial resolution is primarily determined by detector size and choice of reconstruction algorithm, while noise increases with patient size and decreases with radiation dose.

2.9.3.2 Advantages and Disadvantages of CT

CT has many advantages as a medical imaging technology; these include the following:

- It is quick and painless;
- It costs less than MRI;
- It has excellent spatial resolution;
- It can image both bone and soft tissue;
- Modern CT scanners are fast enough to provide real-time images.

The disadvantages of CT can be listed as follows:

- There is a risk to patients because of the relatively high radiation dose;

- Intravenous contrast agents are required under some circumstances e.g. blood vessel imaging;
- It is expensive in comparison to ultrasound imaging;
- Interfaces at which there is a large change in density produce artefacts e.g. bone-air and tissue-metal (implant);
- It is not always available.

2.9.3.3 CT Imaging of Muscle

Advances in CT technology, such as helical scanning with a multi-row detector, have helped in imaging muscle tissue with this modality. Since contrast depends on density differences, CT is able to visualize fatty infiltration, but not scar formation (fibrosis) in deep and superficial muscles. CT has the disadvantage of using ionizing radiation, and this makes it a relatively unattractive modality for repeated imaging, such as follow-up studies to assess the progression of muscle disease (Pillen 2011).

In a CT angiography study conducted by Mulatti et al (2012) to diagnose arteriovenous fistula, it was evident from the contrast-enhanced images that with appropriate windowing of the digital images, it is possible to distinguish thigh muscle boundaries as shown in Figures 2.18 and 2.19. The study also highlighted the effect of motion artefacts on the acquired images; these artefacts appeared as streaks as shown in Figure 2.20. Despite this drawback, it is clear that CT may be used to image muscle and, with appropriate enhancement, reveal muscle boundaries. Swash et al. (1995) demonstrated the ability of CT to acquire calf muscle images and to depict the borders of the medial and lateral heads of gastrocnemius muscle (Figure 2.21).

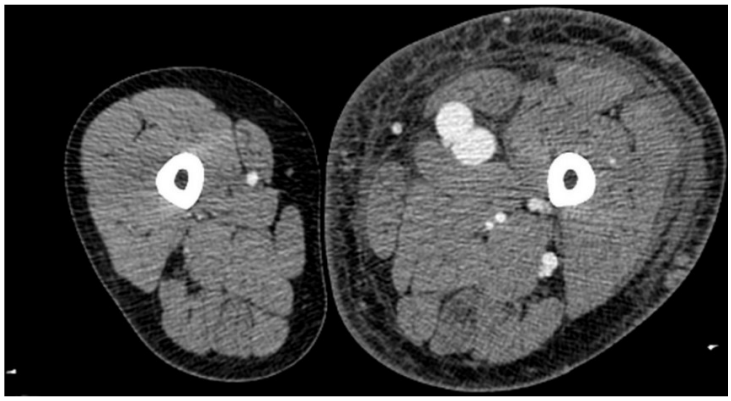

Figure 2.18: Transverse CT image of the thighs (Malatti et al 2012).

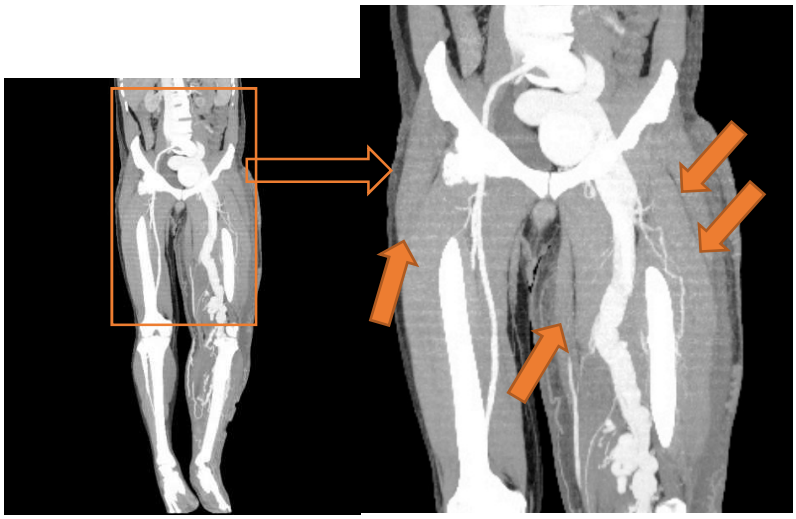

Figure 2.19: Coronal view CT image of the thighs (Malatti et al 2012). Arrows indicate muscle boundaries.

Figure 2.20: CT axial view with motion artefact (Malatti et al 2012).

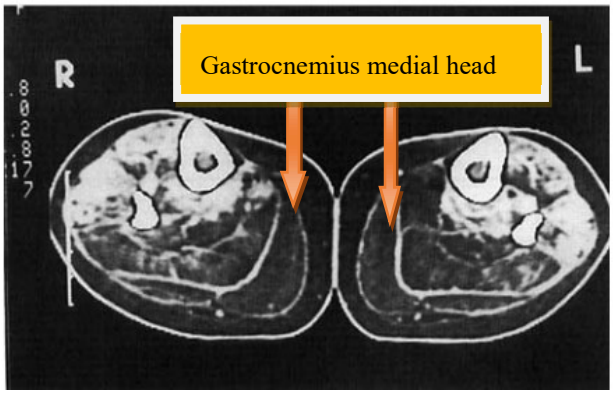

Figure 2.21: Transverse CT images of calf muscles - gastrocnemius, soleus and peroneal (Swash et al 1995).

CT has been applied relatively widely to the study of muscle dystrophy and similar conditions. For example, Saitoh (1991) concluded that measurement of muscle CT number and cross-sectional area could be used for the differential diagnosis of different types on muscular dystrophy.

Horikawa et al. (1992) applied CT scans of lower limb and trunk muscles in facioscapulohumeral muscular dystrophy and showed that there was a decrease in muscle density and size. For the lower limb, scans showed proximal distribution; the effect was manifest in the hamstrings first, the adductor muscles second and then the

muscular involvement progressed to the quadriceps femoris muscle. In the lower leg, the gastrocnemius and soleus muscles were relatively spared in comparison with the tibialis anterior muscle.

Arai et al. (1995) used CT to investigate skeletal muscles in patients with Duchenne muscular dystrophy (DMD) and Becker muscular dystrophy (BMD) during the preclinical and early stages. They measured muscle CT number at the levels of the mid-thigh, the maximum circumference of the calf and the third lumbar vertebra. No muscular degeneration was noted in the pre-clinical stage and only slight intramuscular low density areas and muscular atrophy were ascertained on gross visual inspection of the CT scans in patients from the age of 3 years onward in DMD. However, the mean CT numbers calculated for individual muscles clearly decreased with increasing age in all muscles except anterior and posterior tibialis, indicating that they were well preserved. Comparison of the rates of CT number decrease revealed that a rapid change in the paravertebral group commenced in the muscles on the lateral side, while among the adductors of the thigh, gracilis tended to be comparatively well preserved; this is the pattern of muscle involvement characteristic of symptomatic patients. In BMD, the atrophic change was extremely slight, and the CT numbers of the muscles were higher than the corresponding values for DMD in the same age group. It was concluded that CT numbers represent more objective indices for the assessment of muscular lesions as compared with gross visual inspection of skeletal muscle CT scans at the preclinical stage.

Swash et al. (1995) assessed twenty patients with muscular dystrophy and other conditions clinically and by CT imaging. CT images revealed abnormalities in about half of the muscles that were graded as clinically normal. In another study, the reliability and accuracy of CT images of skeletal muscles to identify muscle dystrophies reported poor inter-observer agreement and the sensitivity of diagnosis was only 40% (Dam et al., 2012). Nevertheless, the authors suggested that CT images can be used as additional step to clinical diagnosis in determining muscle dystrophies.

2.9.3.4 Application to Muscle Injury

CT is not routinely used in imaging muscle injury (Lee *et al.* 2012). As the assessment of this condition is usually undertaken by either MRI or ultrasound, there is no large body of published studies describing the role of CT in the diagnosis muscle injury. However, Brandser et al. (1995) investigated the differential impact of using different imaging modalities (projection radiography, conventional tomography, CT, and MRI) on the diagnosis of clinically proven hamstring muscle injury in 22 patients. They found that radiological and conventional tomographic appearances were confusing but CT was helpful in identifying healing of an avulsion of the ischial apophysis. However, MRI was the most useful modality at all times post injury for the evaluation of tendon and bone as well as muscle.

2.10. Accuracy of imaging muscle injury

The clinical assessment of muscle injury based on inspection, palpation and testing is not always conclusive and is not completely accurate. Imaging has been used to improve diagnostic accuracy but this depends on the modality and the site and nature of the injury. Cross-sectional imaging of muscle and muscle injury is usually undertaken by MRI and/or ultrasound. Other techniques such projection radiography, CT and nuclear medicine are not routinely used in imaging muscle injury (Lee *et al*., 2012). Thus, it is not surprising that no published studies have been found that assess the accuracy of CT for imaging muscle injury.

Connel et al. (2002) compared ultrasound with MRI for hamstring muscle injuries in the thigh, and concluded that both modalities were sensitive and effective. Because ultrasound was as sensitive as MRI and its costs were lower, it was reckoned to be the most cost-effective modality for diagnosis. However, MRI was the preferable choice for monitoring the healing process. Zhi-Jun et al. (2014) found that MRI was useful in the initial investigation of Grade 1 hamstring strains footballers and in the determination of recovery time for an individual injury.

DOMS (delayed onset of muscular soreness) refers to the pain that is felt several hours or even days after hard training. In DOMS, there is structural damage to the microscopic contracting functional units present in muscular fibres with metabolic changes, which lead to an alteration of the muscular tone. However, there is no macroscopic damage to the fibres and all that appears with ultrasound is greater echogenicity of the whole muscle and a slight enlargement of the muscle due to oedema. MRI, on the other hand, reveals diffuse signal hyperintensity with undefined edges due to interstitial and perifascial oedema. Given these factors, MRI is a preferred imaging modality for the diagnosis of DOMS (Manara *et al.,* 2013).

Megliola et al. (2006) evaluated the role of ultrasound compared with MRI as the reference method in football players with a history of traumatic muscle injury in the lower leg. In this study, 81 subjects were examined by both modalities. The MRI scans revealed 26 minor and 55 major cases of trauma while ultrasound gave 10 false negative results (6 minor and 4 major traumas). Both modalities showed complete agreement in 71 subjects in terms of site, type and extent of injury. For the correct of identification of muscle injury, ultrasound had an overall sensitivity of 88%; for major traumas, the sensitivity was 93% and it was 77% for minor traumas, 57% for DOMS, 83% for contractures, 80% for lengthenings, 84% for strains, 88% for mild contusions and 100% for severe contusions. The researchers concluded that ultrasound could be used as the first line modality for assessing muscle injuries. However, MRI was able to reveal injuries that might be missed by ultrasound and could yield a more accurate total assessment of site and extent of injury.

A rigorous review (Jean *et al.,* 2015) of shoulder injury imaging, which included 82 articles identified during a systematic search of three databases, revealed high and stable specificity and diagnostic accuracy for both ultrasound and MRI. The injuries were mainly those of the rotator cuff (RC), a group of tendons and muscles in the shoulder connecting the humerus to the scapula; the RC tendons provide stability to the shoulder while the muscles allow the shoulder to rotate. This study revealed equivalent performance for the modalities with sensitivity in the range 0.90–0.91 and specificity in the range 0.86–0.90. Based on accuracy, cost and safety, ultrasound was

recommended for the confirmation of pathologies in patients with severe full-thickness RC tears associated with pain in the shoulder, on the basis of clinical evaluation tests in acute cases. However, the modality may not perform as well in cases of lower grade muscle trauma.

The findings of this study were matched by those reported by Samira et al. (2016), which showed that ultrasound and MRI were comparable in terms of sensitivity and specificity in RC tear, although the former was considered preferable for screening due to its availability and low cost, on condition that high-resolution equipment and well-trained radiologists were available.

Naqvi et al. (2009) compared the accuracy of ultrasound and MRI for the detection of full thickness RC tears and used operative findings as the reference standard. Ultrasound correctly diagnosed 15 out of 17 tears giving a sensitivity of 88%, while there were 17 true negative and 2 false positive results giving a specificity of 89%. MRI, on the other hand, correctly identified 33 of 36 tears (sensitivity 91%), while there were 3 false positive and 16 true negative tears (specificity 84%). Positive predictive values for MRI and ultrasound were 92% and 88% respectively and the corresponding negative predictive values were 84% and 89%. The overall accuracy of MRI was 89.1% as compared to 88.9% for US. The researchers concluded that both modalities were of comparable accuracy, but that ultrasound could be used as the first line investigation for rotator cuff tear because of its relatively low cost and availability.

In a more recent study of RC injury conducted by Day et al. (2016), 80 patients were enrolled to diagnose muscle tears. Of these, 74 had MRI within 3 months of ultrasound imaging and therefore were suitable for evaluation. With MRI as the reference method, ultrasound correctly diagnosed the presence or absence of a tear in 74% of patients. However, the accuracy decreased to 61% for the correct diagnosis of RC pathology (no tear, partial thickness tear or full thickness tear). Furthermore, for the first 40 patients the accuracy was 51%, while for the remaining patients the accuracy reached 69%. Therefore, the accuracy of ultrasound increased with the number of patients scanned and it was concluded that ultrasound imaging requires significant operator training and practice to provide a clinically useful level of diagnostic accuracy.

Both ultrasound and MRI have their advantages and disadvantages for the assessment of different types of muscle injury. Appropriate implementation of each can yield a more accurate diagnosis than that obtained without imaging, which increases the likelihood of timely and correct treatment. The goal is to provide the right test for the right patient at the right time (Malik, 2015).

2.10.1 Gold Standard in Imaging Muscle Injury

Studies that evaluate a new diagnostic test, procedure or method should do so by comparing it with a time honoured alternative that is considered to be the current standard in the field. In this context, the meaning of the word standard is an authoritative or recognised exemplar of quality or correctness. “Gold standard” is the popular term to describe such a test. Gold standard is a historical term borrowed from economists. It signifies a monetary standard, under which a country’s basic unit of currency was defined by a stated quantity of gold, which made it possible to compare these different currencies for international trading. Thus, a medical diagnostic gold standard denotes the best tool available at the time to compare different measures (Claassen, 2005).

There are relatively few blinded research studies that directly compare ultrasound with MRI for muscle imaging in general. Furthermore, many sonographic studies are limited to small subject groups without the use of a gold standard. Additional research is needed to determine ultrasound's true effectiveness in evaluating the musculoskeletal system relative to magnetic resonance imaging (Manara *et al.,* 2013).

It is also the case that a definitive study has not been performed to compare MRI scans with ultrasound scans for the diagnosis of muscle injury. However, it is generally accepted that MRI is superior, in part due to the operator-dependent nature of ultrasound examination. Another reason is that when comparing ultrasound and MRI in minor muscle strains, the ultrasound operator needs to be able to distinguish between the low echogenicity of muscle oedema at the injury site and the low to intermediate echogenicity of the surrounding normal muscle architecture. This distinction is much more readily made by MRI (Koulouris and Connell, 2005).

For these reasons, MRI was used as the reference gold standard method in this study of the usefulness of pQCT in the characterization of the gastrocnemius muscle. In addition, the study was conducted in a setting in which MRI was routinely used for the assessment of muscle injury.

2.11 Characterisation of Medical Images Using Texture Analysis

2.11.1 Introduction

Imaging plays a very important role in modern medicine and the large majority of modalities and individual devices produce digital images. A digital image consists of an array of picture elements (pixels) as depicted in Figure 2.22. Each pixel corresponds to a single number in computer memory and the image is stored as a matrix of these numbers. Stored numbers represent the grey level intensities (grey scale) of the pixels. The extraction of texture features involves the analysis of significant variations in these intensities using computational techniques.

In medicine, texture analysis is an objective and quantitative method of tissue characterisation, which aims to describe the structure of tissues (Morris, 1988(b)). It can be applied to digital images from a range of modalities (Doi, 2005) and be regarded as a form of machine vision to aid perception of pixel intensity variations and to overcome the limitations of the human eye in detecting textured image patterns. The outcome of this processing might lead to image classification and segmentation as illustrated in Figure 2.22.

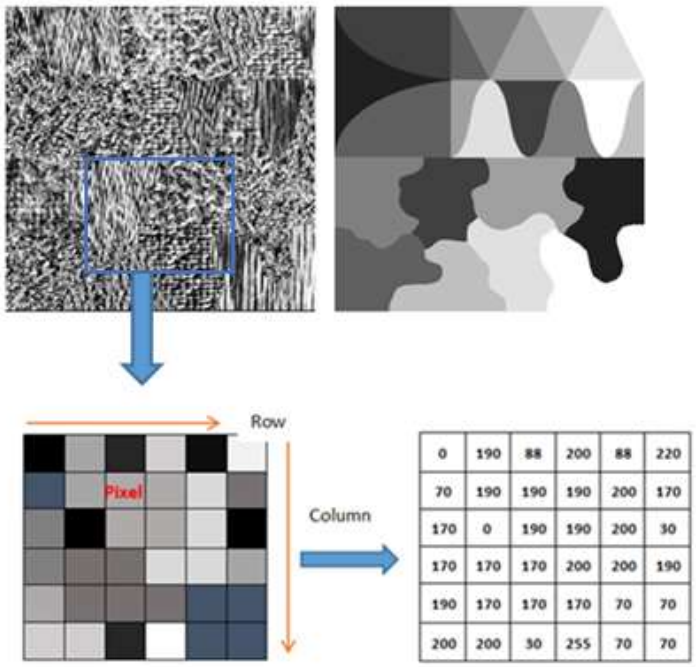

Figure 2.22: Example of image texture patterns and segmentation: numerical statistics or quantities that describe texture can be computed from the grey level intensities.

The application of texture analysis to medical images dates back to the 1970s. For example, it was used by Hall et al. (1971) in the identification of pulmonary disease to discriminate between normal and abnormal lungs. Since that time, texture analysis has become a successful technique to characterise many types of tissue and to distinguish normal from pathological, offering an increased level of diagnostic information extracted from a wide range of medical images (Mir *et al.*, 1995). Texture analysis methods are useful for discriminating and studying both distinct and subtle textures in multi-modality medical images, reducing the burden on an operator to make subtle distinctions by eye alone. Statistical texture analysis techniques are constantly being refined and the range of applications is increasing.

However, practical implementation requires careful consideration of the power of individual features to discriminate between textures. This is essential to reduce the influence that heavily correlated features, and features with little discriminatory power, have on the overall classification.

2.11.2 Advantages and Disadvantages of Texture Analysis Methods

Texture analysis methods may be broadly classified as structural, statistical, model-based and transform (Section 2.11). An advantage of the structural method is that it provides a good symbolic representation of the image; however, this feature is more useful for synthesis than analysis. Despite this, mathematical morphology provides a powerful tool for structural texture analysis. For example, it may be used for bone image analysis such as the detection of changes in bone microstructure (Serra, 1982; Chen and Dougherty,1992).

In contrast to structural methods, statistical methods do not attempt to achieve an explicit understanding of texture hierarchical structure. In an alternative way, they represent texture indirectly by non-deterministic features that control the relationships and distributions between image grey levels. Statistical methods yield higher classification rates than structural methods.

Model based texture analysis tries to interpret image texture by producing a generative or stochastic model. The texture model is the result of a mathematical procedure that is capable of generating and describing a textured image. Stochastic model parameters are estimated, which results in computational complexity. An example is the autoregressive (AR) model texture feature, which may be used for image segmentation (Hassner and Sklansky, 1981).

Of the transform methods of texture analysis, Fourier transforms tend to perform poorly in practice due to the lack of spatial localisation. Gabor functions provide better spatial precision, but there is no single function to localise a spatial texture structure. The wavelet transform has many advantages such as providing a wide range of choices for every specific texture application. However, a problem with wavelet transform is that it is not translation-invariant (with transformation at least infinite in one direction) (Srinivasan and Shobha, 2008).

2.11.3 Choice of Texture Parameters

Structural analysis methods were not suitable for this project and so reliance was placed on the statistical, model-based and transform approaches. Problems are associated with first order statistical quantities because they are often dependent on image acquisition parameters and may be affected by a change in image format and scaling during transfer from one software environment to another. In addition, first order statistics have limitations because they do not provide information about pixel values relative to each other and their positions within the image i.e. there is no information on the spatial relationship between neighboring pixels (Srinivasan and Shobha, 2008). Furthermore, it has been claimed that first order statistical parameters provide far fewer relevant and distinguishable features than other texture parameters, such as wavelet transform (Aggarwal *et al.,* 2012).

In general, therefore, texture analysis in medical diagnostic imaging is restricted to higher-order texture parameters. They are not affected by factors such as scaling and they take adjacent pixel values into account e.g. second order statistics consider pixels in pairs. In this project, emphasis was placed on texture parameters derived from second order statistics, model-based analysis and transform methods; in the thesis, they are collectively called 'second order parameters'.

However, some higher-order texture parameters, especially those derived from the co-occurrence matrix, may be correlated with those of first order (Materka, 2004). To avoid this unwanted phenomenon, the implementation of an image normalisation process before texture extraction is recommended. In its basic form, normalisation controls raw image grey level variation that comes from the scanner or image acquisition device (Materka, 2004, Collewet *et al.,* 2004). For example, in MRI the source of variation could be radiofrequency (RF) field inhomogeneity, while in x-ray devices, it could be the statistical variation in the photon count per pixel. Texture analysis software packages such as MaZda contain different normalisation options and in this project, image normalisation was a standard step before extraction texture parameters.

2.11.4 Medical Applications of Image Texture Analysis

Texture analysis (TA) has been used to characterise and classify tissues or organs and also to the segment a given anatomical structure, based on the texture characteristics of that structure. It has been shown to increase the level of diagnostic information extracted from medical images and to differentiate quantitatively between healthy and diseased tissue (Svolos and Todd-Pokropek, 1998). It is particularly useful for those cases in which change cannot be detected by direct inspection of the image. The application of texture analysis has been boosted by a revolution in the use of digital imaging technology and advances in computer science. It has contributed to the development of computer aided diagnosis (CAD), which provides a computer-generated second opinion in early detection of abnormalities, the quantification of disease progress and the differential diagnosis of lesions (Prasad and Krishna, 2011).

Texture analysis has been applied to images obtained with photography or photomicroscopy using visible light. For example, Ji et al. (2000) used the technique for characterising and recognising diagnostically important typical vascular patterns relating to cervical lesions from colposcopic images. They introduced a generalised method in which conventional statistical and structural textural analysis approaches were combined to create a set of texture measures that described the specific characteristics of cervical textures as perceived during medical examinations. With these measures, they demonstrated the effectiveness of the proposed approach in discriminating between texture patterns indicative of different stages of cervical lesions.

However, most applications of TA have involved images obtained with radiological imaging modalities such as projection radiography, MRI, ultrasound and x-ray CT.

2.11.4.1 Texture Analysis in Magnetic Resonance Imaging

There is a large body of literature about the texture analysis of magnetic resonance images. One of the important applications of MRI is in neurology and texture analysis has been widely applied to images of the human brain. For example, Kovalev et al. (1999) used texture parameters derived from gradient vectors and from generalised

co-occurrence matrices for the characterisation T2-weighted brain images. They were able to demonstrate that pathological conditions with widespread manifestations resulted in a change in the textural appearance of brain tissue and succeeded in differentiating the brain images of control subjects and from those of patients suffering from white-matter encephalopathy and/or Alzheimer's disease. They also applied the texture features to the segmentation of diffuse brain lesions.

Saeed and Puri (2002) analysed texture features in order to segment the cerebellum from other brain structures, using T1-weighted three-dimensional MRI. A little later, Alejo et al. (2003) used neighbourhood analysis of texture-based parameters for the semi-automatic segmentation of the hippocampus and corpus callosum.

Herlidou et al. (2003) succeeded in using texture parameters based on the histogram, co-occurrence matrix, gradient and run-length matrix for characterizing and distinguishing between healthy and pathological human brain tissues: white matter, grey matter, cerebrospinal fluid, tumours and oedema. They also confirmed that images obtained during routine procedures in three different MRI units contain tissue-specific texture features which can be extracted by mathematical methods.

In a series of studies of T1-weighted cerebral MR images, Bernasconi *et al.,* (2007) and Antel *et al.,* (2002) manipulated a combination of texture parameters and hyperintense T1 signal to determine cortical thickness, and to model blurring of the grey matter/white matter interface. In this way, they were able automatically to detect lesions of focal cortical dysplasia, some of which would have been missed by the human eye. They asserted that the developed computer-based, automated methods may be useful in the pre-surgical evaluation of patients with severe epilepsy related to focal cortical dysplasia.

Mahmoud *et al.,* (2003) used the texture analysis approach based on a three-dimensional co-occurrence matrix in order to improve brain tumour characterisation. They carried out a comparative study to evaluate the performance of this approach compared with the two-dimensional approach, using T1-weighted images in 7 patients with glioma to distinguish between solid tumour, necrosis, oedema and surrounding

white matter. With the three-dimensional approach, they achieved better discrimination between necrosis and solid tumour as well as between oedema and solid tumour. However, using these methods they did not manage completely to separate peritumoral white matter from oedema, nor ipsilateral white matter from contralateral white matter. Nevertheless, they suggested that the three-dimensional approach could provide a new tool for tumour grading and treatment follow-up, as well as for surgery or radiation therapy planning.

Yu et al. (2001) performed a study with patients with unilateral temporal lobe epilepsy characterised by ipsilateral hippocampal sclerosis and an apparently normal contralateral hippocampus. First, they ascertained the existence of texture differences between normal (control) and sclerotic hippocampi. Next, they showed that the apparently normal contralateral hippocampi could be assigned into three categories in terms of texture: apparently healthy, similar to sclerosis. or different from either healthy or sclerotic. They attributed these findings to a certain degree of hippocampal alteration, requiring further investigation to improve characterisation. Bonilha et al. (2003) and Coelho et al. (2003) confirmed the findings using texture parameters based on run-length and co-occurrence matrices. A similar study was undertaken by Jafari-Khouzani et al., (2003), this time using wavelet-based texture features in order to distinguish healthy from pathological hippocampal tissue, with the aim of aiding physicians in the determination of candidates for epilepsy surgery.

Mathias et al. (1999) applied texture analysis to MRI of the spinal cord in an attempt to quantify pathological changes that occur in multiple sclerosis (MS). Texture differences were detected between normal controls and relapsing-remitting MS patients before spinal cord atrophy was visually detectable. They also found a significant correlation between texture changes and disability.

2.11.4.2 Texture Analysis in Ultrasound Imaging

Much research has also been done with the texture analysis of medical ultrasound images to characterise tissues, identify pathological conditions and to establish relationships with the physiological and biochemical properties of tissues. For example, Beekman and Visser (2004) reviewed ultrasound texture analysis in the

assessment of nervous system disorders. They showed that the method was capable of identifying abnormalities of peripheral nerves, distinguishing between nerves and muscle and had the potential to monitor the effect of therapy.

Tissues of the liver (e.g. Garra *et al.,* 1989; Youssef and Sharawi, 1990) and breast (e.g. Garra et al., 1993) have also been widely studied by ultrasound texture analysis. Other anatomical examples include the kidneys (Rubin et al., 1988) and the eye (Romijn *et al.,* 1991). More recently, Aldahlawi et al. (2015) obtained encouraging results with ultrasound TA in the diagnosis of ovarian masses. They found that the co-occurrence matrix and wavelet transform parameters in particular had potential in differentiating benign and malignant masses and also for differentiating benign mass sub-groups. The results of these studies demonstrate the usefulness of the texture approach in quantitative diagnosis.

2.11.4.3 Texture Analysis in CT Imaging

There have been relatively fewer studies involving texture analysis of CT images. Chabat et al. (2003) used 13 texture parameters, derived from the histogram, co-occurrence matrix and run length matrix categories, to differentiate varieties of obstructive lung diseases in thin-section CT images. A set of images was obtained from healthy subjects and from patients with panlobular emphysema, centrilobular emphysema and constrictive obliterative bronchiolitis. The authors demonstrated the feasibility of textural distinction between the lungs of healthy subjects and those of the diseases, which cause decreased attenuation of the lung parenchyma. They concluded that the accuracy of the method was high, and suggested that it should be included as one of the main CT feature extractors for the automated detection of obstructive lung diseases.

Sometime later, Miles et al. (2009) investigated the texture analysis of portal phase hepatic CT images as a potential marker of survival in patients with colorectal cancer. They concluded that this approach is potentially a superior predictor of survival than CT perfusion imaging.

2.11.4.4 Accuracy of Texture Analysis in Medical Imaging

A measure of the usefulness of a method such as texture analysis is its diagnostic accuracy and numerous studies have been conducted to determine the accuracy of TA for different tissues and different imaging modalities.

In a recent study (Nandpuru *et al.,* 2014), an automated classification technique was used to characterise MRI brain images. The classifier was based on a support vector machine (SVM) developed in 1963 by Vapnik and Lerner as the most efficient supervised classifier. For TA, 22 texture features were extracted from each image to construct a co-occurrence matrix. After training the SVM classifier, accuracy was validated using a test set. This process yielded accuracies of 74%, 84% and 76% for SVM linear, quadratic and polynomial functions, respectively. This study stressed the importance of acquiring high quality images to avoid the effect of noise and so a median filter was implemented to remove noise effects while maintaining signal features.

Abou Zaid et al., (2006) developed an automatic diagnostic system for the early detection of liver disease from ultrasound images. They extracted a range of texture parameters (grey level, variance, skewness, kurtosis and wavelet transform) and found an accuracy of 96%. On this basis, the researchers suggested that this approach could be used to provide a second opinion diagnostic tool for diagnosing liver diseases. It was emphasised that defining a tissue region of interest was not a simple matter, as it should encompass lesions and have enough pixels in order to provide an adequate statistical population.

Mala et al., (2006) applied CT for the characterisation of liver tumours and used second-order statistical texture parameters, mainly contrast, homogeneity and entropy. They obtained an accuracy of 92% in comparison with image evaluation by radiologists. They also noted that CT was offered the optimum resolution and capability to examine the entire liver. CT was also the modality employed by Shu et al. (2010), who investigated the accuracy of texture analysis classification of tissues based wavelet-based contourlet packet (WBCP). The researchers used TA parameters

including energy, entropy, mean and standard deviation as the most effective descriptors for WBCP. The results revealed an accuracy of 96–97%.

Peng et al. (2015) investigated the suitability of texture analysis of CT images in order to distinguish thyroid nodules from normal thyroid tissue. Subjects were divided into two groups: Group A consisted of 152 normal thyroid CT images from 55 control subjects while Group B consisted of 134 images with nodules (50 malignant, 84 benign) from 55 patients who underwent thyroid surgery. The final diagnosis was confirmed by histopathology. The extracted texture parameters were grey level, gradient, co-occurrence matrix, contrast and coherence and a support vector machine was used to classify the images. The overall accuracy was 88.95% (±1.86%). In this study, the researchers used an image windowing technique to enhance contrast in the CT images.

It is apparent that texture analysis is capable of good accuracy across a variety of diagnostic situations and imaging technologies.

2.11.5 Texture Analysis of Muscle

Of particular relevance to this thesis is the fact that texture analysis has also been applied to images of muscle acquired by different modalities.

Herlidou et al. (1999) investigated the use of TA for the automated diagnosis of skeletal muscle dystrophy with MRI. They compared the texture approach in 31 subjects (14 healthy and 17 diseased) with diagnosis by visual inspection of a full set of leg transverse slices by 9 senior radiologists. For the texture analysis, the group used 4 texture statistical methods and one structural method. The statistical methods were the histogram, co-occurrence matrix, gradient matrix and run length matrix, whereas the structural method was mathematical morphology. A total of 59 texture parameters were extracted and these were subjected to Correspondence Factorial Analysis, followed by a non-parametric statistical test to achieve the comparison with visual diagnosis. TA yielded a sensitivity of 70% and a specificity of 86% for discrimination between healthy and diseased subjects and it was concluded that the

texture approach can provide useful information which contributes to the diagnosis of skeletal muscle disease.

Skoch et al. (2004) evaluated a method of texture analysis for the description of T1-weighted magnetic resonance images of healthy and injured calf muscles, in comparison with standard radiological evaluation. A total of 93 subjects underwent MRI of calf muscle, followed by the extraction of 7 texture features. Analyses were conducted using a t-test and principal component analysis. Images were classified into 4 diagnostic groups according to the assessment of 3 radiologists and these groups were compared with the TA results. There was 80% agreement between TA and radiologist classification and, in some cases, TA was able to describe changes that were not apparent by visual inspection. The research group concluded that TA of magnetic resonance images can be used as an objective description of calf muscle tissue changes and help the radiologist to distinguish between healthy and injured muscle tissue.

The fact that texture analysis of magnetic resonance images demonstrates more clinical discrimination than visual images analysis has been acknowledged in a recent review (De Certaines *et al.,* 2015). However, a scale gap exists between the spatial resolution of MRI and histological images derived from microscopy of muscle biopsy samples. The histological meaning of MRI textures remains an elusive goal.

As regards ultrasound imaging, Sipila and Suominen (1991) demonstrated that texture analysis could be used to differentiate muscle structure between athletes and untrained individuals, while Basset et al. (1994) showed that TA was capable of revealing the extent of muscle fatigue.

In 2000, Nielsen et al. concluded that first order statistical parameters provided a sensitive and reproducible means of studying muscle tissue although some time later (Nielsen *et al.,* 2006), they discovered that higher order statistics gave a more complete description. In this work, they used ultrasound imaging of the supraspinatus and vastus lateralis muscle. Alqahtani (2010) investigated the use of TA in ultrasound images of the gastrocnemius muscle. He confirmed that higher order statics were less dependent

on scanner operating conditions than first order statistics and found that the AR model and gradient parameters were the most sensitive for distinguishing between healthy and injured muscle.

König et al. (2015) developed a texture-based computer-aided diagnosis system for the identification of myositis. They achieved a sensitivity of 90%, a specificity of 83-85% and diagnostic accuracy of 85-87%. In a recent paper, Sogawa et al. (2017) studied the ability of texture analysis to differentiate neurogenic and myogenic disease on ultrasound images of the medial head of the gastrocnemius muscle. They found that the co-occurrence matrix, the run-length matrix and the auto-regressive model were particularly useful for this purpose and they achieved a correct classification rate of over 90% for patients with the two conditions.

It seems that with MRI, texture analysis can achieve an accuracy of the order of 80% for the identification of muscle injury. No direct reference has been found for the accuracy of ultrasound texture analysis for the same purpose. However, an accuracy of greater than 80% has been demonstrated for the identification of muscle disease and this value might be an indicator of what could be achieved for muscle injury.

2.12 Application of Peripheral Quantitative Computed Tomography

2.12.1 Introduction

X-ray computed tomography is a digital imaging technique that produces transverse cross-sectional slice images of the human body (Section 2.9.3.1) although after reconstruction, the images may be re-formatted in the coronal or sagittal projections. In lay language, a CT scanner is often known as a 'whole body scanner'. The value of each image pixel represents the mean linear attenuation coefficient of a small tissue voxel with a depth equal to the slice thickness, as illustrated in Figure 2.23 (Strang and Dogra, 2007). Conventionally, each pixel value is expressed as a CT number (or Hounsfield unit), which expresses the linear attenuation coefficient of tissue in a voxel relative to that of water.

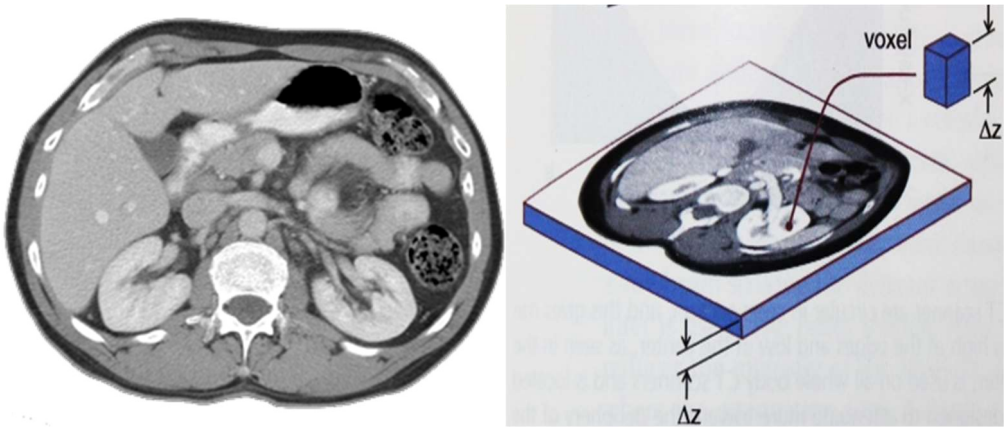

Figure 2. 23: Transverse CT image of the abdomen and a voxel showing the slice thickness Δz (Bushberg et al., 2012).

2.12.2 Quantitative Computed Tomography (QCT)

Linear attenuation coefficient is highly dependent on density and so the average CT number of a region of interest (ROI) within a slice image is a measure of the average density of tissue in that ROI. The measurement of tissue density using CT has become known as Quantitative Computed Tomography (QCT). QCT has mainly been applied to the assessment bone disorders (Braun et al., 1998) through the quantification of bone mineral density (BMD) at specific skeletal sites, particular those that are susceptible to atraumatic fracture. Because it is a tomographic technique, it can separate cortical bone from trabecular bone and measure the BMD of each.

An external calibration phantom place beneath the patient is used to convert CT numbers into BMD values (in units of mg/cm^3 for example). The phantom contains reference materials with predetermined attenuation properties, as shown in Figure 2.24 (Adams, 2009). These usually take the form of calcium hydroxyapatite in different concentrations together with water and a fat equivalent material. For BMD measurement, a ROI is drawn within an anatomical region such as the trabecular bone in a spinal vertebra. BMD is calculated from the mean CT number of pixels in the ROI using a calibration graph derived from ROIs in the reference materials. For diagnostic purposes, patient BMD is compared with an age and sex matched reference range derived from a normal population.

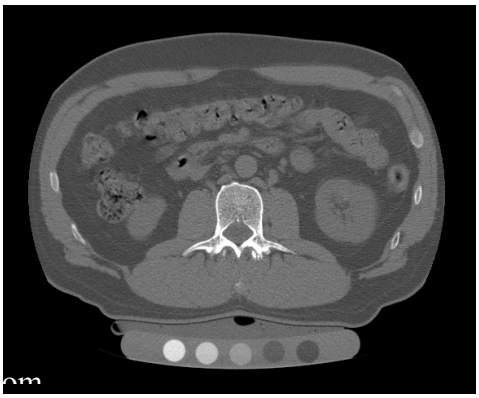

*Figure **2.24:** CT slice of the abdomen showing the calibration phantom used for QCT (www.metabolicimaging.org).*

2.12.3 Peripheral Quantitative Computed Tomography (pQCT)

Limited access to whole-body CT scanners and the relatively high radiation dose of QCT prompted the development of dedicated peripheral QCT (pQCT) scanners that were specifically used for the measurement of BMD at peripheral skeletal sites (Gordon *et al.,* 1996). Thus pQCT is the application of QCT to the appendicular skeleton such as the bones of the arms (humerus, radius and ulna) or legs (femur, tibia and fibula) (Engelke et al., 2008). Like QCT, pQCT can make separate measurements of cortical and trabecular BMD. In addition, the scanner is capable of measuring total bone cross-sectional area, cortical bone area, marrow area and marrow density. According to the scanner manufacturer, the in vivo precision of BMD measurement is 1% (Stratec Medizintechnik, 2007).

A pQCT scanner has a smaller diameter bore, a more compact gantry and is much smaller in size than a whole-body scanner. It is also mobile, relatively inexpensive and easy to use and delivers a significantly lower patient radiation dose, even though the scan time is considerably longer. For pQCT the effective dose is less than 10 μSv compared with a typical value of 300 μSv for body QCT (Damilakis *et al.,* 2010; Huda and Morin, 1996). Typical scan times are a few minutes and a few seconds for pQCT and QCT respectively; the relatively long pQCT scan acquisition time increases the risk of motion artefacts. Typical spatial resolution is in the range 0.2-0.5 mm (Lala *et al.,* 2014). A technical description of the XCT 2000 pQCT scanner (Stratec

Medizintechnik GmbH, Pforzheim, Germany) used in this project is given in Appendix B.

2.12.4 Muscle Measurement with pQCT

Although pQCT has been developed and used mainly as a tool for assessing bone, it has also been shown to be valuable for measuring soft tissue components such as muscle and fat (Blew *et al.,* 2014). Measured quantities include total soft tissue cross-sectional area, muscle area and density, fat area and density and the ratio of the areas and densities of bone, muscle and fat. Furthermore, pQCT has been used to investigate relationships between bone, muscle and fat. For example, Macdonald et al. (2005) used the bone/muscle area ratio as an index of the strength of bone relative to that of muscle while Farr et al. (2011) used muscle density as an index of muscle quality, which is related to skeletal muscle fat content.

A recent review by Erlandson et al. (2016) compared pQCT with MRI and dual-energy X-ray absorptiometry for the analysis of muscle. They argued that CT and MRI were the most accurate 'gold standard' methods of measuring muscle size (as assessed by muscle area) and muscle quality (as assessed by muscle density and the infiltration of fat). However, due to their high cost and operational complexity, other techniques such as DXA and pQCT were most popular in both clinical and research settings. They recognised that pQCT is increasingly used for assessing skeletal muscle in limbs, particularly as a research tool. In comparison with MRI, pQCT had the advantages of low cost, portability and the lack of need for highly trained operators. However, MRI has better reproducibility and reliability. Both techniques suffered from the absence of a universally accepted standardised method of image analysis to extract muscle parameters.

Erlandson et al. (2016) made no mention of texture analysis applied to pQCT images for the investigation of either muscle or bone and no other references to TA in pQCT have been found.

2.13 Discussion

Muscle injury is a relatively frequent consequence of sports activities and one common site of thigh injury is the gastrocnemius muscle. Medical imaging plays an important role in the initial diagnosis and in monitoring the progress of healing. In this context, CT is not routinely used and the modalities of choice are MRI and ultrasound imaging. Ultrasound scanners have several advantages over MRI; these include: low cost, availability, portability, small space requirement and the absence of significant hazards. Their small size and portability means that they can be brought to the patient. However, acquiring high quality ultrasound images requires a highly-trained and experienced operator, while magnetic resonance image acquisition is largely protocol driven.

Because of its operator independence and despite its disadvantages, MRI is generally accepted as the reference method for the investigation of muscle disease and muscle injury. However, with optimal image acquisition and interpretation, ultrasound can perform very well compared with MRI with sensitivity, specificity and diagnostic accuracy in the range 85-90%.

Texture analysis is a mathematical technique that has potential for the automatic characterisation and classification of digital medical images. Like that of other computational approaches, its ultimate goal is to diagnose disease and injury without the need for human intervention. It seeks to produce an objective, quantitative and accurate analysis and remove the subjectivity and bias that is associated with the visual inspection and reporting of images. The method has been applied to images from a range of modalities including MRI, ultrasound and CT. A variety of texture parameters have been defined, but for medical image applications, emphasis has been placed on second order statistics, model based quantities and transform based quantities.

Texture analysis is still an active research topic and further work needs to be done before it has routine clinical application. However, encouraging results have been obtained in the assessment of muscle injury with a reported agreement of 80% between the automated classification and that of experienced radiologists.

The technique that has become known as pQCT was originally developed as an alternative to the use of a whole-body CT scanner for the assessment of bone disease (such as osteoporosis) and the measurement of mineral density in the bones of the arm and the leg. However, it has been adopted for the measurement of muscle size and muscle quality. The technology takes the form of a miniature CT scanner, which has similar advantages to ultrasound in terms of cost, portability and space requirement. It also has the advantage of MRI as regards the absence of need for a highly skilled operator. A disadvantage is the fact that it uses ionising radiation and so delivers a radiation dose to the subject. However, the dose is much less than one day's worth of natural background radiation and so the risk is very small.

There are no reports of texture analysis being applied to pQCT images. However, the texture approach has been used to analyse muscle images acquired with ordinary CT and pQCT has been used to study muscle. On this basis, it is reasonable to hypothesise that texture analysis may be useful in the diagnosis of muscle disease and injury with pQCT images. Furthermore, the relatively low cost and compactness of the pQCT scanner makes it attractive compared with the large-scale installations required for whole-body CT and MRI and, for this reason, poorer diagnostic accuracy might be acceptable compared with these other modalities. However, ultrasound has the same practical advantages and so, to be effective, the performance of pQCT would need to match that of ultrasound imaging.

This project is the first exploration of the usefulness of texture analysis of pQCT images in the assessment of muscle injury, with a particular focus on the gastrocnemius muscle.

Chapter 3 pQCT Scans of Phantom and a Healthy Volunteer

3.1 Introduction

The measurement of texture parameters of a homogeneous tissue such as muscle by a technique such as pQCT requires attention to the scan acquisition parameters as image quality may be affected since the imaging modality is operated at low photon energy (22 Kev) and low radiation dose. X-ray photons strike the image detector in a random pattern with the result that one area of the detector surface may receive more photons than another (Zauner et al. 2006). Therefore, an important variable of interest is the number of detected photons because a low number can cause statistical errors. This phenomenon is termed Poisson noise leading to the appearance of random bright and dark pixels superimposed upon the acquired image as a result of changes in pixel values. To ensure reliable measurement of the acquired image texture features, the optimisation of pQCT scanner parameters (such as pixel size and scan speed) is a potential approach.

The aims of this chapter are as follows:

- To investigate the use of pQCT to image a water phantom since water is a homogenous fluid that has no texture.
- To evaluate the suitability of pQCT for the acquisition of calf muscle tomographic images in a healthy volunteer and the capability of pQCT to detect calf muscle boundaries, specifically in the gastrocnemius muscle.

3.2 Phantom Study

3.2.1 Introduction

Water is considered a suitable phantom material for x-ray imaging purposes. Water possesses similar x-ray attenuation properties to soft tissue (such as muscle) but has no texture. Therefore, no variability in texture parameter values is expected during the modification of image acquisition and analysis factors. Quantifying extracted texture

parameters at each combination of pixel size and scan speed is a potential approach, the results of which may identify consistent image acquisition settings for implementation as a characterising tool for image texture analysis.

3.2.2 Materials and Methods

3.2.2.1 Image Acquisition

A cylindrical phantom of 12 cm external diameter was filled with tap water and aligned along the central z-axis of the pQCT system, as illustrated in Figure 3.1. Intended to simulate the attenuation of human leg muscle tissue, the water phantom was constructed from plastic and was completely uniform in design. It was confirmed that the water phantom did not contain any air. The process of scanner optimisation involves the use of a range of pixel sizes combined with a range of scan speeds in order to determine the optimum combinations for consistent texture parameters and to measure repeatability at each combination. In addition, it involves assessing the suitability of the texture parameters that don't change when image acquisition parameters are changed (pixel size and scan speed). Scan speeds used were 3, 5, 10, 15, 20, and 30 mm/sec, with pixel sizes of 0.2, 0.4, 0.6, and 0.8 mm. For image reconstruction, 180 projections were used (discussed in Chapter 2). At each of the six scan speeds, the phantom was scanned at each of the four pixel sizes 20 times (Dae-Cheol et al. 2010); thus, the phantom was scanned 480 times in total.

A single large circular region of interest (ROI) of 14216 pixels in area was defined to encompass the entire acquired image, avoiding the phantom's edges, as shown in Figure 3.1. Texture analysis was performed using the software package MaZda 3.2 (Institute of Electronics, Technical University of Lodz, Poland). The types of extracted texture parameters were first order statistical parameters including grey level, variance, skewness, and kurtosis, and second order statistical parameters including the co-occurrence matrix, run length and gradient, auto-regressive model and wavelet transform.

Figure 3.1: Water phantom in isolation (left), positioned in the pQCT scanner (middle), and acquired image with ROI placement (right).

3.2.2.2 Image Transfer

Following completion of the pQCT scans; the images were saved and exported as Comma Separated Values text files (.CSV) of 32-bit depth. The saved images were subsequently imported into ImageJ software package, an image processing software package capable of importing text files as text images. The images were then saved by ImageJ in an 8-bit bitmap (BMP) format in order to allow processing by the texture analysis software.

3.2.2.3 ImageJ Software

In this study, ImageJ software (v1.47q) (National Institute of Health, USA) was used to transform the image format from CSV to BMP. Image transformation changed the image depth from 32-bit to 8-bit and was used to improve image visualisation ('windowing'). ImageJ is a public domain multi-platform image processing software written in Java. Capable of reading different image formats, such as BMP, DICOM (Digital Imaging and Communication in Medicine) and CSV, it has the additional capability to plot image histograms. Images were then exported from ImageJ into MaZda Software.

3.2.2.4 Image Texture Analysis

MaZda 4.6 software (Institute of Electronics, Technical University of Łódź, Poland) was used to extract texture features from the acquired images. A brief explanation of the MaZda software is presented in the next section.

3.2.2.4.1 MaZda Software

MaZda is a powerful software package for the quantitative analysis of image texture (see Chapter 2 for further details on texture analysis). The programme's name is an abbreviation of the Polish words 'Macierz Zdarzen', corresponding to the English term 'co-occurrence matrix'. MaZda was developed in 1998-2002 for quantitative textural analysis of magnetic resonance images as part of the European COST B11 objectives (Szczypinsky et al., 2007).

The MaZda programming codes are C++ and Delphi, with an open source library. It is compiled for use with the Microsoft Windows operating system (Szczypinsky *et al.,* 2007). Other programme packages, such as Key-Res and LS2W, are non-commercial and provide limited functionality compared with MaZda software (www.keyres-technologies.com,www.maths.bris).

A flowchart of the texture analysis pathways in MaZda is given in Figure 3.2 below.

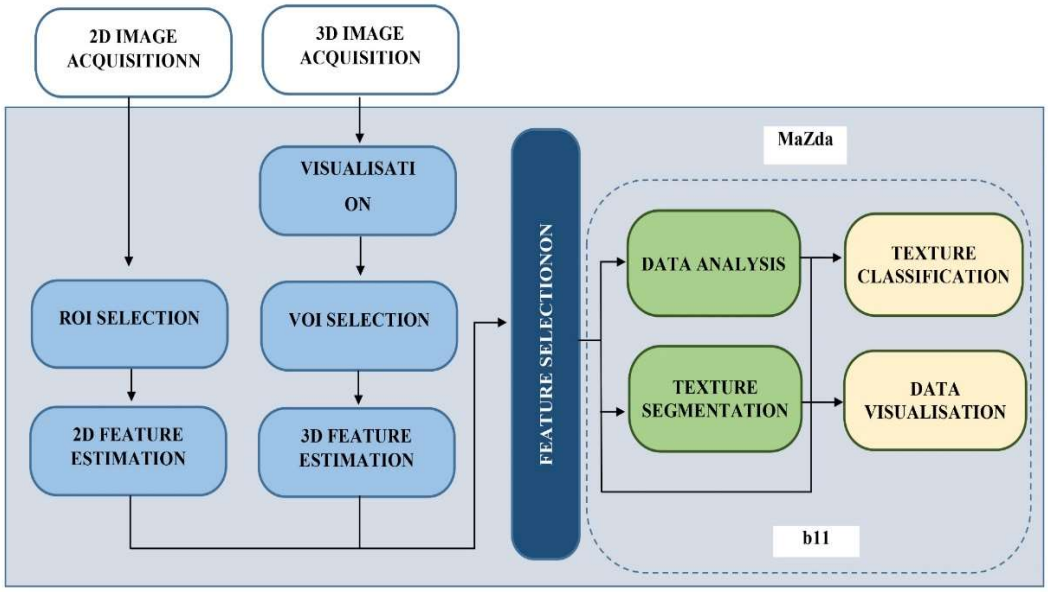

Figure 3.2: Flowchart of analysis pathways in the MaZda package, adapted from Szczypinski et al. (2007).

Image analysis in MaZda initiates with data input through the loading of a digital image, such as a pQCT scan. MaZda allows the user to select analysis of the image as whole or analysis of predefined regions of interest. A region of interest (ROI) is a group of pixels in a 2D image selected for analysis specifically to relate to the aim of the analysis and therefore minimise computation burden and avoid unnecessary processing (Szczypinsky et al., 2009). With MaZda, ROIs of various shapes can be used, such as squares, rectangles, circles, and freehand drawings. The software allows the definition of up to 16 ROIs within a single loaded image. MaZda can calculate texture parameters available from a list of 279 different definitions.

In summary, MaZda features can be listed as follows:

- 1st commercial software (1998-2002) capable of accomplishing quantitative texture analysis.
- Capable of loading images as windows Bitmap, DICOM with 8 or 16 bits.

- Able to define 16 ROIs in different shapes (arbitrary shape, circle, rectangle, and polygon) by graphical tool, which can be analysed simultaneously.
- Manipulation of defined ROI such as filling, moving and duplicating.
- Capable of computing 279 texture parameters from a single ROI.
- Capable of analysing colour images (2D and 2D).
- Capable of implementing image segmentation, data classification and analysis automation.

Prior to the computation of the texture parameters, the image fragments of the ROI were normalised. The aim of normalisation is to reduce variation in the image due to differences in scanner settings as discussed in previous chapter (Chapter 2) (Collewet et al., 2004).

MaZda software has three options for image normalisation:

1. The default option, where analysis is conducted with the original image range of intensity 2^n, where n is the number of bits.
2. $\pm\sigma$, where the image mean value μ and the standard deviation σ are computed, and analysis is then conducted with a grey-scale range between $\mu-3\sigma$ and $\mu+3\sigma$.
3. 1-99%, where the grey-scale range is between 1% and 99% of the total accumulated image histogram (Szczypinski et al., 2007, Szczypinski et al., 2009).

A study conducted by Collewet et al., (2004) compared the influence of various grey level normalisation methods on the discriminatory power of texture extraction. The group reported that the $\pm\sigma$ method yielded the best result; this method of normalisation was therefore implemented in this study.

The first step following image normalisation (to minimise the influence of image contrast variation and brightness) is texture feature computation. The output of this stage is used for texture discrimination and classification (Szczypinsky *et al.,* 2007). The MaZda package uses three categories of feature computation, namely statistical, model-based, and image transforming. The statistical approaches correspond to

texture indirectly via non-deterministic properties that control the distribution and relationship between the grey-scale levels of an image (Szczypinsky *et al.,* 2007).

Model-based texture analysis using fractal or stochastic models attempts to interpret image texture by the use of generative image or stochastic models. Transforming methods of texture analysis, e.g. Fourier, Gabor or wavelet transforms, represent an image in a space with a co-ordinate system correlating to the characteristics of the texture (Cohen, 1989; Bovik *et al.,* 1990; Daugman, 1998).

From each ROI, the classes of extracted texture parameters were as follows:

- First order statistical features including grey level mean, variance, skewness, and kurtosis (four texture parameters).
- Second order statistical parameters including co-occurrence matrix, run length matrix and gradient. With reference to the co-occurrence matrix, 220 parameters (four directions and five inter-pixel distances) were extracted from each ROI. For the run length matrix, 20 parameters (five run length matrix-based features at four directions each) were extracted from each ROI. For the gradient, five parameters were extracted from each ROI. For each of these parameter types, the sum was considered for analysis.
- Model-based parameters: only the auto-regressive (AR) model was used. Five parameters were extracted for each ROI and the sum of these was considered for analysis.
- Wavelet transform parameters: 12 parameters were extracted from each ROI and their sum was considered for analysis. Only first, second and third scale parameter values were considered. MaZda software was unable to compute the fourth, fifth and sixth scale parameters values from a small ROI. These wavelet parameters were thus excluded from feature selection.

3.2.2.5 Repeatability

How closely the results of successive measurements of the same parameter match when carried out under the same conditions of measurement is the repeatability of that parameter, indicating the consistency of a measurement. The repeatability conditions include: the same measurement procedure, the same measuring instrument under the same conditions and the same observer (Barry and Chris, 1997). The texture parameters of acquired images are subject to random variations as a result of fluctuations in the pQCT scanner (number of detected photons) during image acquisition. Hence, repeatability refers to repeated measurements on the same subject without repositioning. As texture analysis is capable of quantifying information that is not visually perceptible, it is critical to note that two images of similar visual appearance might not necessarily be texturally similar (Bocchi et al., 1997). For every acquired image of the 480 scans, an equal area size ROI was drawn and the same texture features were extracted for further analysis.

3.2.2.6 Influence of ROI area size on extracted texture parameters

In order to investigate influence of ROI area size on the extracted texture parameters, a group of ROIs was used. The first ROI was defined to cover the whole of the water phantom acquired image. Further ROIs were defined and adjusted by removing some pixels until the desired size was obtained (Figure 3.3). The areas were 10000, 5000, 2500, 1500, 500, 300, 200 and 100 pixels. Texture parameters were extracted from images acquired with a scan speed of 10 mm/s and pixel size of 0.8 mm. Regression analysis was used to identify the relationship between extracted texture parameter (dependent variable) and ROI area (independent variable). A model of the relationship was hypothesised, and estimates of the parameter values were used to develop an estimated regression equation. Regression and correlation analysis are related in the sense that both deal with relationships among variables. The correlation coefficient is a measure of linear association between two variables. Values of the correlation coefficient are always between -1 and +1. A correlation coefficient of +1 indicates that

two variables are perfectly related in a positive linear sense, a correlation coefficient of -1 indicates that two variables are perfectly related in a negative linear sense, and a correlation coefficient of 0 indicates that there is no linear relationship between the two variables. For linear regression, the sample correlation coefficient is the square root of the coefficient of determination (R^2). The correlation coefficient measures only the degree of linear association between two variables (texture parameter and ROI area size). Thus, a significance test is recommended to decide whether there is evidence of a real relationship between the variables (Evans 1996). This is accomplished by testing a null hypothesis (H_0) against an alternative hypothesis (H_1):

- H_0: p=0: There is no linear correlation.
- H_1: p≠0: There is a linear correlation.

P< 0.05 was considered significant (www.socscistatistics.com).

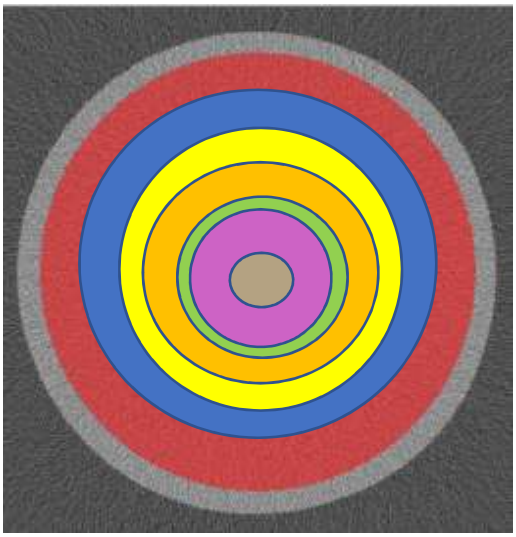

Figure 3.3: Simulation of ROI definition and reduction.

3.2.2.7 Statistical analysis

The mean and standard deviation (SD) were calculated for each texture parameter, and the coefficient of variation (CV) was determined in order to evaluate the variation in texture parameters for every repeated scan in the range of pixel sizes and scan speeds. The CV is the ratio of the standard deviation (SD) to the overall mean and is expressed as a percentage. SPSS for Windows Version 20 (SPSS Inc., Chicago, Illinois, USA)

was used for the statistical analysis. To explore the effect of increasing pixel sizes on the overall mean extracted texture parameter values and individually on each of the nine texture scores, a one way MANOVA (Multiple Variate Analysis of Variance) was conducted. In the same manner, a one-way MANOVA was used to test the main effects of various scan speeds on the overall mean values of each of the nine texture analysis parameters.

3.2.3 Results

The results of the water phantom studies are presented in Figure 3.4. Tables 3.1-3.24 show the mean values, SD and %CV of 20 times computation of water phantom texture parameters at a range of pixel sizes and scan speeds Figures 3.4 – 3.22 show plots of effect of increasing pixel size on extracted texture parameters.

3.2.3.1 Image Acquisition Texture Analysis

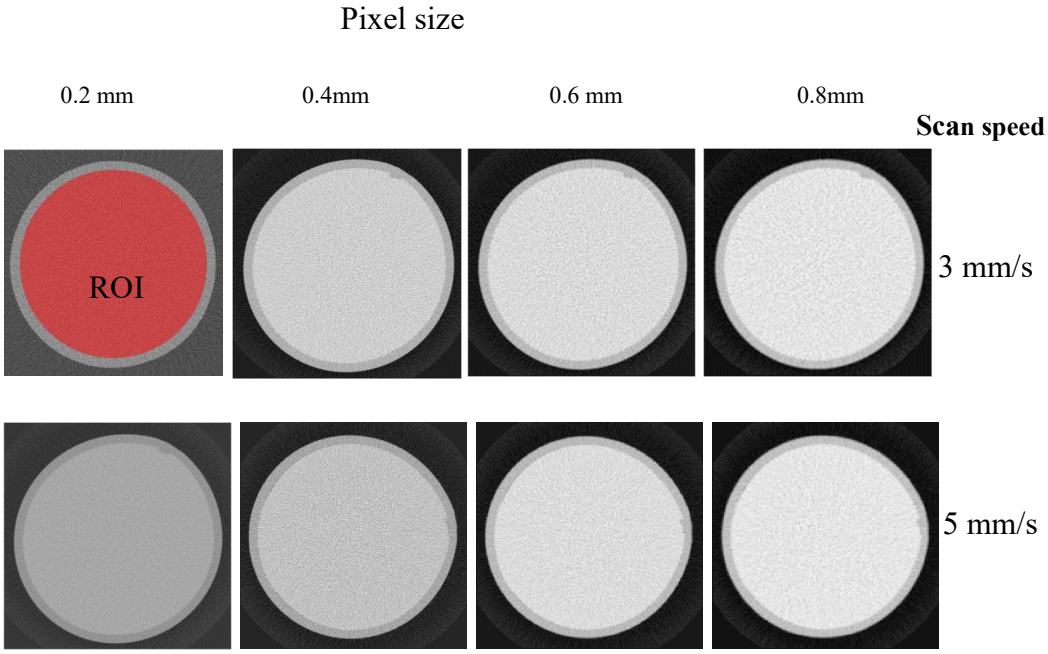

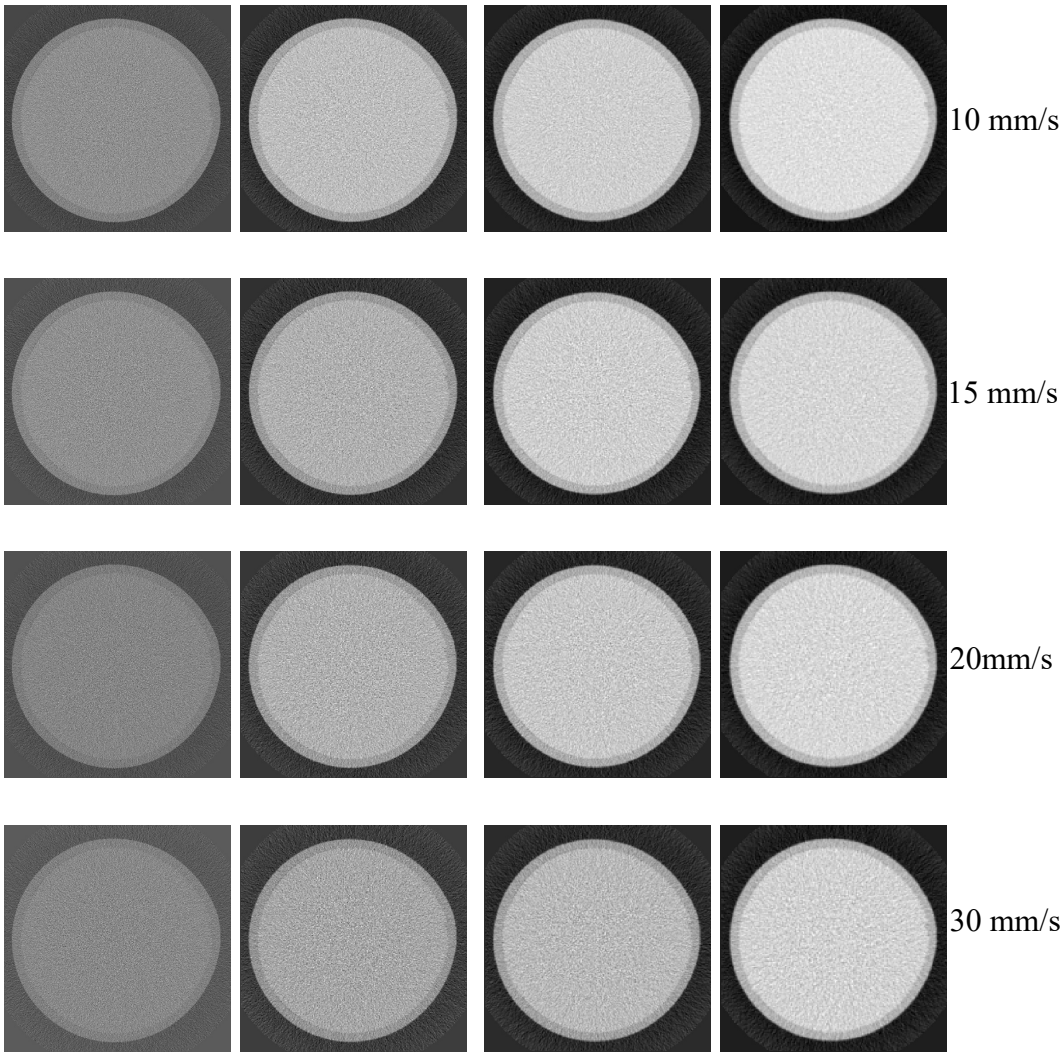

Figure 3.4: Water phantom acquired images at different pixel size and scan speed settings.

Table 3.1: SD, mean and %CV of extracted texture parameters of water phantom acquired images (n=20) at pixel size of 0.2 mm and scan speeds of 3 mm/s.

	Texture parameter @ pixel size=0.2 mm and scan speed =3 mm/s								
	GL	**Variance**	**Skewness**	**Kurtosis**	**Cooccurrence matrix**	**RL matrix**	**Gradient**	**AR model**	**Wavelet transform**
SD	3.7387	20.0479	0.0196	0.0503	1676.8462	90.3945	19.4130	0.0114	308.2183
Mean	169.7591	428.4064	0.0010	0.0193	211230.6083	55238.3877	1728.0890	1.2124	50461.9814
%CV	2.2024	4.6796	1972.4692	260.9196	0.7938	0.1636	1.1234	0.9420	0.6108

Table 3.2: SD, mean and %CV of extracted texture parameters of water phantom acquired images (n=20) at pixel size of 0.2 mm and scan speeds of 5 mm/s.

	Texture parameter @ pixel size=0.2mm and scan speed =5 mm/s								
	GL	**Variance**	**Skewness**	**Kurtosis**	**Cooccurrence matrix**	**RL matrix**	**Gradient**	**AR model**	**Wavelet transform**
SD	3.8133	30.0745	0.0152	0.0368	1058.3736	105.7561	16.9620	0.0121	267.8870
Mean	161.0030	523.5688	0.0026	0.0035	211239.9062	55362.2641	1731.3686	1.2057	50560.4355
%CV	2.3685	5.7441	576.0587	1049.1787	0.5010	0.1910	0.9797	1.0022	0.5298

Table 3.3: SD, mean and %CV of extracted texture parameters of water phantom acquired images (n=20) at pixel size of 0.2 mm and scan speeds of 10 mm/s.

	Texture parameter @ pixel size=0.2 mm and scan speed =10 mm/s								
	GL	**Variance**	**Skewness**	**Kurtosis**	**Cooccurrence matrix**	**RL matrix**	**Gradient**	**AR model**	**Wavelet transform**
SD	3.7574	35.2112	0.0193	0.0359	1267.0303	62.1079	24.2878	0.0146	281.9191
Mean	149.3949	670.1539	0.0055	-0.0081	211083.4160	55594.2937	1738.0885	1.2051	50617.8540
%CV	2.5151	5.2542	349.5504	-442.4052	0.6003	0.1117	1.3974	1.2105	0.5570

Table 3.4: SD, mean and %CV of extracted texture parameters of water phantom acquired images (n=20) at pixel size of 0.2 mm and scan speeds of 15mm/s.

	Texture parameter @ pixel size=0.2 mm and scan speed =15 mm/s								
	GL	Variance	Skewness	Kurtosis	Cooccurrence matrix	RL matrix	Gradient	AR model	Wavelet transform
SD	6.6855	55.1701	0.0210	0.0311	929.3755	112.2013	13.7524	0.0100	223.1785
Mean	141.5668	710.5478	0.0095	-0.0103	211161.1095	55600.7387	1727.0479	1.2099	50639.5188
%CV	4.7225	7.7644	220.2561	-300.7276	0.4401	0.2018	0.7963	0.8226	0.4407

Table 3.5: SD, mean and %CV of extracted texture parameters of water phantom acquired images (n=20) at pixel size of 0.2 mm and scan speeds of 20 mm/s.

	Texture parameter @ pixel size=0.2 mm and scan speed =20 mm/s								
	GL	Variance	Skewness	Kurtosis	Cooccurrence matrix	RL matrix	Gradient	AR model	Wavelet transform
SD	4.5276	45.1808	0.0175	0.0416	924.3490	72.2772	24.5028	0.0088	273.1707
Mean	137.1414	754.0845	0.0101	-0.0139	211113.2303	55635.8448	1737.5840	1.2037	50769.7532
%CV	3.3014	5.9915	174.0365	-299.4027	0.4378	0.1299	1.4102	0.7294	0.5381

Table 3.6: SD, mean and %CV of extracted texture parameters of water phantom acquired images (n=20) at pixel size of 0.2 mm and scan speeds of 30 mm/s.

	Texture parameter @ pixel size=0.2 mm and scan speed =30 mm/s								
	GL	Variance	Skewness	Kurtosis	Cooccurrence matrix	RL matrix	Gradient	AR model	Wavelet transform
SD	5.6341	60.7355	0.0158	0.0494	809.3612	87.2746	22.6447	0.0137	235.7622
Mean	135.7771	841.1316	0.0056	-0.0076	210915.9293	55695.5394	1729.6430	1.2036	50814.0967
%CV	4.1495	7.2207	284.8924	-648.6135	0.3837	0.1567	1.3092	1.1423	0.4640

Table 3.7: SD, mean and %CV of extracted texture parameters of water phantom acquired images (n=20) at pixel size of 0.4 mm and scan speeds of 3 mm/s.

	Texture parameter @ pixel size=0.4 mm and scan speed =3 mm/s								
	GL	Variance	Skewness	Kurtosis	Cooccurrence matrix	RL matrix	Gradient	AR model	Wavelet transform
SD	2.5457	4.8703	0.0217	0.0360	2120.8788	116.6221	25.8204	0.0108	490.1024
Mean	208.4562	144.6727	0.0061	-0.0181	211556.5572	53872.6326	1743.6869	1.1975	50029.0441
%CV	1.2212	3.3664	353.4662	-198.9847	1.0025	0.2165	1.4808	0.9028	0.9796

Table 3.8: SD, mean and %CV of extracted texture parameters of water phantom acquired images (n=20) at pixel size of 0.4 mm and scan speeds of 5 mm/s.

	Texture parameter @ pixel size=0.4 mm and scan speed =5 mm/s								
	GL	Variance	Skewness	Kurtosis	Cooccurrence matrix	RL matrix	Gradient	AR model	Wavelet transform
SD	2.5886	4.2070	0.0194	0.0378	1865.4137	98.2385	24.5018	0.0110	543.6009
Mean	201.5134	189.4377	0.0019	0.0171	211674.3240	54197.2889	1750.7149	1.2001	50283.6316
%CV	1.2846	2.2208	1027.9172	221.3071	0.8813	0.1813	1.3995	0.9168	1.0811

Table 3.9: SD, mean and %CV of extracted texture parameters of water phantom acquired images (n=20) at pixel size of 0.4 mm and scan speeds of 10 mm/s.

	Texture parameter @ pixel size=0.4 mm and scan speed =10 mm/s								
	GL	Variance	Skewness	Kurtosis	Cooccurrence matrix	RL matrix	Gradient	AR model	Wavelet transform
SD	3.3464	11.9012	0.0257	0.0427	1752.7886	97.9953	23.7571	0.0164	415.6307
Mean	189.6459	284.3716	0.0041	0.0128	211304.6453	54722.3036	1740.4677	1.2053	50477.4223
%CV	1.7645	4.1851	628.8023	333.8549	0.8295	0.1791	1.3650	1.3592	0.8234

Table 3.10: SD, mean and %CV of extracted texture parameters of water phantom acquired images (n=20) at pixel size of 0.4 mm and scan speeds of 15 mm/s.

	Texture parameter @ pixel size=0.4 mm and scan speed =15 mm/s								
	GL	Variance	Skewness	Kurtosis	Cooccurrence matrix	RL matrix	Gradient	AR model	Wavelet transform
SD	3.5947	19.1831	0.0201	0.0507	1441.9954	73.1544	22.1539	0.0128	248.9748
Mean	181.4217	350.8031	-0.0013	0.0009	211062.8217	54968.4345	1736.1369	1.2021	50574.7854
%CV	1.9814	5.4683	-1490.7116	5593.9146	0.6832	0.1331	1.2760	1.0634	0.4923

Table 3.11: SD, mean and %CV of extracted texture parameters of water phantom acquired images (n=20) at pixel size of 0.4 mm and scan speeds of 20 mm/s.

	Texture parameter @ pixel size=0.4 mm and scan speed =20 mm/s								
	GL	Variance	Skewness	Kurtosis	Cooccurrence matrix	RL matrix	Gradient	AR model	Wavelet transform
SD	5.2914	32.2907	0.0151	0.0461	1491.5968	106.3306	25.7174	0.0159	343.7914
Mean	174.0938	397.2397	0.0036	0.0266	211395.1046	55153.8351	1745.8450	1.2014	50445.1947
%CV	3.0394	8.1288	423.5535	173.1240	0.7056	0.1928	1.4731	1.3251	0.6815

Table 3.12: SD, mean and %CV of extracted texture parameters of water phantom acquired images (n=20) at pixel size of 0.4 mm and scan speeds of 30 mm/s.

	Texture parameter @ pixel size=0.4 mm and scan speed =30 mm/s								
	GL	Variance	Skewness	Kurtosis	Cooccurrence matrix	RL matrix	Gradient	AR model	Wavelet transform
SD	3.0429	26.6914	0.0219	0.0444	1149.8491	74.6707	20.0767	0.0112	319.2128
Mean	167.7913	485.9891	0.0101	0.0170	211085.1898	55310.4553	1738.0550	1.2055	50628.0987
%CV	1.8135	5.4922	216.1186	261.5177	0.5447	0.1350	1.1551	0.9292	0.6305

Table 3.13: SD, mean and %CV of extracted texture parameters of water phantom acquired images (n=20) at pixel size of 0.6 mm and scan speeds of 3 mm/s.

	Texture parameter @ pixel size=0.6 mm and scan speed =3 mm/s								
	GL	Variance	Skewness	Kurtosis	Cooccurrence matrix	RL matrix	Gradient	AR model	Wavelet transform
SD	3.8655	2.7484	0.0227	0.0435	3881.5728	138.3882	42.4795	0.0144	706.2336
Mean	220.1237	74.4922	0.0040	0.0486	211784.6445	52764.7413	1746.4147	1.1988	49559.4468
%CV	1.7561	3.6895	563.3098	89.3936	1.8328	0.2623	2.4324	1.2011	1.4250

Table 314: SD, mean and %CV of extracted texture parameters of water phantom acquired images (n=20) at pixel size of 0.6 mm and scan speeds of 5 mm/s.

	Texture parameter @ pixel size=0.6 mm and scan speed =5 mm/s								
	GL	Variance	Skewness	Kurtosis	Cooccurrence matrix	RL matrix	Gradient	AR model	Wavelet transform
SD	2.3509	2.0690	0.0205	0.0553	3062.9433	144.9166	31.2023	0.0073	585.8904
Mean	220.6215	74.3700	0.0073	0.0315	212489.0539	52861.8634	1750.7552	1.2004	49432.6322
%CV	1.0656	2.7821	280.9969	175.5716	1.4415	0.2741	1.7822	0.6106	1.1852

Table 3.15: SD, mean and %CV of extracted texture parameters of water phantom acquired images (n=20) at pixel size of 0.6 mm and scan speeds of 10 mm/s.

	Texture parameter @ pixel size=0.6 mm and scan speed =10 mm/s								
	GL	Variance	Skewness	Kurtosis	Cooccurrence matrix	RL matrix	Gradient	AR model	Wavelet transform
SD	2.8736	4.6333	0.0214	0.0525	2574.3226	143.2745	35.6180	0.0120	673.9581
Mean	211.6455	126.0804	0.0023	0.0373	211547.5527	53604.2215	1751.7639	1.2047	49749.3054
%CV	1.3578	3.6748	922.4711	140.6738	1.2169	0.2673	2.0333	0.9959	1.3547

Table 3.16: SD, mean and %CV of extracted texture parameters of water phantom acquired images (n=20) at pixel size of 0.6 mm and scan speeds of 15 mm/s.

	Texture parameter @ pixel size=0.6 mm and scan speed =15 mm/s								
	GL	Variance	Skewness	Kurtosis	Cooccurrence matrix	RL matrix	Gradient	AR model	Wavelet transform
SD	2.9837	6.9534	0.0210	0.0471	1541.2565	130.0954	21.3038	0.0114	545.7293
Mean	205.1760	166.2064	-0.0074	0.0291	212308.7726	54025.6523	1758.8622	1.2009	49927.5589
%CV	1.4542	4.1836	-283.8823	161.8595	0.7260	0.2408	1.2112	0.9529	1.0930

Table 3.17: SD, mean and %CV of extracted texture parameters of water phantom acquired images (n=20) at pixel size of 0.6 mm and scan speeds of 20 mm/s.

	Texture parameter @ pixel size=0.6 mm and scan speed =20 mm/s								
	GL	Variance	Skewness	Kurtosis	Cooccurrence matrix	RL matrix	Gradient	AR model	Wavelet transform
SD	2.7996	9.9525	0.0175	0.0398	2069.6030	150.2684	28.8638	0.0148	537.8878
Mean	198.5707	196.0795	0.0059	0.0483	211729.8678	54214.3211	1749.5583	1.2068	50093.0094
%CV	1.4099	5.0757	295.7065	82.4534	0.9775	0.2772	1.6498	1.2237	1.0738

Table 3.18: SD, mean and %CV of extracted texture parameters of water phantom acquired images (n=20) at pixel size of 0.6 mm and scan speeds of 30 mm/s.

	Texture parameter @ pixel size=0.6 mm and scan speed =30 mm/s								
	GL	Variance	Skewness	Kurtosis	Cooccurrence matrix	RL matrix	Gradient	AR model	Wavelet transform
SD	2.2055	10.3857	0.0175	0.0432	1346.4102	84.4136	22.7448	0.0127	491.3837
Mean	193.3380	260.0367	0.0027	0.0242	212573.0654	54556.4910	1761.8777	1.2020	50306.9433
%CV	1.1408	3.9940	646.4962	178.7945	0.6334	0.1547	1.2909	1.0589	0.9768

Table 3.19: SD, mean and %CV of extracted texture parameters of water phantom acquired images (n=20) at pixel size of 0.8 mm and scan speeds of 3 mm/s.

	Texture parameter @ pixel size=0.8 mm and scan speed =3 mm/s								
	GL	Variance	Skewness	Kurtosis	Cooccurrence matrix	RL matrix	Gradient	AR model	Wavelet transform
SD	2.0242	1.7042	0.0654	0.1601	4786.5350	257.8614	48.9808	0.0121	765.4700
Mean	229.2496	44.4045	-0.0199	0.0333	213861.6681	51891.2549	1790.9002	1.2059	48202.6027
%CV	0.8830	3.8379	-328.2365	480.2054	2.2381	0.4969	2.7350	1.0041	1.5880

Table 3.20: SD, mean and %CV of extracted texture parameters of water phantom acquired images (n=20) at pixel size of 0.8 mm and scan speeds of 5 mm/s.

	Texture parameter @ pixel size=0.8 mm and scan speed =5 mm/s								
	GL	Variance	Skewness	Kurtosis	Cooccurrence matrix	RL matrix	Gradient	AR model	Wavelet transform
SD	1.8789	1.4117	0.0730	0.1443	3502.2359	222.5119	34.1188	0.0138	686.1493
Mean	229.3773	43.5206	-0.0133	0.0531	212589.2692	51869.1332	1787.9501	1.2031	47982.2600
%CV	0.8191	3.2436	-548.7348	271.7769	1.6474	0.4290	1.9083	1.1503	1.4300

Table 3.21: SD, mean and %CV of extracted texture parameters of water phantom acquired images (n=20) at pixel size of 0.8 mm and scan speeds of 10 mm/s.

	Texture parameter @ pixel size=0.8 mm and scan speed =10 mm/s								
	GL	Variance	Skewness	Kurtosis	Cooccurrence matrix	RL matrix	Gradient	AR model	Wavelet transform
SD	2.3023	2.1478	0.0214	0.0474	3576.7647	219.3474	30.9214	0.0122	768.3025
Mean	224.3756	60.3219	-0.0023	0.0810	211461.5274	52391.3536	1783.0001	1.2095	48851.6356
%CV	1.0261	3.5606	-941.4719	58.5003	1.6914	0.4187	1.7342	1.0084	1.5727

Table 3.22: SD, mean and %CV of extracted texture parameters of water phantom acquired images (n=20) at pixel size of 0.8 mm and scan speeds of 15 mm/s.

	Texture parameter @ pixel size=0.8 mm and scan speed =15 mm/s								
	GL	Variance	Skewness	Kurtosis	Cooccurrence matrix	RL matrix	Gradient	AR model	Wavelet transform
SD	2.6432	10.0556	0.0124	0.0540	2792.5156	254.8493	32.8590	0.0125	659.8913
Mean	216.4005	94.9660	-0.0114	0.0712	213466.0508	53118.4509	1797.0983	1.2037	48963.8918
%CV	1.2215	10.5887	-108.6568	75.9368	1.3082	0.4798	1.8284	1.0412	1.3477

Table 3.23: SD, mean and %CV of extracted texture parameters of water phantom acquired images (n=20) at pixel size of 0.8 mm and scan speeds of 20 mm/s.

	Texture parameter @ pixel size=0.8 mm and scan speed =20 mm/s								
	GL	Variance	Skewness	Kurtosis	Cooccurrence matrix	RL matrix	Gradient	AR model	Wavelet transform
SD	3.2330	3.7449	0.0233	0.0432	3053.3315	164.2823	22.1188	0.0126	660.9975
Mean	214.6510	102.4934	-0.0066	0.0886	213131.6165	53274.0160	1799.5677	1.2120	49244.4103
%CV	1.5062	3.6538	-355.5499	48.7479	1.4326	0.3084	1.2291	1.0369	1.3423

Table 3.24: SD, mean and %CV of extracted texture parameters of water phantom acquired images (n=20) at pixel size of 0.8 mm and scan speeds of 30 mm/s.

	Texture parameter @ pixel size=0.8 mm and scan speed =30 mm/s								
	GL	**Variance**	**Skewness**	**Kurtosis**	**Cooccurrence matrix**	**RL matrix**	**Gradient**	**AR model**	**Wavelet transform**
SD	2.3404	4.7116	0.0262	0.0358	2287.6617	135.7822	31.9803	0.0105	552.7810
Mean	208.9648	137.3788	-0.0040	0.0902	212428.5321	53715.6165	1798.7563	1.2071	49419.0024
%CV	1.1200	3.4296	-661.6040	39.6716	1.0769	0.2528	1.7779	0.8690	1.1186

3.2.3.2. Statistical Analysis

Table 3.25: Overall effect of various pixel sizes on each of the nine extracted texture parameters.

Texture parameter	*F (3,467) =*	*P*	ηp^2
GL	807.9	<0.001	0.836
Variance	761.0	<0.001	0.827
Skewness	0.2	0.906	0.001
Kurtosis.	56.4	<0.001	0.262
Co-occurrence matrix	12.7	<0.001	0.074
RL matrix	543.1	<0.001	0.774
Gradient.	108.7	<0.001	0.406
AR model	5.6	0.001	0.034
Wavelet Transform.	230.7	<0.001	0.592

Table 3.26: Repeated contrast (comparison) results for comparing the effects of various pixel sizes on the means of the nine extracted texture parameters.

			Dependent Variables								
Pixel Levels Repeated Contrast			**Grey Level**	**Variance**	**Skewness**	**Kurtosis**	**Co-occurrence Metrix**	**RL-Matrix**	**Gradient Level**	**AR Model**	**Wavelet Transform.**
0.2 Level Vs. Level 0.4	**Contrast Estimate**		-38.047	345.897	-6.33E-05	-0.007	-222.407	817.02	-10.5	0.005	237.6
	Hypothesized Value		0	0	0	0	0	0	0	0	0
	Difference (Estimate - Hypothesized)		-38.047	345.897	-6.33E-05	-0.007	-222.407	817.02	-10.5	0.005	237.6
	Std. Error		1.557	13.125	0.002	0.006	304.86	74.241	3.6	0.002	77.4
	Sig.		0	0	0.975	0.198	0.466	0	0	0.004	0
	95% Confidence Interval for Difference	**Lower Bound**	-41.106	320.106	-0.004	-0.019	-821.446	671.139	-17.6	0.002	85.5
		Upper Bound	-34.987	371.687	0.004	0.004	376.631	962.9	-3.4	0.008	389.6
0.4 Level Vs. Level 0.6	**Contrast Estimate**		-21.092	159.208	0.001	-0.019	-725.719	1,032.94	-10.7	0	561.5
	Hypothesized Value		0	0	0	0	0	0	0	0	0
	Difference (Estimate - Hypothesized)		-21.092	159.208	0.001	-0.019	-725.719	1,032.94	-10.7	0	561.5
	Std. Error		1.557	13.125	0.002	0.006	304.86	74.241	3.6	0.002	77.4
	Sig.		0	0	0.582	0.001	0.018	0	0	0.872	0
	95% Confidence Interval for Difference	**Lower Bound**	-24.151	133.417	-0.003	-0.031	-1,324.76	887.063	-17.8	-0.003	409.5
		Upper Bound	-18.033	184.999	0.005	-0.008	-126.68	1,178.82	-3.6	0.003	713.6
0.6 Level Vs. Level 0.8	**Contrast Estimate**		-12.257	69.03	-0.001	-0.042	-750.951	961.244	-39.7	-0.005	1067.5
	Hypothesized Value		0	0	0	0	0	0	0	0	0
	Difference (Estimate - Hypothesized)		-12.257	69.03	-0.001	-0.042	-750.951	961.244	-39.7	-0.005	1067.5
	Std. Error		1.557	13.125	0.002	0.006	304.86	74.241	3.6	0.002	77.4
	Sig.		0	0	0.484	0	0.014	0	0	0.004	0
	95% Confidence Interval for Difference	**Lower Bound**	-15.316	43.239	-0.005	-0.053	-1,349.99	815.364	-46.8	-0.008	915.5
		Upper Bound	-9.198	94.821	0.003	-0.03	-151.913	1,107.13	-32.6	-0.001	1219.6

Table 3.27: Overall effects of various scan speed levels on each of the nine texture measures.

Texture Parameter	*F (5, 474) =*	*P*	ηp²
GL	15.5	0.000	0.14
Variance	14.4	0.000	0.132
Skewness.	1.6	0.158	0.017
Kurtosis.	0.5	0.786	0.005
Co-occurrence matrix	1.0	0.422	0.01
RL matrix	20.4	0.000	0.177
Gradient.	0.3	0.915	0.003
AR model	1.0	0.404	0.011
Wavelet transform.	8.9	0.000	0.086

Table 3.28: Repeated Contrast results for comparing the effects of various Scan Speeds on the means of each of the nine extracted texture parameters.

Scan Speed Repeated Contrast			Dependent Variable								
			Grey Level	Variance	Skewness	Kurtosis	Co-occurrence Metrix	RL-Matrix	Gradient Level	AR Model	Wavelet Transform.
3mm/Sec Versus 5 mm/Sec	Contrast Estimate		3.768	-34.73	-0.001	0.003	110.231	-130.883	-2.925	0.001	-1.471
	Hypothesized Value		0	0	0	0	0	0	0	0	0
	Difference (Estimate - Hypothesized)		3.768	-34.73	-0.001	0.003	110.231	-130.883	-2.925	0.001	-1.471
	Std. Error		4.373	36.143	0.002	0.008	386.879	173.826	5.743	0.002	142.238
	Sig.		0.389	0.337	0.62	0.759	0.776	0.452	0.611	0.508	0.992
	95% Confidence Interval for Difference	Lower Bound	-4.824	-105.751	-0.006	-0.014	-649.98	-472.448	-14.21	-0.003	-280.967
		Upper Bound	12.361	36.29	0.004	0.019	870.442	210.681	8.361	0.005	278.025
5 mm/Sec Versus 10 mm/Sec	Contrast Estimate		9.363	-77.508	0.003	0.002	648.853	-505.406	1.867	-0.004	-359.314
	Hypothesized Value		0	0	0	0	0	0	0	0	0
	Difference (Estimate - Hypothesized)		9.363	-77.508	0.003	0.002	648.853	-505.406	1.867	-0.004	-359.314
	Std. Error		4.373	36.143	0.002	0.008	386.879	173.826	5.743	0.002	142.238
	Sig.		0.033	0.033	0.191	0.811	0.094	0.004	0.745	0.058	0.012
	95% Confidence Interval for Difference	Lower Bound	0.771	-148.528	-0.002	-0.014	-111.358	-846.97	-9.418	-0.008	-638.81
		Upper Bound	17.956	-6.487	0.008	0.018	1,409.06	-163.841	13.152	0	-79.819
10 mm/Sec Versus 15 mm/Sec	Contrast Estimate		7.624	-45.399	0.003	0.005	-650.403	-350.276	-1.456	0.002	-102.384
	Hypothesized Value		0	0	0	0	0	0	0	0	0
	Difference (Estimate - Hypothesized)		7.624	-45.399	0.003	0.005	-650.403	-350.276	-1.456	0.002	-102.384
	Std. Error		4.373	36.143	0.002	0.008	386.879	173.826	5.743	0.002	142.238
	Sig.		0.082	0.21	0.212	0.538	0.093	0.044	0.8	0.314	0.472
	95% Confidence Interval for Difference	Lower Bound	-0.968	-116.419	-0.002	-0.011	-1,410.61	-691.84	-12.741	-0.002	-381.88
		Upper Bound	16.217	25.621	0.008	0.021	109.808	-8.712	9.829	0.006	177.111
15 mm/Sec Versus 20 mm/Sec	Contrast Estimate		5.027	-31.843	-0.002	-0.012	157.234	-141.185	-3.352	-0.002	-111.653
	Hypothesized Value		0	0	0	0	0	0	0	0	0
	Difference (Estimate - Hypothesized)		5.027	-31.843	-0.002	-0.012	157.234	-141.185	-3.352	-0.002	-111.653
	Std. Error		4.373	36.143	0.002	0.008	386.879	173.826	5.743	0.002	142.238
	Sig.		0.251	0.379	0.361	0.151	0.685	0.417	0.56	0.365	0.433
	95% Confidence Interval for Difference	Lower Bound	-3.565	-102.864	-0.007	-0.028	-602.977	-482.749	-14.638	-0.006	-391.149
		Upper Bound	13.62	39.177	0.003	0.004	917.445	200.379	7.933	0.002	167.842
20 mm/Sec Versus 30 mm/Sec	Contrast Estimate		4.646	-68.66	-0.001	0.005	91.776	-250.021	1.056	0.001	-153.943
	Hypothesized Value		0	0	0	0	0	0	0	0	0
	Difference (Estimate - Hypothesized)		4.646	-68.66	-0.001	0.005	91.776	-250.021	1.056	0.001	-153.943
	Std. Error		4.373	36.143	0.002	0.008	386.879	173.826	5.743	0.002	142.238
	Sig.		0.289	0.058	0.731	0.517	0.813	0.151	0.854	0.478	0.28
	95% Confidence Interval for Difference	Lower Bound	-3.946	-139.68	-0.006	-0.011	-668.435	-591.586	-10.229	-0.003	-433.439
		Upper Bound	13.239	2.361	0.004	0.022	851.987	91.543	12.341	0.005	125.552

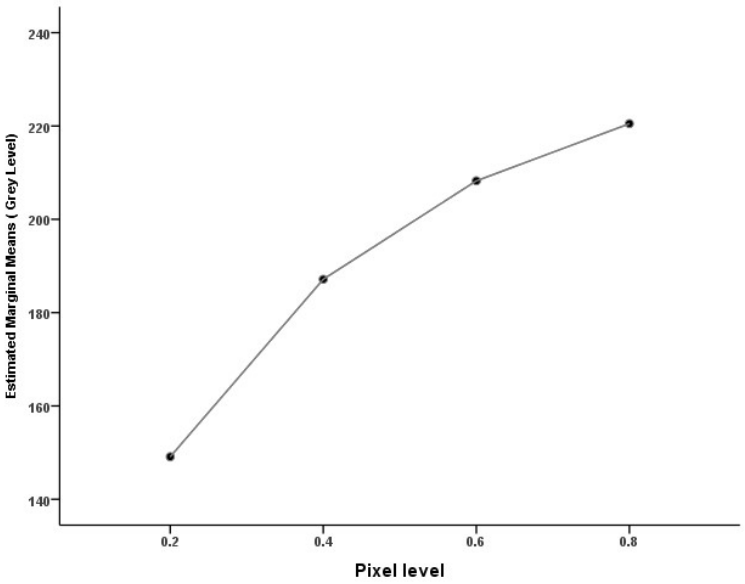

Figure 3.5: Effect of increasing pixel size on GL parameter.

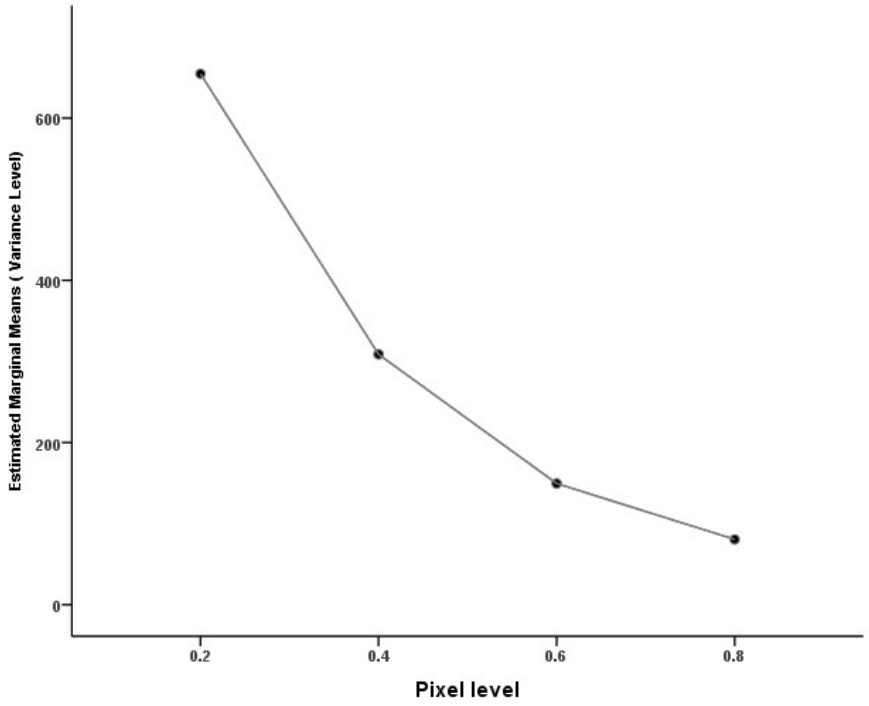

Figure 3.6: Effect of increasing pixel size on variance. parameter.

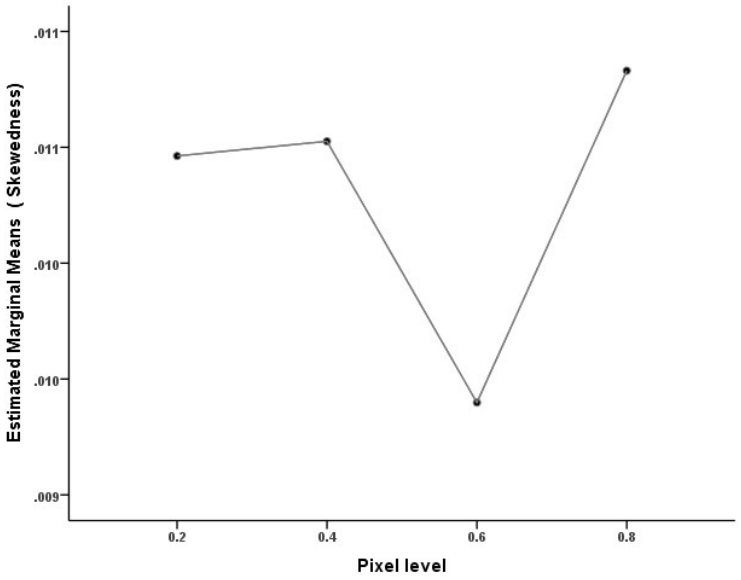

Figure 3.7: Effect of increasing pixel size on skewness parameter.

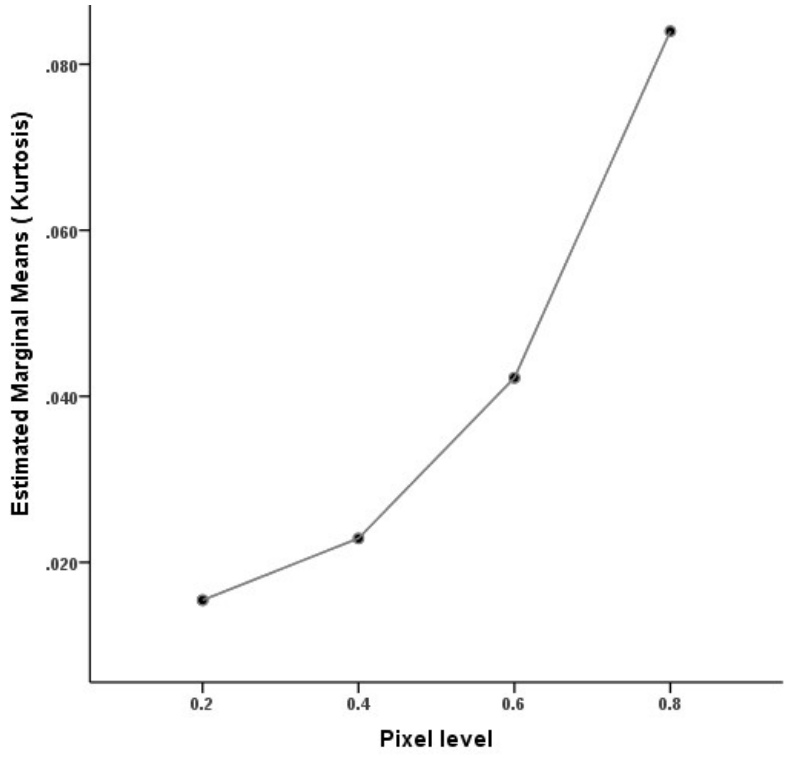

Figure 3.8: Effect of increasing pixel size on kurtosis parameter

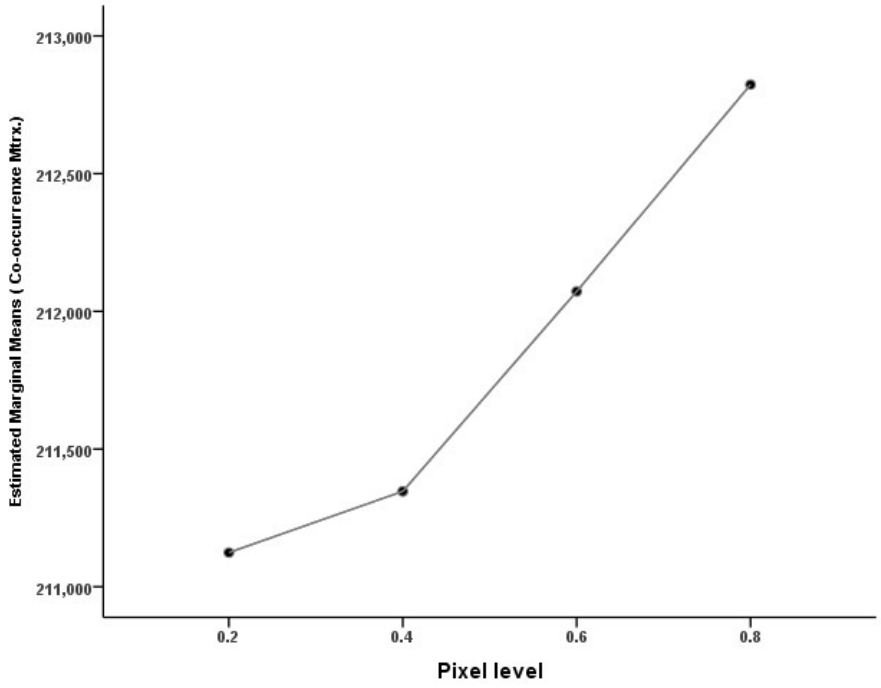

Figure 3.9: Effect of increasing pixel size on co-occurrence matrix parameter.

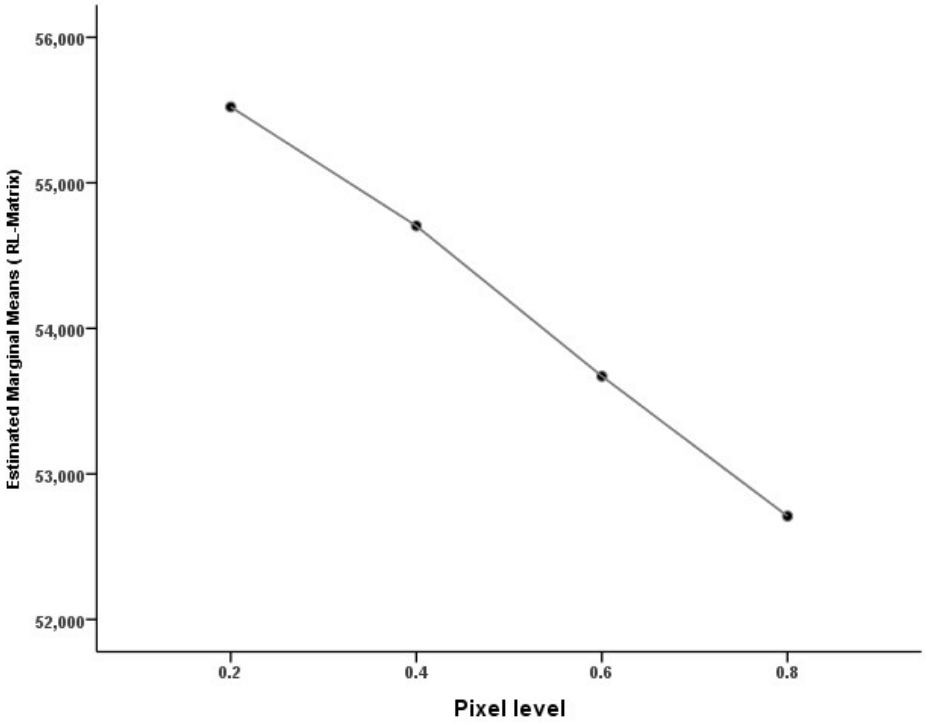

Figure 3.10: Effect of increasing pixel size on RL matrix parameter.

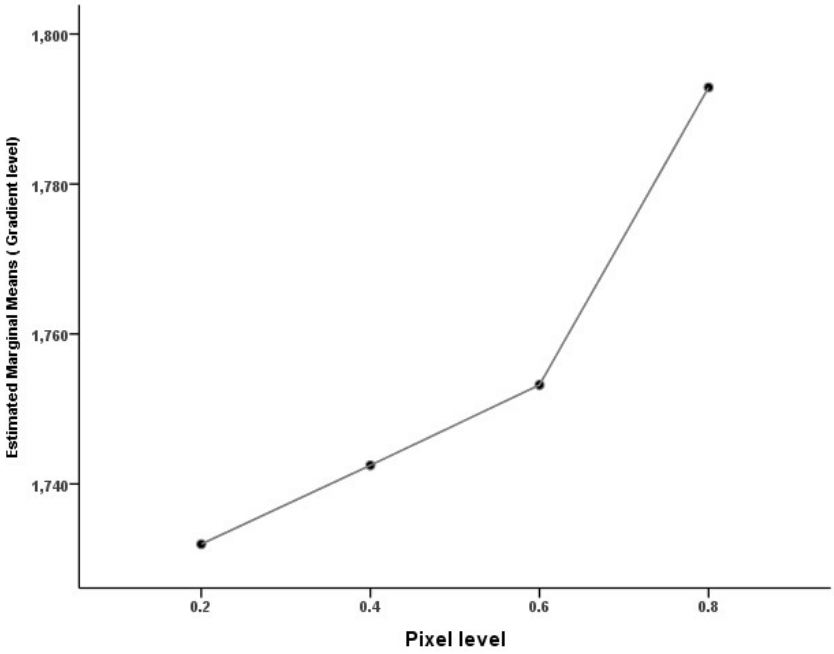

Figure 3.11: Effect of increasing pixel size on gradient parameter.

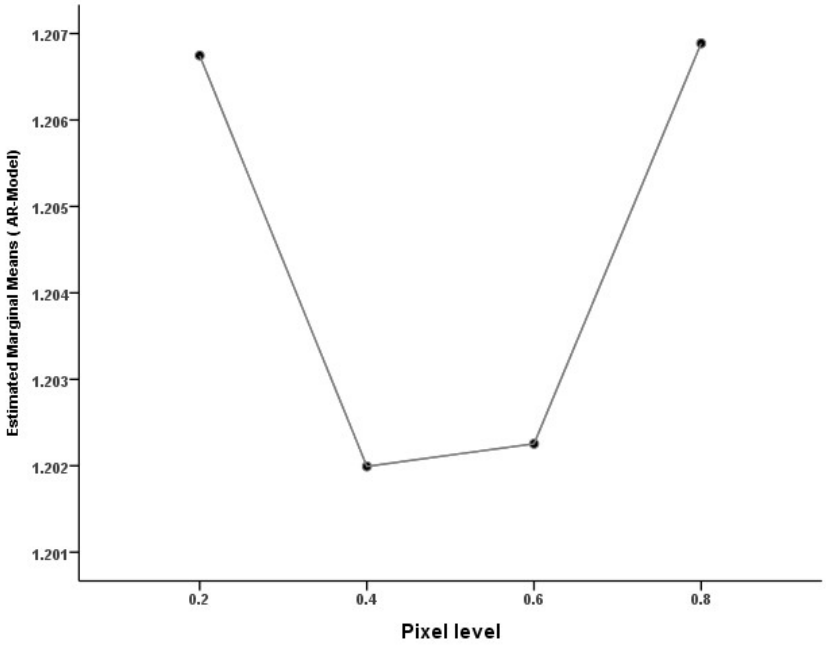

Figure 3.12: Effect of increasing pixel size on AR model. parameter.

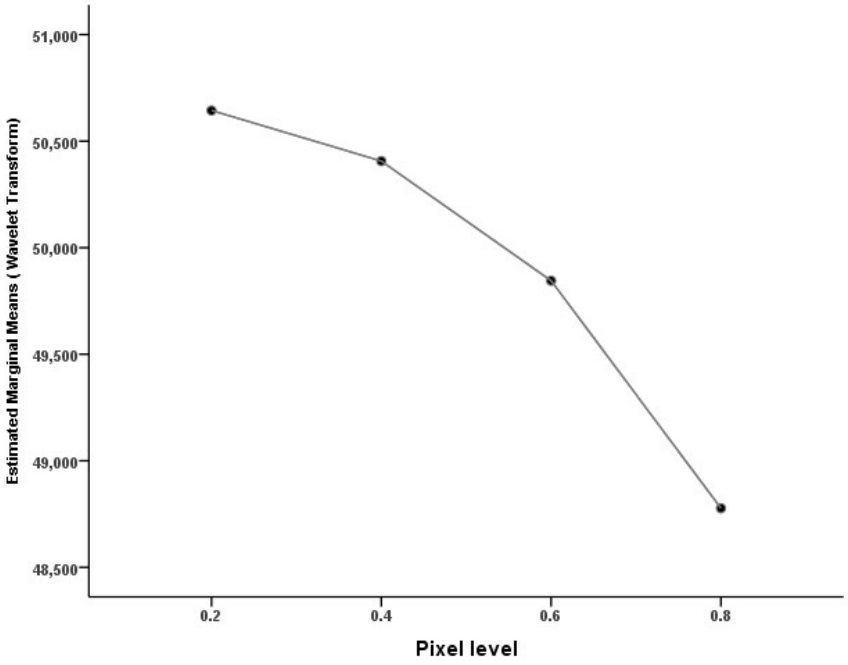

Figure 3.13: Effect of increasing pixel size on wavelet transform parameter.

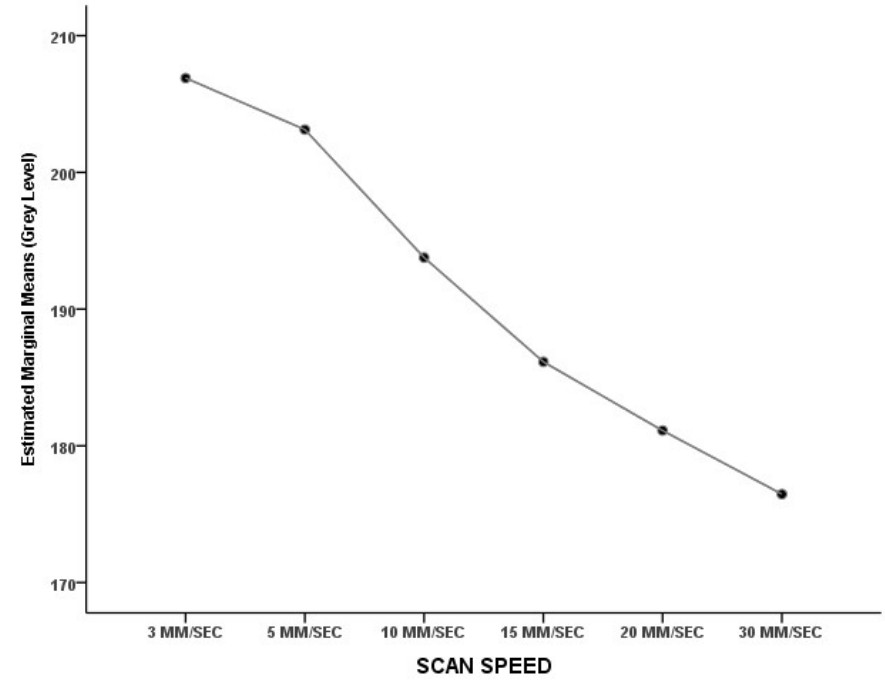

Figure 3.14: Effect of increasing scan speed on GL parameter.

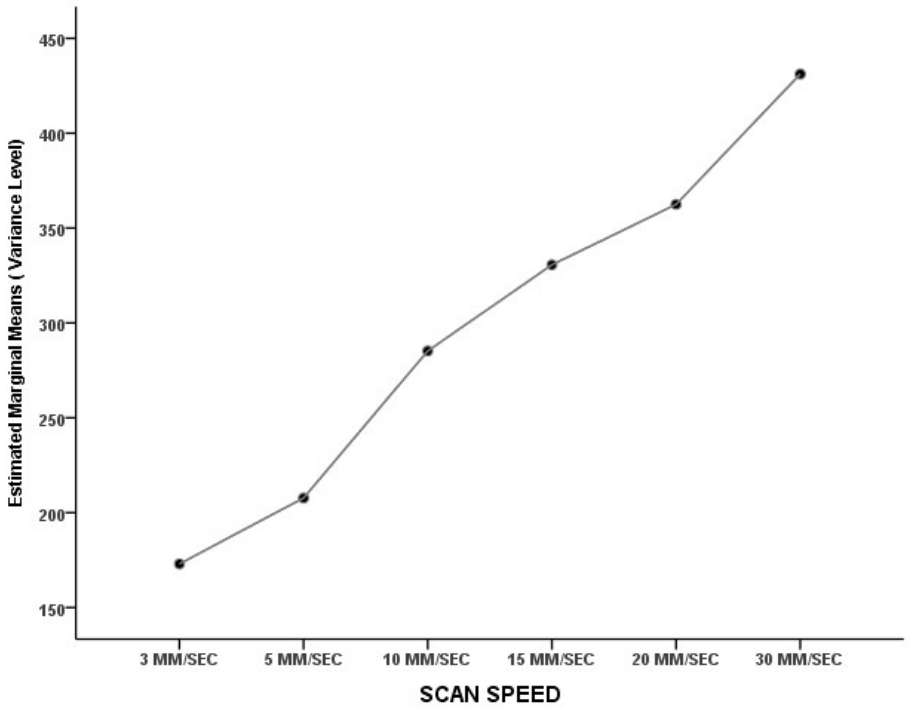

Figure 3.15: Effect of increasing scan speed on variance parameter.

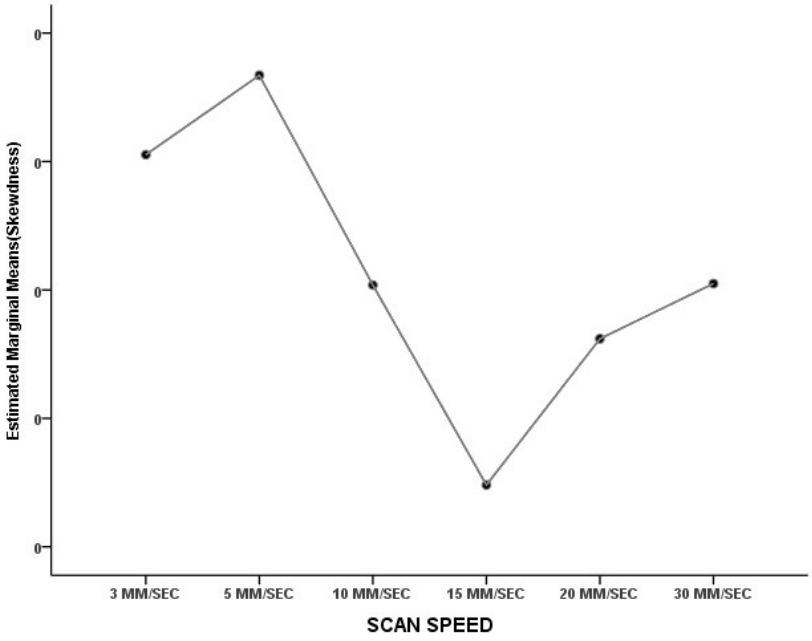

Figure 3.16: Effect of increasing scan speed on skewness parameter.

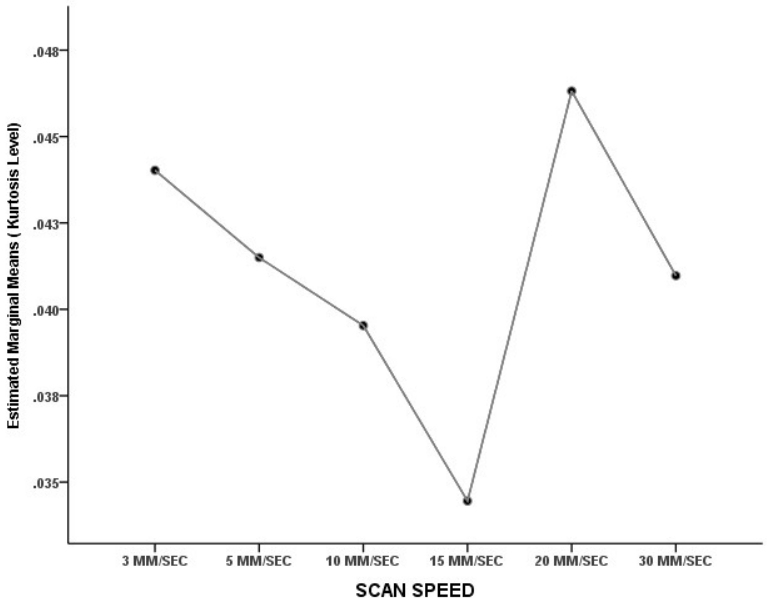

Figure 3.17: Effect of increasing scan speed on kurtosis parameter.

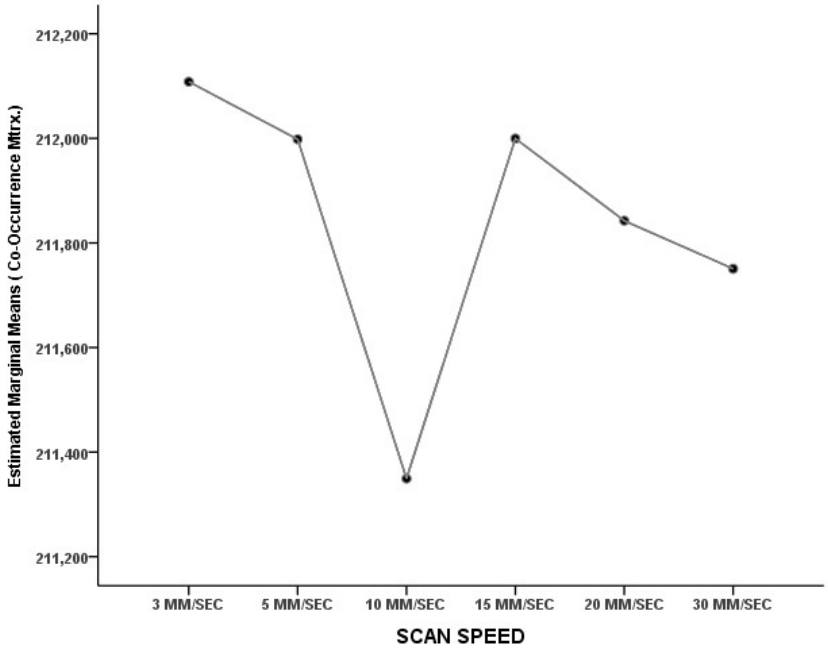

Figure 3.18: Effect of increasing scan speed on co-occurrence matrix parameter.

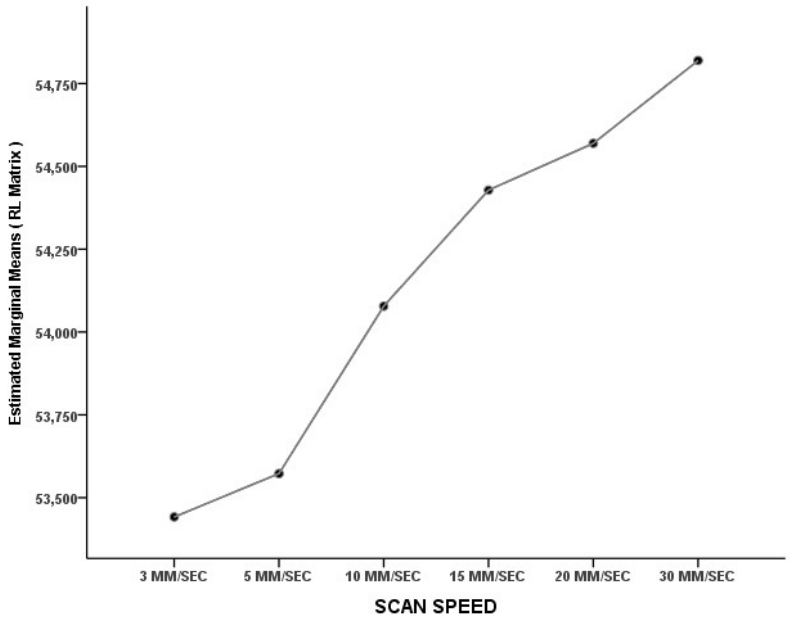

Figure 3.19: Effect of increasing scan speed on RL matrix parameter.

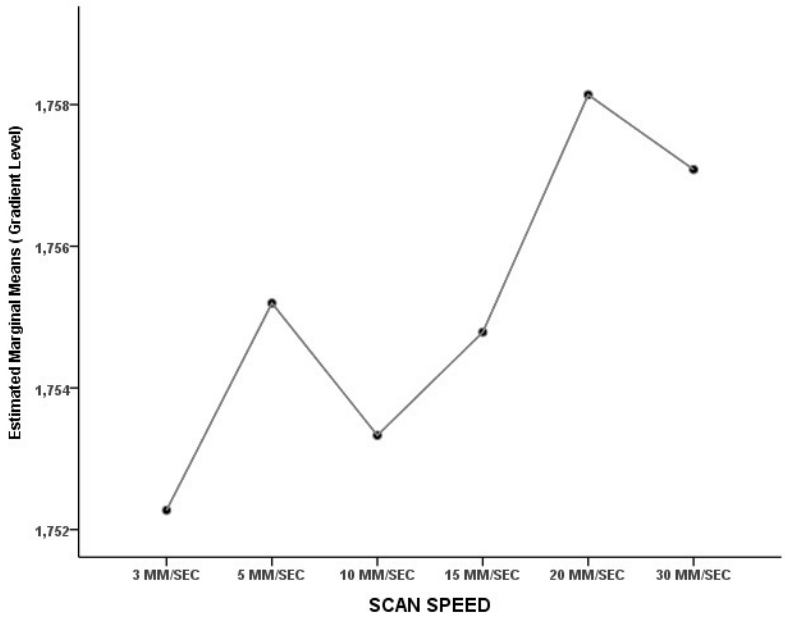

Figure 3.20: Effect of increasing scan speed on gradient parameter.

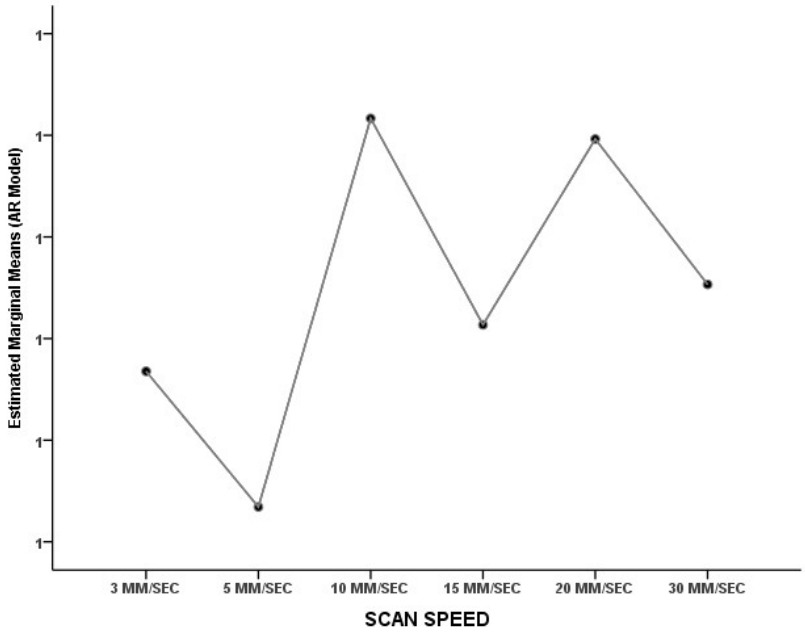

Figure 3.21: Effect of increasing scan speed on AR model parameter.

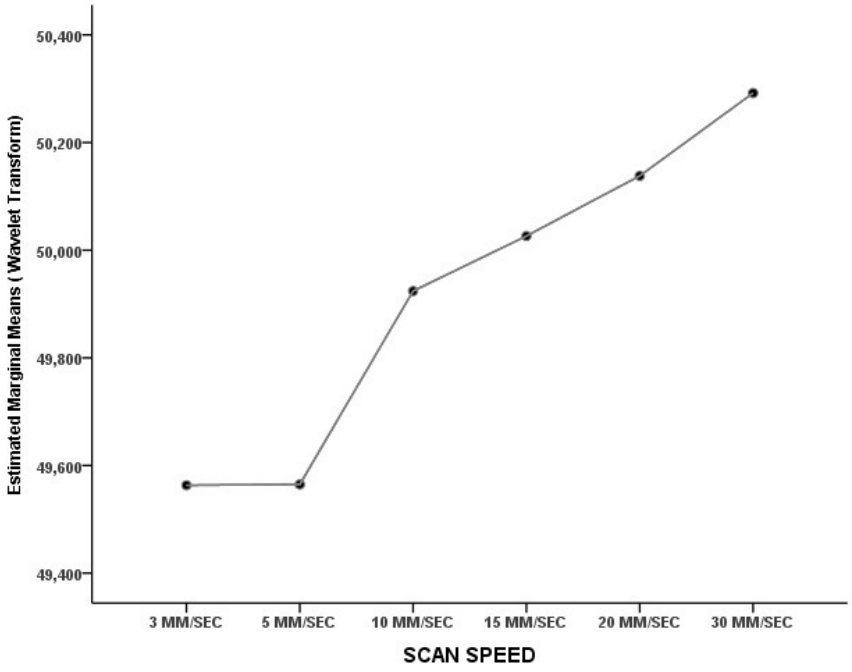

Figure 3.22: Effect of increasing scan speed on wavelet transform parameter.

3.2.3.3 Repeatability

Table 3.29 shows the mean, SD and % CV of water phantom texture parameters calculated over all scan speeds (3, 5, 10, 15, 20 and 30 mm/s) and pixel sizes (0.2, 0.4, 0.6 and 0.8 mm).

Table 3.29: Mean of texture parameters at range of pixel sizes and range of scan speeds. Mean, SD and %CV were calculated.

		Texture parameter								
Scan speed (mm/s)	Pixel size (mm)	GL	Variance	Skewness	Kurtosis	Co-occurrence	RL	Gradient	AR	Wavelet
3	0.2	169.7591	428.4064	0.0010	0.0193	211230.6083	55238.3877	1728.0890	1.2124	50461.9814
	0.4	208.4562	144.6727	0.0061	-0.0181	211556.5572	53872.6326	1743.6869	1.1975	50029.0441
	0.6	220.1237	74.4922	0.0040	0.0486	211784.6445	52764.7413	1746.4147	1.1988	49559.4468
	0.8	229.2496	44.4045	-0.0199	0.0333	213861.6681	51891.2549	1790.9002	1.2059	48202.6027
5	0.2	161.0030	523.5688	0.0026	0.0035	211239.9062	55362.2641	1731.3686	1.2057	50560.4355
	0.4	201.5134	189.4377	0.0019	0.0171	211674.3240	54197.2889	1750.7149	1.2001	50283.6316
	0.6	220.6215	74.3700	0.0073	0.0315	212489.0539	52861.8634	1750.7552	1.2004	49432.6322
	0.8	229.3773	43.5206	-0.0133	0.0531	212589.2692	51869.1332	1787.9501	1.2031	47982.2600
10	0.2	149.3949	670.1539	0.0055	-0.0081	211083.4160	55594.2937	1738.0885	1.2051	50617.8540
	0.4	189.6459	284.3716	0.0041	0.0128	211304.6453	54722.3036	1740.4677	1.2053	50477.4223
	0.6	211.6455	126.0804	0.0023	0.0373	211547.5527	53604.2215	1751.7639	1.2047	49749.3054
	0.8	224.3756	60.3219	-0.0023	0.0810	211461.5274	52391.3536	1783.0001	1.2095	48851.6356
15	0.2	141.5668	710.5478	0.0095	-0.0103	211161.1095	55600.7387	1727.0479	1.2099	50639.5188
	0.4	181.4217	350.8031	-0.0013	0.0009	211062.8217	54968.4345	1736.1369	1.2021	50574.7854
	0.6	205.1760	166.2064	-0.0074	0.0291	212308.7726	54025.6523	1758.8622	1.2009	49927.5589
	0.8	216.4005	94.9660	-0.0114	0.0712	213466.0508	53118.4509	1797.0983	1.2037	48963.8918
20	0.2	137.1414	754.0845	0.0101	-0.0139	211113.2303	55635.8448	1737.5840	1.2037	50769.7532
	0.4	174.0938	397.2397	0.0036	0.0266	211395.1046	55153.8351	1745.8450	1.2014	50445.1947
	0.6	198.5707	196.0795	0.0059	0.0483	211729.8678	54214.3211	1749.5583	1.2068	50093.0094
	0.8	214.6510	102.4934	-0.0066	0.0886	213131.6165	53274.0160	1799.5677	1.2120	49244.4103
30	0.2	135.7771	841.1316	0.0056	-0.0076	210915.9293	55695.5394	1729.6430	1.2036	50814.0967
	0.4	167.7913	485.9891	0.0101	0.0170	211085.1898	55310.4553	1738.0550	1.2055	50628.0987
	0.6	193.3380	260.0367	0.0027	0.0242	212573.0654	54556.4910	1761.8777	1.2020	50306.9433
	0.8	208.9648	137.3788	-0.0040	0.0902	212428.5321	53715.6165	1798.7563	1.2071	49419.0024
	SD	30.0726	247.8225	0.0077	0.0321	824.6870	1222.0837	24.1426	0.0039	805.8066
	Mean	191.2524	298.3649	0.0007	0.0281	211841.4360	54151.6306	1755.1347	1.2045	49918.1048
	%CV	15.7241	83.0602	1141.3363	113.8698	0.3893	2.2568	1.3755	0.3223	1.6143

3.2.2.4 Influence of ROI Area on Extracted Texture Parameter

The influence of ROI area size on extracted texture parameters of water phantom image acquired with scan speed of 10 mm/s and pixel size of 0.8 mm is shown in Table 3.30.

Table 3.30: Influence of ROI area size on extracted texture parameters of water phantom image acquired with scan speed of 10 mm/s and pixel size of 0.8 mm.

	ROI size									
Texture paraeter	**14216**	**10000**	**5000**	**2500**	**1500**	**500**	**300**	**200**	**100**
GL	225.2745	225.2368	225.1944	225.1828	225.3667	225.2840	225.3767	224.9300	224.7800
Variance	61.4750	66.8479	75.1674	76.4286	78.8442	74.7593	76.3815	81.3151	69.6116
Skewness	0.0214	0.0324	0.0273	0.0776	0.1012	0.1186	0.0468	-0.0051	0.1992
Kurtosis	0.0822	0.0261	-0.0141	-0.0550	0.0305	0.1744	0.0574	0.1355	0.3689
Cooccurrence matrix	212762.8751	213611.6070	210446.1879	206802.0699	204036.0629	211480.2410	213630.5639	202665.6491	200355.6424
RL matrix	52540.3277	37202.4135	18695.2578	9399.5953	5681.1652	1898.7761	1145.3658	764.9448	393.2342
Gradient	1799.4312	1761.6071	1737.8860	1668.9250	1665.8191	1739.1700	1811.3886	1815.0150	1394.2720
AR model	1.2003	1.2048	1.1945	1.1843	1.1767	1.1432	1.1119	1.1407	0.8734
Wavelet transform	49955.2848	50296.8517	48419.8942	50104.1657	48591.2162	48594.9164	48739.7230	52210.7765	50663.6199

Figures 3.23 – 3.31 represent the influence of ROI area on extracted texture parameters with fitted regression lines.

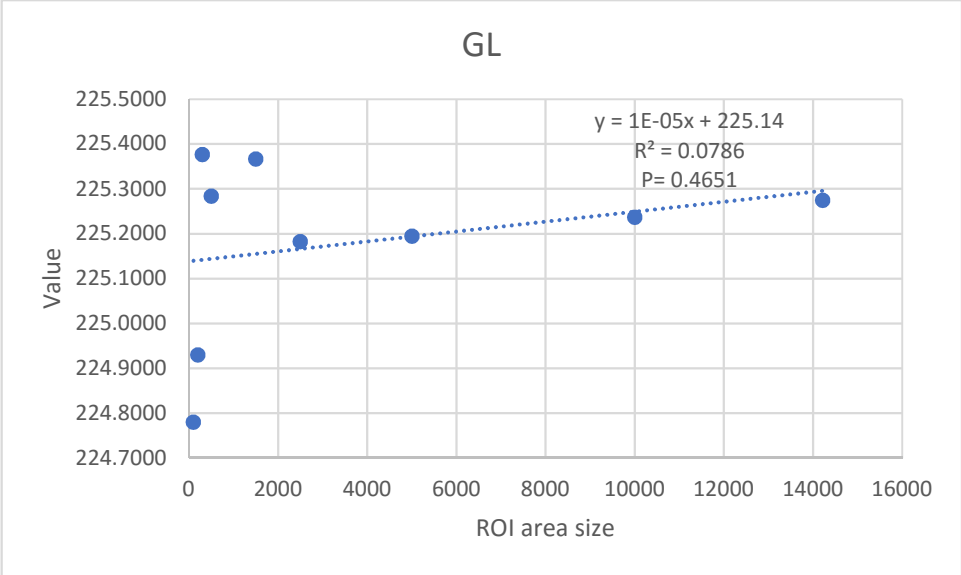

Figure 3.23: The fitted regression line between the GL values of the 9 ROI sizes.

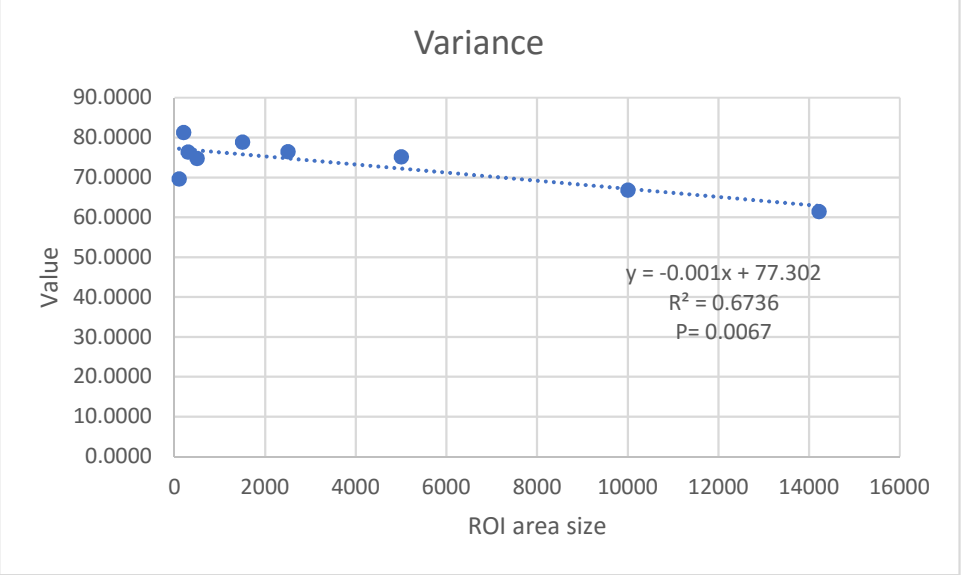

Figure 3.24: The fitted regression line between the variance values of the 9 ROI sizes.

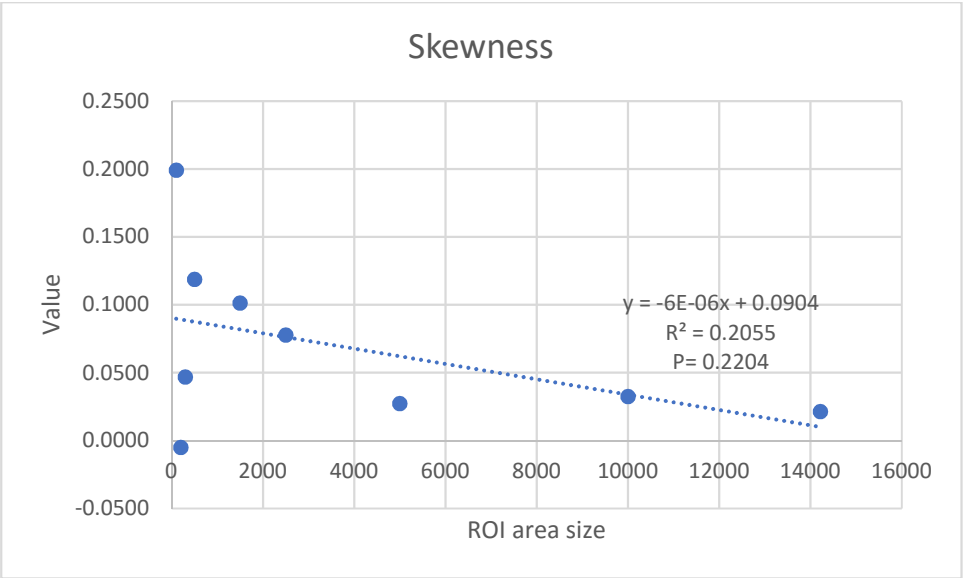

Figure 3.25: The fitted regression line between the skewness values of the 9 ROI sizes.

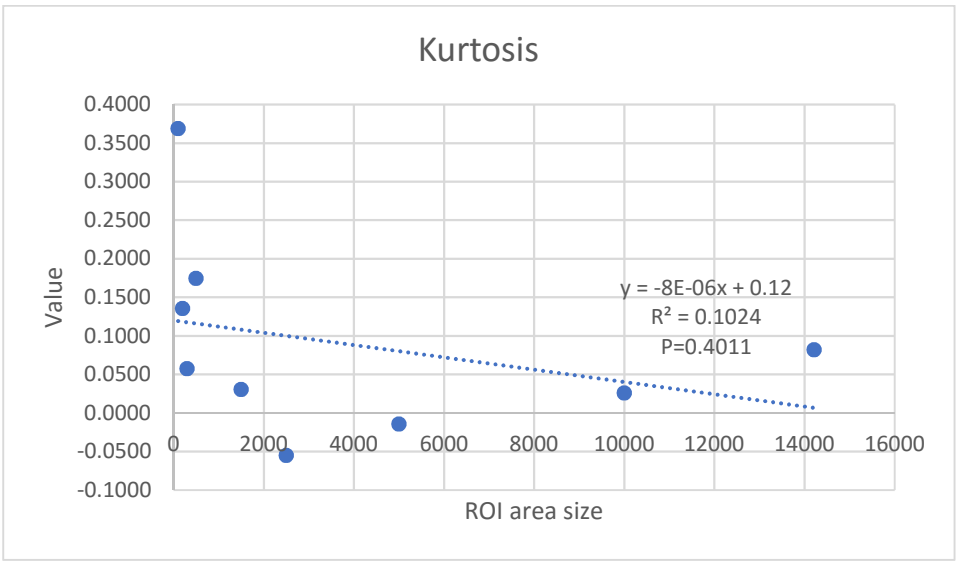

Figure 3.26: The fitted regression line between the kurtosis values of the 9 ROI sizes.

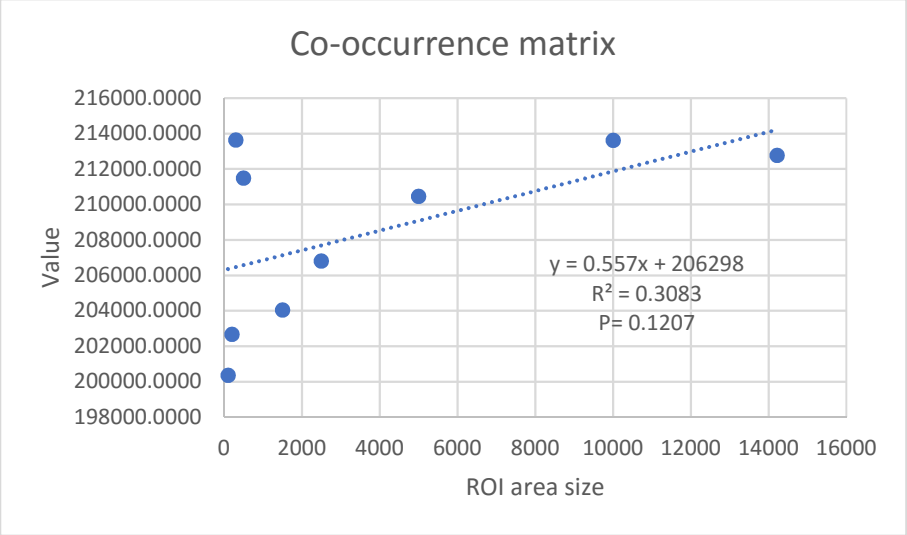

Figure 3.27: The fitted regression line between the co-occurrence matrix values of the 9 ROI sizes.

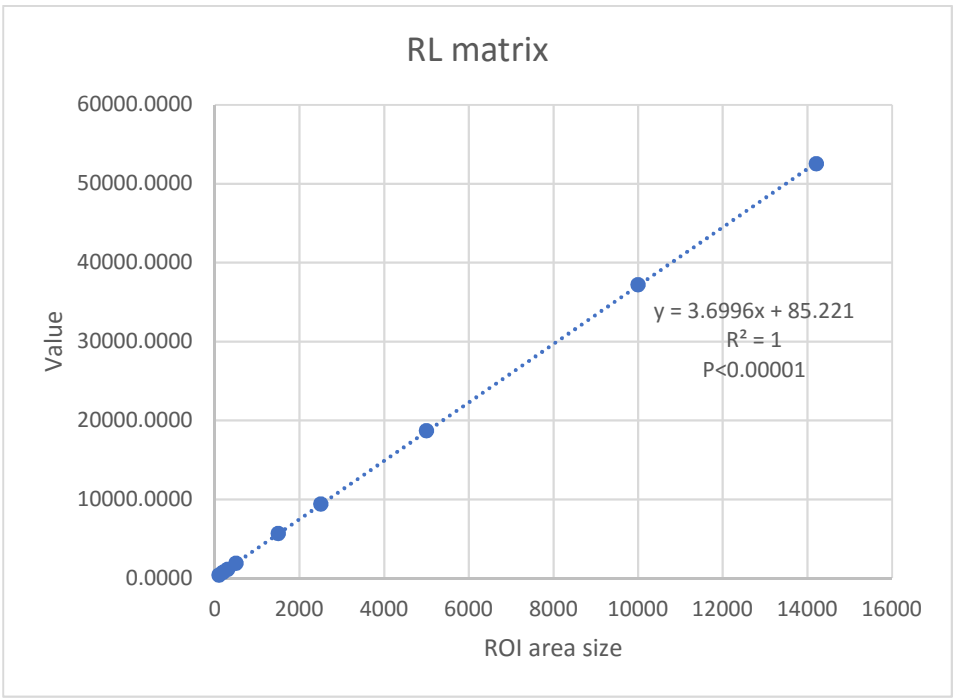

Figure 3.28: The fitted regression line between the RL matrix values of the 9 ROI sizes.

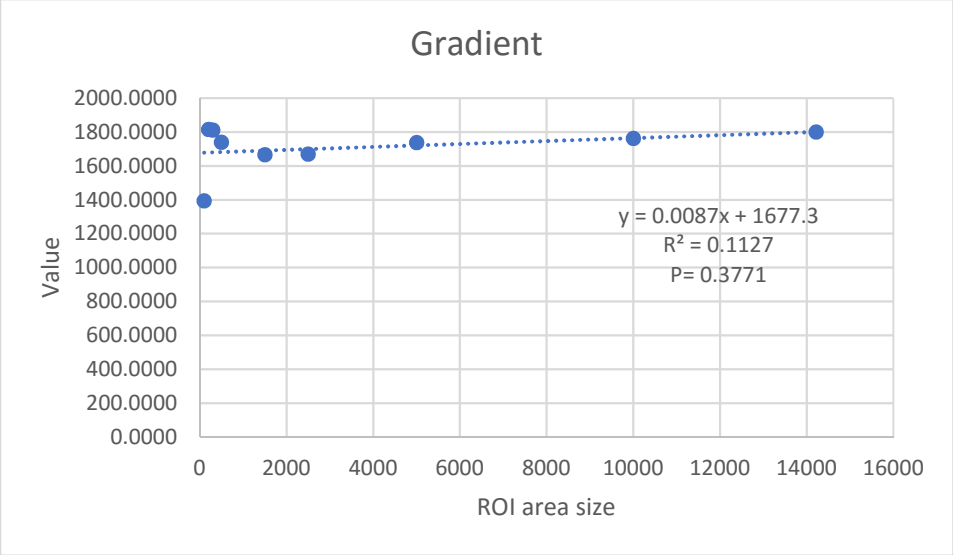

Figure 3.29: The fitted regression line between the gradient values of the 9 ROI sizes.

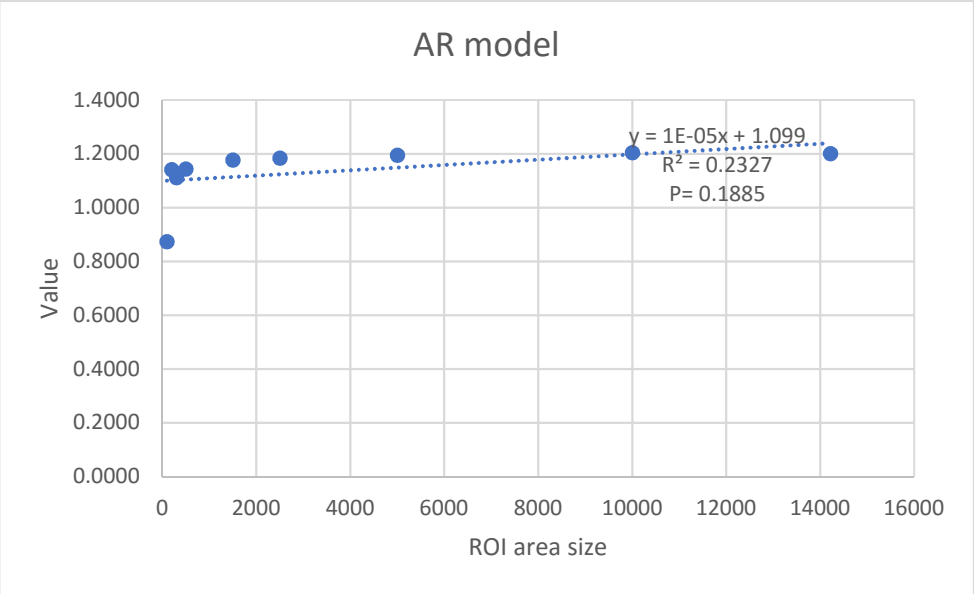

Figure 3.30: The fitted regression line between the AR model values of the 9 ROI sizes.

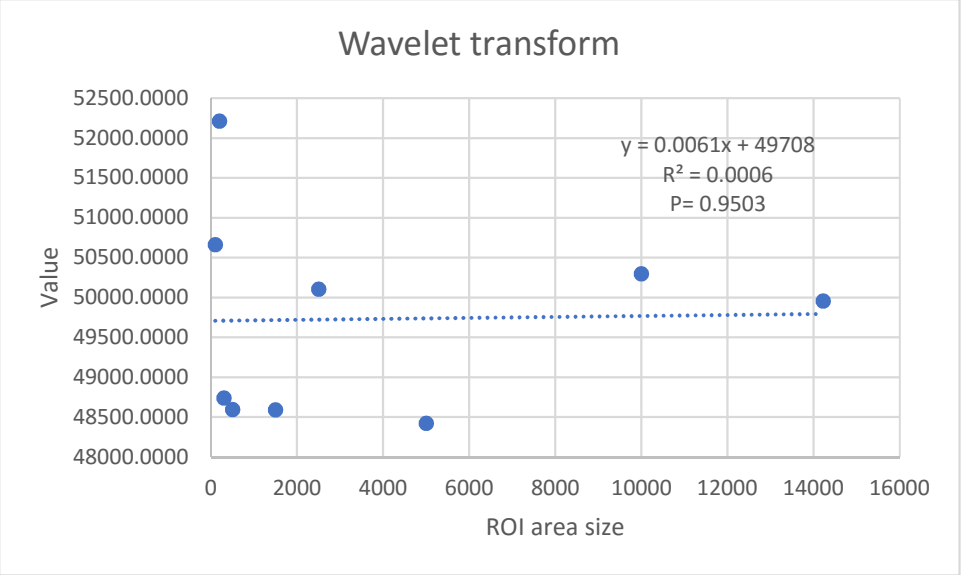

Figure 3.31: The fitted regression line between the wavelet transform values of the 9 ROI sizes.

Table 3.31: Summarises p values of influence of ROI area reduction on extracted texture parameters (significant at $p<0.05$).

Texture Parameter	R^2	r	P-value	Significance
GL	0.0786	0.2803	0.4651	No (>0.05)
Variance	0.6736	0.8207	0.0067	Yes (<0.05)
Skewness	0.2055	0.4533	0.2204	No
Kurtosis	0.1024	0.32	0.4011	No
Cooccurrence matrix	0.3083	0.5552	0.1207	No
RL matrix	1	1	<0.00001	Yes
Gradient	0.1127	0.3357	0.3771	No
AR model	0.2327	0.4823	0.1885	No
Wavelet transform	0.0006	0.0244	0.9503	No

3.2.4 Discussion

The scanning of the water phantom was designed to mimic the human leg, whose soft tissue structures have an effective atomic number (7.64) and tissue density (1040 kg/m^3) similar to those of water (7.51, 1000 kg/m^3) (Carlton and Adler, 2013). Despite the superimposition on the water phantom images of visual (Poisson) noise, the identification of extracted texture parameters that were less sensitive to noise was possible. Some texture parameters change greatly with acquisition parameters, others change too, but not as much. Pixel values (grey level) are related to the linear attenuation coefficient (LAC) of the matter in the corresponding voxels. Linear attenuation coefficient is proportional to density. Statistical noise in the acquired images causes apparent variations in the density from pixel to pixel within the defined image. The range of these variations was evaluated by calculating the standard deviation (SD). Therefore, the SD of the grey level was considered a measure of image noise, also known as the noise index (Goldman, 2007; Bushberg et al., 2012). Standard deviation is the square root of variance (extracted texture parameter).

In CT, each slice is formed and divided into a matrix of volume elements (voxels). In general, the voxels in the slice of tissue are represented by pixels. The size of an individual voxel plays a critical role in image quality and patient dose. The pixel size is determined by the field of view (FOV) divided by the matrix size (number of pixels in each direction). During the subject scan, x-rays penetrate the subject and are attenuated in proportion to the product of LAC and thickness of tissue in the x-ray beam as described in Chapter 2. Furthermore, during the image reconstruction (back projection) process, the linear attenuation coefficient of each individual voxel is calculated and is represented by the value of the corresponding pixel in the acquired image.

The variation in CT image pixel value depends on the number of attenuated photons. In other words, the precision of measurement increases as the number of detected photons increases due to decreased noise. The standard deviation (SD) is proportional to the square root of average number of photons in each measurement, i.e., the number of detected photons (Bushberg et al. 2012). To achieve greater photon detection at a specific radiation dose (note that the pQCT dose is fixed for a given value of scan speed), pixel size must be increased.

The effect of increasing pixel size on the overall mean extracted texture parameters was shown in Table 3.25. The MANOVA test showed that increasing pixel size had a significant effect ($p<0.05$) on grey level, variance, kurtosis, co-occurrence matrix, RL matrix, gradient, AR model and wavelet transform, but not on skewness. In other words, there was a statistically significant effect of the pixel size on grey level — $F(3,467) = 807.9$, $p<0.001$, $\eta p^2 = 0.84$ — (ηp^2= partial eta squared is an effect size statistic which shows the magnitude of the effect of the varying the pixel size on GL, partial eta squared has ranges that helps us to classify the effect as small, medium or large), (F ratio test is the test of significance in use for MANOVA and it shows the ratio between accurately predicted GL values to the errors , i.e., noise in predicting the GL score value).This means that varying the pixel size has a very strong effect on grey level as illustrated in the pairwise comparison Tables (Tables 3.26). Moreover, there was a statistically significant effect of varying pixels on variance levels — $F(3,467) = 761$, $p<0.001$ — with a very strong effect size as well, which means the overall effect for increasing pixel size on the variance level was large — $\eta p^2 = 0.83$. Likewise, the varying pixel levels had a significant impact on kurtosis — $F(3,467) = 56.4$, $p<0.001$ — with a strong effect of pixels on kurtosis — $\eta p^2 = 0.262$. In the same way, for the relationship between pixel levels and the co-occurrence matrix, $F(3,467) = 12.7$, $p<0.001$ and $\eta p^2 = 0.074$, denoting a moderately small effect. In addition, the pixel levels had a significant effect on the RL matrix and gradient levels — $F(3,467) = 543.1$, $p<0.001$, $\eta p^2 = 0.262$, and $F(3,467) = 5.6$, $p<0.001$, $\eta p^2 = 0.003$, respectively — denoting an overall strong effect of varying levels of pixels on the RL matrix, and a similar but small effect of varying pixel size on the gradient level. The varying sizes of pixels were found to affect the wavelet transform score significantly — $F(3,467) = 230$, $p<0.001$, $\eta p^2 = 0.6$ — which is a very strong effect. Lastly, there was no significant effect of pixel levels on skewness of the image — $F(3,467) = 0.2$, $p=0.906$, $\eta p^2 = 0.001$. The MANOVA test was followed by post-hoc test comparing means of the nine texture parameters values between each successive pairs of pixel size to identify points of statistically significant differences as illustrated in Table 3.26.

The series of repeated t-tests (pairwise comparisons) showed that there was a significant difference of the mean grey levels between the 0.2 mm pixels and 0.4 mm

pixels ($p<0.001$, 95% CI for mean difference = -41 to -35), between 0.4 mm pixels and 0.6 pixels ($p<0.001$, 95% CI for mean difference = -18 to -12.3) and also between 0.6 pixels and 0.8 pixels ($p<0.001$, 95% CI for mean difference = -15.3 to -9.2), denoting an overall significant increase in grey level with an increased pixel size as shown in Figure 3.5. Likewise, when we compared the means of variance levels, there was a statistically significant difference between the four ranges of pixel sizes (0.2 pixels versus 0.4 pixels: $p<0.001$, 95% CI for mean difference = 320.1 to 371.7; 0.4 pixels versus 0.6 pixels: $p<0.001$, 95% CI for mean difference = 133.4 to 185; and 0.6 pixels versus 0.8 pixels: $p<0.001$, 95% CI for mean difference = 43.2 to 95). The mean variance value levels differed significantly across the increasing pixel sizes, where the increasing pixel size was associated with significantly decreasing variance, as can be seen in the Figure 3.6. Worth noting is that the kurtosis value was contrasted across the various levels of pixels, and pairwise comparisons indicated that there were no statistically significant differences on mean kurtosis value between 0.2 pixels and 0.4 pixels, $p=0.198$, but there was a significant difference in mean kurtosis between 0.4 pixels and 0.6 pixels ($p=0.001$, 95% CI mean difference = -0.03 to -0.008) and between 0.6 pixels and 0.8 pixels ($p<0.001$, 95% CI for mean difference = -0.053 to -0.03), denoting an overall increasing trend in mean kurtosis values with increasing pixel sizes, as shown in Figure 3.8. Similarly, when we compared the co-occurrence matrix values across the various pixel sizes, there were no significant differences between the 0.2 pixel and 0.4 pixel sizes, $p=0.466$, but there was a statistically significant difference between each of the pairs of 0.4 versus 0.6 pixel sizes, and 0.6 versus 0.8 pixel sizes ($p=0.018$ and $p=0.014$, respectively). Please note the 95% CIs for the mean difference for these comparisons in the Table 3.26. Figure 3.9 displays the relationship between co-occurrence matrix and the increasing pixel size; it is clear that an overall increase in the co-occurrence matrix occurs as pixel sizes increase. The repeated contrasts also showed that each of the RL matrices tended to vary significantly with increasing pixel sizes. For example, there was statistically significant difference in the mean RL matrix level between the 0.2 and 0.4 pixel sizes when compared, $p<0.001$, and between 0.4 pixels and 0.6 pixels, $p<0.001$ and between 0.6 pixels and the 0.8 pixels, denoting an overall decrease in the RL matrix as the pixel values went from 0.2 to 0.8 as depicted in Figure 3.10. Please note the 95% CI for mean differences for these comparisons (0.2 pixels versus 0.4 pixels 95% CI = 671.1 to 963; for 0.4 pixels versus

0.6 pixels 95% CI = 887.1 to 1179; and for 0.6 pixels versus 0.8 pixels 95% CI = 961.2 to 74.2). The gradient values also differed significantly across the various sizes of pixels, as can be noted from the p values and their respective 95% CIs. The overall trend, as can be seen in Figure 3.11, shows an overall significant increase in gradient values with increased pixel sizes (note the 95% CI for mean differences for these contrasts in Table 3.26). The AR model mean value showed a pattern of decrease, then increase across various values of pixels, where 0.4 pixels and 0.6 pixels demonstrated overall lower levels in mean AR model values than 0.2 pixels and 0.8 pixels as shown in Figure 3.12. However, when we contrasted them using repeated comparisons, all the contrasts showed a statistically significant difference. Last, but not least, the wavelet transform value also differed significantly across the various pixel sizes when comparisons were conducted on mean AR model across successive pixel sizes. Moreover, the pairwise comparisons between successive pixel sizes showed a statistically significant difference in mean wavelet transform value between the 0.2-pixel size and the 0.4-pixel size ($p=0.002$. 95% CI mean difference = 85.5 to 389.6), between 0.4 pixels and 0.6 pixels ($p<0.001$, 95% CI for mean difference = 409.5 to 713.6) and also between 0.6 pixels and 0.8 pixels ($p<0.001$, 95% CI for mean difference = 915 to 1219.6), denoting an overall increase in the mean wavelet transform score as the pixel levels went from 0.2 to 0.8 (Figure 3.13).

However, the results from one-way MANOVA showed that the main effects of various scan speed levels on the overall mean of each of the nine extracted texture parameters was statistically significant. The one-way MANOVA's equality of variance assumption was violated for seven out of the nine texture parameters, and was met for the remaining two tests namely (AR model and the Gradient value). As a result of the violations in the assumption of equality of variance, the Pillai's trace test of significance was used, and it showed statistically significant effect for scan speed on mean texture analysis ($F(45.2350) = 4.4$, $p<0.001$, Pillai's trace=0.390, partial eta squared=0.078). This denotes that there was a statistically significant but moderately small effect (partial eta squared, $\eta p^2=0.078$) on the "change" in the mean of the nine texture parameters with increasing scan speeds from 3 mm/sec to 30mm/sec. However, the main MANOVA test was followed by tests for linear trends (i.e., change in in the individual nine texture parameters for increase, decrease or fluctuations) , these tests are depicted in the Figures 3.14 -3.22.The statistical effect and significant

tests (f-tests) for increasing scan speeds on each of the nine texture parameters are displayed in Table 3.27 to illustrate the effect of varying scan speed, the one-way MANOVA showed that there were significant differences in mean grey levels across various scan speed levels — $F(5,474)=15.5$, $p<0.001$, $\eta p^2=0.14$ — denoting that the increasing scan speeds had a moderately high effect on the mean grey levels. Figure 3.14 shows that there was a substantial drop in the mean grey level as the scan speed went from 3mm/sec to 30mm/sec. Also, the increasing scan speeds had a moderately high effect on the mean variance texture value — $F(5,474)=14.4$, $p<0.001$, $\eta p^2=0.132$ — which is depicted in Figure 3.15; the overall variance texture estimate tended to increase with an increase in scan speed. In the same manner, the mean RL matrix tended to increase as the scan speed went from 3mm/sec to 30 mm/sec (Figure 3.19), with an overall significant and moderately high effect — $F(5,474)=20.4$, $p<0.001$, $\eta p^2=18$ (rounded) — which shows that the overall effect of increasing scan speed had the biggest impact on the RL matrix level thus far. Nonetheless, the wavelet transform appeared to have been significantly impacted by the increasing scan speed, but in a moderately small way — $F(5,474)=8.9$, $p<0.001$, $\eta p^2=0.09$ (rounded). Figure 3.22 shows that as the scan speeds increased, the overall mean wavelet transform texture tended to increase as well. The increasing scan speed did not have a statistically significant effect on the means of the remaining texture parameters (i.e. skewness, kurtosis, co-occurrence matrix gradient and AR model), as depicted in Table 3.28 previously.

The data in Tables 3.1 - 3.24 shows that as pixel size increases (0.2 to 0.8 mm), the variance decreases due to greater photon detection at larger pixel sizes, as discussed previously. Therefore, a pixel size of 0.8 mm was selected as one optimised parameter of the pQCT scanner. The other parameter to be optimised was the scan speed. As artefacts caused by subject movement have a significant impact on image quality (due to image degradation), the scan time should be as short as possible. At a pixel size of 0.8 mm, a scan speed of 10 mm/s yielded a good variance value (60.3219) in comparison with other scan speeds tested (3, 5, 15, 20, and 30 mm/s). In general, a balance between image quality and subject movement was the objective.

The texture parameters that demonstrate consistency (i.e. comparatively little variation of < 5 %) across the combinations of scan speeds and pixel sizes (Table 3.29) were

the co-occurrence matrix (0.3893 %), RL (2.2568 %), gradient (1.3755 %) auto-regressive (AR) model (0.3223 %) and wavelet transform (1.6143 %). Based on these observations, these parameters were deemed suitable for characterisation of the gastrocnemius muscle. The first order statistical parameters (grey level, variance, skewness and kurtosis), showed higher %CV. Variations may have been related to scan settings and noise. For GL, there is an association with scan speed and pixel size. As scan speed increases, GL decreases for a fixed pixel size. Skewness and kurtosis were excluded from any further analysis as they displayed large coefficients of variation (% CV) in comparison to the other parameters (Table 3.29). These findings suggested that grey level was dependent on image noise level. As grey level increases, variance decreases. CV was shown to remain quite consistent (approximately <5%) at a pixel size of 0.8 mm and various scan speeds for all remaining texture parameters (Table 3.29).

The analysis of influence of ROI area reduction showed no significance difference found in GL, skewness, kurtosis, co-occurrence matrix, gradient, AR model and wavelet transform, but for variance and RL matrix were affected significantly. As the first order parameters are affected by normalisation process of each ROI. In addition, their computation based on single pixel values only. The variance is an index for image noise and due x-ray nature, noise is a random phenomenon within acquired images.

The RL texture parameter are on the ROI area dependent. The linear behavior (Figure 3.28) is due to its definition. It squares the number of the run length for each calculated intensity level. Therefore, for a larger ROI there will be more runs and vice versa. It is concluded that ROI area size must be kept constant when considering extracting the texture parameters specifically the RL. This finding matched previous study conducted by Alqahtani (2010).

3.2.5 Conclusion

Important conclusions drawn from this work include:

- Noise in the acquired images can be quantified from the extracted variance values.
- Four texture parameters of the water phantom (co-occurrence matrix, RL, gradient, AR model and wavelet transform) produced consistent values (the smallest %CV) over the range of scan speeds and pixel sizes.

- The larger the size of the pixel, the less is the noise (variance).
- A pixel size of 0.8 mm (the largest pixel size studied) yielded a smooth image with lowest noise values compared to other pixel sizes.
- The optimal water phantom image was acquired at a pixel size of 0.8 mm and scan speed of 10 mm/sec. This represented a balance between the scan time and acceptable image noise level compared with other combinations.
- The pQCT scanner showed reliable repeatability over all scans at a range of pixel sizes (0.2, 0.4, 0.6 and 0.8 mm) and scan speeds (3, 5, 10, 15, 20 and 30 mm/s) for all extracted parameters except skewness and kurtosis as they showed the highest % CV.
- The texture parameters of skewness and kurtosis were excluded as potential parameters for the characterisation of acquired images as they showed high data dispersion (the largest %CV among all data).
- There was an overall significant increase in GL, kurtosis, co-occurrence matrix, gradient matrix and wavelet transform texture parameters with an increase of pixel size.
- There was an overall significant decrease in variance and RL with an increase of pixel size.
- The AR model texture parameter showed a decreasing followed by an increasing pattern across various pixel sizes.
- Scan speed had a moderately high effect on mean GL and variance texture parameters.
- Scan speed had the biggest effect on the RL matrix texture parameter.
- Scan speed had a moderately small effect on mean wavelet transform texture parameter.
- Scan speed had no effect on skewness, kurtosis, co-occurrence matrix, gradient matrix and AR model.
- ROI size has a significant influence on the variance and the RL matrix extracted values.
- ROI size must be kept constant when considering extraction of RL matrix texture parameter.

3.3 Healthy Volunteer Study

3.3.1 Introduction

From the previous section, it was determined that scan speed and pixel size were the main factors in the acquisition of pQCT images of the water phantom. This section describes how these findings were verified with a healthy human volunteer. Furthermore, the same texture parameters that were extracted for the water phantom were also extracted for the volunteer.

The aim of this study was to assess the suitability of pQCT for the acquisition of human calf muscle tomographic images and to assess the ability of pQCT to detect calf muscle boundaries, specifically in the gastrocnemius muscle. In addition to assessment of ROI position effect on extracted texture parameters which might reflect muscle tissue homogeneity and to decide which of the remaining 7 texture parameters are suitable for use with pQCT in human volunteers.

3.3.2 Materials and Methods

3.3.2.1 Subject

For this study, a healthy volunteer of age 63 years was recruited. Informed consent was obtained from the subject following an explanation of the aims, protocols and procedures in the study (see Appendix C). The subject declared that he was of normal health with no history of musculoskeletal disorders. The study was approved by the ethics committee of the Cardiff University School of Engineering.

3.3.2.2 Image Acquisition

Cross-sectional right leg scans were acquired by a pQCT scanner (Stratec XCT 2000, Stratec Medizintechnik GmbH, Pforzheim, Germany) at 66% of the distance from the medial malleolus to the medial condyle of the tibia. This distance represents the maximum calf diameter, as shown in Figure 3.32 (Rittweger et al. 2000).

The procedure for scanning the subject's right leg was as follows:

1. The subject was asked to read a scan information sheet.

2. The subject was asked to sign a consent form confirming that he was not suffering from any calf muscle injury.
3. The subject's weight and height were taken.
4. The distance from the malleolus to the medial condyle was measured with a tape measure.
5. A skin marker was used to draw a line indicating the 66% (maximum calf diameter) distance on the subject's right leg.
6. The following subject data were recorded: name, date of birth, gender, measurement mask, the side of the object (left or right leg), the object's length, measurement diameter, pixel size, subject's height and weight, number of blocks and the scan speed. The pQCT software (v6.0) is capable of performing various bone and muscle cross sectional area measurements, and each type of measurement is given a mask (or name). Muscle mask was selected as the integrated algorithm automatically discriminates muscle tissue from subcutaneous fat tissue and total bone. The number of blocks specifies the projection range: one block specifies a range of 180 projections within 180° by angular distance of 1°, and two blocks specifies 360 projections within 360° by angular distance of 0.5°, as described in Chapter 2. According to the findings of the water phantom scans, a balance should exist between scan time and image noise. Therefore, one block was selected. It was mandatory to enter the object length and measurement diameters although they are related to bone rather than muscle studies. A fixed distance was entered for each scan as follows: 400 mm for the object length and 100 mm for the measurement diameter.
7. The subject was seated comfortably on a chair facing the pQCT gantry with the right leg positioned in the scanner and resting on a leg holder, as shown in Figure 3.32.
8. The height of the leg holder was adjusted to ensure that the weight of the leg was not resting entirely on the pQCT gantry and that the leg clamp was closed.
9. The subject's foot was secured in a plantar flexed position by the Velcro strap of the attachment.
10. The subject was requested to remain as still as possible and to refrain from talking during the scan (whilst the amber x-ray light was on).

11. At the position of the skin mark, 2.4 mm slice images were acquired five times (without repositioning). To do this, for each combination of scan speed (3, 10 and 30 mm/s) and pixel size (0.2 and 0.8 mm), the gantry laser indicator was positioned on the skin mark. At a scan speed of 3 mm/s and pixel size of 0.2 mm, the scan was performed only in triplicate as the subject suffered discomfort from the prolonged scan time.
12. The acquired images were saved and exported into CSV format files for the purpose of analysis.

Figure 3.32: Calf muscle and subject position in the pQCT scanner.

3.3.2.3 Image Windowing

With medical images in digital form, it is possible to perform a variety of image processing procedures. One of the most useful processing procedures is image windowing. Image windowing is a technique for improving image appearance to give maximum visibility of image details.

An image histogram is a graph representing the intensity incidence in an image. The horizontal axis represents intensity values, starting at 0 and extending to the maximum

intensity value (255 in an 8-bit image). The vertical axis represents the number of times the corresponding intensity occurred in the image (Phillips and Dwayne, 2000). For the visualisation of subtle image details, the image should be windowed. Windowing is a common method of image contrast enhancement that is achieved by displaying a portion of the total range of an image histogram. In other words, it is a 'stretch and shift' of the original image histogram to cover all 256 available levels. For example, for an image of minimum pixel value (intensity) 0 and maximum 230, where contrast enhancement of the brighter portion must be applied, a window from 100 to 230 could be selected. Pixels with values of 0 to 100 are therefore displayed at the darkest intensity and will not be visible. Pixels with values of 230 will be displayed at the maximum intensities, as shown in Figure 3.33. Pixels within the range 100-230 will be assigned intensities according to monitor specifications (as determined by a digital look up table). In conclusion, windowing is a visualisation method to identify information not previously perceptible. Thus, image windowing was only implemented to identify calf muscle boundaries only as it enhances image contrast which results in changing image grey level (intensity) value. In other words, it is to be used as guidance tool to define ROI within medial head of gastrocnemius muscle in unwindowed images (raw images). The MaZda software package was used to extract 9 texture parameters as described previously (Section 3.3.2.2.1).

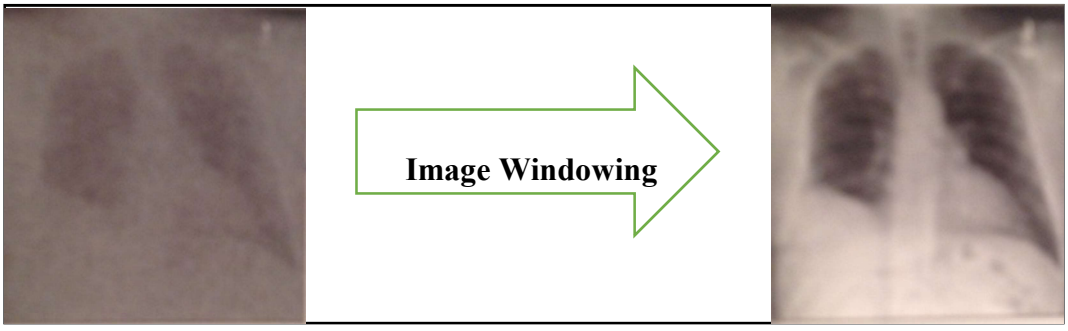

Figure 3.33: Image windowing effect.

3.3.2.4 Repeatability

As described in water phantom study (Section 3.2.2.2) repeatability is how closely the results of successive measurements of the same parameter match when carried out under the same conditions of measurement. The repeatability indicates the consistency

of a measurement. For all acquired images mentioned in image acquisition protocol (Section 3.3.2.2, step 11), a single circular region of interest (ROI) of 228 pixels in area was defined in the same position within medial head of gastrocnemius muscle and the same texture features were extracted for further analysis. Mean, SD and %CV were calculated to assess pQCT repeatability.

3.3.2.5 Determination of Cut-off ROI Area

Cut-off ROI area is the minimum area that yields numerical values of texture parameters. In order to assess the influence of ROI area on extracted texture parameters, a range of circular ROIs were defined following the image transfer procedure. Images were acquired with a scan speed of 10 mm/s and pixel size of 0.8 mm. The ROI areas were 15, 30, 60, 90, 100, 110, 130, 150, 160, 200, and 228 pixels as shown in Figure 3.34. At each ROI size, texture parameters were extracted. Analysis was performed and the ROI cut-off area was subsequently defined. The cut-off area is the ROI area where it is not possible to extract texture parameters with the MaZda software. In other words, it is the minimum ROI area at which numerical values for texture parameters can be obtained.

Figure 3.34: Examples of ROIs of different areas drawn within the medial head of the gastrocnemius muscle.

3.3.2.6 Influence of ROI Area on Extracted Texture Parameters

In order to investigate factors other than the scan parameters, which could potentially influence the texture parameters, a group of ROIs was defined for five acquired images to investigate the effect of differences in ROI area on the reliability of texture parameters. In other words, in MaZda if computation results are an unpresentable or an undefined, output displayed as NaN (not a number). The initial ROI was defined to include the entire medial head of the gastrocnemius muscle. Reduction of ROI area was performed using a built-in feature of the MaZda software package (erosion) which yielded a consistent area reduction, as shown in Figure 3.35. Erosion is a method of shape shrinking (Costa and Cesar 2009). The ROI areas were 1700, 1424, 1159, 906, 665, 439, and 233 pixels. The mean values of texture parameters at every individual ROI area were calculated for the five images acquired with a scan speed of 10 mm/s and a pixel size of 0.8 mm.

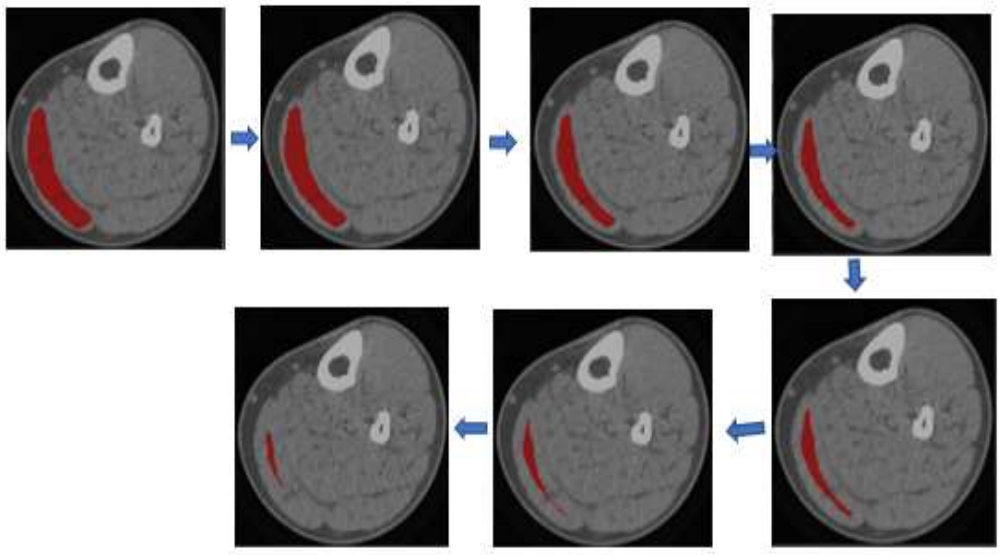

Figure 3.35: Eroded ROI areas to determine the effect of ROI size on extracted texture parameters.

3.3.2.7 Influence of ROI Position on Extracted Texture Parameters

As the volunteer was healthy with no calf muscle injury, muscle tissue should be homogeneous. To assess homogeneity, equally-sized circular ROIs of 228 pixels in area were drawn at different positions within the gastrocnemius medial head boundary of 5 acquired images (at a pixel size of 0.8 mm and a scan speed of 10 mm/s); the ROI

area was greater than the cut-off of 200 pixels as shown in Figure 3.36. The same texture parameters were extracted using MaZda. Image windowing was implemented to identify the muscle boundaries. This was accomplished to investigate the influence of ROI position within the gastrocnemius muscle boundary on texture parameter values. This influence was tested by using repeated measures ANOVA test.

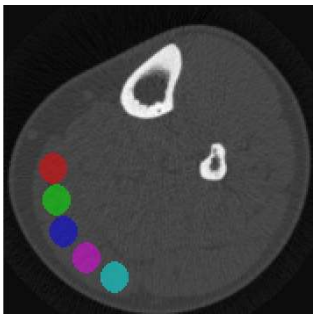

Figure 3.36: Five circular ROIs of area 228 pixels drawn in 5 different positions within the medial head of the gastrocnemius muscle.

3.3.3 Results

3.3.3.1 Image Windowing

The results of the healthy subject studies are shown in Figures 3.37 - 3.42. Each figure consists of two images: on the left side is the image without windowing and on the right side is the image after windowing. After image windowing, it is possible to define a circular ROI avoiding the muscle boundary. Figure 3.37 shows a typical image acquired at a low scan speed (3 mm/s) and small pixel size (0.2 mm) resulting in a superior signal to noise ratio (SNR) than that in Figures 3.38 and 3.39 which were acquired at an equal pixel size but a higher scan speed (10 and 30 mm/s). Spatial resolution is determined by pixel size (as the parameters of the construction algorithm are unchanged) while SNR decreases as scan speed increases.

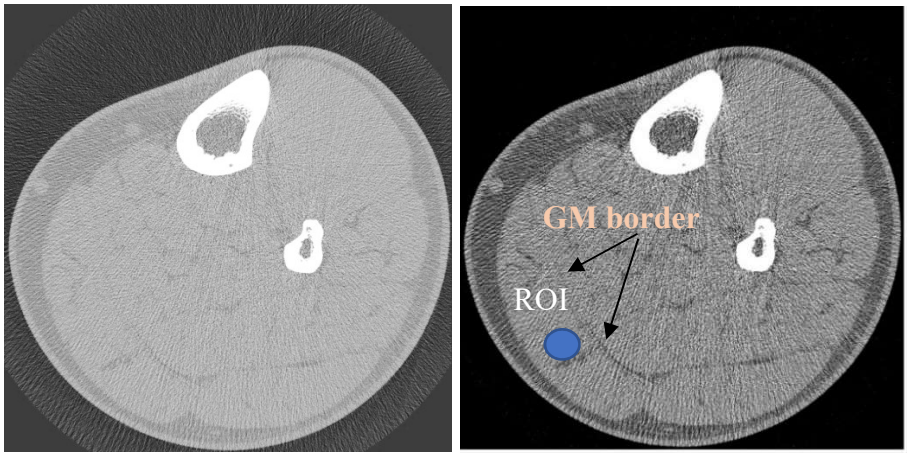

Figure 3.37: pQCT acquired image at pixel size 0.2 mm and scan speed 3 mm/s before and after windowing showing the gastrocnemius muscle (GM) border and a circular ROI.

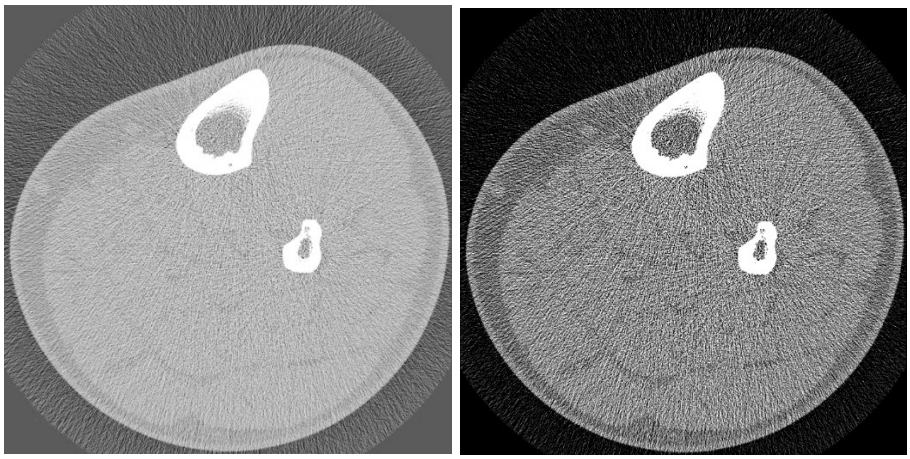

Figure 3.38: pQCT acquired image at pixel size 0.2 mm and scan speed 10 mm/s before and after windowing.

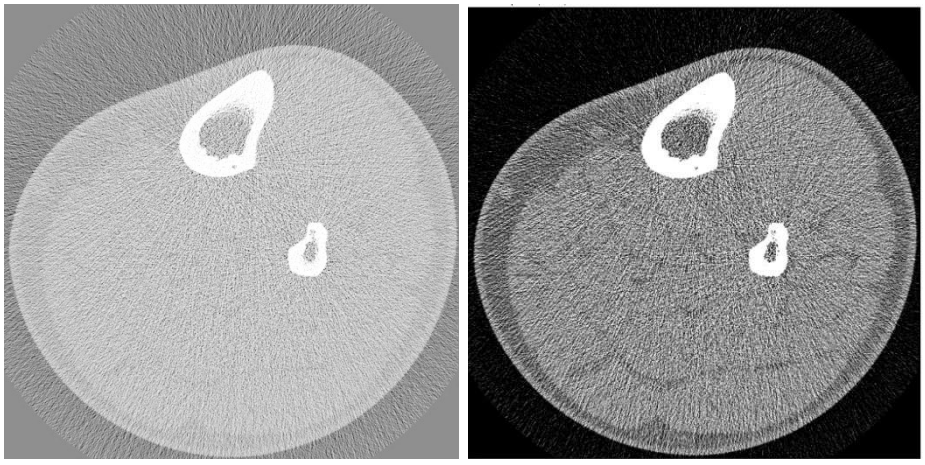

Figure 3.39: pQCT acquired image at pixel size 0.2 mm and scan speed 30 mm/ before and after windowing.

Figure 3.40 shows a typical image acquired at a low scan speed (3 mm/s) and large pixel size (0.8 mm), again resulting in a superior SNR than that in Figures 3.41 and 3.42 which were acquired at an equal pixel size but a higher scan speed (10 and 30 mm/s).

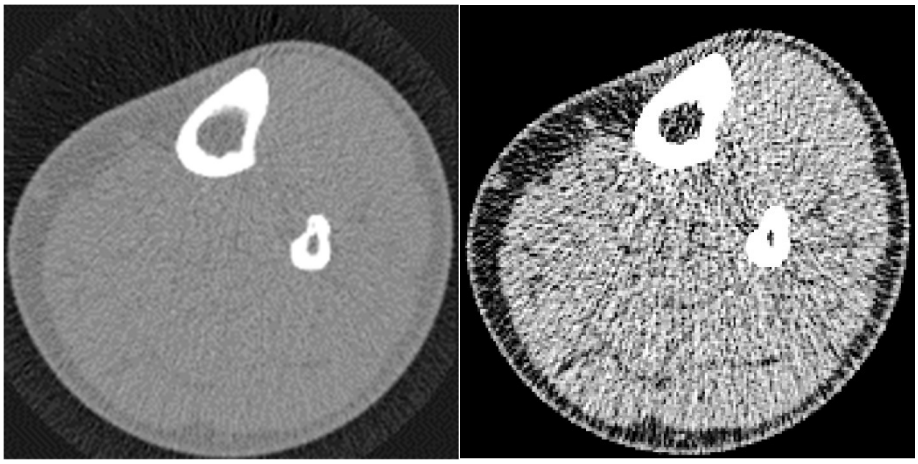

Figure 3.40: pQCT acquired image of pixel size 0.8 mm and scan speed 3 mm/s before and after windowing.

.

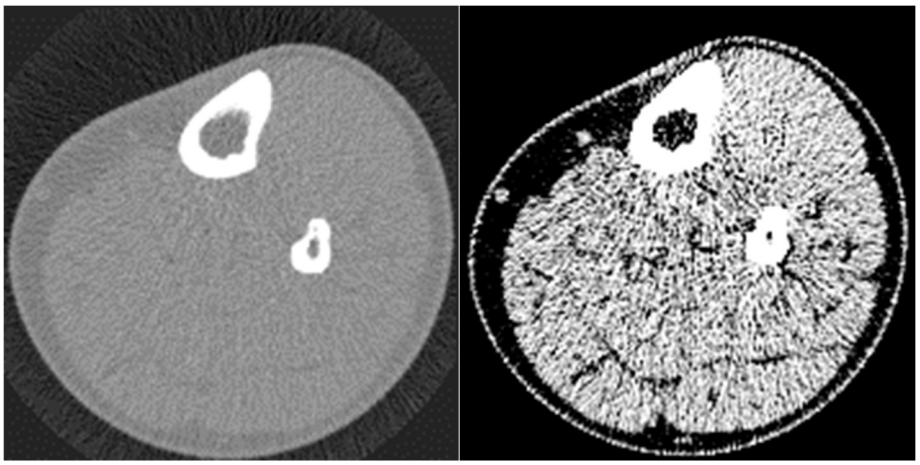

Figure 3.41: pQCT acquired image of pixel size 0.8 mm and scan speed 10 mm/s before and after windowing.

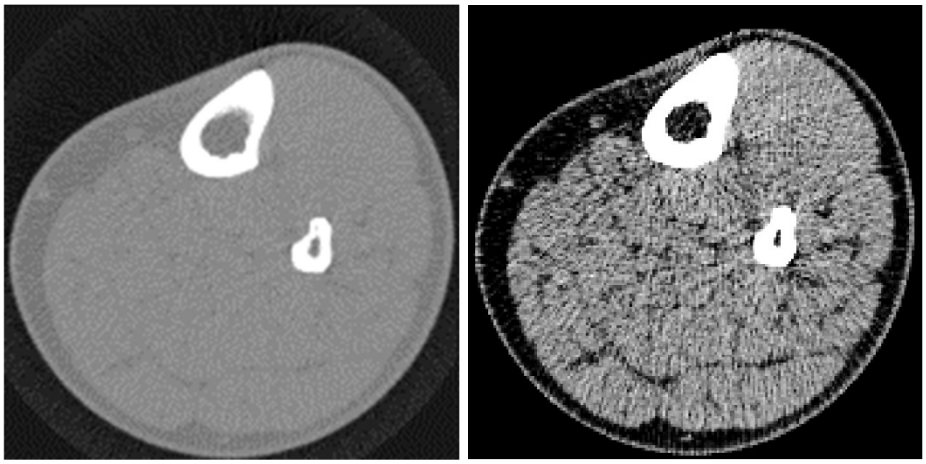

Figure 3.42: pQCT acquired image at voxel size 0.8mm and scan speed 30 mm/s before and after windowing.

.

3.3.3.2 Repeatability

Table 3.32 shows the mean values for 5 scans (only 3 scans at a scan speed of 3 mm/s with pixel size of 0.2 mm) of first order statistical parameters (grey level and variance, skewness and kurtosis) extracted from a ROI of area 228 pixels defined within the medial head of gastrocnemius muscle. Additionally, the second order statistical parameters are shown: co-occurrence matrix, run length matrix and gradient, autoregressive model and wavelet transform at different scan speeds and pixel sizes. The %CV of skewness and kurtosis are more than 10 %. Therefore, they will be excluded from further analysis. This match the finding of water phantom study.

Table 3.32: Mean, SD and %CV of texture parameters of acquired subject images at different pixel sizes and scan speeds.

Pixel size (mm)	Scan speed (mm/s)	Scan Time (s)	Calculated parameter	Texture parameter								
				GL	Variance	Skewness	Kurtosis	Co-occurrence	RL	Gradient	AR	Wavelet
0.2	3	850	Mean	77.1696	65.7864	0.0186	-0.0503	211182.6439	870.1768	1624.8614	1.2027	50487.3570
			SD	4.9183	10.3464	0.2065	0.1515	7948.1338	6.0994	119.2318	0.1138	2135.7411
			%CV	6.3734	15.7273	1108.8147	301.4588	3.7636	0.7009	7.3380	9.4595	4.2302
	10	275	Mean	84.7991	134.7613	-0.0529	-0.1299	210259.3607	887.3858	1674.4976	1.2172	49963.8040
			SD	6.7440	29.9567	0.1087	0.1776	7268.6229	16.5786	260.2331	0.1308	1747.3446
			%CV	7.9529	22.2294	205.4348	136.6999	3.4570	1.8683	15.5410	10.7456	3.4972
	30	137	Mean	94.0772	224.8515	-0.0490	-0.0378	208251.1433	888.9775	1636.9414	1.2584	49908.4393
			SD	5.6053	27.8601	0.2234	0.2132	7052.8989	14.7650	77.4537	0.1275	1817.0405
			%CV	5.9582	12.3905	456.2155	564.5948	3.3867	1.6609	4.7316	10.1310	3.6407
0.8	3	850	Mean	69.3395	9.7176	-0.7161	1.3682	185125.8259	760.2673	1057.8524	1.1386	43269.0404
			SD	1.3522	1.1606	0.1678	0.7876	6514.3630	19.3377	151.6761	0.0525	1719.5546
			%CV	1.9501	11.9435	23.4278	57.5674	3.5189	2.5435	14.3381	4.6147	3.9741
	10	275	Mean	70.8868	8.6525	-0.1515	0.0708	215217.7147	764.8182	1582.9411	1.1605	44110.8169
			SD	1.2955	1.3023	0.1704	0.3334	12133.4439	28.0254	284.4181	0.1066	2864.1553
			%CV	1.8275	15.0511	112.5378	470.7929	5.6378	3.6643	17.9677	9.1820	6.4931
	30	137	Mean	72.4149	20.3114	-0.1387	-0.0366	198256.8903	822.6839	1483.0899	1.1121	45739.9104
			SD	1.2643	0.6202	0.1120	0.3839	6520.1333	20.5999	51.7736	0.1355	1491.3405
			%CV	1.7459	3.0534	80.7114	1049.9167	3.2887	2.5040	3.4909	12.1871	3.2605

Figures 3.43 to 3.45 illustrate %CV of the extracted texture parameters at different scanning conditions.

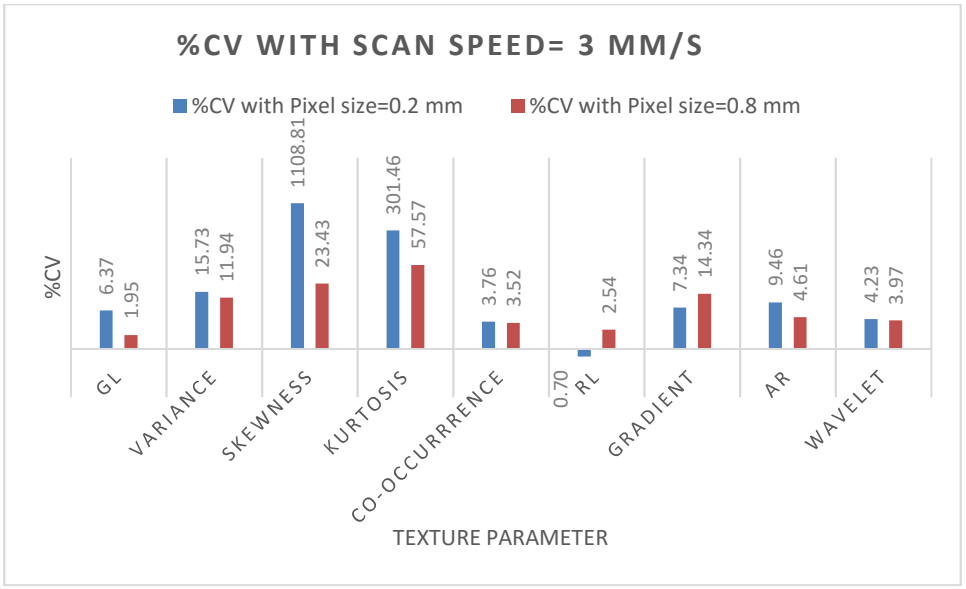

Figure 3.43: %CV of extracted texture parameters of the healthy subject with scan speed of 3 mm/s.

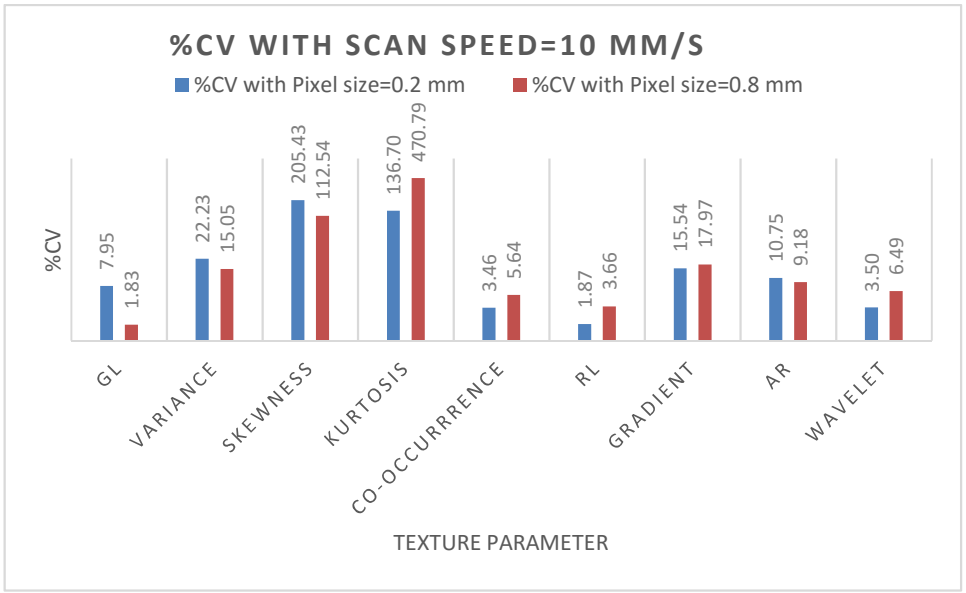

Figure 3.44: %CV of extracted texture parameters of the healthy subject with scan speed of 10 mm/s.

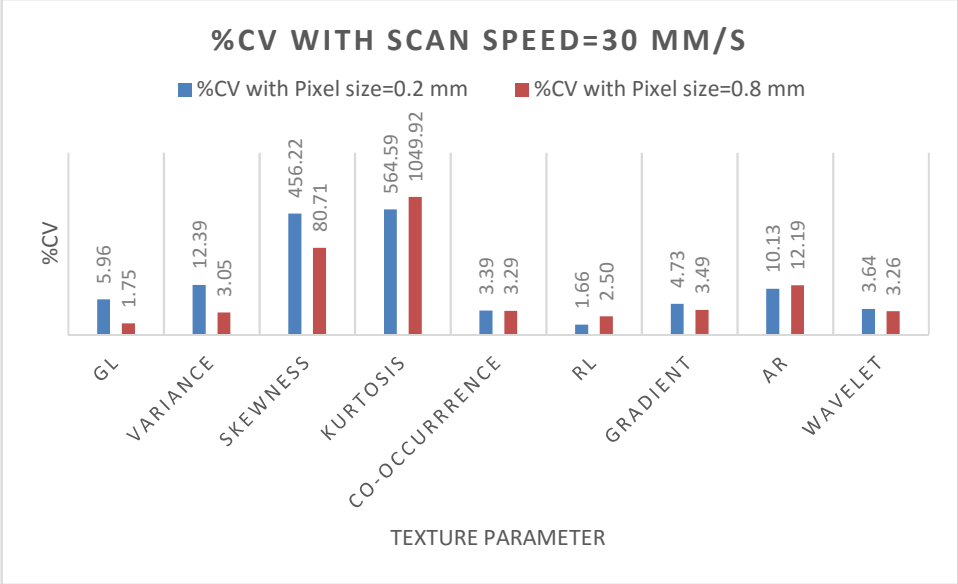

Figure 3.45: %CV of extracted texture parameters of the healthy subject with scan speed of 30 mm/s.

3.3.3.3 Cut-off ROI Area

Table 3.33 illustrates the influence of ROI area on the ability to extract numerical values of texture parameters; a range of ROI areas were defined within an image acquired at a pixel size of 0.8 mm and a scan speed of 10 mm/s. At ROI areas of 15 to 228 pixels, texture parameters that have a numerical value could be extracted for grey level, variance, run length, gradient and AR. In contrast, the co-occurrence parameter was partially affected at ROI areas of 15 and 30 pixels. The co-occurrence consists of 11 parameters calculated in 5 pixels distance and 4 angles which yield 220 parameters as described previously (Section 3.2.2.3.1). Part of these parameters at ROI sizes of 15 and 30 pixels gave 0 values. The ability to extract numerical values of the wavelet parameter was achieved with ROI areas of 228 pixels and higher. In summary, wavelet transform texture parameter was the most sensitive to ROI area. Therefore, ROI area should be ≥ 228 pixels to extract numerical values for all texture parameters.

Table 3.33: Influence of ROI size on texture parameter features values. ROI size of 228 pixels and higher had no effect on the ability of MaZda software to extract complete numerical texture parameter values. Therefore, 228 pixels was specified as the cut-off ROI size for extracting reliable texture parameters. Grey background represents the affected texture parameters by ROI Area.

	ROI area (Pixels)										
Texture parameter	**15**	**30**	**60**	**90**	**100**	**110**	**130**	**150**	**180**	**200**	**228**
GL	71.07	71.33	71.57	71.42	71.34	71.25	71.31	71.21	71.17	71.29	71.45
Variance	7.26	10.56	12.88	11.27	10.64	10.68	10.43	11.15	10.81	10.52	10.75
Co-occurrence	98562.70	156197.37	213830.53	228066.95	216251.17	213182.04	230141.49	212197.97	205346.47	199540.34	203152.54
RL	72.23	133.76	233.92	321.93	356.24	384.35	461.33	525.88	631.14	692.69	781.02
Gradient	2095.40	1807.62	2823.31	2675.07	2566.84	2605.77	2701.80	2283.10	2156.10	2117.22	2080.86
AR	0.26	1.57	1.13	1.20	1.24	1.23	1.14	1.28	1.17	1.17	1.19
Wavelet	49610.28	44282.91	45467.79	45579.11	45414.89	44556.16	49748.62	45015.79	45256.16	45524.52	45614.30

3.3.3.4 Influence of ROI Position on Texture Parameters

Tables 3.34 – 3.39 present values of extracted texture parameters for circular ROIs of equal area (228 pixels) at five different positions within the boundary of the medial head of the gastrocnemius muscle. At each ROI position, five images were acquired at the same scan speed and pixel size were analysed; mean was calculated for all the texture parameters.

Table 3.34: Extracted texture parameter values for ROI position 1 within the boundary of the medial head of the gastrocnemius muscle on five repeated image acquisitions.

	Image#	**1**	**2**	**3**	**4**	**5**	
	ROI Position	**Red(1)**					**Mean**
Texture Parameter	**GL**	71.2864	67.8273	70.7409	69.3136	70.1182	69.8573
	Variance	12.0407	10.0883	12.5556	13.1153	14.8133	12.5226
	Co-occurrence	206968.9397	205412.8738	200273.3364	195775.7027	199334.9637	201553.1632
	RL	775.9474	756.7336	779.0161	787.2574	775.8264	774.9562
	Gragdient	1436.9627	1456.1689	1319.0063	1321.5365	1510.1074	1408.7564
	AR	1.3114	1.4183	1.4954	1.5370	1.5141	1.4552
	Wavelet	44441.5412	43333.3024	45230.7397	45700.9774	47957.4353	45332.7992

Table 3.35: Extracted texture parameter values for ROI position 2 within the boundary of the medial head of the gastrocnemius muscle on five repeated image acquisitions.

	Image#	1	2	3	4	5	
	ROI position	Green(2)					Mean
Texture parameter	GL	70.1182	67.4636	70.8227	69.0955	70.2455	69.5491
	Variance	13.5224	11.3669	11.0004	12.4591	12.5307	12.1759
	Co-occurrence	204696.1831	211949.4571	216658.5899	223572.6201	219374.7825	215250.3265
	RL	740.3402	757.2918	753.7756	740.7990	726.4914	743.7396
	Gragdient	2105.7357	1603.8456	1749.1900	2008.7884	1542.0122	1801.9144
	AR	1.5989	1.4513	1.4619	1.5088	1.4636	1.4969
	Wavelet	45803.5847	46823.7815	48694.7018	48286.1329	48615.5765	47644.7555

Table 3.36: Extracted texture parameter values for ROI position 3 within the boundary of the medial head of the gastrocnemius muscle on five repeated image acquisitions.

	Image#	1	2	3	4	5	
	ROI position	Blue (3)					Mean
Texture parameter	GL	71.5545	68.4182	71.7545	70.0455	70.8591	70.5264
	Variance	11.0743	8.7888	6.6943	10.4343	9.0120	9.2007
	Co-occurrence	211893.7084	207820.4846	188934.1264	227008.1973	220702.5646	211271.8162
	RL	752.0832	731.1238	754.1585	744.9013	738.3293	744.1192
	Gragdient	2089.8818	1599.2691	1774.6474	2135.8687	2322.4758	1984.4286
	AR	1.0507	1.4326	1.1635	1.2594	1.1494	1.2111
	Wavelet	45061.5311	44005.9401	47337.5390	45501.7751	48918.1324	46164.9835

Table 3.37: Extracted texture parameter values for ROI position 4 within the boundary of the medial head of the gastrocnemius muscle on five repeated image acquisitions.

	Image#	1	2	3	4	5	
	ROI position	Violet (4)					Mean
Texture parameter	GL	71.5500	68.4955	71.6273	70.6773	71.0136	70.6727
	Variance	9.5202	6.6773	7.4429	9.3277	9.3953	8.4727
	Co-occurrence	214111.8801	198381.6245	226765.1612	211993.4287	208845.8153	212019.5820
	RL	752.7440	783.7042	746.5481	756.4806	748.9573	757.6868
	Gragdient	1714.5019	1725.5470	2037.3698	1958.3463	1921.0780	1871.3686
	AR	1.1264	0.9074	1.2148	1.0865	1.0896	1.0849
	Wavelet	43975.7981	42265.7296	43821.8891	42078.0033	43430.1536	43114.3147

Table 3.38: Extracted texture parameter values for ROI position 5 within the boundary of the medial head of the gastrocnemius muscle on five repeated image acquisitions.

	Image#	1	2	3	4	5	
	ROI position	Cayan(5)					Mean
Texture parameter	GL	69.8000	67.1818	70.4955	69.0182	69.9773	69.2945
	Variance	15.6509	12.2397	17.5227	16.0088	16.5586	15.5961
	Co-occurrence	223705.1864	223527.6776	206172.4639	224894.9966	205584.1439	216776.8937
	RL	728.3339	721.6074	760.8853	761.0444	759.1642	746.2071
	Gragdient	2141.2984	1659.2152	1465.1496	1922.1868	1606.7812	1758.9263
	AR	1.5024	1.5532	1.4691	1.5056	1.4041	1.4869
	Wavelet	53621.9698	50906.2198	49081.3341	44809.8709	47804.1811	49244.7152

Table 3.39: Summary of the mean of the extracted texture parameters at the five positions within medial head of the gastrocnemius muscle on five repeated image acquisitions.

		ROI Position #				
		1	2	3	4	5
Texture parameter	GL	69.8573	69.5491	70.5264	70.6727	69.2945
	Variance	12.5226	12.1759	9.2007	8.4727	15.5961
	Co-occurrence	201553.1632	215250.3265	211271.8162	212019.5820	216776.8937
	RL	774.9562	743.7396	744.1192	757.6868	746.2071
	Gradient	1408.7564	1801.9144	1984.4286	1871.3686	1758.9263
	AR	1.4552	1.4969	1.2111	1.0849	1.4869
	Wavelet	45332.7992	47644.7555	46164.9835	43114.3147	49244.7152

Data was structured into repeated measures format as displayed into the above-mentioned table (Table 3.39), with the numbers 1, 2,3,4 and 5 denoting the ROI positions, and the 9 texture parameters denoting the cases (i.e., the individual measures of texture analysis). Data was imported to the SPSS program specifying the repeats as the images. An overall test Repeated Measures ANOVA showed that there were no statistically significant differences between images on the overall mean of the texture measures combined, F (4,5) =1.213, wilks lambda= 0.508) denoting that the five images did not differ statistically when comparting their overall texture analysis (mean of the 9 measures within each image). Moreover , the test *within* each of these (9) measures (i.e., within each of the 9 texture parameters across the images) was also not significantly different between images, but the Mauchly's test of sphericity (assumption of equal error measurements across images) was violated as such the GreenHouse-Geisser f-test is reported to adjust the degrees of freedom accordingly F(1.2, 9.8)= 1.46, p= 0.263 , denoting that the nine texture parameters did not change significantly as we move from position 1 to 5 . To clarify this difference for example as we change the position of ROI from 1 to 5 the GL did not change significantly, and

the same applies to the rest of the eight texture parameters. To sum up, the five regions of interest did not differ significantly on their overall texture value. Also, they did not differ significantly on their specific nine texture values.

3.3.3.5 Influence of ROI Area on Extracted Texture Parameters

Tables 3.40 - 3.46 represent values of the extracted texture parameters of the gastrocnemius muscle with reduction of ROI size. The analysis was performed on five acquired images with scan speed of 10 mm/s and pixel size of 0.8 mm.

Table 3.40: Extracted texture parameters from an irregular ROI of area 1700 pixels within the gastrocnemius muscle for five repeated image acquisitions with the same scan speed and pixel size. The mean value was calculated in each case.

	Image #	1	2	3	4	5	
	ROI size (Pixel)	**1700**	**1700**	**1700**	**1700**	**1700**	**Mean**
Texture Parameter	**GL**	71.0471	68.1118	71.3071	69.7494	70.6206	70.1672
	Variance	11.4966	9.3663	10.4704	11.3737	11.6155	10.8645
	Co-occurrence	200611.9206	198737.2893	195477.0304	217257.9938	219508.4401	206318.5348
	RL	5619.2428	5525.2421	5670.5436	5673.1375	5622.8282	5622.1988
	Gradient	1717.0473	1519.1571	1541.8661	1861.6090	1868.2248	1701.5809
	AR	1.4340	1.4602	1.4127	1.4469	1.3907	1.4289
	Wavelet	43520.3334	43755.8028	41831.8835	46141.9551	44844.6589	44018.9267

Table 3.41: Extracted texture parameters from an irregular ROI of area 1424 pixels within the gastrocnemius muscle for five repeated image acquisitions with the same scan speed and pixel size. The mean value was calculated in each case.

	Image #	1	2	3	4	5	
	ROI size (Pixel)	**1424**	**1424**	**1424**	**1424**	**1424**	**Mean**
Texture Parameter	**GL**	70.9867	68.0140	71.2374	69.6784	70.5765	70.0986
	Variance	12.0160	9.5223	10.7793	11.6423	11.9323	11.1785
	Co-occurrence	206861.6600	203585.4829	199117.6145	223119.8335	224709.1500	211478.7482
	RL	4720.9928	4634.0196	4780.7525	4752.8629	4722.9252	4722.3106
	Gradient	1753.5419	1582.5897	1518.9400	1950.9673	1886.2113	1738.4500
	AR	1.4435	1.5002	1.4587	1.4734	1.3955	1.4543
	Wavelet	44358.4486	44556.3075	42662.2404	46793.6283	45673.9140	44808.9078

Table 3.42: Extracted texture parameters from an irregular ROI of area 1159 pixels within the gastrocnemius muscle for five repeated image acquisitions with the same scan speed and pixel size. The mean value was calculated in each case.

	Image #	1	2	3	4	5	
	ROI size (Pixel)	1159	1159	1159	1159	1159	Mean
Texture Parameter	GL	70.8939	67.9154	71.1079	69.6143	70.4443	69.9952
	Variance	12.1691	10.0515	11.0988	12.1869	12.2866	11.5586
	Co-occurrence	209990.7014	212468.6769	202932.9128	211236.0928	213365.6488	209998.8065
	RL	3823.0789	3777.6594	3863.3592	3882.5466	3825.9483	3834.5185
	Gradient	1779.8029	1656.2826	1521.7663	1808.9979	1792.1832	1711.8066
	AR	1.4314	1.4874	1.4669	1.4662	1.4155	1.4535
	Wavelet	45128.5385	45193.5628	42850.9137	42861.1504	50653.9816	45337.6294

Table 3.43: Extracted texture parameters from an irregular ROI of area 906 pixels within the gastrocnemius muscle for five repeated image acquisitions with the same scan speed and pixel size. The mean value was calculated in each case.

	Image #	1	2	3	4	5	
	ROI size (Pixel)	906	906	906	906	906	Mean
Texture Parameter	GL	70.7219	67.8642	71.0475	69.4923	70.3830	69.9018
	Variance	12.2825	10.2564	11.1821	12.6451	12.7507	11.8233
	Co-occurrence	211353.9845	216179.3343	203405.4175	203068.4493	200383.8834	206878.2138
	RL	3029.3309	3058.0189	3018.0722	3055.6652	2981.7810	3028.5736
	Gradient	1814.9861	1676.7991	1571.6254	1783.3399	1700.6388	1709.4779
	AR	1.4481	1.5257	1.4793	1.4545	1.4386	1.4693
	Wavelet	45280.3626	45454.8474	43130.3928	47540.1652	46412.8891	45563.7314

Table 3.44: Extracted texture parameters from an irregular ROI of area 665 pixels within the gastrocnemius muscle for five repeated image acquisitions with the same scan speed and pixel size. The mean value was calculated in each case.

	Image #	1	2	3	4	5	
	ROI size (Pixel)	665	665	665	665	665	Mean
Texture Parameter	GL	70.5308	67.7098	70.9293	69.3850	70.2436	69.7597
	Variance	12.9107	10.7714	11.7559	13.0819	13.4925	12.4025
	Co-occurrence	201307.4651	207398.9472	197913.4356	210999.9350	207333.6918	204990.6950
	RL	2252.3198	2257.1977	2213.3436	2243.9062	2191.1375	2231.5810
	Gradient	1803.5379	1534.6229	1466.2409	1850.2946	1716.3413	1674.2075
	AR	1.4374	1.5642	1.4948	1.5109	1.4680	1.4950
	Wavelet	49030.0284	49878.8334	47265.2246	47380.1953	46491.7310	48009.2025

Table 3.45: Extracted texture parameters from an irregular ROI of area 439 pixels within the gastrocnemius muscle for five repeated image acquisitions with the same scan speed and pixel size. The mean value was calculated in each case.

	Image #	1	2	3	4	5	
	ROI size (Pixel)	439	439	439	439	439	Mean
Texture Parameter	GL	70.3531	67.5581	70.7745	69.1595	70.0911	69.5872
	Variance	13.0803	11.0758	12.2931	14.3254	14.1375	12.9824
	Co-occurrence	203210.4344	212233.9137	203230.7851	205801.6437	196852.3205	204265.8195
	RL	1491.5281	1504.8016	1478.2594	1474.6098	1459.2378	1481.6874
	Gradient	2057.1447	1523.2805	1539.8764	1814.6325	1596.0671	1706.2003
	AR	1.4516	1.6012	1.4873	1.4308	1.4383	1.4818
	Wavelet	48885.1844	49694.0476	46864.8685	50650.4230	49915.9197	49202.0887

Table 3.46: Extracted texture parameters from an irregular ROI of area 233 pixels within the gastrocnemius muscle for five repeated image acquisitions with the same scan speed and pixel size. The mean value was calculated in each case.

	Image #	1	2	3	4	5	
	ROI Size (Pixel)	233	233	233	233	233	Mean
Texture Parameter	GL	70.1717	67.4421	70.5408	68.8927	69.7597	69.3614
	Variance	14.1165	12.0836	12.4543	14.4906	13.5903	13.3471
	Co-occurrence	182918.3753	208921.8803	179067.9313	195370.3362	194105.3743	192076.7795
	RL	848.6518	827.8921	821.1446	834.3687	780.5985	822.5311
	Gradient	2224.7679	1695.4330	1586.8914	1588.8831	1456.8677	1710.5686
	AR	1.5511	1.6470	1.6313	1.3445	1.4768	1.5301
	Wavelet	51366.7309	49018.1268	50544.9697	49760.5458	53290.8809	50796.2508

Figures 3.46-3.52 show the effect of the erosion of ROI area on the mean value of extracted texture parameters. Data have been analysed using linear regression and correlation. Mostly affected were the GL, variance, RL and wavelet texture parameters. Figure 3.49 depicts the strong linear relationship between ROI area reduction and the extracted value of the RL matrix.

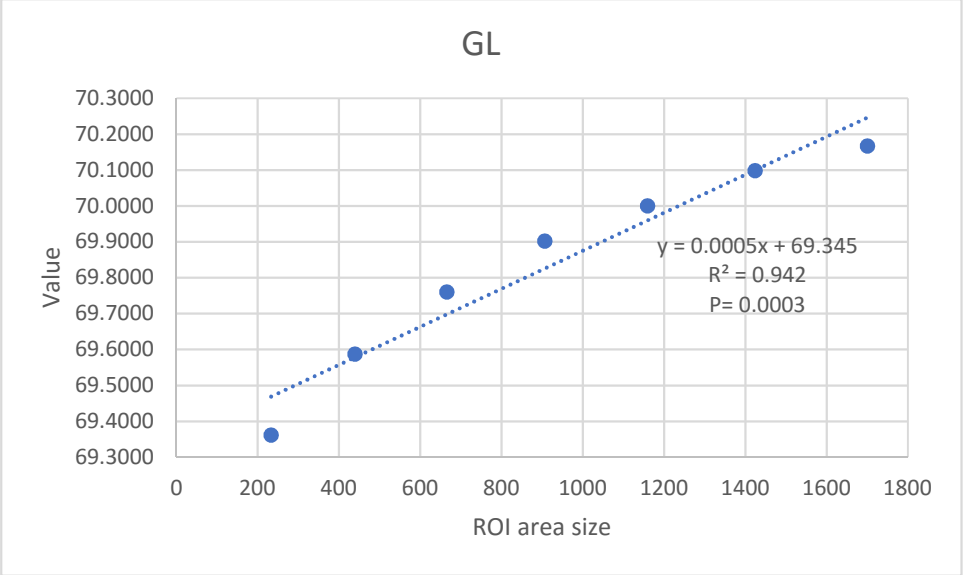

Figure 3.46: The fitted regression line between the GL values of the 7 ROI eroded area.

.

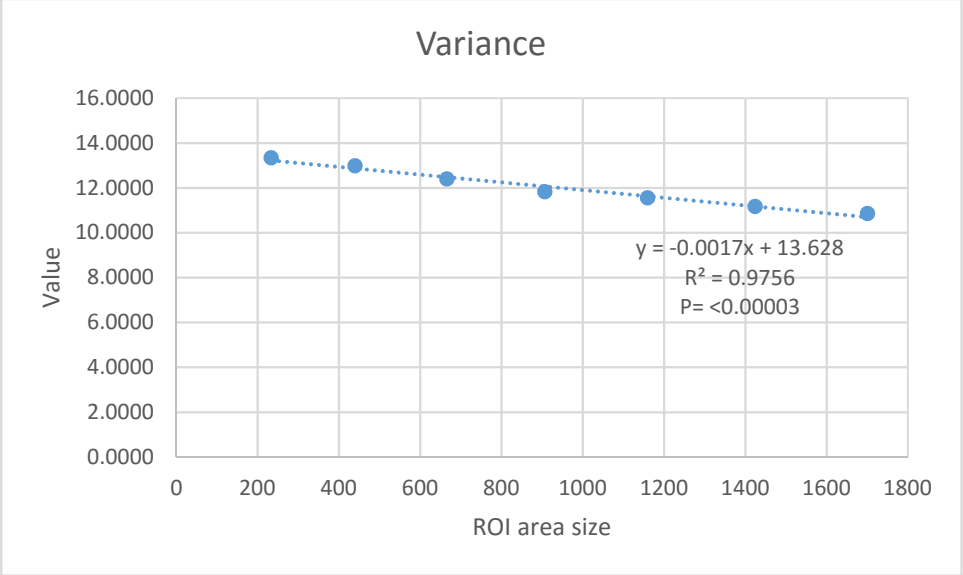

Figure 3.47: The fitted regression line between the variance values of the 7 ROI eroded areas.

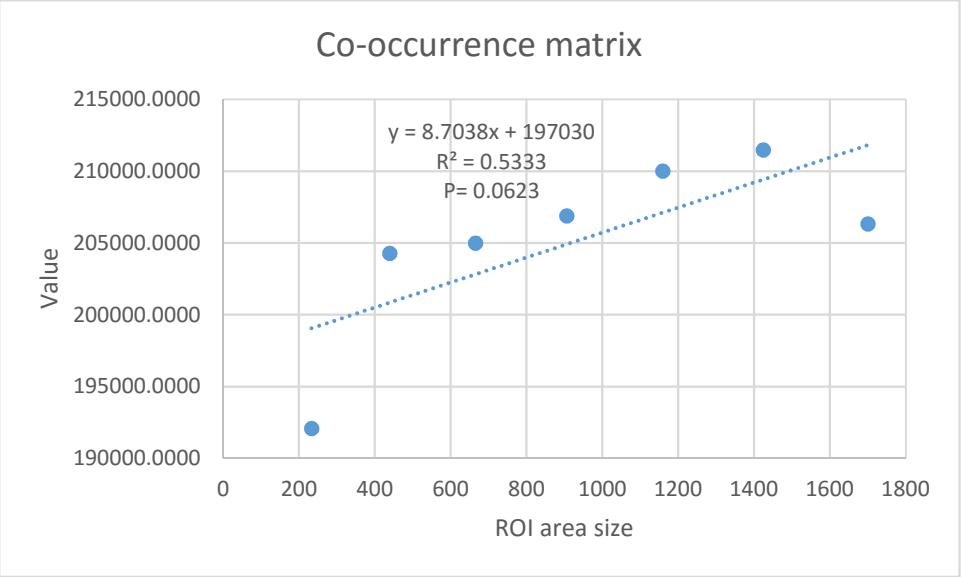

Figure 3.48: The fitted regression line between the co-occurrence matrix values of the 7 eroded ROI areas.

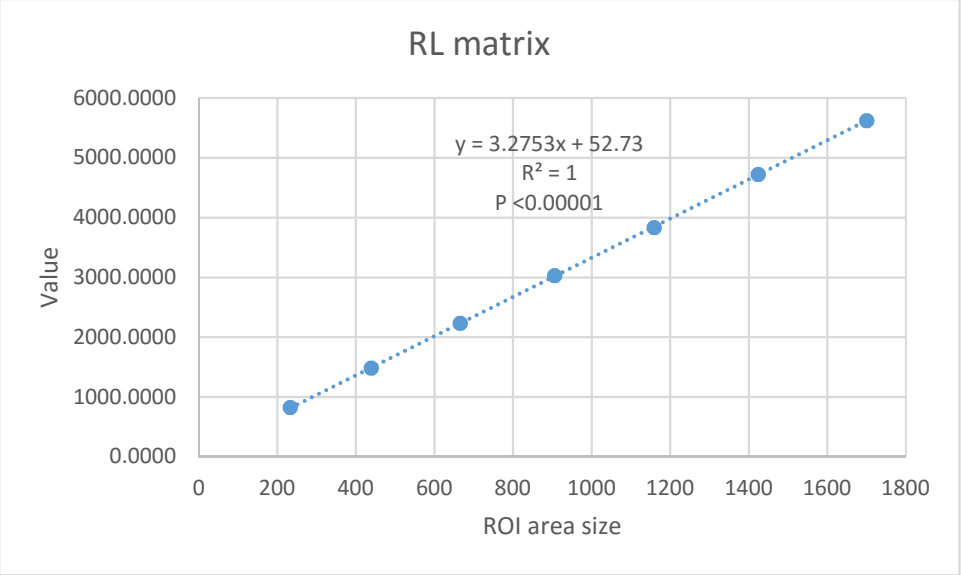

Figure 3.49: The fitted regression line between the RL matrix values of the 7 eroded ROI areas.

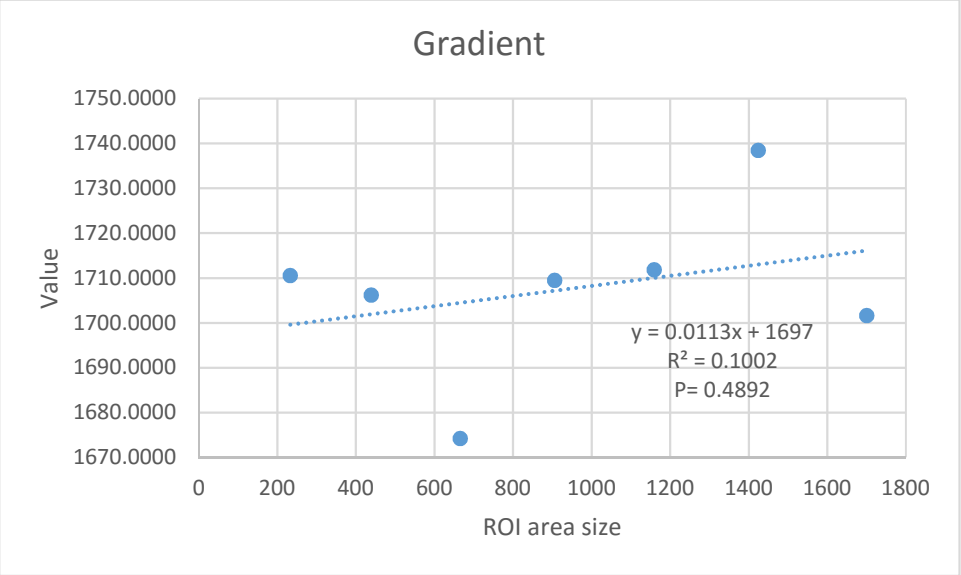

Figure 3.50: The fitted regression line between the gradient values of the 7 eroded ROI areas.

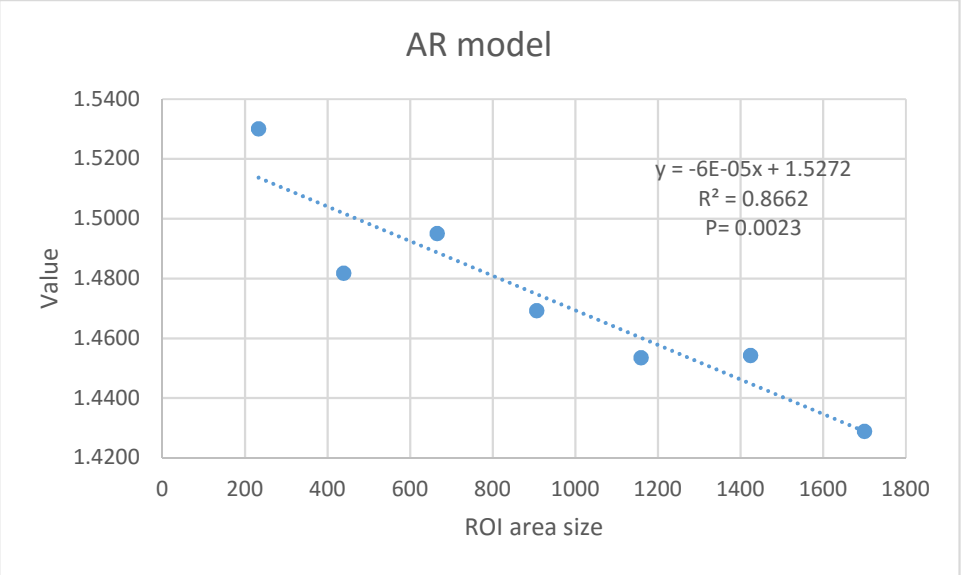

Figure 3.51: The fitted regression line between the AR model values of the 7 eroded ROI areas.

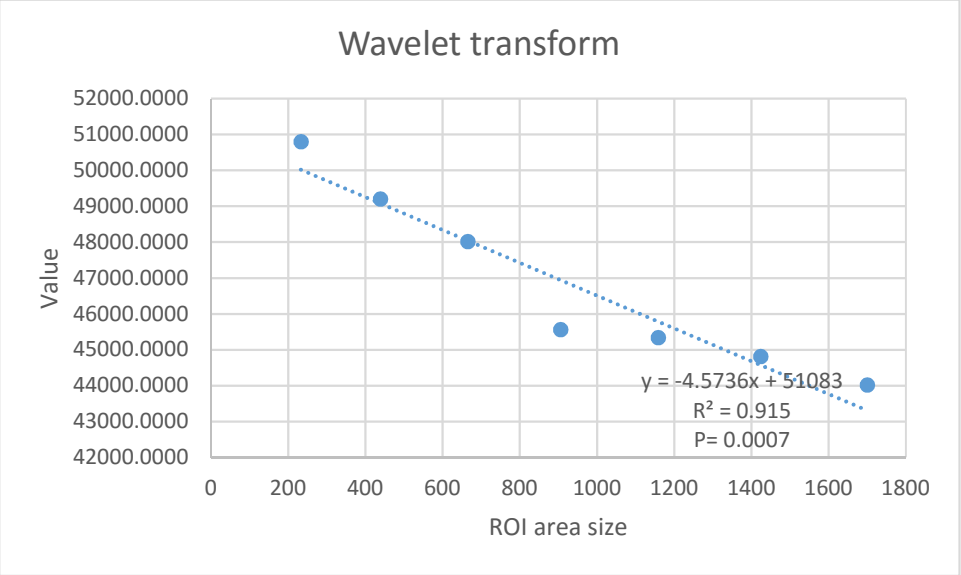

Figure 3.52: The fitted regression line between the wavelet transform values of the 7 eroded ROI areas.

Table 3.47 summarises the level of influence of the ROI area erosion on extracted texture parameters.

Table 3.47: Correlation coefficient and P values of influence of ROI area reduction on extracted texture parameters (significant at p<0.05).

Texture Parameter	R^2	r	P value	Significance
GL	0.9420	0.9706	0.0003	Yes (<0.05)
Variance	0.9756	0.9877	0.00003	Yes
Co-occurrence	0.5333	0.7303	0.0623	No (>0.05)
RL	1.0000	1.0000	<0.00001	Yes
Gradient	0.1002	0.3165	0.4892	No
AR	0.8662	0.9307	0.0023	Yes
Wavelet	0.9150	0.9566	0.0007	Yes

3.3.4 Discussion

The capability of the pQCT scanner to acquire calf muscle images was demonstrated in this study. Findings were consistent with those shown in the previous section, which concluded that noise decreased as pixel size increased. Data from Table 3.48 have shown that at a pixel size of 0.8 mm, noise (as expressed by variance) was reduced compared to a pixel size of 0.2 mm. Table 3.48 below summarises the variance results for comparison.

Table 3.48: Comparison between variance values at different scan speed and pixel sizes.

		Variance	
		Pixel Size= 0.2 mm	**Pixel Size= 0.8 mm**
Scan Speed (mm/s)	**3**	65.7864	9.7176
	10	134.7613	8.6525
	30	224.8515	20.3114

This study demonstrated that the position of ROI within a normal gastrocnemius medial head had no significant effect reflecting homogeneity of muscle tissue as concluded by Repeated Measures ANOVA test.

The values of %CV for the computed texture parameters reflected the consistency which were less than 10 %. Nevertheless, %CV for grey level at a pixel size of 0.8 mm was lower than at a 0.2 mm pixel size. For improved image, spatial resolution, a smaller pixel size should be selected. However, the achievement of a higher resolution image necessitates a slower scan speed to maintain SNR. The criterion for choosing scan speed was comfort of the subject (and hence the acceptability of the scan procedure by the subject). At a scan speed of 3 mm/s, the acquisition time was 14.2 minutes, whereas at 10 mm/s it was only 4.6 minutes. Therefore, the scan speed should be relatively fast to avoid artefacts due to subject movement. A need exists for a balance between the scan speed and the resolution of images. Therefore, the selection of the scan parameters of 0.8 mm and 10 mm/s for pixel size and scan speed respectively was validated. A windowing approach yielded clear calf muscle borders as illustrated in Figures 3.30 -3.32. This study provided evidence that MaZda software

was capable to compute texture parameters at small ROI area (15 and 30 pixels) for all texture parameters except co-occurrence matrix and wavelet transform. This study (Table 3.33) revealed that ROI area of 200 pixels was the cut-off size for the wavelet transform parameter and, to a lesser extent, for the co-occurrence matrix parameter. Therefore, the number of pixels in the ROI must be at least 200 to obtain numerical statistical values for the majority of the texture parameters.

This study demonstrated the extent of effect that area of ROI can have for computed texture parameters. addition, the ROI must be kept constant in area during texture parameters extraction as GL, variance, RL and wavelet transform were significantly affected. In other words, the ROI area must be kept constant when extracting these parameters. In a study conducted by Herlidou et al, (1999) and Harrison et al (2008) implemented texture parameters for clinical diagnosis application failed to acknowledge the effect of variation of ROI area on the RL matrix. In contrast, a study conducted by Sikio et al, (2015) found that RL matrix parameter was linearly dependent on ROI area. Furthermore, according to a study by Lerski et al, (2015), for homogeneous texture RL has long pixel runs (i.e. a large value), while for rough texture, RL has short runs (i.e. a small value).Therefore, RL could be a good texture parameter to assess tissue homogeneity. In this study, it was found the values of RL at the five circular ROI positions were all of the order of 750 pixels (746, 757, 744, 743 and 774), which indicates gastrocnemius muscle tissue homogeneity. ROI position has no significant effect (p=0.263) on extracted texture parameters as shown in section 3.3.3.4

3.3.5 Conclusion

The main findings of this study can be summarised as follows:

1. A pQCT scanner was capable of acquiring calf muscle images.
2. The pQCT image was capable of distinguishing calf muscle boundaries.
3. Image windowing was deemed a useful approach for identifying muscle boundaries.

4. The optimal healthy subject image was acquired at a pixel size of 0.8 mm and scan speed of 10 mm/sec. This represented a balance between the scan time and acceptable image noise.
5. Texture parameters, including GL (grey level mean), co-occurrence matrix, RL (run length) matrix, AR model, and wavelet transform showed a CV of less than 10% during repeated measurement.
6. ROI area was shown to exert an influence on texture parameters.
7. It was determined that the number of pixels in the ROI must be greater than 200 pixels for all texture parameters in order to obtain numerical statistical values.
8. It was determined that ROI area must be kept constant as GL, variance, run length and wavelet were significantly affected by variations in ROI area.
9. ROI position within the boundary of the medial head of the gastrocnemius muscle has no significant effect on extracted texture parameters.
10. RL parameter might be used as muscle tissue homogeneity index.

3.4 Image Scaling

3.4.1 Introduction

Part of the image acquisition protocol was to save pQCT acquired images in CSV format (32-bit) and then to transform them to yield 8-bit BMP images in order to extract texture features with the MaZda package software. As mentioned previously (section 3.1), water possesses similar x-ray attenuation properties to soft tissue (such as muscle) but has no texture. Nevertheless, Table 3.49 below depicts a noticeable difference between the GL (grey level) value of water in the phantom (Table 3.30 with ROI area = 200 pixels) and muscle in a healthy subject (Table 3.46 with ROI area = 228 pixels). This prompted an investigation into the reasons for this difference. Furthermore, to confirm that first order statistics were performed adequately for the two studies (water phantom and single healthy subject).

Table 3.49: Similarities and differences between water phantom and single healthy subject in terms of extracted texture parameters.

Texture Parameter	Heathy Subject	Water Phantom	Status
GL	70.8868	224.9300	Difference
Co-occurrence	215217.7147	202665.6491	Similarity
RL	764.8182	764.9448	Similarity
Gradient	1582.9411	1815.0150	Similarity
AR	1.1605	1.1407	Similarity
Wavelet	44110.8169	52210.7765	Similarity

3.4.2 Materials and Methods

It was hypothesised that during image format transfer from 32-bit to 8-bit, transferred images were scaled to the densest material within the images (bone for the human subject and water for the phantom). Two additional software packages were used to confirm that the first order (GL) texture parameter produced by MaZda was adequately performed; These two additional software packages were ImageJ and Medical Image Processing, Analysis and Visualisation (MIPAV). Validation was performed on acquired images of the human subject and water phantom in 8-bit BMP format. The pQCT scan acquisition parameters were a pixel size of 0.8 mm and a scan speed of 10 mm/s. ROIs were drawn in exactly the same position within the image using the three software packages. The water phantom image ROI areas were 1080 and 98 pixels. The human subject image ROI areas were 336, 200 and 98 pixels. GL texture values produced by MaZda and MIPAV software were extracted from both images for comparison.

To simulate the effect of bone as a high-density material within the image, an aluminum (Al) rod was inserted into the water phantom. Two water GL values were measured in identical images of different format (CSV and BMP) after immersing the Al rod into the water phantom and re-scanning at a pixel size of 0.8 mm and scan speed of 10 mm/s, as shown in Figure 3.53. The Al rod simulates bone as a high-density material embedded in muscle. Images were imported into ImageJ software in CSV format, and ROIs were defined on which grey level was measured. Images were saved in 8-bit BMP format, ROIs were defined and then texture parameters extracted.

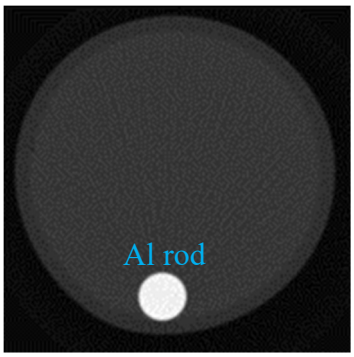

Figure 3.53: Water filled phantom loaded with an aluminium (Al) rod to simulate high dense material (bone).

As the ImageJ software package is limited to specific image texture parameters (GL, variance, skewness and kurtosis) the MaZda software package was used with DICOM image format to investigate the image scaling effect on the remaining texture parameters (co-occurrence matrix, RL matrix, gradient, AR model and wavelet transform). To accomplish this task, the CSV image format was transformed to DICOM using the MATLAB software package. MATLAB stands for Matrix Laboratory. It was written to allow easy manipulation of matrices. MATLAB is an advanced performance language for technical computing. It includes computation, visualisation and programming (Caltech 2005).

Images were loaded to MATLAB and saved into 8-bit DICOM (. dcm) format. MaZda software was used to perform texture analysis. ROI areas were 546, 200 and 98 pixels and be ROIs were located within the gastrocnemius medial head muscle boundary.

The human subject muscle grey level was measured using two image formats, CSV and 8-bit BMP as shown in Figure 3.54. In order to quantify the scaling factor, maximum pixel values in the entire right leg subject images were measured in both formats. The scaling factor was subsequently calculated as the ratio of the maximum pixel values in the CSV and 8-bit BMP formats.

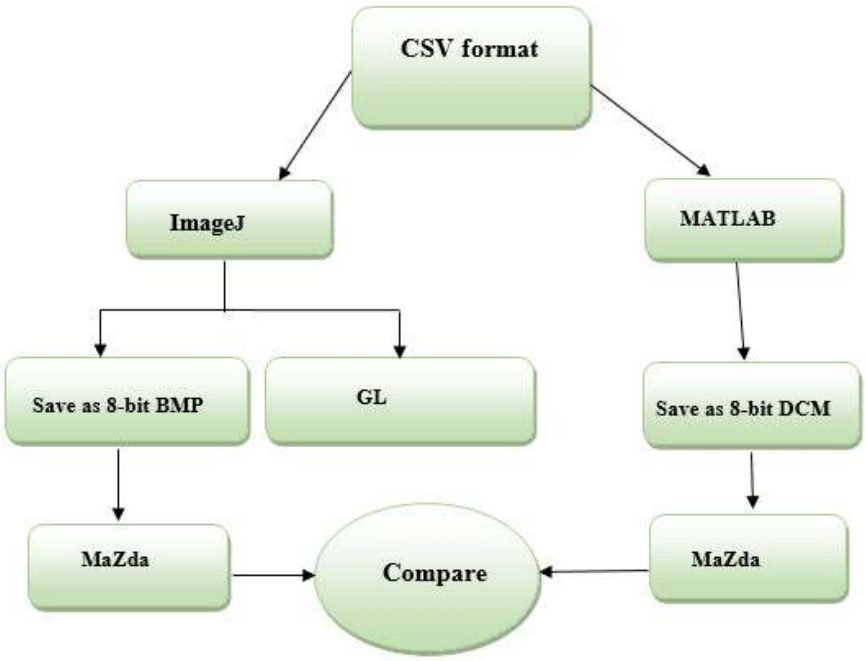

Figure 3.54: Flow chart of acquired image processing using ImageJ, MATLAB, and MaZda software packages.

3.4.3 Results

3.4.3.1 Texture Analysis Software Validation

Confirmation that first order statistics (GL) was extracted adequately are shown in Table 3.50 which depicts GL values of the heathy subject images measured by three different software packages (MIPAV, ImageJ, and MaZda). In addition, Table 3.51 depicts GL values of a water phantom image that were measured by the same three software packages.

Table 3.50: Grey level (GL) values for 3 ROIs drawn within the gastrocnemius muscle image (BMP), measured by three different software packages.

	GL		
ROI area (pixels)	MIPAV	ImageJ	MaZda
546	68.2020	68.2527	69.7880
200	70.7150	70.5556	71.7150
98	70.8469	70.8469	71.8470

Table 3.51: Grey level (GL) values for 2 ROIs drawn within the water phantom image (BMP), measured by three different software packages.

	GL		
ROI area (pixels)	MIPAV	ImageJ	MaZda
1080	222.9639	222.9639	222.9600
378	222.8122	222.8122	222.8100

3.4.3.2 Scaling Factor Magnitude

Table 3.52 depicts grey level values measured by ImageJ software for the water phantom image with immersed aluminum rod in CSV and BMP image format. The magnitude of the calculated scaling factor that results from image transfer into different format for the water phantom images was 3.89.

Table 3.52: Grey level (GL) values of ROI drawn within water phantom images (CSV and BMP) with immersed aluminum (Al) rod measured by ImageJ software.

	GL	
ROI area size (pixels)	CSV	BMP
378	218.03439	56.00529

Table 3.53 depicts scaling magnitude for the single healthy subject with pixel sizes of 0.2 and 0.8 mm and scan speeds of 3, 10 and 30 mm/s.

Table 3.53: Scaling factor magnitudes of maximum pixel values of subject images at various scan speeds and pixel sizes.

Scan Speed (mm/s)	Pixel Size (mm)	Max Pixel value (CSV)	Max Pixel value (BMP)	Scaling factor magnitude
3	0.2	1211	255	4.75
	0.8	967	255	3.80
10	0.2	1442	255	5.66
	0.8	957	255	3.75
30	0.2	1786	255	7.00
	0.8	997	255	3.91

Table 3.54 shows a comparison between the same extracted texture parameters from images of the same subject in different image formats (BMP and DICOM). There were no consequences of image scaling on co-occurrence matrix, RL matrix, gradient, AR model and wavelet transform.

Table 3.54: High-order statistics texture parameters for pQCT acquired image of one subject computed in two different image formats.

	Co-occurrence	RL	Gradient	AR	Wavelet
BMP Image Format (8 Bits)	171608.34	733.18	1352.83	1.27	47800.74
DICOM Image Format (8 Bits)	171645.21	734.94	1351.71	1.25	47795.51

3.4.4 Discussion

The validation of the software used for texture analysis (MaZda) demonstrated its power for texture parameter computation. The results of the re-scan of the water phantom with an aluminium rod, and computation of the acquired image grey level parameter in two image formats (CSV and BMP) illustrated the problem of rescaling after saving images in an 8-bit BMP format. During the process of saving the calf muscle-acquired images, grey level values were scaled to the highest density material (bone) within the image, as shown in Table 3.52 and Table 3.53. Despite the effect of image scaling on GL, investigation of co-occurrence matrix, RL matrix, gradient, AR model and wavelet transform values in DICOM format showed no effect as illustrated in Table 3.56. In general, for medical diagnostic imaging, information is restricted to higher-order texture parameters which are not affected by scaling as a result of implementation of normalisation process (see section 3.2.2.3.1). This finding validated the recommendation of Materka (2004), who claimed that some higher-order texture parameters, especially those derived from the co-occurrence matrix, are correlated with first-order texture parameters. To avoid this unwanted phenomenon, he recommended implementation of a normalisation process before texture extraction. Thus, in this project the normalisation process was a standard step before extraction texture parameters. Aggarwal et, al. (2012) claimed that first order statistical parameters provide far less number of relevant and distinguishable feature in comparison to wavelet transform was implemented as one of higher order texture feature in this project. BMP image format was implemented rather than the DICOM

format, which is used in a networked environment and applied to the integration of medical devices distributed geographically (Rosslyn, 2011).

3.4.5 Conclusion

Key conclusions drawn from this work include:

- The MaZda texture analysis software was shown to be an accurate and reliable tool when transforming acquired images from CSV to 8-bit BMP format.
- The texture parameter most affected by image format transformation was grey level (GL).
- First order texture parameters should be excluded for characterisation of acquired images and so BMP image format maybe used.
- The texture parameters not affected by image transformation were the second order ones: co-occurrence matrix, RL matrix, gradient, AR model and wavelet transform.

3.4.6 Summary

The effect of pQCT scanner settings on extracted texture parameters was investigated with the aim of defining a specific scan setting (pixel size and scan speed) for acquisition of calf muscle images. It was determined that a pixel size of 0.8 mm and scan speed of 10 mm/s were the optimal settings. Furthermore, the ability of the pQCT scanner to identify the calf muscle border was evaluated, and an image windowing technique was applied to highlight the muscle borders. Small ROI sizes were shown to have a limited effect on the extracted texture parameters. RL matrix was linearly related to ROI size. The texture analysis software (MaZda) was validated against other two software packages and found to be accurate for assessment of grey level. The effect of image format transformation from the CSV to BMP format was examined, and it was concluded that the only affected texture parameter was GL parameter.

Chapter 4 MR and pQCT Imaging of the Gastrocnemius Muscle in Healthy Volunteers

4.1 Introduction

At present, the gold-standard imaging technique for the assessment of muscle injury in athletes is Magnetic Resonance Imaging (MRI). However, this technique requires specialised and expensive equipment and facilities. Peripheral Quantitative Computed Tomography (pQCT) utilises a small-bore, low-dose x-ray scanner. Portable and less costly than MRI, pQCT has become an established technique for three-dimensional measurement of bone parameters (Engelke et al., 2008) and a valuable tool for evaluating soft tissue components such as muscle and fat (Blew et al., 2014). Furthermore, previous research has applied pQCT in the quantification of the relationship between muscle quality and bone density (Farr et al., 2011; Macdonald et al., 2005).

The purpose of the investigation was to assess pQCT as a method for muscle characterisation in relation to MRI and to investigate the variability of muscle texture parameters. During this work, it became apparent that subject movement was a problem to be taken into account.

4.2 Materials and Methods

4.2.1 *Subjects*

Five healthy volunteers (group A) (mean age ± SD, 28.4 ± 5.6 years, range 19 to 32 years), and seven additional healthy volunteers (group B) (mean age ±SD, 29.3 ± 5.6 years, range 19 to 37 years) were recruited to this study. The initial group of five was imaged by both MRI and pQCT. The seven additional volunteers were subjected to pQCT scanning only.

Data were used for a variety of purposes including the definition of reference ranges for extracted texture parameters. To test the pQCT reference ranges, all 12 subjects

were combined and divided into two groups: a training group (Group C with 8 subjects) and a test group (Group D with 4 subjects) as illustrated in Figure 4.1.

Informed consent was obtained from all participants followed by an explanation of the aims, protocols, and procedures of the study (see Appendix C). All volunteers declared that they were of normal health with no prior history of musculoskeletal disorders. For MRI scanning, the completion of a safety questionnaire was required of group A (the initial five volunteers). The study was approved by the ethics committee of the Cardiff University School of Engineering.

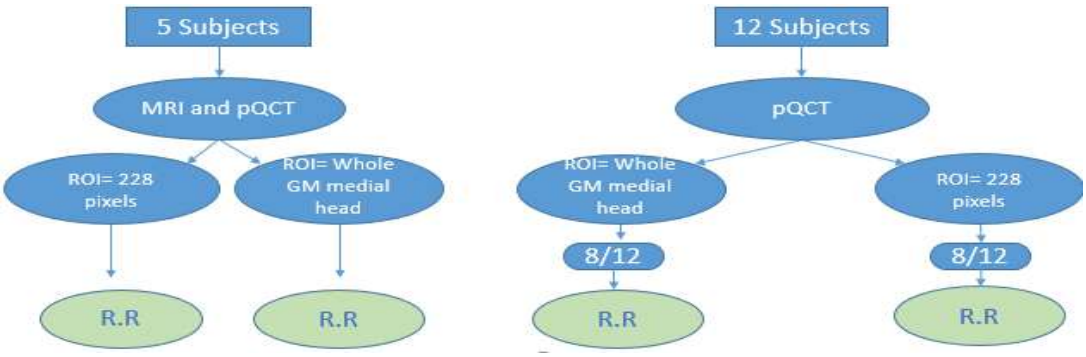

Figure 4.1: Methodology of defining reference ranges for both modalities (left) and defining and testing pQCT reference ranges (right).

4.2.2 *Magnetic Resonance Image Acquisition Protocol*

MRI is a sensitive modality for imaging soft tissue. Cross-sectional right and left leg scans were acquired by MRI (GE Medical Systems, Signa,1.5 T) in group A (five healthy young volunteers), at 66% of the distance from the medial malleolus to the medial condyle of the tibia. This distance represents the maximum calf diameter (Masani K et al., 2014). An oil capsule was attached to each participant's leg to identify the position of the cross-sectional slice during analysis, as shown in Figure 4.2.

The MRI protocol was as follows:

1. Each subject was asked to complete an MRI procedure safety questionnaire (see Appendix C).
2. The distance of the medial malleolus to the medial condyle of the tibia was measured and labelled by a skin marker as shown in Figure 4.2.
3. An oil capsule was placed at the skin mark to identify the slice location during MRI.
4. An MRI proton density weighted image protocol with a slice thickness of 5 mm was used to acquire images (TE = 34 ms, TR = 3600 ms, FOV = 20 cm, and matrix = 512 x 512 pixels).
5. Images were saved and exported for further analysis.

Figure 4.2: Marking of subject's leg to identify the maximum diameter of calf muscle and the specific slice location.

4.2.3 *Peripheral Quantitative Computed Tomography Image Acquisition Protocol*

Cross-sectional right and left leg scans were acquired using pQCT (Stratec XL 2000, Stratec Medizintechnik GmbH, Pforzheim, Germany) from five healthy volunteers, soon after MRI. The images were acquired at 66% of the distance from the medial

malleolus to the medial condyle of the tibia, as described above. pQCT images were acquired specifically with a pixel size of 0.8 mm and scan speed of 10 mm/s.

4.2.4 *Image Transfer*

MR images were retrieved using generic GE Medical Systems software. Specific slices as marked by oil capsules were exported as 8-bit Microsoft Windows Bitmap (BMP) images. pQCT images were saved and exported in CSV image format, and analysed as described in Chapter 3.

4.2.5 *Image Texture Analysis*

Image windowing was implemented to identify muscle boundaries as described in Chapter 3. This also revealed motion artefacts with greater clarity and these were assessed visually by three independent observers.

Equal sized circular regions of interest (ROIs) of area 228 pixels were defined within the gastrocnemius muscle medial head boundary in the images obtained from all subjects. ROI size was chosen as a result of the analysis in Chapter 3 (Figure 4.10). Additional free hand-drawn ROIs covering the whole GM medial head were defined for all acquired images as shown in Figure 4.3. The same texture parameters as applied to the previous study of the water phantom and healthy volunteer images (Chapter 3) were extracted using the MaZda software package. First order texture parameters were excluded from analysis as they are affected by scaling. These data were used for a variety of purposes including: determining the variation of texture parameters within the group of healthy subjects, establishing reference ranges for the texture parameters, comparing mean values between right and left legs and comparing mean values between MRI and pQCT.

The influence of ROI position on extracted texture features for the MRI scans was investigated by placing circular ROIs of equal size (area 350 pixels) at 5 different locations within the medial head of the gastrocnemius muscle (Figure 4.35).

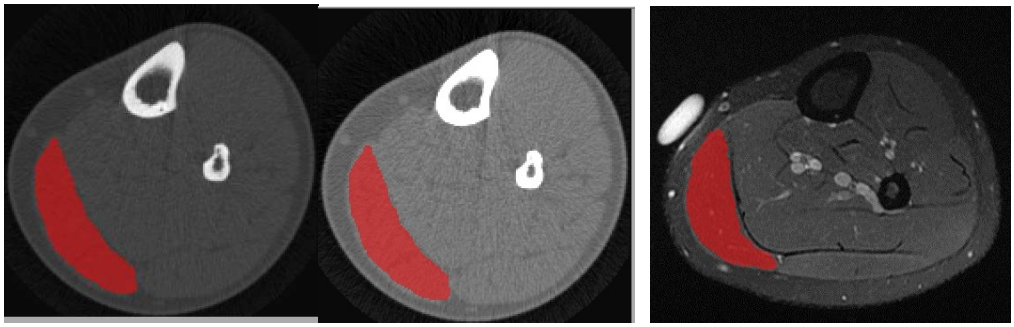

Figure 4.3: Example of ROI area covering the whole gastrocnemius muscle (GM) medial head for pQCT (left and centre) and MRI (right) images. For pQCT image windowing was used to display the GM boundary.

4.2.6 *Data Analysis*

Mean and standard deviations were calculated for each texture parameter. The coefficient of variation (CV) was calculated to evaluate the variation in texture parameters of the gastrocnemius muscle among the healthy subjects. The CV is defined as the ratio of the standard deviation and the overall mean, expressed as a percentage (as described in Chapter 3).

For each texture feature, a 95% reference range was calculated. This is the interval between (mean + 1.96SD) and (mean - 1.96SD), into which 95% of the normal subject data was expected to fall

Several statistical tests were performed to evaluate the findings of this study. Due to the small sample size of the study, a Shapiro-Wilk test was used to test the normality of the data ($p > 0.05$ was considered a normal distribution). A paired t-test and one-way ANOVA test were used for normally distributed data. The Kruskal-Wallis test was used for non-normally distributed data (p values of less than 0.05 were considered statistically significant). Both tests were used to determine whether a significant difference existed between texture parameters for the right and left legs and for pQCT and MRI acquired images. A One-way Repeated Measures ANOVA (RM-ANOVA) was used to analyse whether ROI position exerts an influence on extracted texture parameters values.

For the assessment of motion artefacts on image quality, an inter-class correlation coefficient test (ICC) was used to assess consistency between the scores of the three observers. The ICC value ranges from 0 to 1, with values closer to 1 representing stronger consistency. A high ICC with a value greater than 0.75 was considered as excellent consistency; an ICC value of 0.74-0.60 indicates good consistency; between 0.59-0.40 shows fair consistency and below 0.4 indicates poor consistency (Faul et al., 1999; Rosner, 2010). SPSS v20 (SPSS Inc., Chicago, Illinois, USA) was used for the statistical analysis.

4.3 Results of Image and Texture Analysis

4.3.1 *MRI Images*

Figure 4.4 shows transverse MRI images at the maximum diameter of the calf muscle for the five subjects in Group A. Image labelling indicates the subject number (1-5) and the laterality of the leg (left L or right R). Muscle boundaries can be readily distinguished.

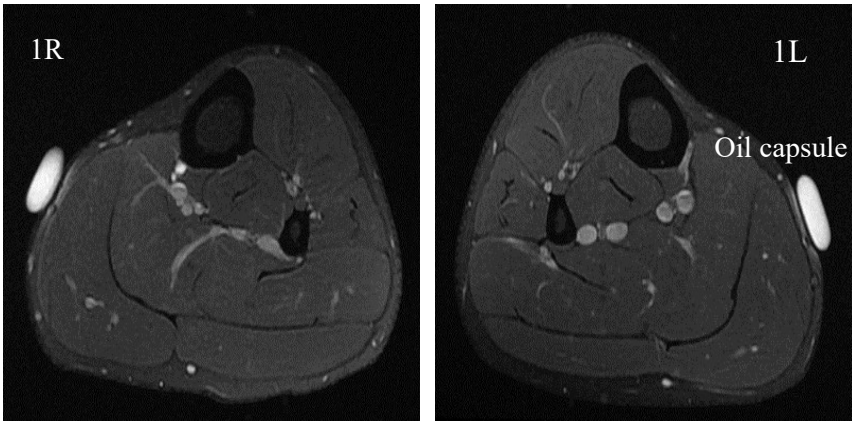


2R

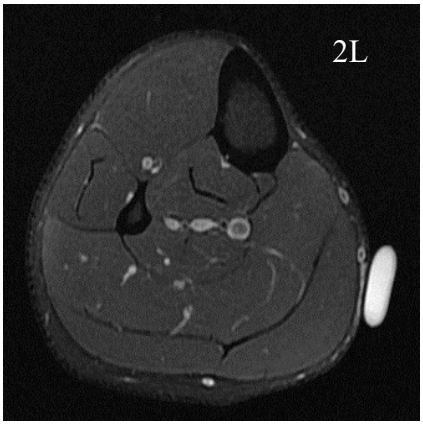
2L

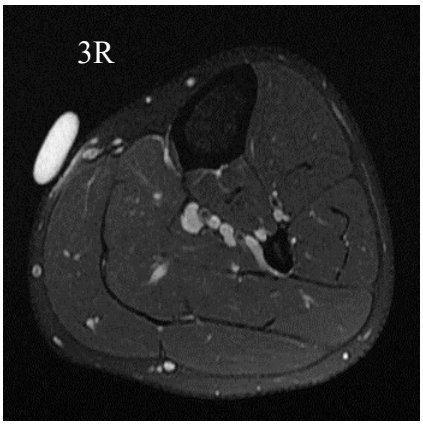
3R

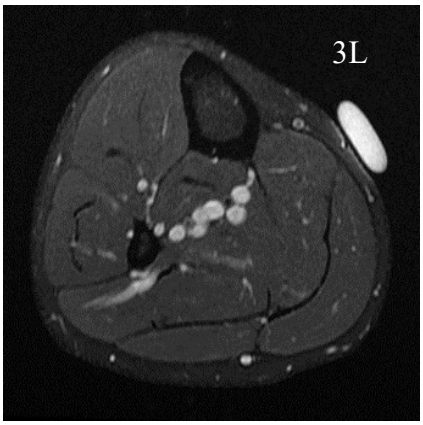
3L

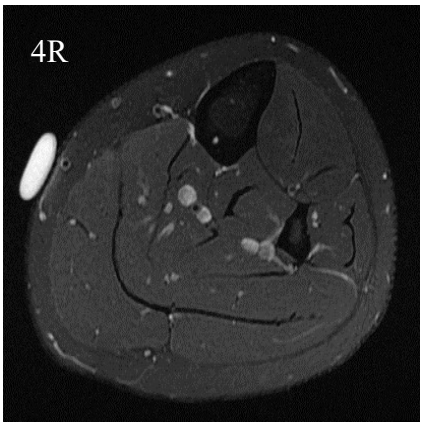
4R

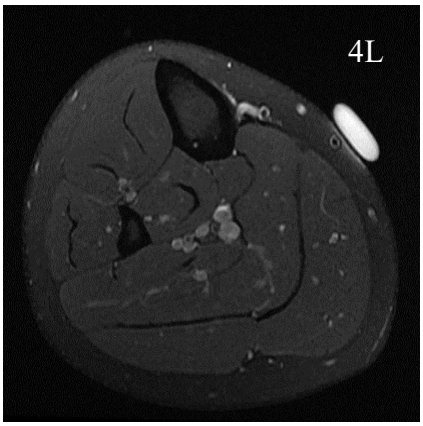
4L

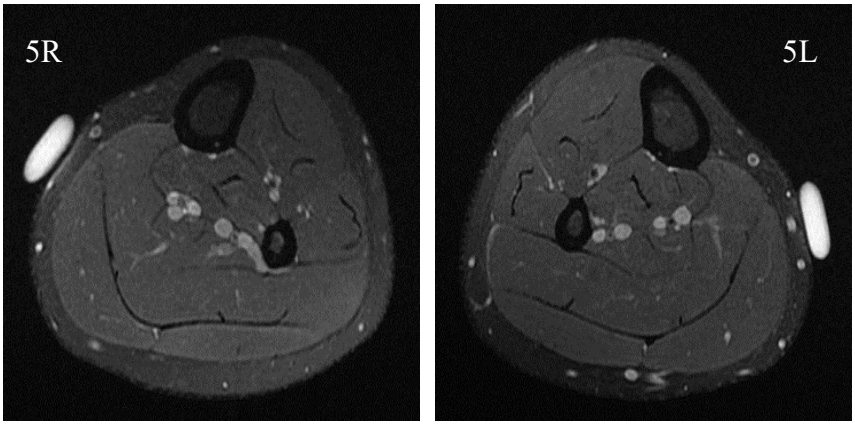

Figure 4.4: MRI images of the right (R) and left (L) lower legs in a group of five subjects (Group A).

4.3.2 *pQCT Images*

4.3.2.1 *Group A Healthy Subjects*

Figure 4.5 shows images acquired by pQCT for the five healthy subjects in Group A. Again, image labelling indicates the subject number (1-5) and the laterality of the leg (left L or right R). In selected images, such as 1L, 3R, and 3L, subject movement can be observed as streak lines. Figure 4.6 shows the histogram for one image; this is a graph that indicates the number of pixels which have particular intensities (pixel values or grey levels). The distribution includes all tissues and materials (muscle, fat, bone and air) over an intensity range of 0 to 255.

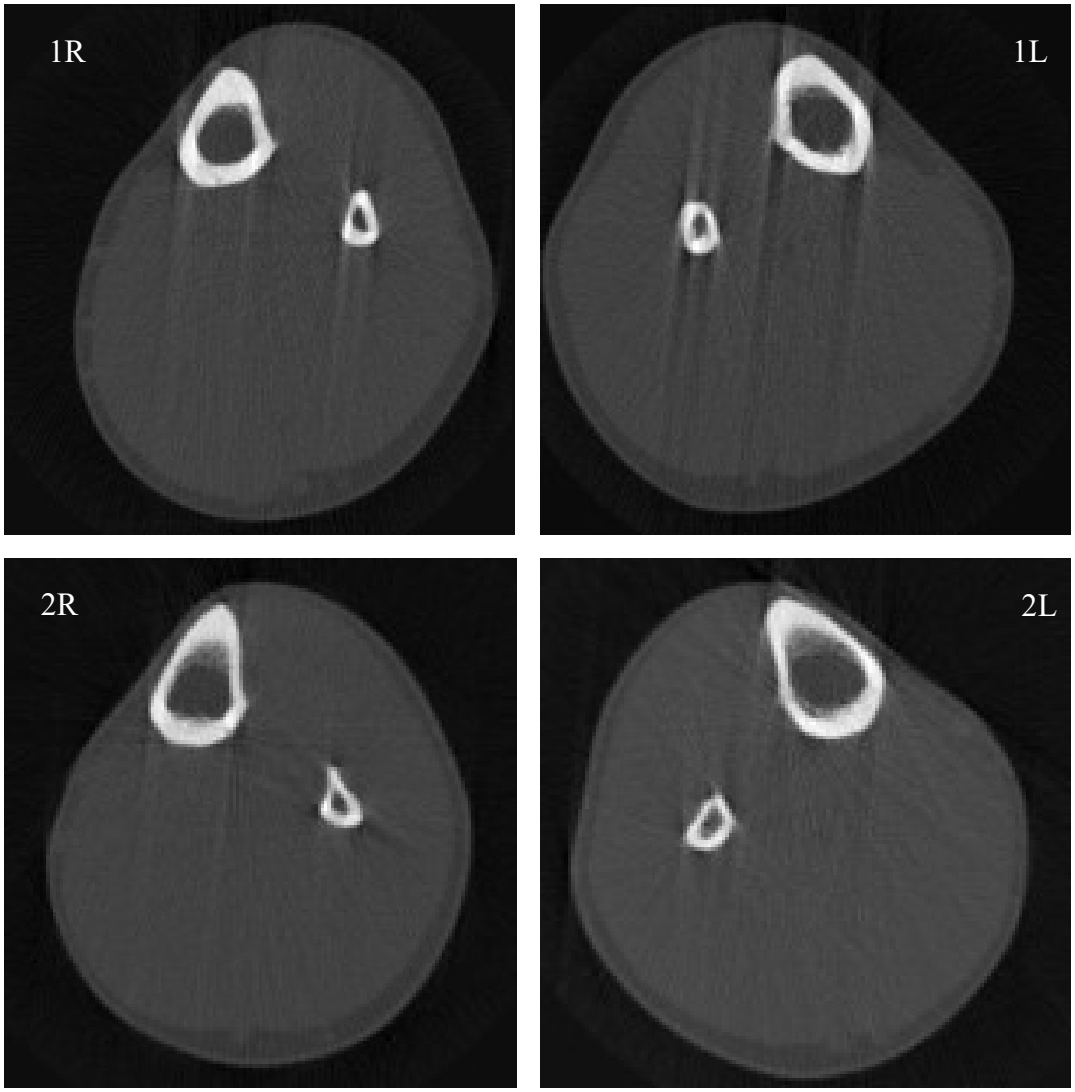
1R
1L
2R
2L


3R

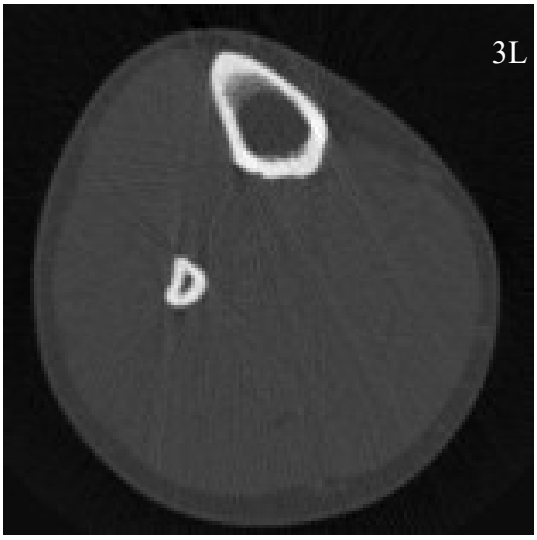
3L

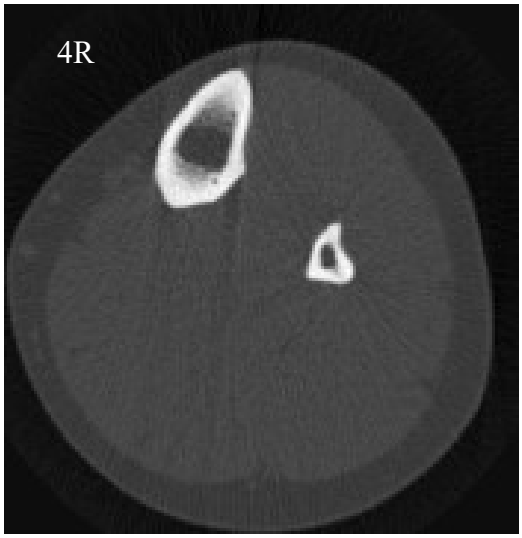
4R

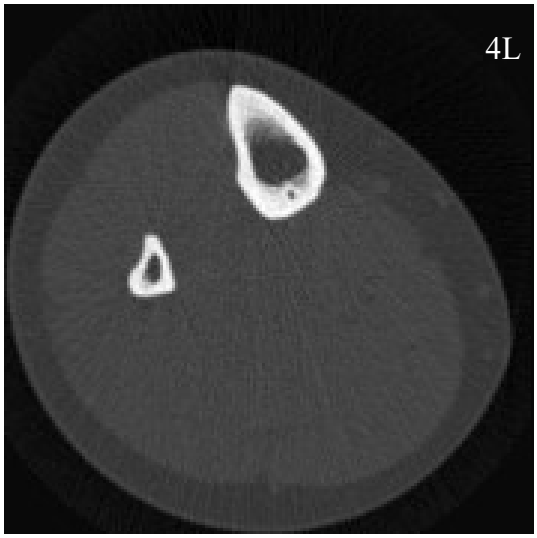
4L

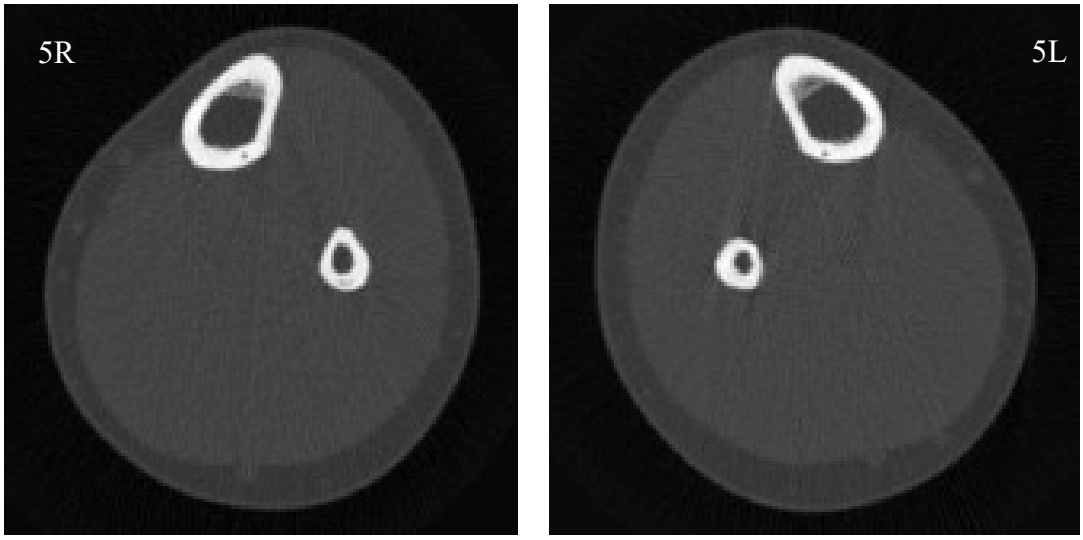

Figure 4.5: pQCT images of the right (R) and left (L) lower legs in a group of five subjects (Group A).

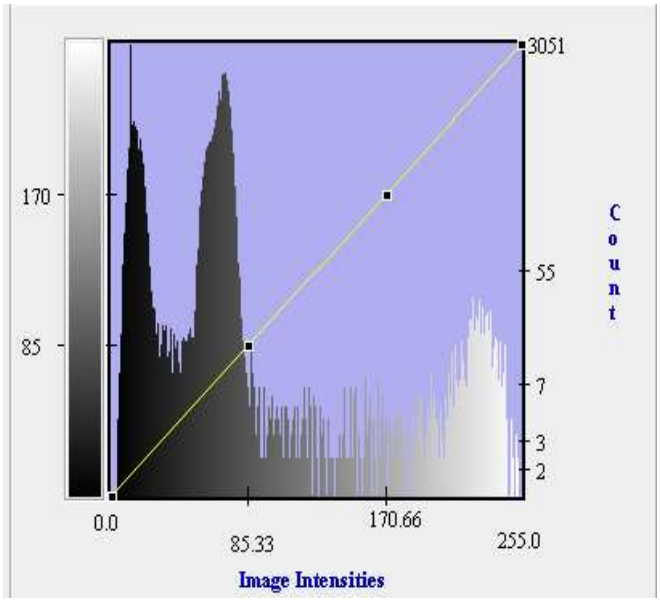

Figure 4.6: Histogram of the right leg pQCT image for one subject in Group A, showing the distribution of individual intensities (pixel values in the range 0-255).

4.3.2.1.1 pQCT Image Windowing

Figure 4.7 displays images acquired by the pQCT scanner of all five subjects in Group A following implementation of an image windowing procedure. The applicable image

histogram is represented in Figure 4.8. The purpose of image windowing is to identify muscle boundaries, which facilitates ROI definition (as described in Chapter 3). Muscle boundaries appear in images the images for subjects 1, 3, and 4. However, the procedure also highlights the motions artefacts (streaks).

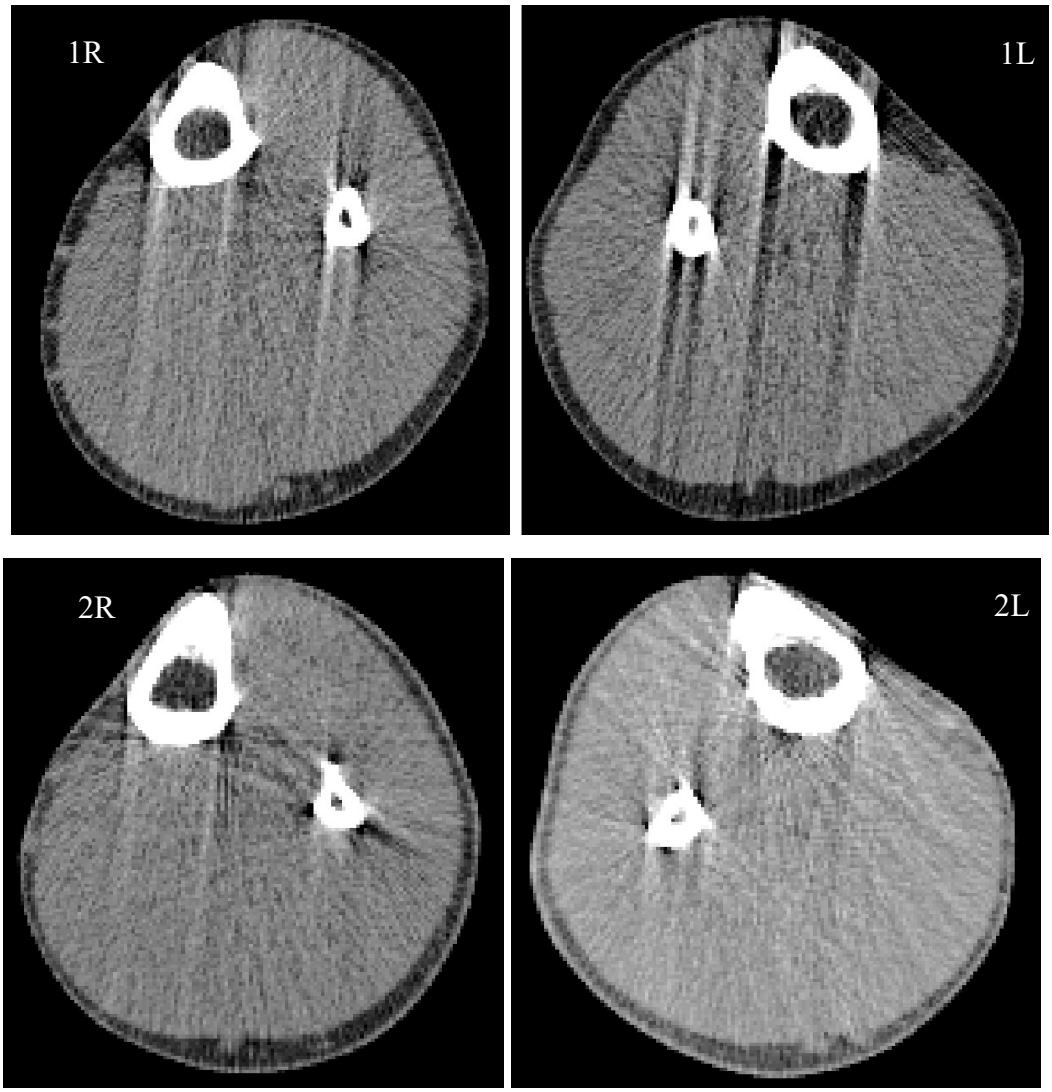

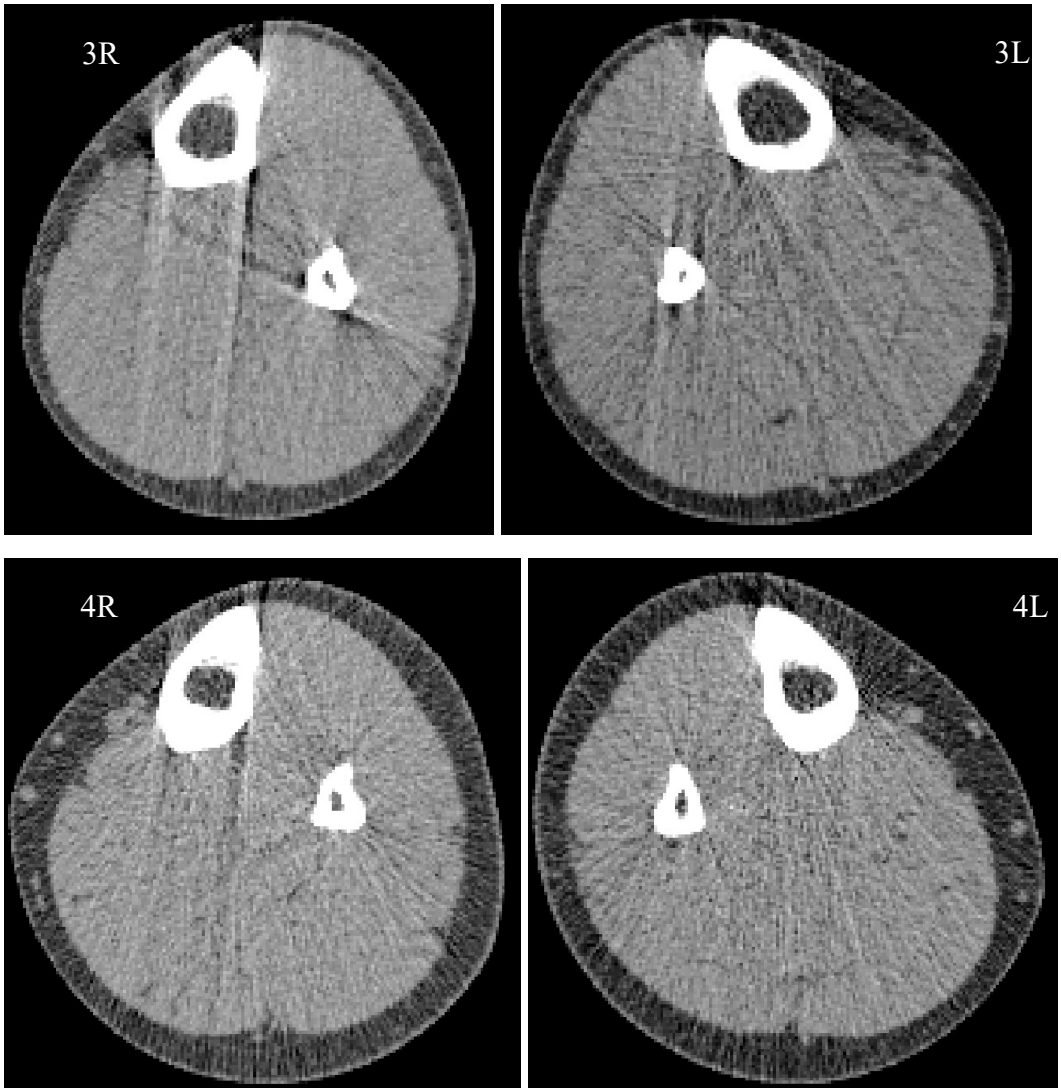
3R
3L
4R
4L

Figure 4.7: Windowed pQCT images for the five healthy subjects in Group A.

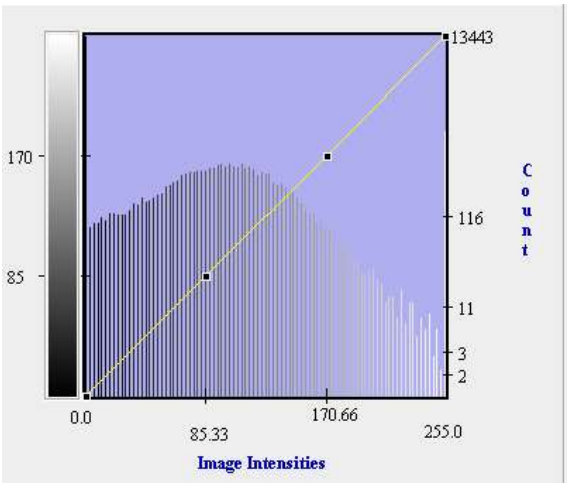

Figure 4.8: Histogram of the right leg pQCT image for one subject in Group A after windowing.

4.3.2.2 *Group B Healthy Subjects*

Figure 4.9 shows pQCT images acquired from the additional seven healthly volunteers with windowing applied. In each case, the window was adjusted until the gastrocnemious muscle border was as clear and distinguishable as possible.

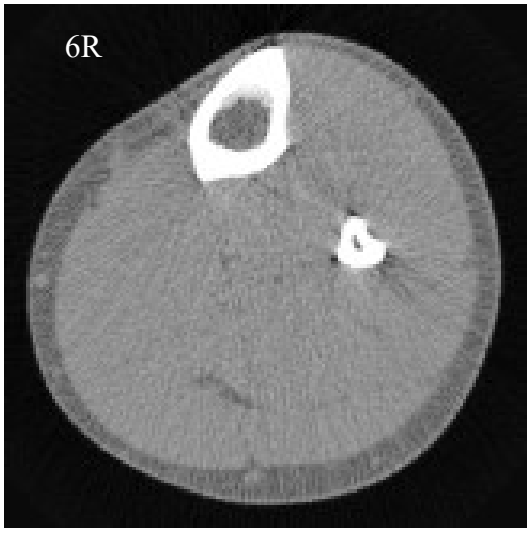
6R

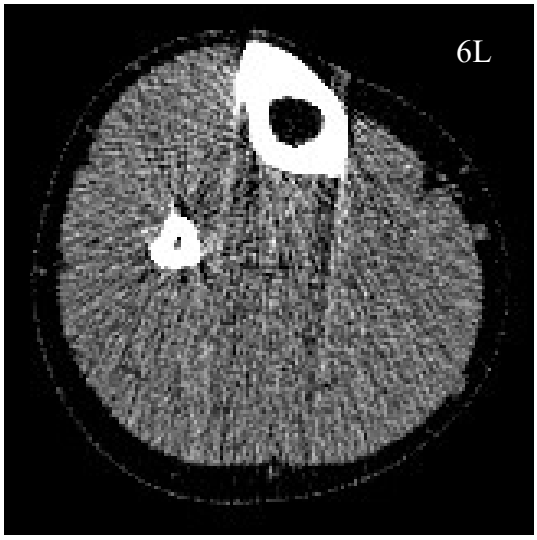
6L

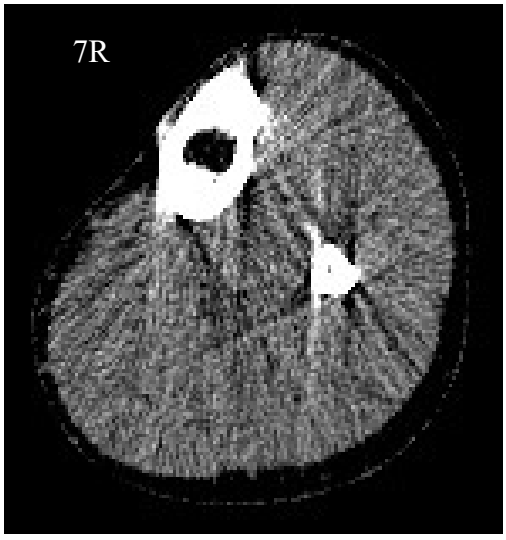
7R

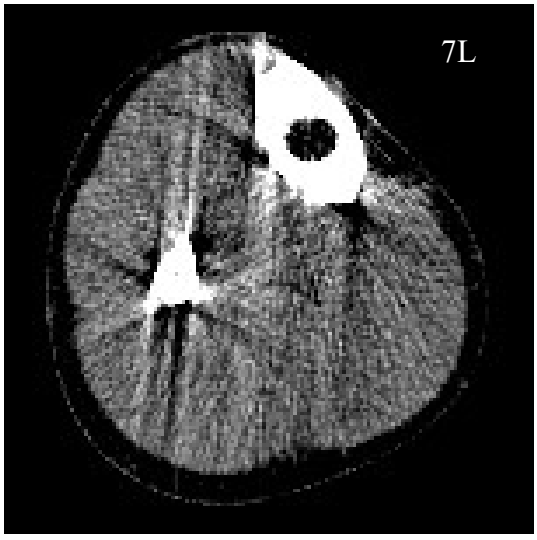
7L

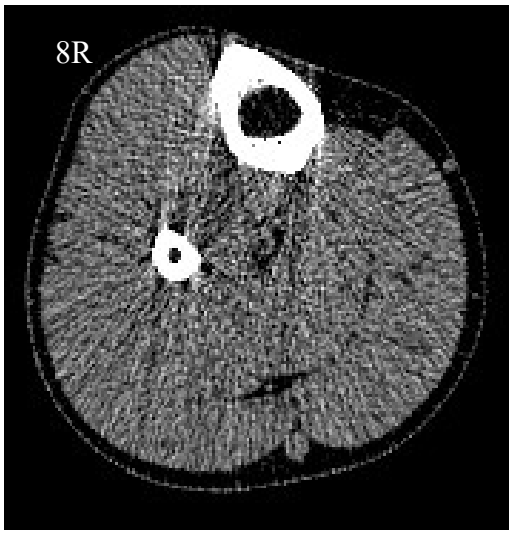
8R

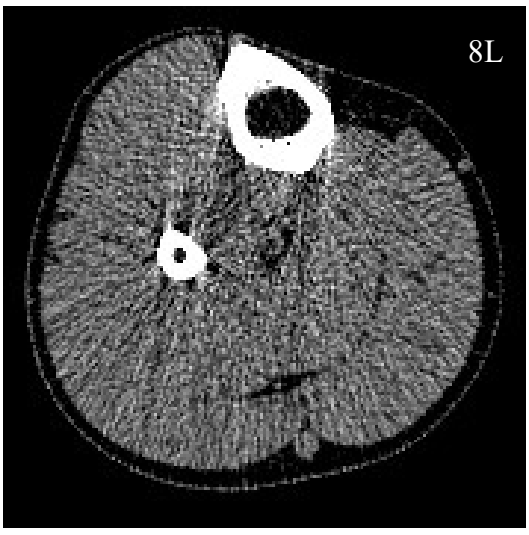
8L

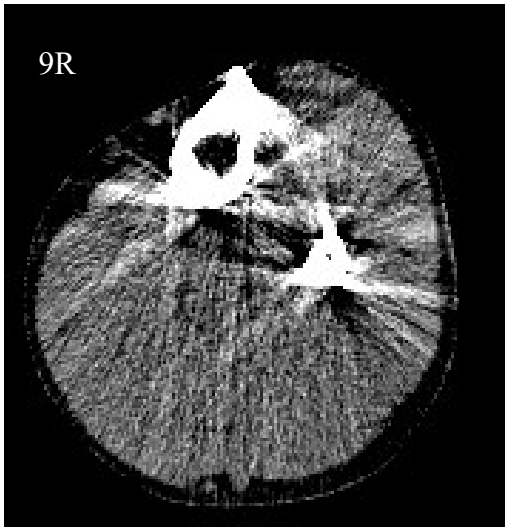
9R

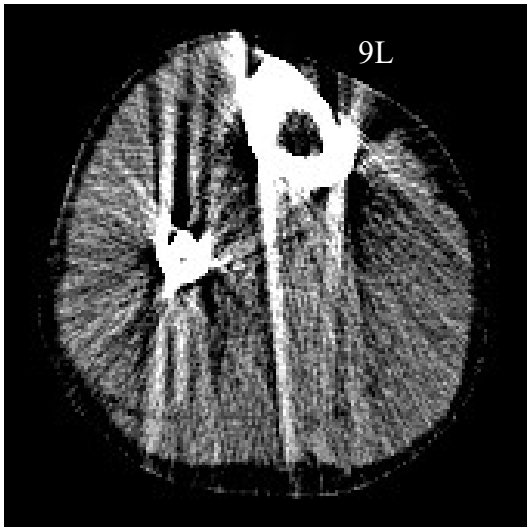
9L

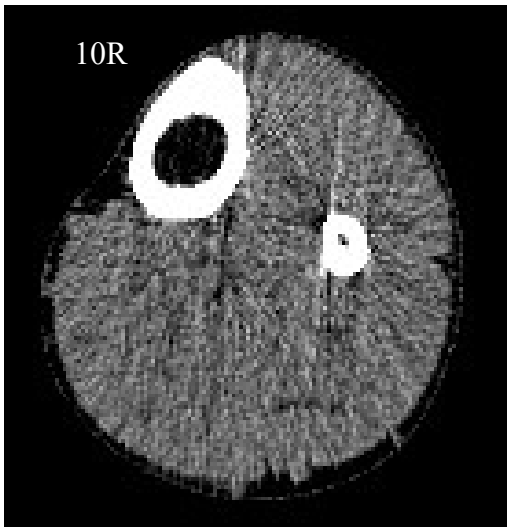
10R

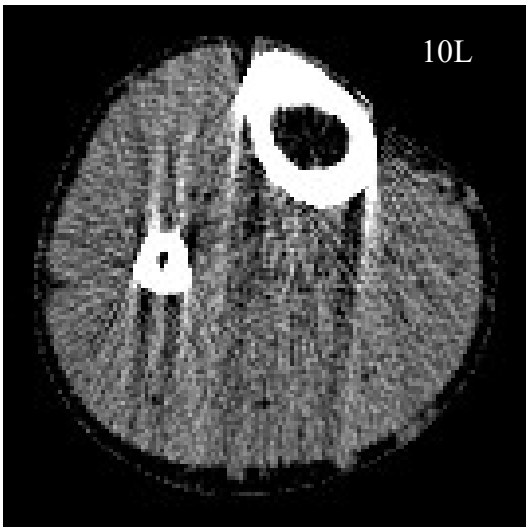
10L

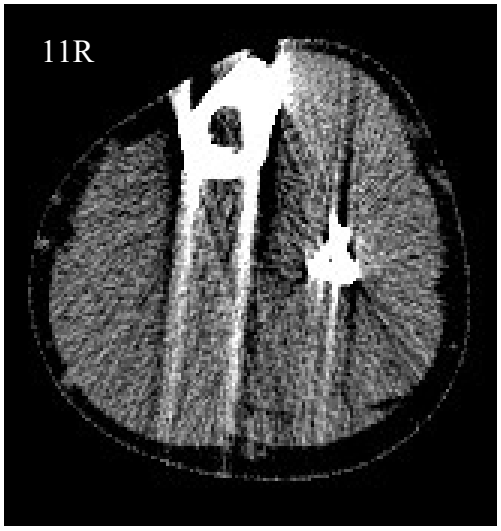
11R

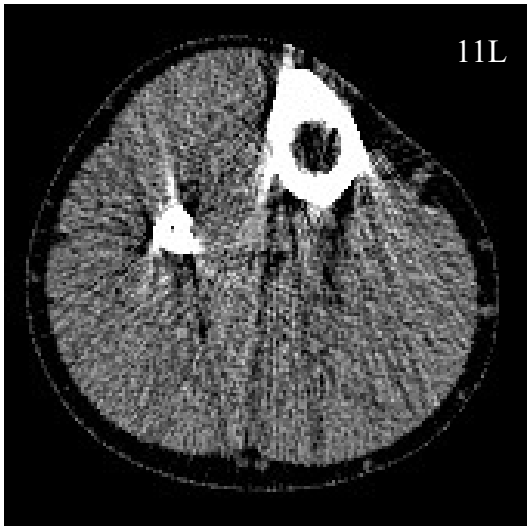
11L

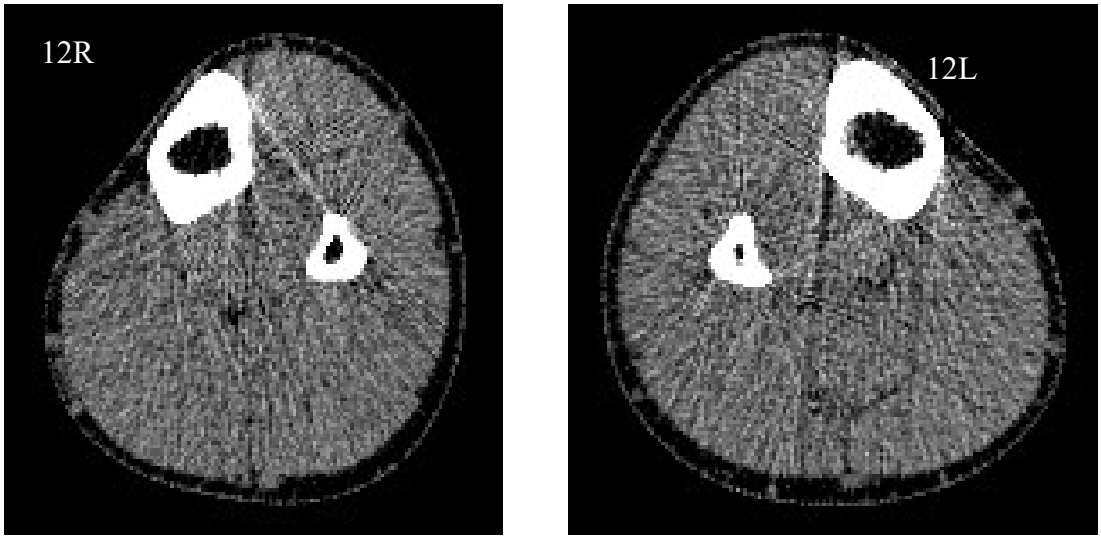

Figure 4.9: Windowed pQCT images for the seven healthy subjects in Group B.

4.3.3 *Texture Analysis of pQCT and MRI Images with a Circular ROI in the Gastrocnemius Muscle Medial Head*

Circular ROI placement within the medial head of the gastrocnemius muscle boundary in pQCT and MRI images is shown in Figure 4.10. Tables 4.1-4.6 display values of the second order statistical parameters (co-occurrence matrix, run length matrix, gradient, autoregressive model and wavelet transform) for both legs of the subjects in Group A (five subjects) and Group C (training group with eight subjects). As previously described, the total of twelve healthy subjects were divided into two groups: a training group of eight subjects (Group C) and test group of four subjects (Group D).

These data were extracted from identical circular ROIs of 228 pixels in area for all texture parameters for both imaging modalities and both legs. The mean, standard deviation and %CV of all texture parameters were calculated and also reference ranges. Values of %CV for pQCT and MRI texture parameters are presented in Figures 4.11-4.16. In general, the data are inconsistent although %CV values for the co-occurrence matrix and wavelet transform are consistently less than 10%, suggesting that these parameters vary less than the others within a normal population.

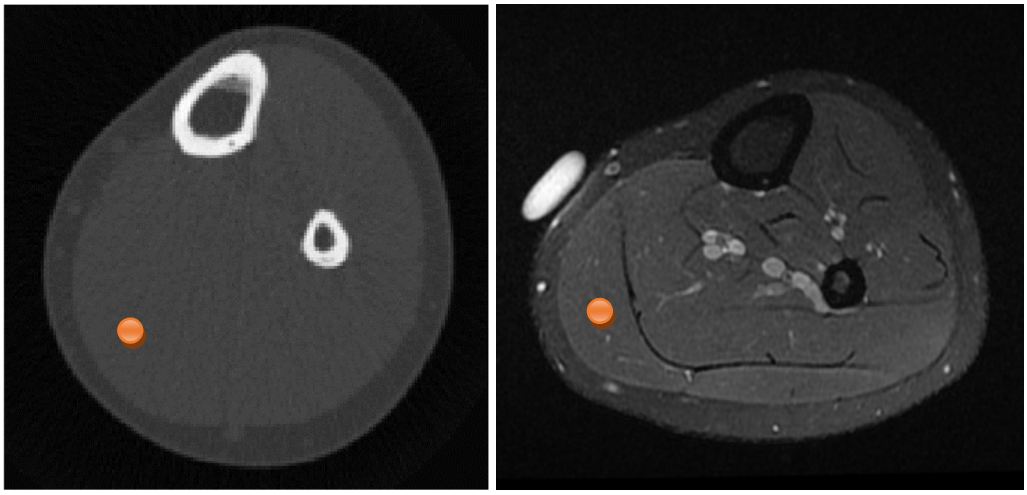

Figure 4.10: pQCT (left) and MRI (right) images with a circular ROI drawn within the gastrocnemius muscle boundary.

Table 4.1: Mean, standard deviation (SD), coefficient of variation (%CV) and reference range (95% CI) for pQCT images of the right leg (Group A) with a circular ROI of area 228 pixels in the medial head of the gastrocnemius muscle.

Texture parameter	Mean	SD	%CV	Reference Range	
Co-occurrence	196963.7300	11279.0600	5.7300	174856.7724	219070.6876
Run length	742.1000	23.3800	3.1500	696.2752	787.9248
Gradient	1437.2900	92.9000	6.4600	1255.2060	1619.3740
AR model	1.2100	0.0400	2.9900	1.1316	1.2884
Wavelet	46324.3100	1619.4900	3.5000	43150.1096	49498.5104

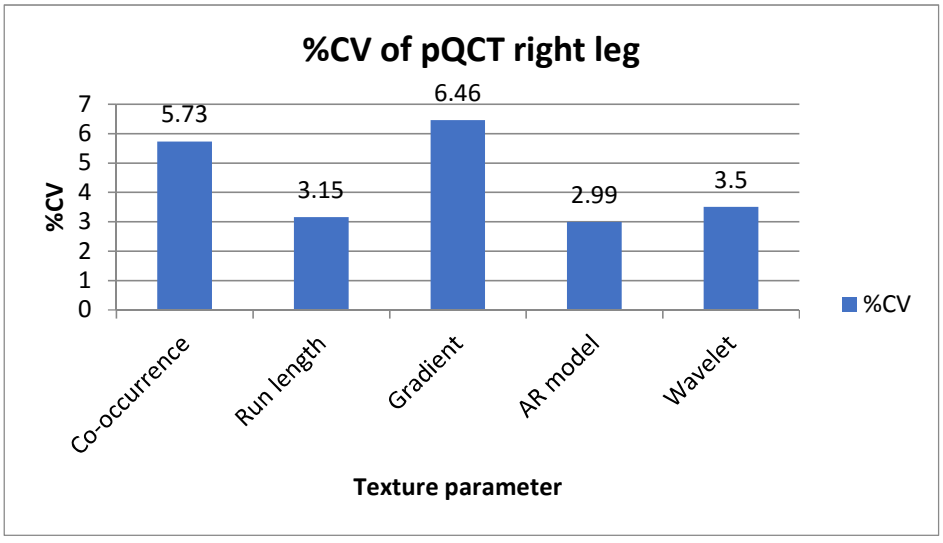

Figure 4.11: The coefficient of variation (%CV) for group A (five subjects) right leg images (pQCT).

Table 4.2: Mean, standard deviation (SD), coefficient of variation (%CV) and reference range (95% CI) for pQCT images of the left leg (Group A) with a circular ROI of area 228 pixels in the medial head of the gastrocnemius muscle.

Texture parameter	Mean	SD	%CV	Reference Range	
Co-occurrence	216838.1900	17318.5700	7.9869	182893.7928	250782.5872
Run length	725.9600	29.3700	4.0457	668.3948	783.5252
Gradient	1451.7800	125.2900	8.6301	1206.2116	1697.3484
AR model	1.3600	0.1700	12.5000	1.0268	1.6932
Wavelet	44929.3900	2973.6700	6.6185	39100.9968	50757.7832

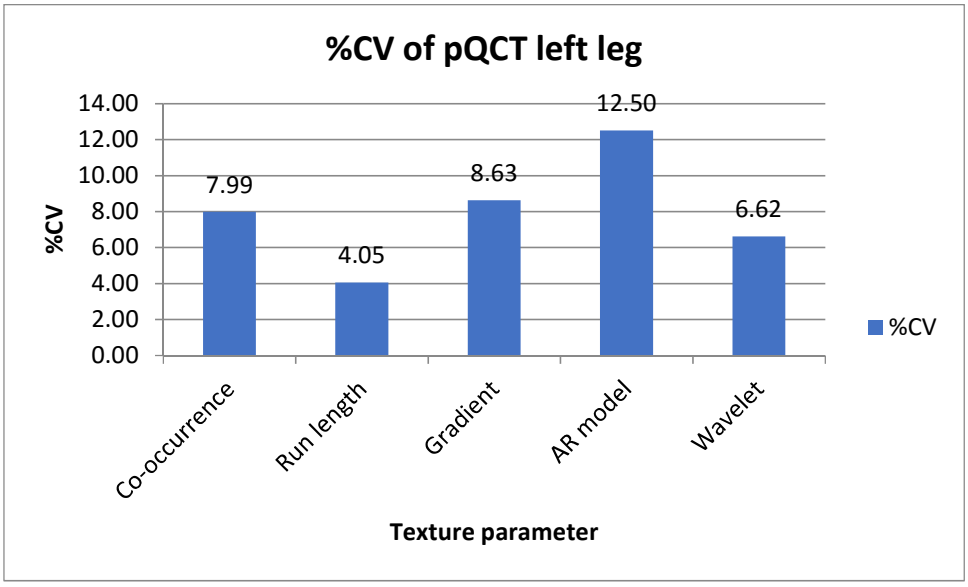

Figure 4.12: The coefficient of variation (%CV) for group A (five subjects) left leg images (pQCT).

Table 4.3: Mean, standard deviation (SD), coefficient of variation (%CV) and reference range (95% CI) for MRI images of the right leg (Group A) with a circular ROI of area 228 pixels in the medial head of the gastrocnemius muscle.

Texture parameter	Mean	SD	%CV	Reference Range	
Co-occurrence matrix	226362.3400	8126.7100	3.5900	210433.9884	242290.6916
Run length	372.8800	67.8700	18.2000	239.8548	505.9052
Gradient	1774.7600	50.8600	2.8700	1675.0744	1874.4456
AR model	1.1200	0.1400	12.9300	0.8456	1.3944
Wavelet	45355.9700	640.4000	1.4100	44100.7860	46611.1540

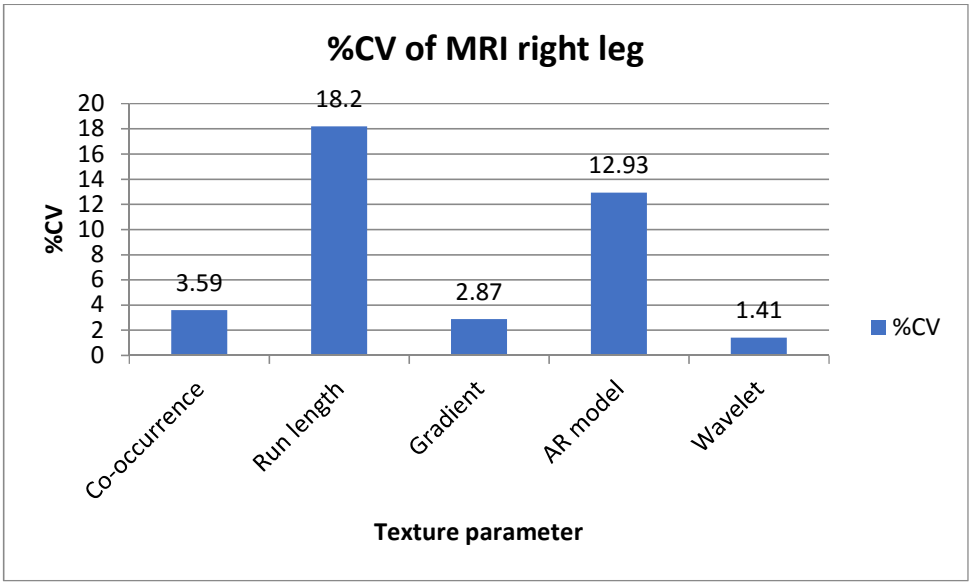

Figure 4.13: The coefficient of variation (%CV) for group A (five subjects) right leg (MRI) images.

Table 4.4: Mean, standard deviation (SD), coefficient of variation (%CV) and reference range (95% CI) for MRI images of the left leg (Group A) with a circular ROI of area 228 pixels in the medial head of the gastrocnemius muscle.

Texture parameter	Mean	SD	%CV	Reference Range	
Co-occurrence matrix	226097.7790	9103.9614	4.0266	208254.0148	243941.5433
Run length	382.8073	59.7379	15.6052	265.7211	499.8935
Gradient	1735.8640	25.6558	1.4780	1685.5785	1786.1495
AR model	1.1383	0.4825	42.3888	0.1926	2.0841
Wavelet transform	45848.8720	481.1888	1.0495	44905.7419	46792.0021

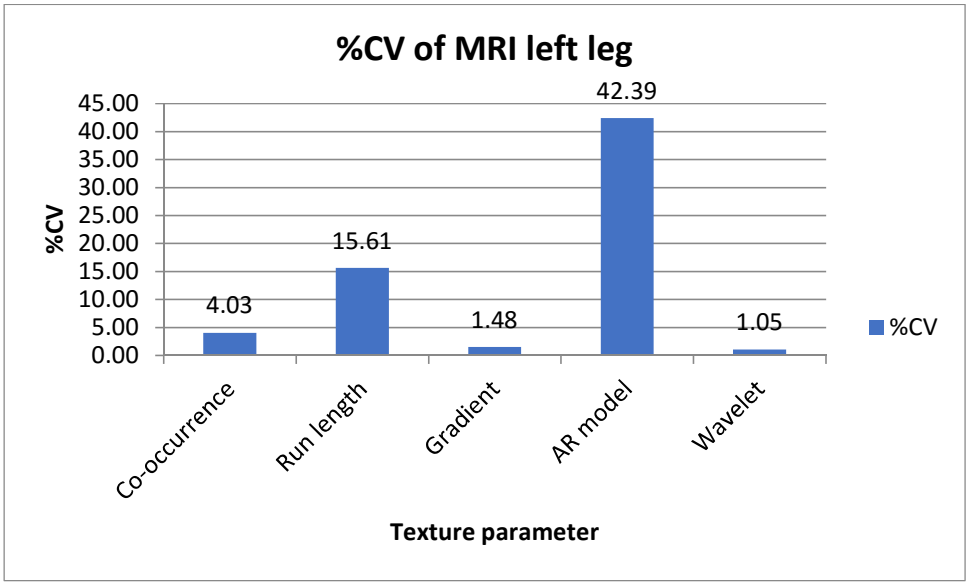

Figure 4.14: The coefficient of variation (%CV) for group A (five subjects) left leg (group A) (MRI) images.

Table 4.5: Mean, standard deviation (SD), coefficient of variation (%CV) and reference range (95% CI) for pQCT images of the right leg (Group C) with a circular ROI of area 228 pixels in the medial head of the gastrocnemius muscle.

Texture parameter	Mean	SD	%CV	Reference Range	
Co-occurrence matrix	212515.9123	20253.6044	9.5304	172818.8477	252212.9768
RL matrix	736.1938	17.1806	2.3337	702.5197	769.8678
Gradient	1748.2420	451.1100	25.8036	864.0664	2632.4177
AR model	1.2952	0.0655	5.0537	1.1669	1.4235
Wavelet transform	45646.2343	2492.5020	5.4605	40760.9304	50531.5381

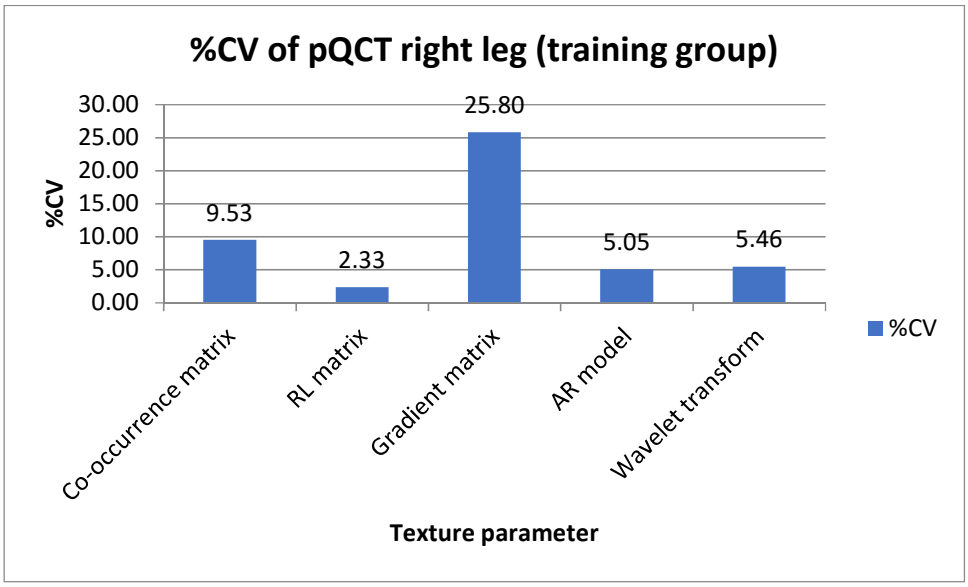

Figure 4.15: The coefficient of variation (%CV) for Group C (training group - eight subjects) right leg images (pQCT).

Table 4.6: Mean, standard deviation (SD), coefficient of variation (%CV) and reference range (95% CI) for pQCT images of the left leg (Group C) with a circular ROI of area 228 pixels in the medial head of the gastrocnemius muscle.

Texture parameter	Mean	SD	%CV	Reference Range	
Co-occurrence matrix	208295.2124	17942.0194	8.6137	173128.8544	243461.5704
RL matrix	736.0037	28.1001	3.8179	680.9276	791.0799
Gradient	1786.5818	356.0717	19.9303	1088.6814	2484.4823
AR model	1.3592	0.1559	11.4730	1.0535	1.6648
Wavelet transform	45018.4939	2633.0791	5.8489	39857.6588	50179.3289

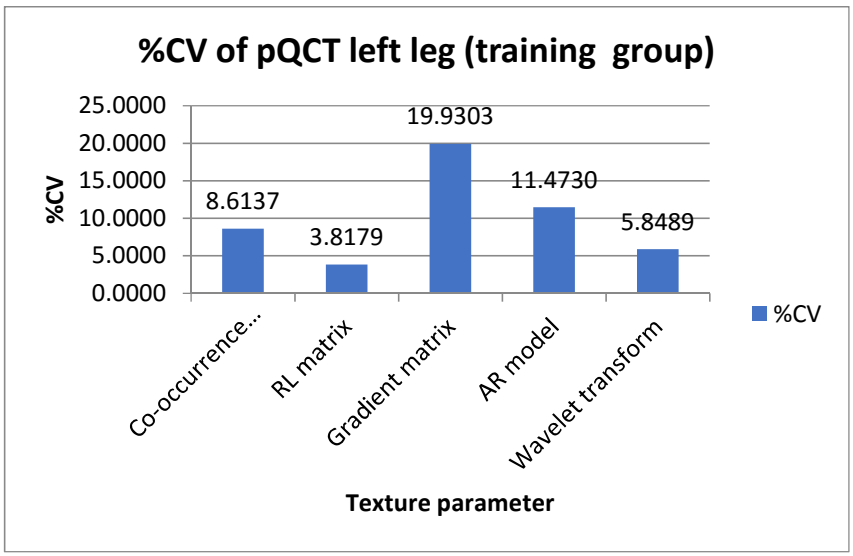

Figure 4.16: The coefficient of variation (%CV) for Group C (training group - eight subjects) left leg images (pQCT).

The pQCT texture parameter reference ranges obtained with a circular ROI (area 228 pixels) for the right and left legs of the training group (Group C) are collated in Table 4.7.

Table 4.7: Texture feature reference ranges (95% CI) for Group C (training group - 8 subjects) for pQCT images of right leg (RL) and left (LL) leg with a circular ROI of area 228 pixels in the medial head of the gastrocnemius muscle.

	Reference Range			
	(pQCT RL)		(pQCT LL)	
Texture parameter	Lower	Upper	Lower	Upper
Co-occurrence matrix	172818.8477	252212.9768	173128.8544	243461.5704
RL matrix	702.5197	769.8678	680.9276	791.0799
Gradient	864.0664	2632.4177	1088.6814	2484.4823
AR model	1.1669	1.4235	1.0535	1.6648
Wavelet	40760.9304	50531.5381	39857.6588	50179.3289

Tables 4.8 and 4.9 depict the results of right and left leg texture analysis respectively for pQCT images of the test group of four subjects (Group D).

Table 4.8: Extracted texture parameters for right leg pQCT images of the 4 individual subjects in Group D (test group) obtained with a circular ROI of area 228 pixels.

	Subject			
Texture parameter	1	2	3	4
Co-occurrence matrix	220664.8761	225876.9573	192754.4182	205257.5653
RL matrix	723.3666	738.7687	739.0697	704.7604
Gradient	1860.2494	1859.9365	1516.7123	1723.4202
AR model	1.2275	1.1818	1.2254	1.1779
Wavelet transform	41912.7624	41628.6811	42793.8804	46761.6444

Table 4.9: Extracted texture parameters for left leg pQCT images of the 4 individual subjects in Group D (test group) obtained with a circular ROI of area 228 pixels.

	Subject			
Texture parameter	1	2	3	4
Co-occurrence matrix	227127.6080	194684.0637	211149.9928	224270.2726
RL matrix	744.4180	736.8252	775.2872	697.9693
Gradient	1912.4925	1580.3136	1805.6740	2447.1970
AR model	1.4694	1.2877	1.3640	1.0700
Wavelet transform	42553.2838	46957.3226	43366.7547	40437.3186

The results from the test group of 4 normal subjects (Group D) were used to validate the reference ranges derivded from the training group of 8 normal subjects (Group C). Figures 4.17-4.26 show individual values of texture parameters for the 4 subjects in the test group plotted against a background of reference ranges (95% CIs) derived from the 8 subjects in the training group. Texture features were extracted with a circular ROI placed in the medial head of the gastrocnemius muscle. All test results fell within the reference ranges.

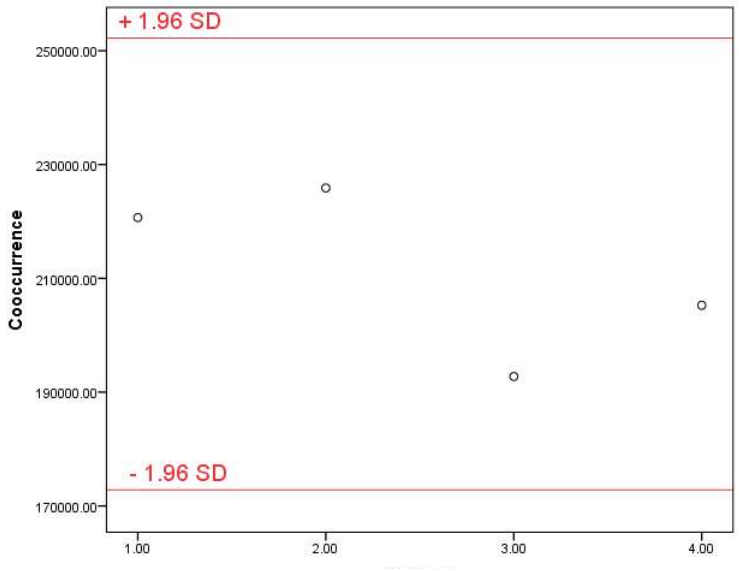

Figure 4.17: Right leg gastrocnemius muscle pQCT co-occurrence matrix values of 4 individuals in the test group (Group D) against a reference range derived from the training group of eight subjects (Group C) with a circular ROI of area 228 pixels.

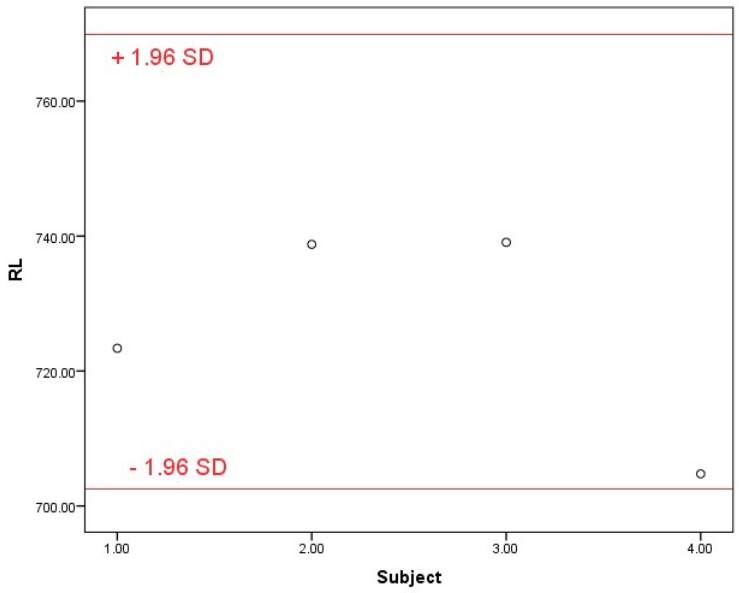

Figure 4.18: Right leg gastrocnemius muscle pQCT RL matrix values of 4 individuals in the test group (Group D) against a reference range derived from the training group of eight subjects (Group C) with a circular ROI of area 228 pixels.

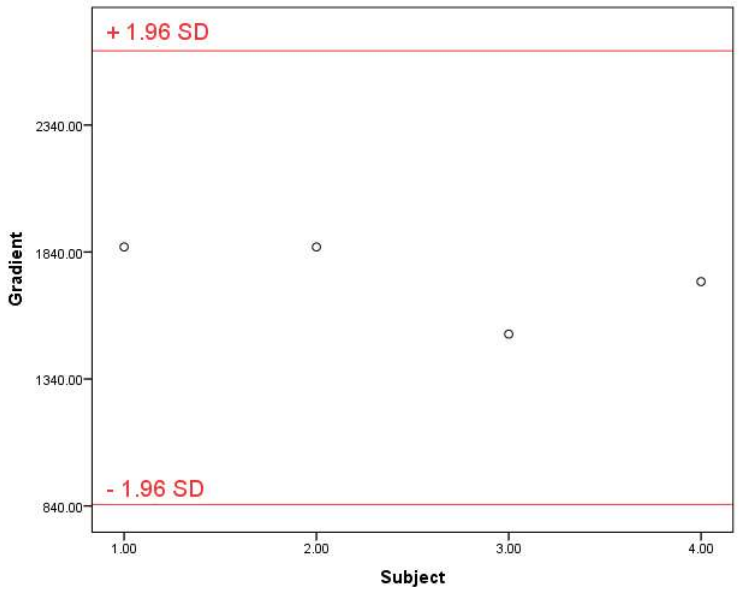

Figure 4.19: Right leg gastrocnemius muscle pQCT gradient values of 4 individuals in the test group (Group D) against a reference range derived from the training group of eight subjects (Group C) with a circular ROI of area 228 pixels.

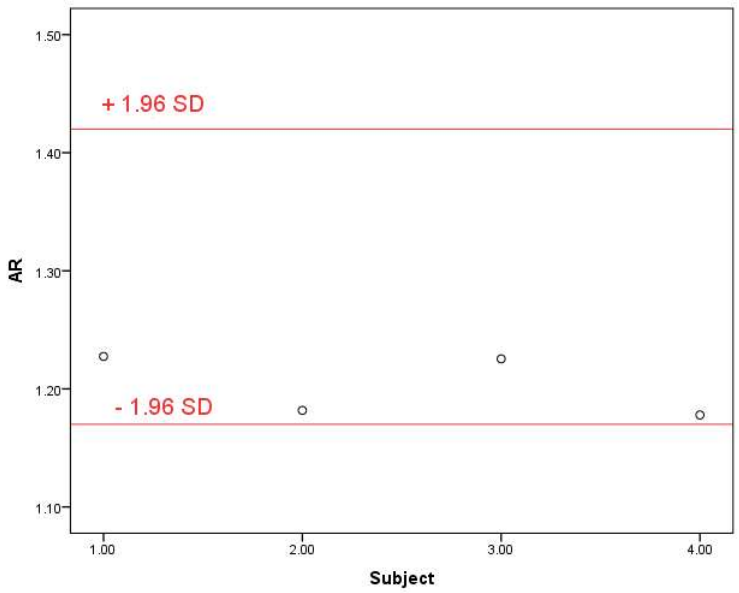

Figure 4.20: Right leg gastrocnemius muscle pQCT AR model values of 4 individuals in the test group (Group D) against a reference range derived from the training group of eight subjects (Group C) with a circular ROI of area 228 pixels.

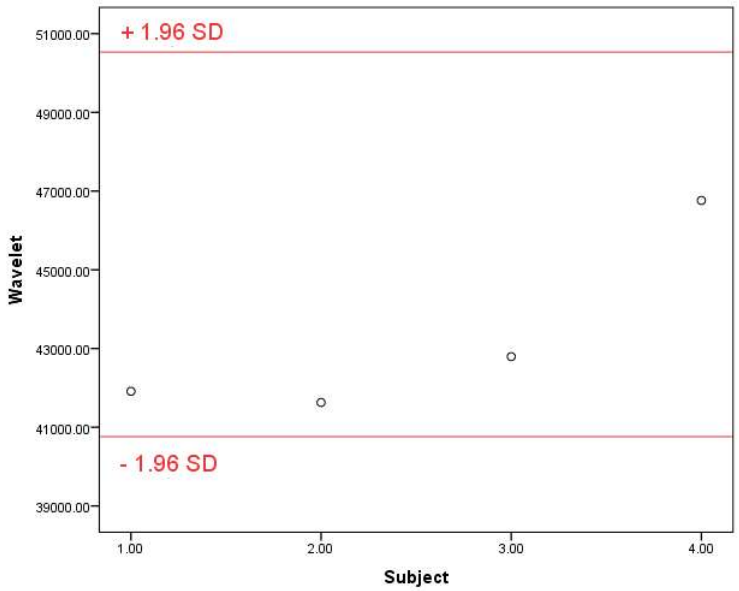

Figure 4.21: Right leg gastrocnemius muscle pQCT wavelet transform values of 4 individuals in the test group (Group D) against a reference range derived from the training group of eight subjects (Group C) with a circular ROI of area 228 pixels.

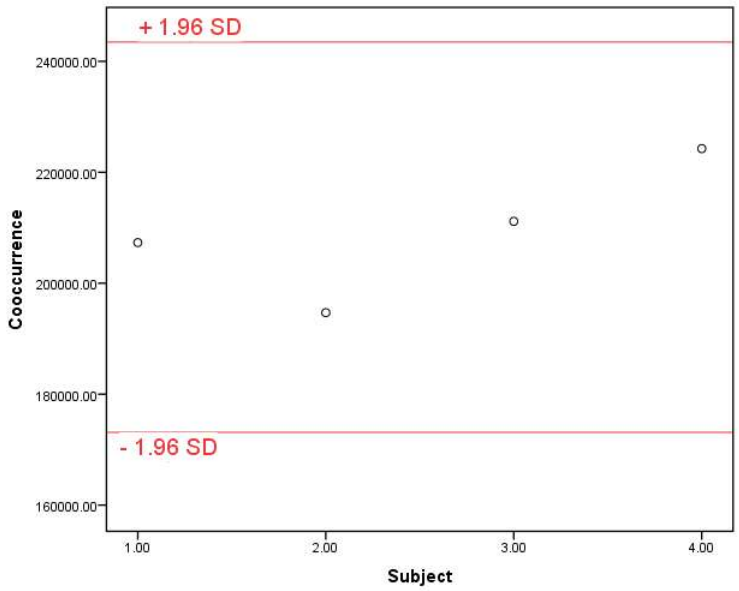

Figure 4.22: Left leg gastrocnemius muscle pQCT co-occurrence matrix values of 4 individuals in the test group (Group D) against a reference range derived from the training group of eight subjects (Group C) with a circular ROI of area 228 pixels.

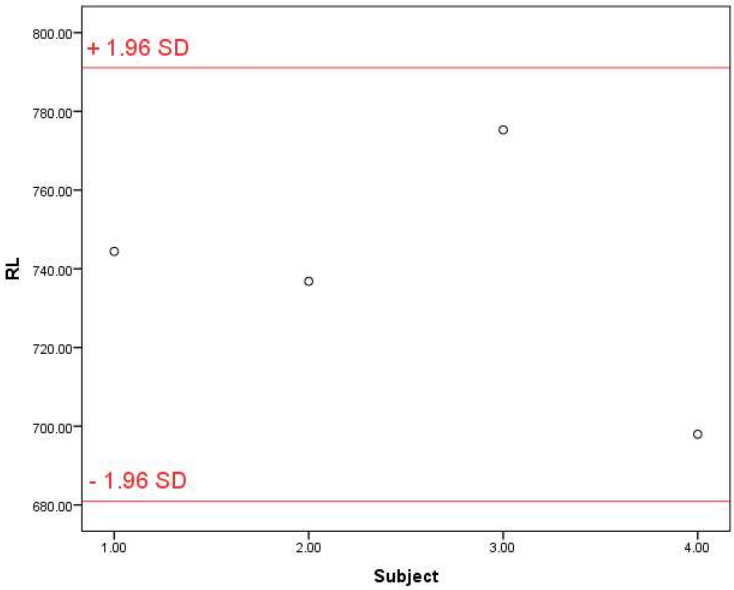

Figure 4.23: Left leg gastrocnemius muscle pQCT RL matrix values of 4 individuals in the test group (Group D) against a reference range derived from the training group of eight subjects (Group C) with a circular ROI of area 228 pixels.

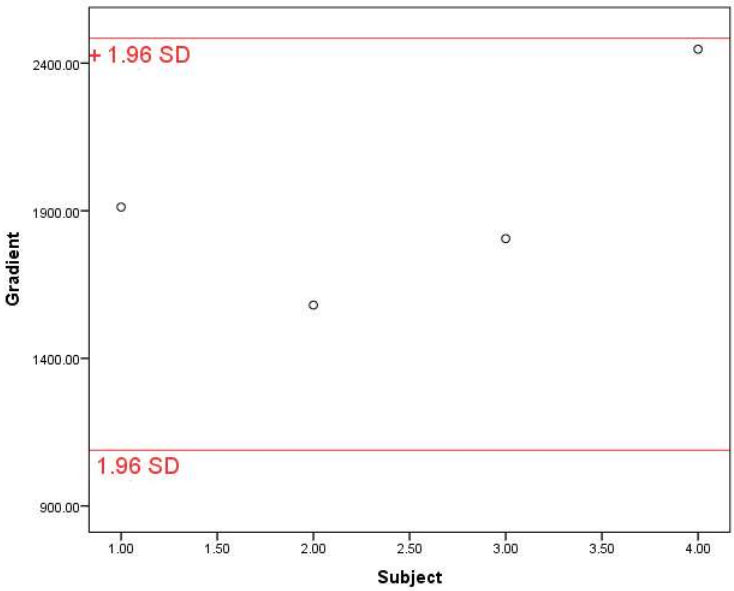

Figure 4.24: Left leg gastrocnemius muscle pQCT gradient values of 4 individuals in the test group (Group D) against a reference range derived from the training group of eight subjects (Group C) with a circular ROI of area 228 pixels).

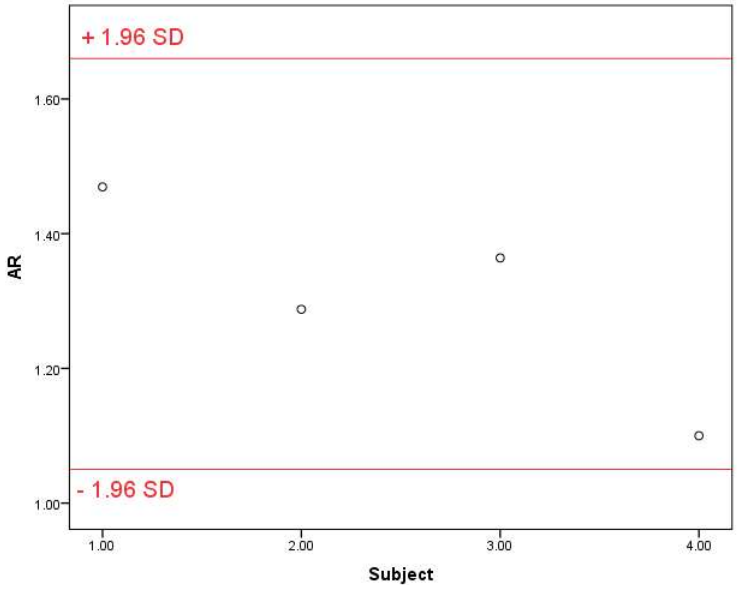

Figure 4.25: Left leg gastrocnemius muscle pQCT AR model values of 4 individuals in the test group (Group D) against a reference range derived from the training group of eight subjects (Group C) with a circular ROI of area 228 pixels.

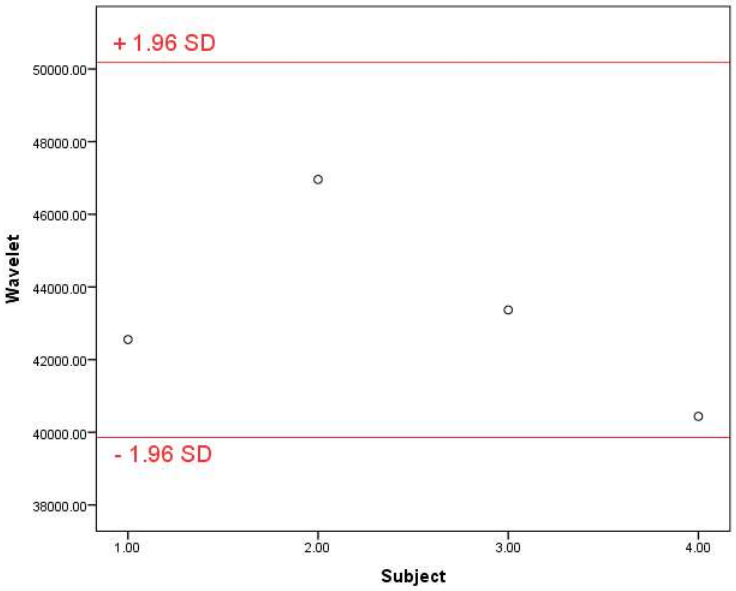

Figure 4.26: Left leg gastrocnemius muscle pQCT wavelet transform values of 4 individuals in the test group (Group D) against a reference range derived from the training group of eight subjects (Group C) with a circular ROI of area 228 pixels.

4.3.4 Texture Analysis of MRI and pQCT Images of the Whole Gastrocnemius Muscle Medial Head

The MRI and pQCT images were also analysed using a ROI that covered the whole of the medial head of the gastrocnemius muscle, but avoiding the muscle boundary, as shown in Figure 4.3. The reference ranges (95% CIs) calculated for the initial group of 5 healthy subjects (Group A) are shown in Tables 4.10 and 4.11. The RL matrix ranges for both modalities were very large because this texture feature is dependent on ROI area (Chapter 3).

Table 4.10: Texture parameter reference ranges (95% CIs) for MRI images of the right leg (RL) and left leg (LL) in Group A (5 subjects) for ROI covering the whole of the gastrocnemius muscle medial head.

	Reference Range			
	(MRI RL)		(MRI LL)	
Texture parameter	Lower	Upper	Lower	Upper
Co-occurrence matrix	136783.53	238761.00	166800.45	207498.69
RL matrix	1212.99	16028.89	2673.64	16091.57
Gradient	1472.13	2721.97	463.05	3354.89
AR model	1.42	1.66	1.24	1.80
Wavelet transform	46851.35	50251.37	43014.86	49774.03

Table 4.11: Texture parameter reference ranges (95% CIs) for pQCT images of the right leg (RL) and left leg (LL) in Group A (5 subjects) for ROI covering the whole of the gastrocnemius muscle medial head.

	Reference Range			
	(pQCT RL)		(pQCT LL)	
Texture parameter	Lower	Upper	Lower	Upper
Co-occurrence matrix	156340.41	192884.92	152688.57	221574.40
RL matrix	9162.93	19599.62	8189.10	23165.63
Gradient	841.97	1345.86	671.71	1660.70
AR model	1.26	1.33	1.25	1.44
Wavelet transform	43299.19	46546.55	40266.71	52195.50

As for the analysis with the circular ROI, pQCT reference ranges were also calculated for the training group of 8 subjects (Group C); these are presented in Table 4.12.

Table 4.12: Texture parameter reference ranges (95% CIs) for pQCT images of the right leg (RL) and left leg (LL) for the training group of 8 subjects (Group C) with a ROI covering the whole of the gastrocnemius muscle medial head.

	Reference Range			
	(pQCT RL)		(pQCT LL)	
Texture parameter	Lower	Upper	Lower	Upper
Co-occurrence matrix	158753.8442	190275.6748	155360.4633	211758.5826
RL matrix	9003.2953	18173.1211	7777.7862	21128.3846
Gradient	875.0054	1308.9046	720.3963	1557.3276
AR model	1.2031	1.3402	1.1671	1.4373
Wavelet transform	43193.7518	46522.7376	40212.5438	50612.9296

Table 4.13 depicts the results of texture analysis in the test group of four subjects (Group D) for right leg pQCT images with a ROI covering the whole of the medial head of the gastrocnemius muscle. In Figures 4.27-4.30, the texture parameters are plotted against a background of the corresponding reference range (95% CI) derived from the training group of eight (Group C). There were large variations in muscle area and therefore in ROI area. Thus RL matrix values were excluded because of their dependence on ROI size. All the remaining test texture feature values fell within the reference ranges.

Table 4.13: Extracted texture parameters for pQCT images of the right leg (RL) for the test group of 4 subjects (Group D) with a ROI covering the whole of the gastrocnemius muscle medial head.

	Subject RL			
Texture parameter	1	2	3	4
Co-occurrence matrix	164277.9813	184612.1735	181624.8234	178136.4129
RL matrix	9371.1839	12843.7439	14258.8439	13578.8103
Gradient	1072.7342	1178.9727	1273.531	1092.6732
AR model	1.261	1.2381	1.2328	1.2078
Wavelet transform				

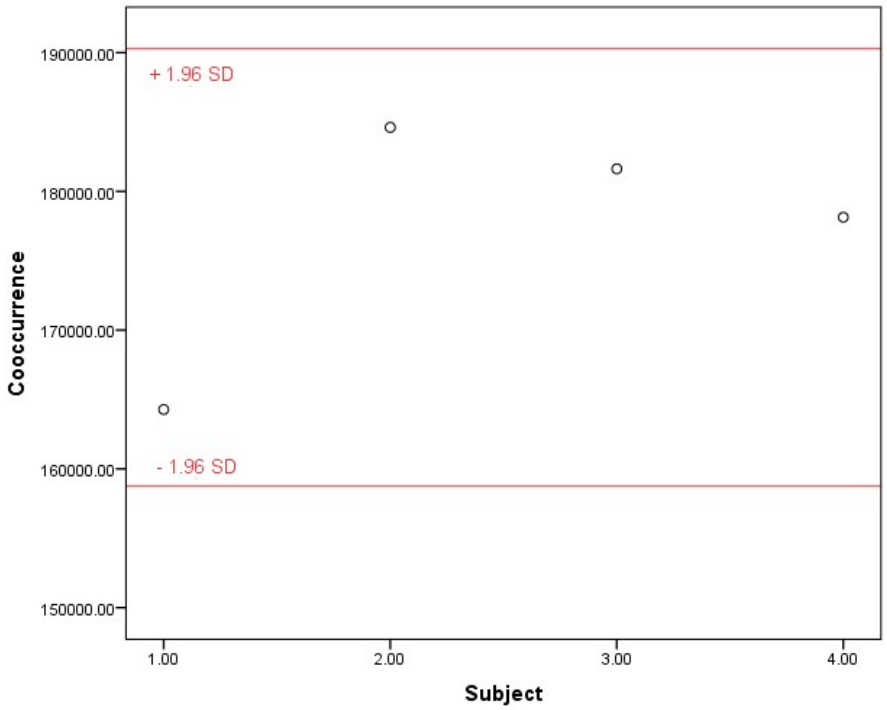

Figure 4.27: Right leg gastrocnemius muscle pQCT co-occurrence matrix values of four individuals in the test group (Group D) against a reference range derived from the training group of eight subjects (Group C) with a ROI over the whole of the medial head.

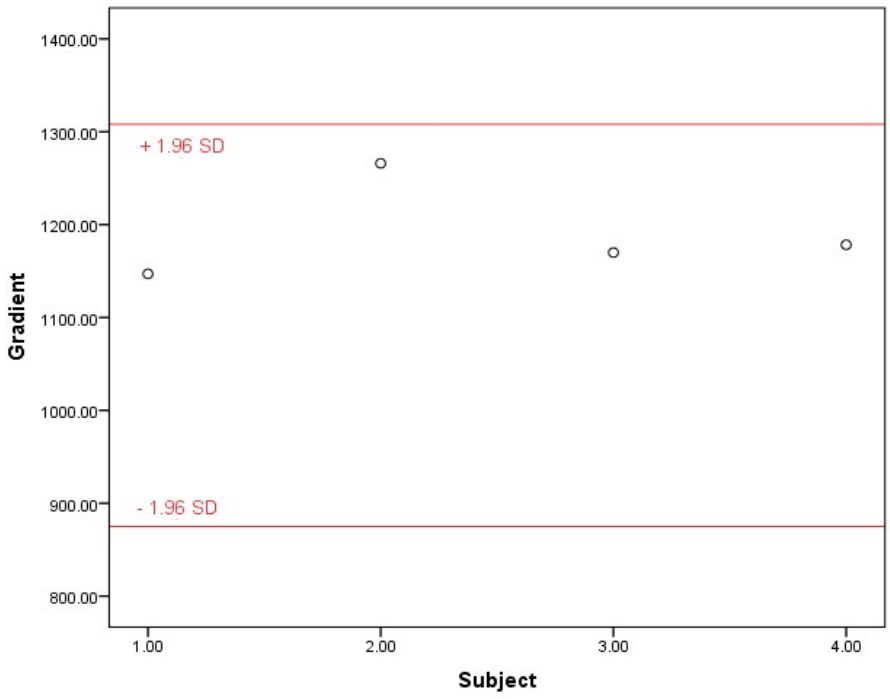

Figure 4.28: Right leg gastrocnemius muscle pQCT gradient values of four individuals in the test group (Group D) against a reference range derived from the training group of eight subjects (Group C) with a ROI over the whole of the medial head.

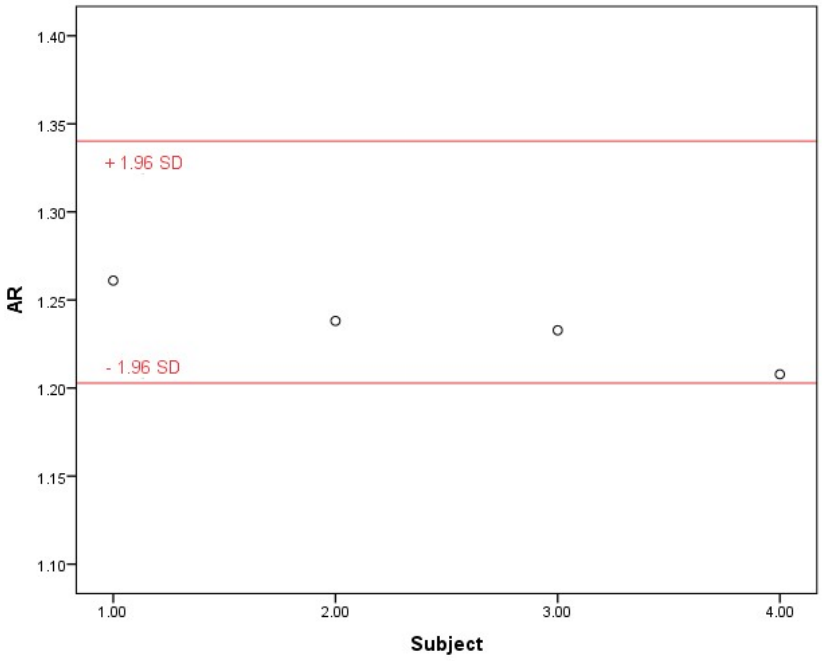

.

Figure 4.29: Right leg gastrocnemius muscle pQCT AR model values of four individuals in the test group (Group D) against a reference range derived from the training group of eight subjects (Group C) with a ROI over the whole of the medial head.

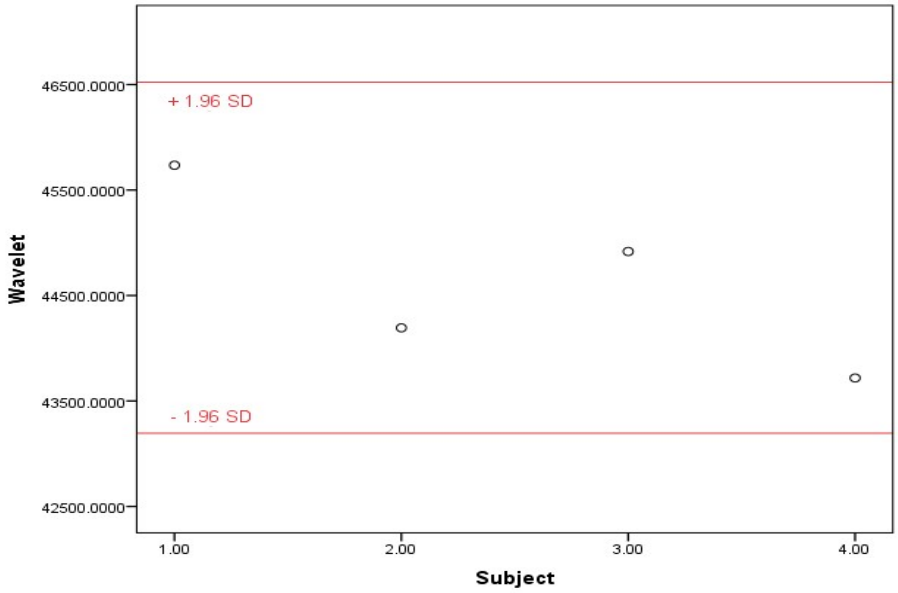

Figure 4.30: Right leg gastrocnemius muscle pQCT wavelet transform values of four individuals in the test group (Group D) against a reference range derived from the training group of eight subjects (Group C) with a ROI over the whole of the medial head.

Table 4.14 and Figures 4.31-4.34 show the corresponding data for texture parameter values extracted from left leg pQCT images with a ROI covering the

whole muscle. Again, RL marix was not plotted and all the remaining test texture feature values fell within the reference ranges.

Table 4.14: Extracted texture parameters for pQCT images of the left leg (LL) for the test group of 4 subjects (Group D) with a ROI covering the whole of the gastrocnemius muscle medial head.

	Subject LL			
Texture parameter	1	2	3	4
Co-occurrence matrix	171267.1784	184612.1735	184478.1426	171842.5633
RL matrix	9783.2987	11765.4581	13926.1274	12837.8115
Gradient	1146.9586	1265.9182	1169.924	1178.3091
AR model	1.2580	1.2172	1.2781	1.2258
Wavelet transform	44654.8148	45012.7581	43691.9654	44192.7139

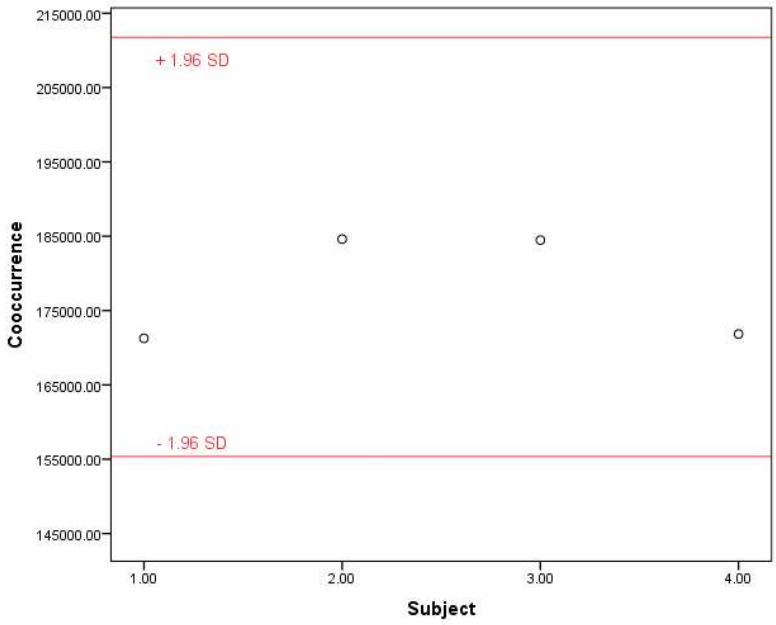

Figure 4.31: Left leg gastrocnemius muscle pQCT co-occurrence matrix values of four individuals in the test group (Group D) against a reference range derived from the training group of eight subjects (Group C) with a ROI over the whole of the medial head.

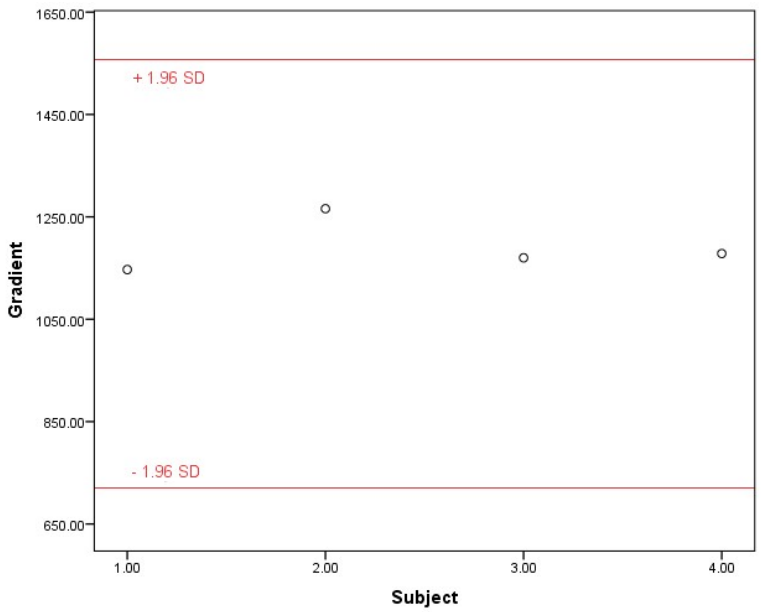

Figure 4.32: Left leg gastrocnemius muscle pQCT gradient values of four individuals in the test group (Group D) against a reference range derived from the training group of eight subjects (Group C) with a ROI over the whole of the medial head.

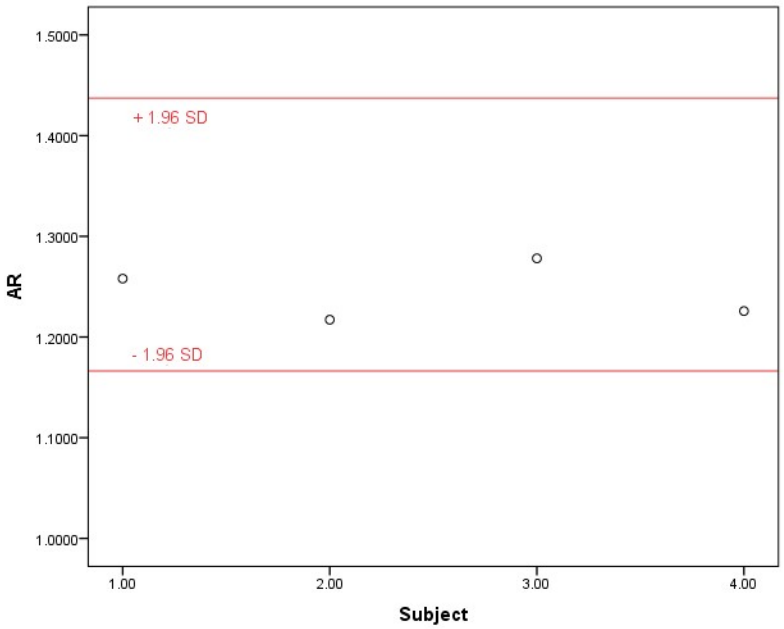

Figure 4.33: Left leg gastrocnemius muscle pQCT AR model values of four individuals in the test group (Group D) against a reference range derived from the training group of eight subjects (Group C) with a ROI over the whole of the medial head.

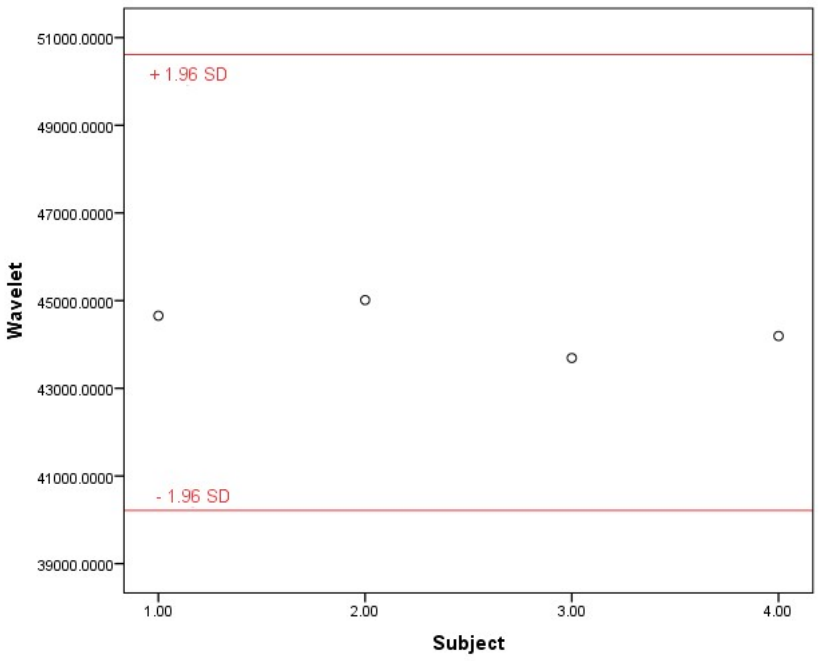

Figure 4.34: Left leg gastrocnemius muscle pQCT wavelet transform values of four individuals in the test group (Group D) against a reference range derived from the training group of eight subjects (Group C) with a ROI over the whole of the medial head.

As part of the process of validating the reference ranges, the data for the entire group of 12 subjects were analysed to look for (1) dependence of texture values on leg laterality (left or right) and (2) variation in overall texture and in values of individual texture parameters across the subjects, bearing in mind the small sample size. It was found that leg laterality had no significant effect on overall texture when tested across subjects ($p = 0.456$) by regarding the leg as a within-person variable.

For variation across subjects, a Repeated Measures ANOVA showed that the sphericity assumption was violated; Mauchly's test was significant ($p<0.001$). Therefore the Greenhouse-Geisser adjusted F statistic was calculated. This showed that the overall mean texture parameters did not differ significantly between the subjects, ($F(1.2,5.9) = 2.93$, $p = 0.138$) and that the interaction between subjects and individual texture parameters was not significant as well ($F(4.7,5.9) = 1.2$, $p = 0.240$). Furthermore, values of the overall mean of the five texture parameters did not show any significant linear (incremental incrase) or cubic (rise and fall) variation between subjects regarded as repeated units of analysis ($F(1,5) = 0.999$, $p = 0.366$ and $F(1,5) =$

0.211, p = 0.922 respectively). Thus these 12 subjects did not differ in their overall texture features and none of their individual texture parameters values differed significantly from the mean value.

As previously described, an initial group of five healthy subjects (group A) were recruited for pQCT scanning, followed by seven additional healthy subjects (Group B). Subsequently, eight of the total of 12 subjects were assigned to a training group (Group C) and the remaining four to a test group (Group D) as shown in Figure 4.1. As a result of the validation of reference ranges derived for the training group with texture values from the test group, data from all 12 subjects were combined to give a more reliable set of reference ranges as shown in Table 4.15.

Table 4.15: Texture parameter reference ranges (95% CIs) for pQCT images of the right leg (RL) and left leg (LL) for the combined group of 12 subjects (Group A and Group B) with a ROI covering the whole of the gastrocnemius muscle medial head.

	Reference Range			
	(pQCT RL)		(pQCT LL)	
Texture parameter	Lower	Upper	Lower	Upper
Co-occurrence matrix	176811.16	230041.17	177885.41	226839.22
RL matrix	691.49	752.52	682.14	766.77
Gradient	1020.86	2117.21	1149.19	2189.17
AR model	1.04	3.31	1.07	3.45
Wavelet transform	39722.50	47476.44	39226.75	47124.76

4.3.5 *Comparison of Texture Parameters extracted from Left and Right Leg Images acquired by MRI and pQCT*

Tables 4.16 and 4.17 show paired t-test p-values for differences in texture features between images of the left and right legs acquired by both modalities for the five subjects in Group A. A circular ROI of area 228 pixels was used for texture analysis Section 4.3.3). No significant difference in texture parameter values between the left

and right medial gastrocnemius muscle were found in either modality, indicating that the muscle of the right leg has similar texture to that of the left leg.

Table 4.16: Paired t-test p-values for second order texture parameters extracted from MRI images of the left and right legs in a group of 5 healthy subjects (Group A) ($p < 0.05$ was considered significant).

Texture Feature	MRI (L & R) p value	Statistical Test
Co-occurrence matrix	0.971	Paired t-test
Run length	0.785	
Gradient	0.977	
AR model	0.925	
Wavelet	0.926	

Table 4.17: Paired t-test p-values for second order texture parameters extracted from pQCT images of the left and right legs in a group of 5 healthy subjects (Group A) ($p < 0.05$ was considered significant)

Texture Feature	pQCT (L & R) p value	Statistical Test
Co-occurrence matrix	0.137	Paired t-test
Run length	0.355	
Gradient	0.215	
AR model	0.164	
Wavelet	0.271	

Table 4.18 depicts p-values for differences between left and right texture features in the combined group of 12 subjects (Group A and Group B) for pQCT images only. None of the differences is significant.

Table 4.18: p-values for second order texture parameters extracted from pQCT images of the left and right legs in a group of 12 healthy subjects (Group A and Group B combined) ($p < 0.05$ was considered significant).

Texture Feature	pQCT (L & R)	Statistical Test
Co-occurrence matrix	0.754	Paired t-test
RL matrix	0.324	Paired t-test
Gradient	0.544	Paired t-test
AR model	0.054	Wilcoxon test
Wavelet	0.689	Paired t-test

4.4 Influence of ROI Position on Texture Parameters Extracted from MRI Images

It has already been shown in Chapter 3 that the position of a circular ROI within the gastrocnemius muscle has no significant effect on extracted texture parameters for pQCT images. This indicated the homogeneity of muscle tissue. The investigation was repeated for right and left leg MRI images using circular ROIs of equal area (350 pixels) placed at five different positions within the boundary of the gastrocnemius muscle medial head as shown in Figure 4.35. Data for the five healthy volunteers in Group A were used and the ROIs were placed in corresponding anatomical locations. Mean values of the second order texture parameters for the right and left leg are shown in Table 4.19 and Table 4.20 respectively.

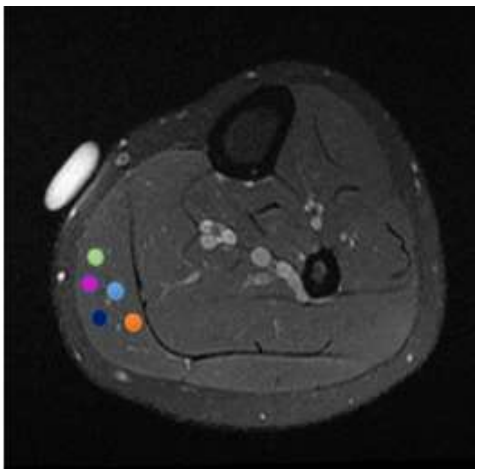

Figure 4.35: MRI image with five circular ROIs at different positions within the gastrocnemius muscle.

Table 4.19: Mean texture parameter values for 5 circular ROI positions within the gastrocnemius muscle on right leg MRI images of 5 healthy subjects (Group A).

Texture Parameter	Position 1	Position 2	Position 3	Position 4	Position 5
Co-occurrence matrix	226072.7800	225024.6100	212500.8400	219723.4156	223519.2461
RL matrix	422.4900	420.4500	390.0700	421.5234	415.7352
Gradient	1821.7300	1739.7300	1749.1900	1762.244	1743.9014
AR model	1.2300	1.2000	1.1000	1.1814	1.1246
Wavelet	43532.1600	46182.5200	44374.2600	45215.2634	44743.1843

Table 4.20: Mean texture parameter values for 5 circular ROI positions within the gastrocnemius muscle on left leg MRI images of 5 healthy subjects (Group A).

Texture Parameter	Position 1	Position 2	Position 3	Position 4	Position 5
Co-occurrence matrix	214392.9700	221010.6300	240120.1300	225279.1643	239602.7185
RL matrix	292.5200	309.7900	317.5100	314.7159	301.915
Gradient	1767.2400	1733.7300	1693.7100	1762.0914	1723.6173
AR model	1.2500	1.2400	1.2400	1.2095	1.2342
Wavelet transform	44935.7200	45792.3600	46238.2700	46023.9163	45928.2753

One-way repeated measures ANOVA (RM-ANOVA) was used to analyse the data for each leg separately in order to test whether any individual texture parameter (co-occurrence matrix, RL matrix, gradient, AR model and wavelet transform) or the overall mean of the five texture parameters varied significantly across the five ROI positions.

For both the right and left legs, RM-ANOVA showed that the overall mean texture value of the five parameters did not differ significantly across the five regions of interest ($F(1,4) = 1$, Wilks' Lambda = 0.2, $p = 0.626$).

When evaluating within-texture parameters (i.e. individual texture values), Mauchly's test of sphericity showed that the assumption of equality of error across the regions was violated for both legs ($p < 0.05$). Therefore, the Greenhouse-Geisser F test was used to adjust the degrees of freedom due to this violation. This test showed that ROI position had no significant effect on individual texture parameters values; for the right leg $F(1.06,4.245) = 1.051$, $p=0.366$, and for the left leg $F(1.001,4.006) = 1.083$, $p=0.357$. This suggests that for both legs, the tissue in the medial head of the gastrocnemius muscle is homogenous on MRI images.

4.5 Assessment of Subject Movement in pQCT Imaging

The combination of a scan acquisition time of several minutes and a somewhat uncomfortable leg clamp means that pQCT images are prone to image degradation as

a result of motion artefacts. Indeed, subject movement represents a practical challenge for satisfactory tomographic imaging with pQCT. This movement could be as subtle as twitches or as obvious as a result of a sneeze or cough.

To investigate this further, a qualitative assessement of subject movement on image quality was performed. Each pQCT image for subjects in Group A and Group B was visually inspected and independently rated by three observers. The assessement was based on the presence of motion artefacts, and the degree to which they affect image quality. The presence of the degree of motion artefact was scored on a scale of 1 to 5, with a score of 1 representing a scan with no movement, 2 very minimal, 3 minimal, 4 moderate and 5 extreme movement. An inter-class correlation coefficient test (ICC) was used to assess consistency between the scores made by the three observers.

4.5.1 Reducing Subject Movement

For a single subject, a knee brace was used in conjunction with the leg clamp to reduce subject movement, as shown in Figure 4.37. The image acquisition protocol was identical to the original protocol previously described. A circular ROI area of 228 pixels was defined in the same position with the gastrocnemius muscle boundary using the MaZda software ROI auto-load feature to assess the effect of the knee brace on computed texture parameters. Texture parameters for the defined ROI were computed as described in Chapter 3. Images acquired with the knee brace were also subjectively assessed by the same three observers.

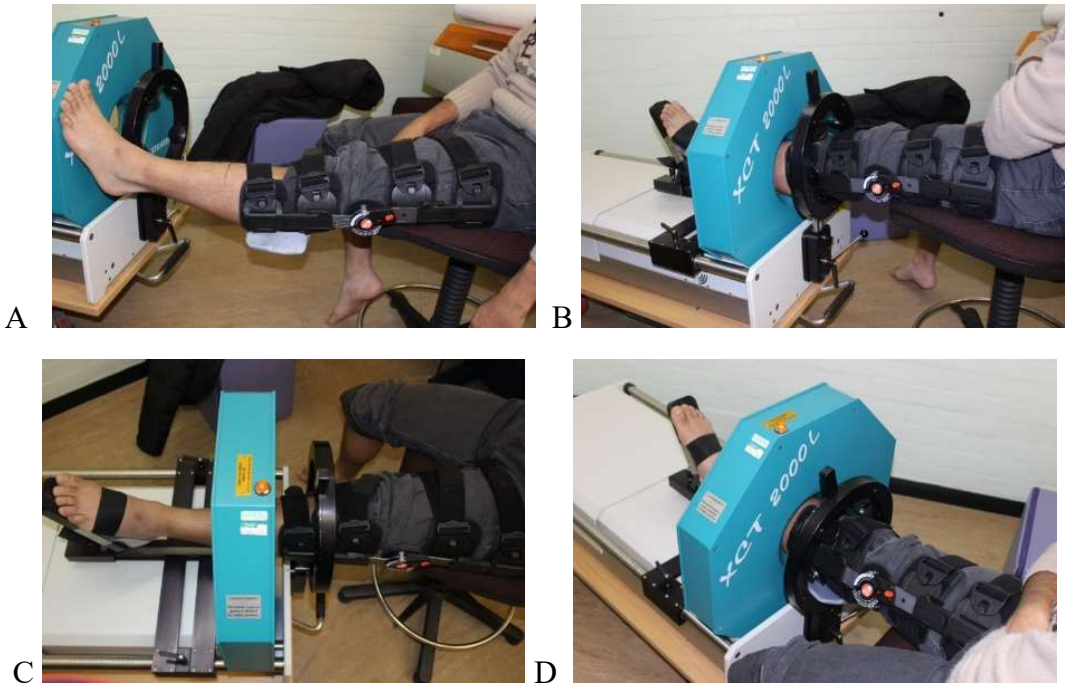

Figure 4.36: A: Fitting the knee brace to the subject's leg. B: Positioning the subject's leg in the scanner gantry for the pQCT scan. C and D: Different views of subject leg positioning.

4.5.2 Results of Assessment of pQCT Images

4.5.2.1 Observers Qualitative Evaluation

Tables 4.21-4.24 present the results of the subjective assessment of movement made by the three observers. These demonstrate the high visual impact of motion artefacts. For the right and left leg images of the five subjects in Group A, the ICC values were 0.882 and 0.920 respectively. For the seven subjects in Group B, the ICC values were 0.901 and 0.909. These data reflect a strong agreement between the scores of all of the observers.

Table 4.21: Subject movement scores and inter-correlation coefficient (ICC) for right leg pQCT images of Group A subjects.

Right Leg					
Image No.	Observer 1	Observer 2	Observer 3	Mean	ICC
1	2	4	4	3.3	0.882*
2	2	4	3	3.0	
3	3	4	3	3.3	
4	2	3	2	2.3	
5	2	3	3	2.6	

*This reflects strong agreement between all the scores.

Table 4.22: Subject movement scores and inter-correlation coefficient (ICC) for left leg pQCT images of Group A subjects.

Left Leg					
Image No.	Observer 1	Observer 2	Observer 3	Mean	ICC
1	3	3	3	3.0	0.920*
2	4	2	2	2.6	
3	3	2	2	2.3	
4	2	2	2	2.0	
5	3	2	3	2.6	

*Indicates strong agreement between all the scores.

Table 4.23: Subject movement scores and inter-correlation coefficient (ICC) for right leg pQCT images of Group B subjects.

Right Leg					
Image No.	Observer 1	Observer 2	Observer 3	Mean	ICC
6	4	4	4	4.0	0.901*
7	4	5	5	4.6	
8	3	3	3	3.0	
9	5	5	5	5.0	
10	2	2	2	2.0	
11	4	5	5	4.6	
12	2	3	3	2.6	

*Indicates strong agreement between all the scores.

Table 4.24: Subject movement scores and inter-correlation coefficient (ICC) for left leg pQCT images of Group B subjects.

Left Leg					
Image No.	Observer 1	Observer 2	Observer 3	Mean	ICC
6	3	2	2	2.3	0.901*
7	5	5	5	5.0	
8	2	3	3	2.6	
9	5	5	5	5.0	
10	3	3	3	3.0	
11	4	3	3	3.3	
12	2	2	2	2.0	

*Indicates strong agreement between all the scores.

4.5.2.2 Effect of Knee Brace on Single Subject pQCT Images and Texture

The images shown in Figure 4.37 represent re-scans of a single subject (subject number 1 from Group A) with the same scan speed and pixel size but using the knee brace to reduce the influence of subject movement on image quality. These may be compared with images 1R and 1L in Figures 4.5 and 4.7. The reduction in artefact is apparent.

The images in Figure 4.37 were also scored by the three observers through visual inspction as before. The results shown in Table 4.25 indicate that the knee brace was very efficient in reducing subject movement. The previous mean scores were 3.3 and 3.0 for the right and left leg respectively (image number 1 in Tables 4.21 and 4.22).

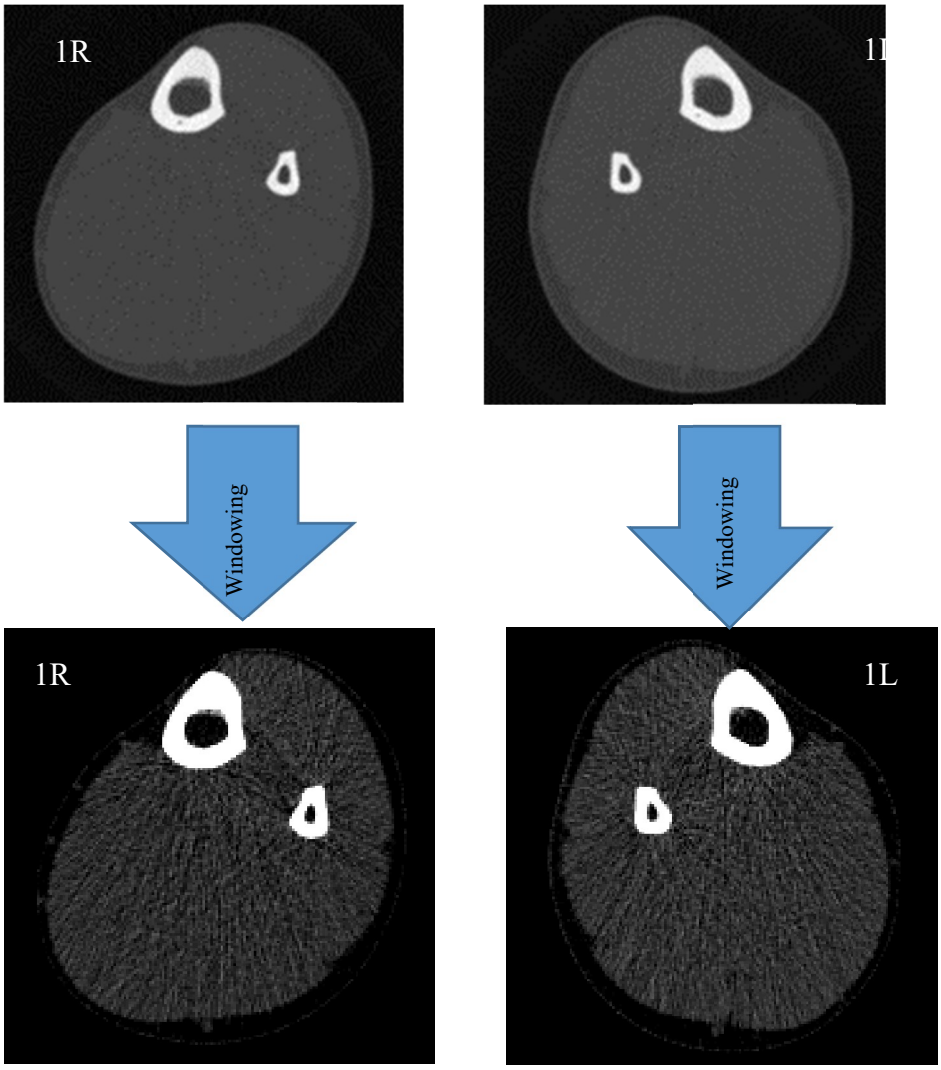

Figure 4.37: pQCT images of the right and left leg of subject number 1 in Group A with the use of a leg brace and the application of image windowing.

Table 4.25: Subject movement scores and inter-correlation coefficient (ICC) for pQCT images of one individual with the use of a knee brace.

Limb Site	Observer 1	Observer 2	Observer 3	Mean	ICC
Right leg	1	1	1	1.0	1
Left leg	1	1	1	1.0	

The pQCT images of the single subject with the knee brace were analysed for texture using a ROI of the same size and position as was used for the original images acquired without the knee brace.

Tables 4.26 and 4.27 show the values of the second order texture parameters with and without the knee brace for the right and left leg respectively. The tables also show the mean values and percentage differences; the latter are illustrated in Figures 4.38 and 4.39.

Table 4.26: Comparison of pQCT texture parameters the right leg of a single subject with and without a knee brace (KB), with mean values and % difference.

Texture Parameter	Right Leg with KB	Right Leg without KB	Mean	% Difference
Co-occurrence Matrix	211291.08	200634.75	205962.91	-5.17
RL Matrix	782.69	727.42	755.05	-7.32
Gradient	1451.00	1388.07	1419.54	-4.43
AR Model	1.11	1.23	1.17	9.92
Wavelet	45047.91	46138.53	45593.22	2.39

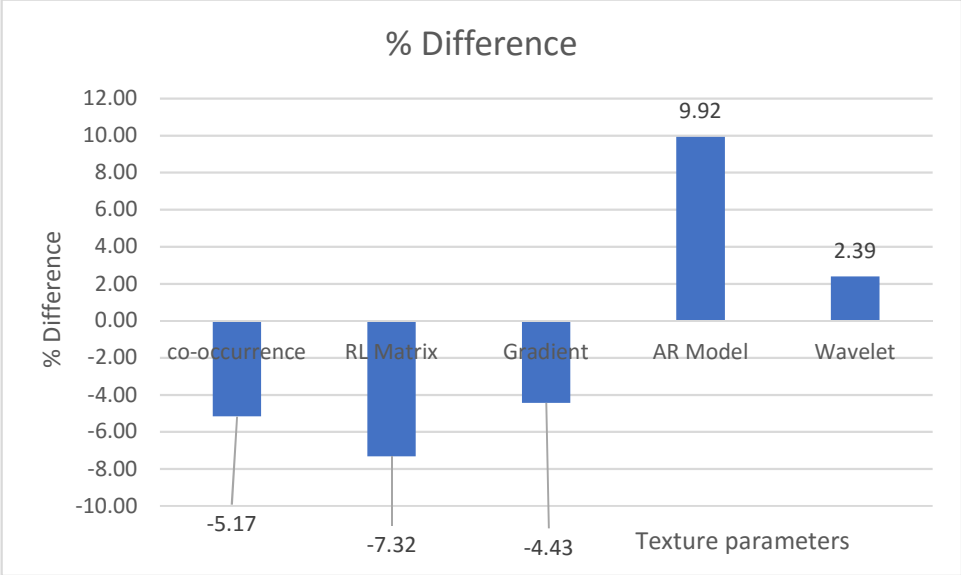

Figure 4.38: The % difference between pQCT texture parameter values of the right leg of a single subject without and with a knee brace.

Table 4.27: Comparison of pQCT texture parameters of the left leg of a single subject with and without a knee brace (KB), with mean values and % difference.

Texture Parameter	Left Leg with KB	Left Leg without KB	Mean	% Difference
Co-occurrence Matrix	196670.40	232007.17	214338.78	16.49
RL matrix	770.79	741.42	756.11	-3.88
Gradient	1383.76	1423.69	1403.72	2.84
AR model	1.10	1.09	1.10	-0.59
Wavelet	46243.48	42553.28	44398.38	-8.31

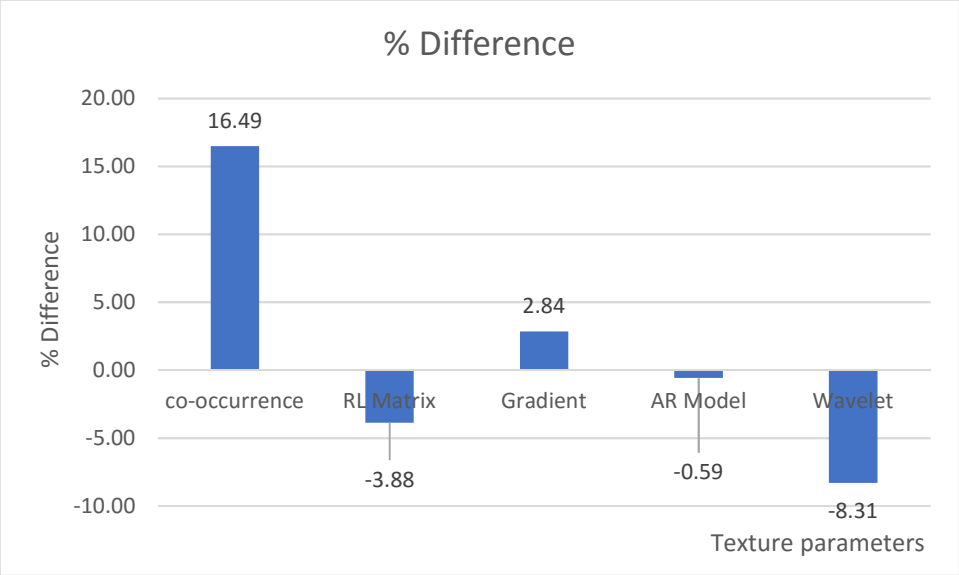

Figure 4.39: The % difference between pQCT texture parameter values of the left leg of a single subject without and with a knee brace.

Tables 4.28 and 4.29 show the values of the second order texture parameters for the right and left leg without and with the knee brace. Again, the tables also show the mean values and percentage differences with the latter being illustrated in Figures 4.40 and 4.41.

Table 4.28: Comparison of pQCT texture parameters of the right and left legs of a single subject without a knee brace (KB), with mean values and % difference.

Texture Parameter	Right Leg without KB	Left Leg without KB	Mean	% Difference
Co-occurrence Matrix	200634.75	232007.17	216320.96	14.50
RL Matrix	727.42	741.42	734.42	1.91
Gradient	1388.07	1423.69	1405.88	2.53
AR Model	1.23	1.09	1.16	-11.57
Wavelet	46138.53	42553.28	44345.91	-8.08

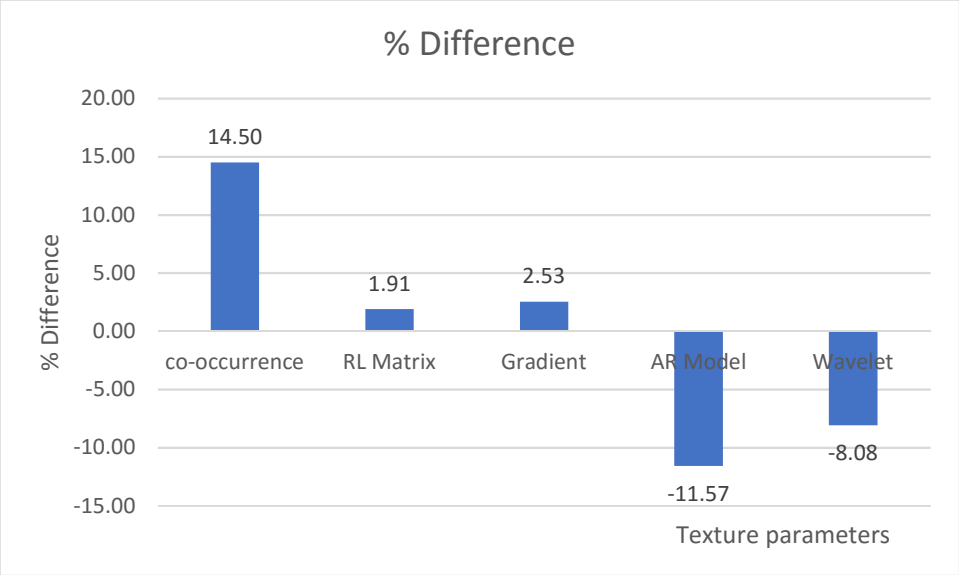

Figure 4.40: The % difference between pQCT texture parameter values right and left legs of a single subject without knee brace.

Table 4.29: Comparison of pQCT texture parameters of the right and left legs of a single subject with a knee brace (KB), with mean values and % difference.

Texture Parameter	Right Leg with KB	Left Leg with KB	Mean	% Difference
Co-occurrence Matrix	211291.08	196670.40	203980.74	-7.17
RL Matrix	782.69	770.79	776.74	-1.53
Gradient	1451.00	1383.76	1417.38	-4.74
AR Model	1.11	1.10	1.11	-1.07
Wavelet	45047.91	46243.48	45645.70	2.62

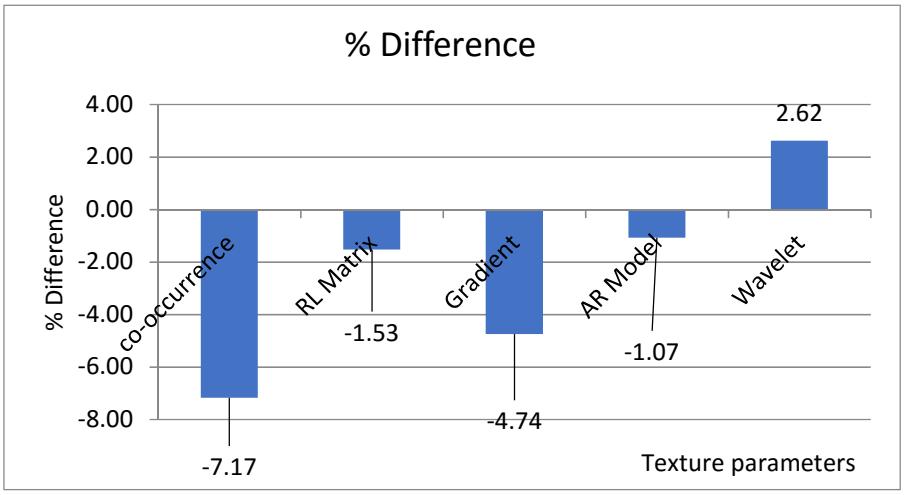

Figure 4.41: The % difference between mean texture parameter values of the right and left legs of a single subject with a knee brace.

Tables 4.26-4.27 and Figures 4.38-4.39 show that the use of the knee brace can result in differences of up to 17% in the values of extracted second order texture indices for the right and left gastrocnemius muscle. Furthermore, Tables 4.28-29 and Figures 4.40-4.41 indicate that, in general, the percent difference in these values between the right and left leg are smaller with the use of the knee brace. Since significant inter-leg differences would not be expected in a healthy normal subject, this suggests that the use of the leg brace has a beneficial effect in improving the consistency of texture indices extracted from pQCT images of the gastrocnemius muscle. This is likely to be due to the reduction in image streaking caused by subject motion as shown in Figure 4.37 (compared with Figures 4.5 and 4.7) and the data in Table 4.25.

4.6 *Comparison of Extracted Texture Parameters for the pQCT and MRI modalities*

The mean values of the second order texture parameters for the initial five healthy subjects (Group A) were compared to assess whether pQCT could be used as a direct substitute for MRI as regards characterisation of the medial head of the gastrocnemius muscle. Images were acquired as described in Sections 4.2.2 and 4.2.3 and texture parameters were extracted with a circular ROI of area 228 pixels in corresponding positions on the right and left legs (section 4.3.3 and Figure 4.10). Since it was found that there were no significant differences between texture parameters of the right and left legs for both modalities (Section 4.3.5), the data for the two legs were combined. The mean value, standard deviation and 95% confidence interval (of the mean) for the two groups of ten images are shown in Table 4.30.

Table 4.30: Mean value, standard deviation (SD) and 95% confidence interval for the five second order texture parameters extracted from ten combined images of the right and left legs for both pQCT and MRI using a circular ROI.

Texture Parameter		Mean	SD	95% Confidence Interval	
				Lower	Upper
Co-occurrence matrix	pQCT	206900.900	5473.206	194519.647	219282.153
	MRI	226230.100	2573.117	220409.304	232050.896
RL matrix	pQCT	734.000	8.369	715.067	752.933
	MRI	377.900	19.146	334.588	421.212
Gradient	pQCT	1444.500	32.926	1370.016	1518.984
	MRI	1755.300	13.695	1724.319	1786.281
AR model	pQCT	1.200	0.133	0.898	1.502
	MRI	1.000	0.149	0.663	1.337
Wavelet transform	pQCT	45626.800	750.805	43928.360	47325.240
	MRI	45602.300	187.807	45177.450	46027.150

A one-way repeated measures ANOVA was used after transposing the data to suit the analysis. This showed that the overall mean of the five texture parameters differed significantly between the pQCT and MRI: $F(5,5) = 86.34$, Wilks' Lambda = 0.011, $p<0.001$. To determine which specific individual texture parameters differed between the modalities, a post-hoc pairwise comparison test was conducted with Bonferroni adjustment to the p-values, with $p < 0.05$ being regarded as significant (Table 4.31). The post-hoc pairwise comparisons showed that the following parameters differed significantly: co-occurrence matrix (mean difference = -19329.2, $p = 0.012$ indicating that the pQCT value was less than that for MRI); RL matrix parameter (mean difference = 356.1, $p<0.001$ indicating that the pQCT value was greater) and gradient (mean difference = - 0.310), $p<0.001$ indications that the pQCT value was less). On the other hand, there were no significant differences in the mean values of the AR model texture parameter ($p = 0.343$) and the wavelet transform ($p = 0.976$), denoting the two last texture parameters (AR model and wavelet transform). Table 4.31 shows the mean difference, the standard deviation of the mean difference, the p value and the 95% confidence interval for the mean difference.

Table 4.31: Pairwise comparisons of the mean values of second order texture parameters extracted for combined pQCT and MRI of the right and left legs using a circular ROI.

Measure	Mean Difference (pQCT- MRI)	SD	p†	95% C.I mean difference.	
				Lower	Upper
Co-occurrence matrix	-19329.2*	6136.606	0.012	-33211.168	-5447.232
RL matrix	356.100*	21.323	0.000	307.864	404.336
Gradient	-310.8*	34.379	0.000	-388.571	-233.029
AR model	0.2	0.200	0.343	-0.252	0.652
Wavelet transform	24.5	803.184	0.976	-1792.429	1841.429

Based on estimated marginal means of texture parameters across the two modalities (pQCT vs. MRI).

* The mean difference is significant with $p < 0.05$.

† Bonferroni adjustment for multiple comparisons.

4.7 Discussion

The capability of the pQCT scanner to acquire calf muscle images as a compact, low radiation dose instrument was demonstrated in a total group of 12 healthy volunteers. Image windowing was shown to be very useful in identifying muscle borders, including those of the gastrocnemius muscle, before extracting texture parameters. However, subject movement during image acquisition resulted in motion artefacts in the form of streaks on the reconstructed images. Some minor movements such as muscle twitches could be unseen by the scanner operator while movement as a result of a sneeze or a cough was more obvious. The effects of these artefacts can severely compromise the quality of the acquired images and may necessitate a re-scan in order to obtain an image of acceptable quality.

Five independent observers made a qualitative assessment of the effect of movement by visual inspection to determine image viability. This assesment confirmed that severe artefacts may be produced (Section 4.5.2.1) and the results agreed with those of a study conducted by Blew et al (2014). The use of a knee brace was proven effective in reducing subject movement and images acquired with the brace were rated as satisfactorly by the observers. In a single healthy volunteer, the use a knee brace

was shown to reduce the difference in values of extracted texture parameters between the right and left legs, suggesting greater consistency in texture analysis (Section 4.5.2.2.). Fortunately, however, the image regions occupied by the medial head of the gastrocnemius muscle were relatively unaffected by the streak artefacts (Figures 4.7 and 4.9) and so it was possible to undertake texture analysis of this muscle in images that were acquired without the use of a knee brace.

With a circular ROI of fixed area, it was shown that ROI position within the medial head of the gastrocnemius muscle of a healthy volunteer does not have a significant effect on the five second order texture parameters extracted from MRI images (Section 4.4). The same effect was found previously for pQCT images (Chapter 3). Furthermore, there was no significant difference in the mean values of texture features between the right and left legs of a group of healthy subjects for either MRI or pQCT (Section 4.3.5). The coefficient of variation (%CV) of the texture parameters within a healthy group was in the approximate range of 1-40% for MRI and 2-25% for pQCT (Figures 4.11-4.16), suggesting that texture values obtained from pQCT might show less normal variation that those for MRI. In addition, %CV values for the co-occurrence matrix and wavelet transform were consistently less than 10%, suggesting that these parameters vary less than the others within a normal population.

Texture indices were also extracted with free hand-drawn ROIs covering whole medial head of the gastrocnemius muscle, with care being taken to avoid the muscle boundary and stay within it. A larger hand-drawn ROI has an advantage over a relatively small circular ROI because it is more likely to include a site of muscle abnormality (such as an injury) when the latter's exact location is not visually apparent. Unlike the circular ROIs, the areas of the hand-drawn ROIs varied from subject to subject according to the size of the muscle.

Data from the original group of five healthy subjects (Group A) were used to produce MRI and pQCT reference ranges for the second order texture parameters in the right and left legs using both a small circular and a larger hand-drawn ROI. However, because of the small number of subjects, for pQCT the exercise was repeated for a larger training goup of eight subjects (Group C) and tested with the remaining four

healthy subjects (Group D). For the hand-drawn ROI, the RL matrix was exluded because its dependence on ROI area has already been demsonstrated (Chapter 3). In all cases, test values fell within the corresponding reference range (Figures 4.17-4.34). This suggests that defining reference ranges for texture parameters based on pQCT imaging of healthy subjects may be a useful approach to the characterisation of injury in the gastrocnemius muscle with this modality. This was reinforced by the finding that in the entire group of 12 healthy subjects, texture parameter values did not depend on leg laterality and that there was no significant difference between subjects in either the overall value of the texture parameters or in the values of individual parameters. However, to be effective, more reliable reference ranges derived from a much larger group of healthy subjects would be needed.

For the five subjects in Group A, a comparison of MRI and pQCT image texture parameters demonstrated that there were no significant differences between the modalities for AR model and wavelet transform (Table 4.31). This suggests that pQCT could be used as a direct substitute for MRI as regards characterisation of the medial head of the gastrocnemius muscle with the application of these two texture indices. Again, this would need to be validated with a sample size that is much greater than that recruited in this project.

4.8 Conclusion

The main findings of this chapter may be summarised as follows:

- The ability of the pQCT scanner to acquire calf muscle images and to identify muscle boundaries through image windowing was confirmed in a group of healthy volunteers.
- Degradation of the quality of reconstructed pQCT images due to subject movement was commonly observed but the medial head of the gastrocnemius muscle was not severely affected by the resulting streak artefacts.

- Reconstructed pQCT images should be visually assessed for motion artefacts and the scan repeated if necessary.
- Subject movement artefacts were reduced with the use of a knee brace but they remain a challenge that needs to be addressed.
- No statistically significant differences were observed in the values of second order texture parameters between the right and left legs for both MRI and pQCT.
- As for pQCT, the position of a circular ROI within the medial head of the gastrocnemius muscle had no significant effect on the values of texture parameters extracted from MRI images.
- The co-occurrence matrix and wavelet transform seemed to show less relative variation (%CV) in a group of healthy subjects compared with the other three texture parameters.
- It was possible to define reference ranges for second order texture parameters for normal gastrocnemius muscle and these may be useful for tissue characterisation such as identifying injured muscle and monitoring the healing process.
- Comparison of texture parameter values obtained by the two imaging modalities showed that there was no significant difference between them as regards AR model and wavelet transform and so these two parameters might allow pQCT to be substituted for MRI to characterise the gastrocnemius muscle.

Chapter 5 Imaging in an Injured Subject

5.1 Introduction

The reason for using medical image texture analysis is the potential of this promising technique to achieve a correct diagnosis from unseen image information. The extracted image texture parameters might lead to an early detection of tissue abnormality. Texture analysis has been used to characterise normal and abnormal tissues (Castellano et al. 2004). Its usefulness has been proved in the characterisation of many diseases as described earlier in Chapter 2. Texture analysis has been implemented in most imaging modalities to quantify differences in appearances. This study is the first one to implement texture analysis in pQCT images to characterise the medial head of the gastrocnemius muscle.

The objective of this chapter is to investigate and demonstrate the performance of specific texture parameters identified in a previous chapter (Chapter 4) in the differentiation of injured gastrocnemius muscle from normal muscle using MRI and pQCT, and to monitor muscle injury healing over a recovery period of 6 weeks.

5.2 Materials and Methods

5.2.1 *Subject*

One female subject (45 years of age) was recruited by distribution of posters in sports injury physiotherapy clinics locally in Cardiff. The potential subject had received a tennis injury in the right leg and she underwent a 15-minute initial injury history and physical examination session by a professional sports injury physician to determine whether or not she met the inclusion criterion of at least a Grade 2 gastrocnemius muscle injury. The subject's description of the injury matched that of a typical tennis leg injury given in Chapter 2. She stated that she had experienced a sudden and sharp sensation at the back of her right calf associated with an audible 'pop' sound. She stated 'I thought someone kicked the back of my leg'. This initial assessment revealed

a Grade 2 injury in the medial part of the gastrocnemius muscle. Approval of the Cardiff University School of Engineering Ethics Committee was obtained to investigate the subject and the participant was fully informed about the study protocol and procedure before obtaining her consent.

5.2.2 *MRI and pQCT Imaging*

The injured right leg of the tennis player was subjected to MRI and pQCT scanning three times over a period of six weeks. The first scans were done two weeks post injury, the second scans four weeks post injury and the third scans six weeks post injury. At two weeks, the uninjured left leg was also scanned by pQCT only. MRI and pQCT scans were performed according to the standard protocols as described in Chapters 3 and 4 except that the slice position was at the distal medial head of the muscle. Radiological interpretation of the initial MRI scans confirmed the injury as a Grade 2 tear of the distal medial head of the gastrocnemius muscle involving the myotendinous junction, with some blood tracking proximally. There was a small area of fibre disruption distally but this was of no significance.

5.3 Texture Analysis

The injury appeared as high intensity region with MRI but it was difficult to visualise the injury on the pQCT images. Therefore, ROIs were defined to cover the whole of the medial head of gastrocnemius muscle (Figure 5.1 and 5.4). They covered as much as possible of the muscle to ensure that the ruptured area was included, but avoided the muscle boundary. The ROIs were drawn by hand and they were approximately equal in size. The second order texture parameters AR model and wavelet transform were extracted and analysed using the MaZda software. These two texture features are ROI area independent as demonstrated in Chapters 3 and 4.

5.4 Characterisation of the Injured Leg

Texture analysis was applied at the diagnostic stage (two weeks post injury) after acquiring MRI and pQCT images. Characterisation was accomplished by comparing the AR model and wavelet transform values of the medial gastrocnemius muscle in the injured subject with predefined right leg normal reference ranges derived from a group of healthy subjects (five subjects for MRI and eight subjects for pQCT). The result of this comparison was classification as normal and abnormal.

The remaining scans over the six week period were done to investigate the suitability of pQCT in monitoring the healing process of muscle injury with time, because this was one of the specific objectives of this project.

5.5 Results

5.5.1 Characterisation of MRI Images

Three MRI images over a period of six weeks are shown in Figure 5.1 while corresponding values of the two extracted texture parameters are shown in Table 5.1. For characterisation purposes, in Figures 5.2 and 5.3 they are plotted alongside reference ranges (95% confidence intervals) derived from a group of five healthy subjects (Table 4.10).

In his study of the gastrocnemius muscle with ultrasound, Alqahtani (2010) derived reference ranges from a mixed group of healthy male and female subjects. This indicates that there is no difference in muscle texture parameters between males and females. No evidence has been found to suggest that this does not apply equally well to MRI, and so reference ranges derived in healthy male subjects may be used for an injured female subject.

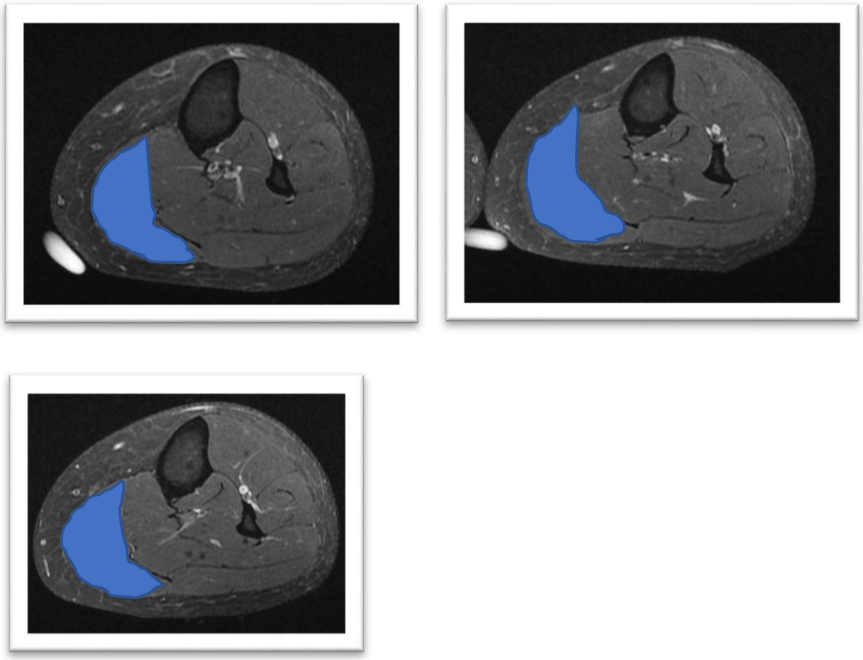

Figure 5.1: MRI images of the injured subject's right leg at 2, 4 and 6 weeks post injury with free hand drawn ROIs that include the whole of the medial head of the gastrocnemius muscle.

Table 5.1 Extracted texture parameters from right leg MRI images of an injured subject.

Texture Parameter	MRI 1st scan	MRI 2nd scan	MRI 3rd scan
AR model	1.19	1.26	1.35
Wavelet transform	56940.41	51281.69	47233.24

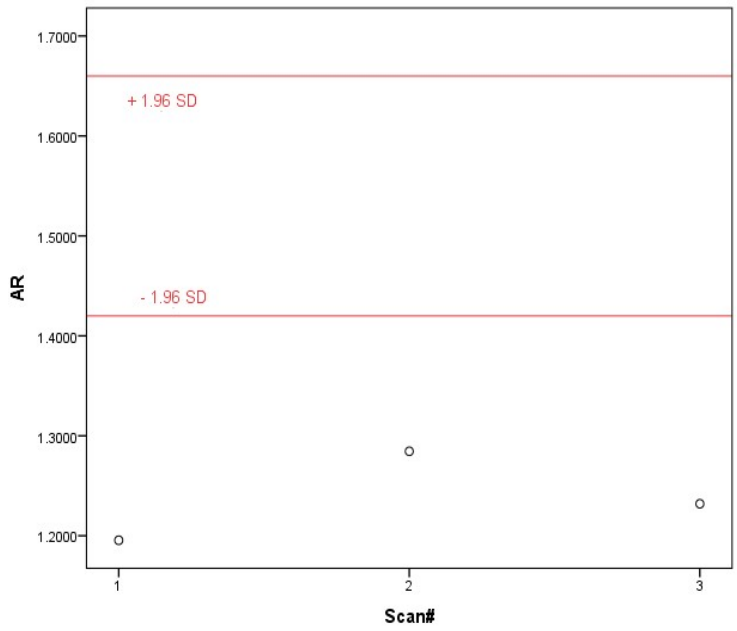

Figure 5.2: Muscle characterisation using the AR model texture parameter extracted from 3 MRI scans at 2, 4 and 6 weeks post injury with reference range. All values fall outside the reference range and are characterised as abnormal.

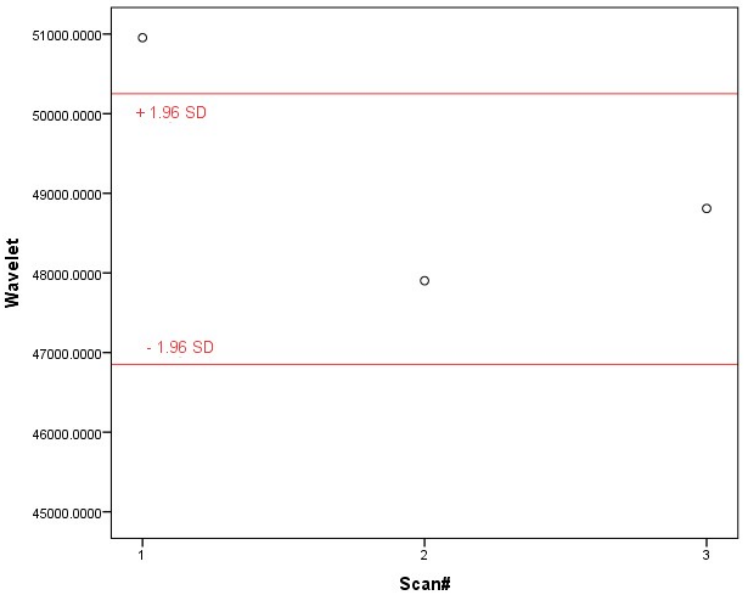

Figure 5.3: Muscle characterisation using the wavelet transform texture parameter extracted from 3 MRI scans at 2, 4 and 6 weeks post injury with reference range. The value for the first scan falls outside the reference range and is characterised as abnormal, while those for the second and third scans fall within the reference range and are characterised as normal.

5.5.2 Characterisation of pQCT Images

Three pQCT images over a period of six weeks are shown in Figure 5.4 while corresponding values of the two extracted texture parameters are shown in Table 5.2. For characterisation purposes, in Figures 5.5 and 5.6 they are plotted alongside reference ranges (95% confidence intervals) derived from the training group of 8 healthy subjects (Table 4.12).

Again, no evidence has been found to suggest that the pQCT reference ranges derived in healthy male subjects may not be applied to an injured female subject. This is supported by the fact that the AR model and wavelet transform values for the female subject's uninjured left leg fell within their respective reference ranges.

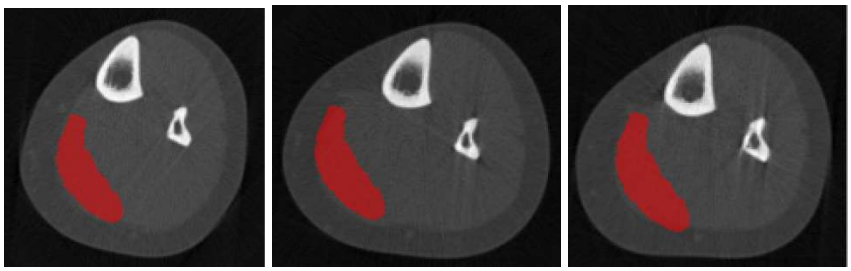

Figure 5.4: pQCT images of the injured subject's right leg at 2, 4 and 6 weeks post injury with free hand drawn ROIs that include the whole of the medial head of the gastrocnemius muscle.

Table 5.2: Extracted texture parameters from right leg pQCT images of an injured subject.

Texture Parameter	pQCT 1st Scan	pQCT 2nd Scan	pQCT 3rd Scan
AR model	1.4424	1.3786	1.4237
Wavelet transform	43602.8058	43103.5087	44046.6469

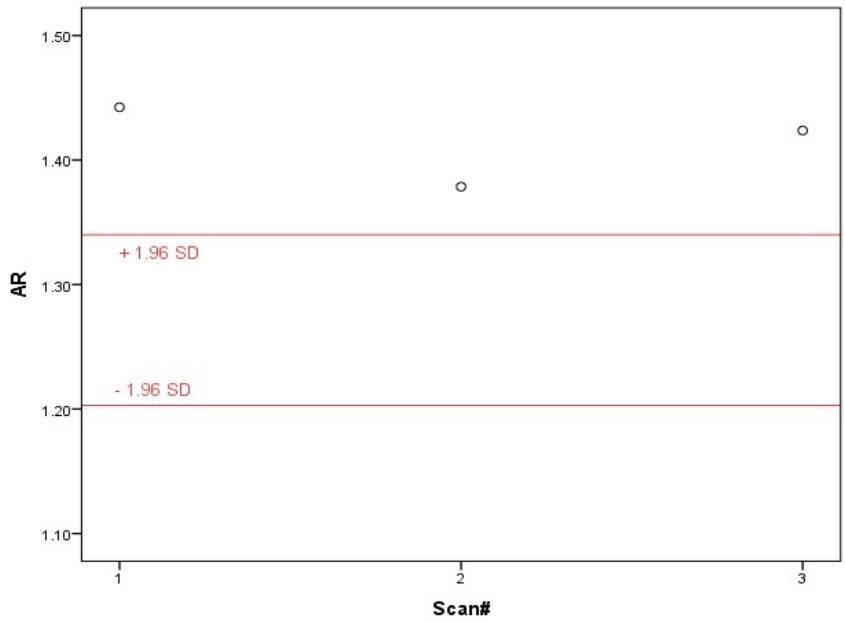

Figure 5.5: Muscle characterisation using the AR model texture parameter extracted from 3 pQCT scans at 2, 4 and 6 weeks post injury with reference range. All values fall outside the reference range and are characterised as abnormal.

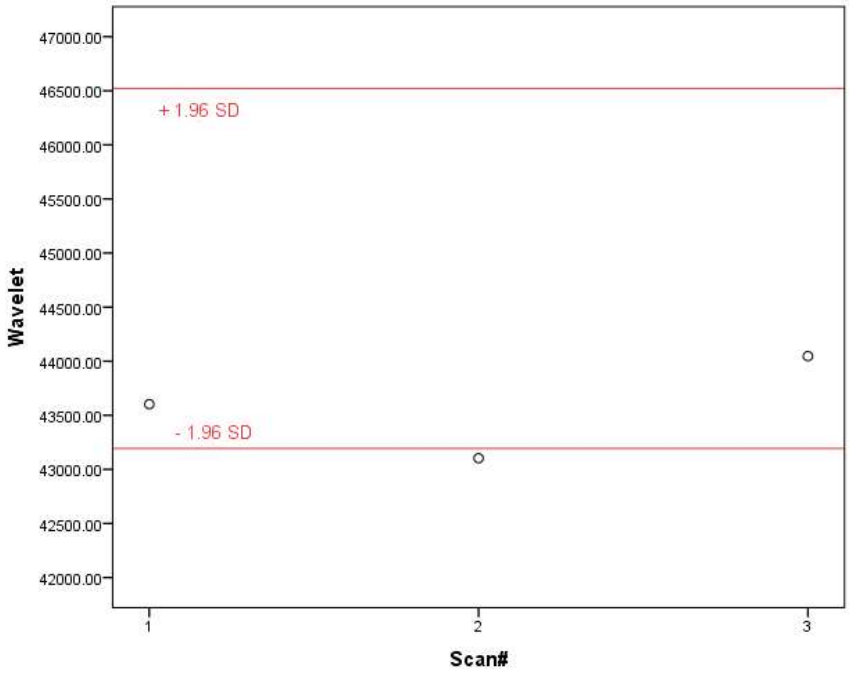

Figure 5.6: Muscle characterisation using the wavelet transform texture parameter extracted from 3 pQCT scans at 2, 4 and 6 weeks post injury with reference range. The values for the first and third scans fall within the reference range and are characterised as normal, while that for the second scan falls outside the reference range and is characterised as abnormal.

5.5.3 Comparision of MRI and pQCT Muscle Characterisation Results

The results of the characterisation of the injured subject's right gastrocnemius muscle with MRI and pQCT are shown together in Table 5.3.

Table 5.3: Comparison of the results of injured muscle characterisation with the two texture parameters extracted from 3 MRI and pQCT scans at 2, 4 and 6 weeks post injury.

	First Scan		**Second Scan**		**Third Scan**	
Texture Parameter	MRI	pQCT	MRI	pQCT	MRI	pQCT
AR model	Abnormal	Abnormal	Abnormal	Abnormal	Abnormal	Abnormal
Wavelet transform	Abnormal	Normal	Normal	Abnormal	Normal	Normal

5.6 Discussion

The tear of the gastrocnemius muscle of the type seen in this injured subject is termed tennis leg; it is a frequent occurrence in elite athletes. The pathogenesis of this injury is associated with tearing of the medial head of the gastrocnemius muscle at the musculotendinous junction. As stated in Chapter 2, the susceptibility of this muscle to tearing is due the presence of high density type II (fast twitch) muscle fibres, its extension across two joints and eccentric action.

Earlier work in this thesis has shown that pQCT might be an alternative modality to MRI for characterising muscle using the AR model and wavelet transform texture parameters because there were no significant differences between their mean values for the two modalities in a group of heathy subjects. This has been partially confirmed by the results of the investigation of a single injured subject. Table 5.3 shows complete agreement of pQCT with MRI with the use of the AR model with regard to classification as normal or abnormal. However, the three values of this parameter were

all below the reference range for MRI and all above the reference range for pQCT and this is an anomaly. With wavelet transform, there is discrepancy between MRI and pQCT at two weeks post injury with the former indicating abnormality and the latter normality. Both modalities show normality at six weeks post injury. At four weeks post injury, MRI shows normality and the pQCT result is only just below the reference range.

The medical radiology reports of the three MRI scans revealed that there was incomplete injury healing over six weeks and so it was not possible to fulfill the objective of monitoring injury healing by texture analysis. The values of the AR texture parameter for both MRI and pQCT remained abnormal during the period of the investigation and in this sense, they agreed with the radiological reports. However, AR values did not approach their respective reference ranges consistently for either modality, contrary to what might be expected if healing was occurring to some extent. It was also the case that the wavelet transform values did not change in a consistent fashion for either MRI or pQCT.

Incomplete healing could be due to the fact that the patient did not limit her activities. Furthermore, there was no confirmation that patient underwent an appropriate course of therapy. Therefore, it is possible that the injury might have been aggravated, although this was not noted on the radiological reports. It would have been better if the patient had been treated under medical supervision and carefully monitored until fully recovered from the injury. Full recovery takes approximately 4 to 8 weeks with good rehabilitation (http://physioworks.com.au/injuries-conditions-1/calf-muscle-tears).

The results of this study were broadly in agreement with those of Alqahtani (2010) who used ultrasound imaging. He found that the AR model was the most sensitive parameter for differentiating normal muscle from injured muscle and that it might be used to monitor the healing process and study the response of injured muscle to different treatment protocols. In Alqahtani's study, the number of healthy subjects recruited was 25 (21 males and 4 females) and this had a beneficial impact on the accuracy of the derived reference range (1.11-1.15) compared with this study (1.20-1.34 for pQCT (Table 4.12) and 1.42-1.66 for MRI (Table 4.10)). The greater the number of subjects, the narrower is the reference range.

Authors such as Lerski et al (2015) have proposed that texture analysis using one or two texture parameters should be more widely applied in hospitals and clinics as a simple diagnostic method. Indeed, the literature review (Chapter 2) indicated more generally that texture analysis for the differentiation of normal tissue from abnormal tissue has achieved very good classification results.

In this study, MRI images were acquired according to a hospital's usual protocol for lower limb injuries, thus providing a sound clinical basis to the subsequent texture analysis. Texture analysis of MRI images in a small group of healthy subjects and one injured subject demonstrated good classification capability of the AR model parameter compared with radiological and clinical findings. The fact that wavelet transform failed to detect abnormality in injured muscle with the exception of the first MRI scan and the second pQCT scan might be due to lack of an accurate reference range. An increased healthy subject sample size might improve muscle characterisation accuracy. The usefulness of either of these texture parameters to assess muscle healing post injury would also require imaging in a larger group of injured subjects and possibly more frequent imaging.

5.7 Conclusions

The main findings can be summarised as follows:

- It appears that the AR model may be a sensitive texture parameter for the identification of muscle injury with both MRI and pQCT in comparison with clinical findings and radiological reports.
- An anomaly was noted in that the injured muscle AR values were below the reference range for MRI and above the reference range for pQCT, and so pQCT may not be suitable as a direct replacement for MRI using this parameter.
- Wavelet transform values did not consistently identify injured muscle.
- Neither AR model nor wavelet transform values changed consistently during a six week period of partial muscle healing.
- A larger group of heathy subjects is required to establish more reliable reference ranges for the initial diagnosis of muscle injury.

- A larger group of injured subjects and more frequent imaging is required to assess the usefulness of the texture parameters in monitoring muscle healing after injury.

Chapter 6 Summary and Conclusion

6.1 Introduction

Texture analysis is a promising technique that can be used as a tool to assist clinicians in the diagnosis of disease. It is an objective, quantitative method that is based on computer image analysis. It may have advantages compared with a subjective method such as the conventional visual inspection and reporting of images. In muscle imaging, for example, the subjective approach may not be sensitive enough to detect minor muscle fibre changes.

In principle, texture analysis is a technique that evaluates the spatial position of pixels in a digital image in relation to grey level (intensity) variation. This evaluation is accomplished by computing statistical parameters of pixel distribution within the image. The process usually consists of the definition of a region of interest (ROI), within muscle for example, followed by texture feature extraction. The latter is accomplished using a dedicated, accurate and reliable software package such as MaZda. The manipulation of the extracted texture parameters is the basis of the application of texture analysis as a diagnostic aid.

Texture analysis has been applied to a range of medical imaging modalities. However, there is no study in which this technique has been applied to muscle images acquired by peripheral quantitative computed tomography (pQCT), a technology that was originally developed for the investigation of bone disease in the limbs. The hypothesis of this thesis was that a pQCT scanner is capable of acquiring soft tissue images, and that the application of texture analysis techniques provides information which can aid the detection of subtle changes in muscle during the early post-injury stage. To the best of the researcher's knowledge, the novelty of this present study lies in the fact it is the first one which has explored the use of pQCT in characterising muscle using texture analysis.

6.2 Summary

Muscle injuries are the most common type of sports injuries and medical imaging plays a very important role in diagnosis. Of the various types of imaging modalities, ultrasound is considered the modality of choice to confirm or exclude a tear in a muscle (such as the gastrocnemius muscle in the thigh) due to its availability, low cost and relative ease of examination. However, magnetic resonance imaging (MRI) is also considered to be a very good modality for imaging muscle injury.

Although pQCT is a promising technique that might be considered an alternative modality due to its relatively low cost and portability (compared to MRI), it cannot visualise a lesion site and so the ROI must cover the whole of the relevant muscle. Furthermore, image artefacts due to subject motion are a limiting factor for the use of pQCT.

The objective of this study was to investigate whether pQCT offers an alternative to MRI for tissue characterisation of the gastrocnemius muscle (GM) using texture analysis. Since it was the intention of the study to compare healthy and pathological images acquired by MRI and pQCT, it was necessary to standardise pQCT image acquisition parameters (scan speed and pixel size) and to identify texture parameters that might be useful to implement for the comparison.

Given that any instrument has random measurement errors, a water phantom was used to simulate human soft tissue in order to determine useful pQCT texture parameters. The water phantom study highlighted the most consistent texture parameters that showed a low variation (as assessed by the coefficient of variation %CV): co-occurrence matrix, gradient, run-length (RL) matrix, auto-regressive (AR) model and wavelet transform. These higher order statistical parameters were deemed potentially useful for further application. Furthermore, image noise was quantified from variance values with each combination of acquisition parameters. This work also demonstrated that the MaZda software package was a reliable research tool for texture analysis.

Normal healthy volunteers were then studied. Initially, a single subject was scanned with pQCT using a range of scan speeds and pixel sizes. Subsequently, a group of 12 healthy volunteers were scanned with standard values of scan speed and pixel size. Of these, 5 (Group A) were also scanned by MRI; Group B comprised the remaining 7

healthy subjects. One of the major strengths of this thesis is that the study of the healthy single subject allowed the development of a well-defined pQCT scan standard protocol, one of the objectives of the project. It also demonstrated the capability of pQCT to acquire calf muscle images and to distinguish the boundary of the medial head of the GM using image windowing.

Subject movement was a challenging factor for pQCT image acquisition, as any movement during the scan could result in image degradation. Motion artefact was apparent on the pQCT images of subjects from both Group A and Group B. It has been reported that 22.7% of high resolution pQCT scans need a re-scan (Braun *et al.* 1998). In this study, care was taken to ensure that the subject remained as still as possible during image acquisition. In addition, a knee brace was used with one subject from Group A and this decreased the artefacts. This study showed that for the optimisation of pQCT acquisition, a balance was needed between good image quality (small pixel size and slow scan speed) and the control of motion artefacts (fast scan speed). The combination of a pixel size of 0.8 mm and a scan speed of 10 mm/s was chosen as it yielded a smooth image (good signal to noise ratio) and a reasonably short scan time.

The repeatability of pQCT texture parameters was tested in the healthy volunteers with these acquisition settings and, in general, found to be reliable. However, the first order statistics texture parameters skewness and kurtosis were excluded as they showed high variation (% CV) compared with other parameters. This result is in line with that from an earlier study using muscle texture analysis on ultrasound images (Alqahtani *et al.,* 2010).

Another significant observation that emerged from this study was that the fact that the run-length matrix parameter was linearly dependent on ROI area. Therefore, it was excluded because a free hand-drawn ROI was used to cover the entire medial head of the GM; to some extent this varied in size from one subject to another since muscle size varied among the recruited subjects. This observation is in agreement with that of Sikio *et al.* (2015) who also found that ROI affected the value the RL matrix.

A further important finding from this study was that image scaling had limited consequences; it affected only the remaining first order texture parameters (particularly grey level). The higher order parameters were not affected because of the

image normalisation process, which isolates first order statistics from higher order ones; the latter were therefore retained for further analysis. This is supported by Materka (2004) and Lerski et al. (2015) who stated that normalisation of acquired images was essential to remove unwanted variations caused by the scanner.

Experiments with a circular ROI provided evidence that a minimum ROI area of 200 pixels is needed to extract numerical texture parameters. This finding is consistent with the findings of Lerski et al. (2015), who recommended that the ROI area should greater than 100 pixels. It was also shown that, ideally, the ROI area should be kept constant as this limits variations in the values of texture parameters. In addition, it was shown that the position of a circular ROI within the medial head of the GM had no significant influence on extracted texture parameters, reflecting muscle homogeneity.

When comparing pQCT with MRI in healthy volunteers, it was found that there was no significant difference between the modalities for the AR model and wavelet transform texture parameters. Furthermore, the results from the healthy subjects showed that there was no significant difference between right and left leg extracted texture parameters for both modalities. Group A results were used to define texture parameter reference ranges (95% confidence intervals) for the GM using MRI. For pQCT, the total of 12 healthy subjects were split into a training group of 8 (Group C) and a test group of 4 (Group D). Reference ranges were derived from the Group C results and tested with the Group D results. All test values fell within the reference ranges, thus validating the ranges.

However, caution should be exercised before generalising these findings because of the small sample size of the reference population, especially for MRI. The small sample size was due to cost and limited accessibility of MRI scans and caution about the exposure of healthy young volunteers to ionising radiation. A larger sample size would be required for more accurate and reliable reference ranges.

One injured subject was studied over a period of 6 weeks following a Grade 2 tear of the medial part of the GM. This work subject suggested that the AR model texture parameter was a sensitive index with which to characterise muscle injury because its values fell outside the corresponding reference ranges for both MRI and pQCT. It performed better than the wavelet transform, whose application was also investigated.

This was supported by the fact that the AR value obtained by pQCT for the uninjured leg fell within the reference range. A weakness of the study is that it did not monitor the entire healing process with both modalities, as there was incomplete injury recovery over the period of investigation. This might be due to the patient's non-adherence to activity limitation or lack of proper treatment in later stages (two weeks after injury). Despite the fact that there is a range of treatment options for every stage and grade of muscle injury, there is no robust clinical trial using objective outcome measures to quantify the efficacy of different treatment options and monitor the healing process with treatment.

6.3 Conclusions

This study aimed to determine the capability a pQCT scanner to acquire GM muscle images and to characterise the medial of the GM. The important conclusions drawn from this work include the following:

- The pQCT scanner is capable of acquiring GM images.
- A quantitative non-invasive method to characterise muscle tissue has been developed for pQCT.
- The MaZda image analysis software package was found to be an accurate and reliable texture analysis tool.
- Normalisation of acquired images is essential to avoid unwanted variations due to the scanner and image scaling effects.
- The first order texture parameter grey level was found to be affected by image format transformation.
- Two other first order texture parameters (skewness and kurtosis) were excluded as they showed large coefficient of variation.
- The pQCT scanner showed reliable repeatability for higher order texture parameters.
- Five higher order texture parameters (co-occurrence matrix, run length matrix, gradient, AR model and wavelet transform) were used to obtain reference ranges of normal muscle using MRI and pQCT.
- Sample size had an adverse impact on the accuracy of normal reference ranges.

- ROI area had a significant effect on RL matrix values and a smaller effect on other texture parameters.
- If the RL matrix parameter is used, the ROI area must be kept constant.
- ROI position within the boundary of the medial head of the GM had no significant effect on extracted texture parameters.
- No significant differences in texture parameters were found between the medial GM in the right and left leg in both modalities (MRI and pQCT).
- The AR model texture parameter was found to be the most sensitive parameter in distinguishing normal muscle from injured muscle.
- Quantitative MRI and pQCT image analysis of the GM using the AR model texture parameter can be used as a tool to characterise the medial head of the GM.

6.4 Contribution to knowledge

This study has demonstrated that a pQCT scanner is capable of acquiring images of the gastrocnemius muscle and that texture analysis of these images may be used to characterise the muscle. Texture parameter reference ranges have been developed for the identification of GM injury.

6.5 Future work

This study serves as a pilot and highlights the possibilities of using a pQCT scanner to acquire muscle images which may be characterised with texture analysis. Reference ranges based on the AR model texture parameter for both MRI and pQCT need to be validated with a larger group of normal healthy subjects.

Another future goal would be to validate the use MRI and pQCT image texture to monitor the healing process of muscle injury with a large group of patients and a well monitored treatment programme. A clinical trial with more than three scans during the healing period is recommended.

In addition, it would be beneficial to conduct an in-depth analysis of each extracted texture parameter, rather than summing second order parameters (co-occurrence matrix, run length matrix and gradient) and wavelet transform. It would also be beneficial to conduct a study with a large sample size using a special programme

available in the MaZda software (the b11 programme) for the auto-classification of data.

References

Abdullah, N., World largest Science, Technology & Medicine Open Access book publisher. The Visible Light Activity of the TiO 2 and TiO 2: V 4 + Photocatalyst.

Aldahlawi RH, Pugh N, Nokes L. 2015. The use of texture analysis in diagnosing ovarian masses. (preliminary results). BJOG: An international journal of obstetrics and gynaecology, volume 122, supplement S3, page 3.

Arai Y, Osawa M., Fukuyama Y. Muscle CT scans in preclinical cases of Duchenne and Becker muscular dystrophy. Brain & Development (1995) 17(2): 95-103.

Azaid, S. A., Fakhr, M.W. & Mohamed, a. F. a., 2006. Automatic Diagnosis of Liver Diseases from Ultrasound Images. 2006 International Conference on Computer Engineering and Systems, (March 2015), pp.313–319.

Adams, J.E., 2009. Quantitative computed tomography. European Journal of Radiology, 71, pp.415–424.

Agur, A.M.R. & Dalley, A.F., 2005. Grant's Atlas of Anatomy Eleventh E. B. Sun, ed., Baltimor, Maryland: Lippincott Williams & Wilkins.

Alameddine Hala S, Michele Dehaupas & Fardeali, M., 1989. Regeneration of Skeletal Muscle Fibers from Autologous Satellite Cells Multiplied in Vitro. An Experimental Mi=odel for Testing Cultered Cell Myogenicity. Muscle and Nerve, 12, pp.544–555.

Armfield, D.R. et al., 2006. Sports-related muscle injury in the lower extremity. Clin Sports Med, 25(4), pp.803–842.

Askling, C.M. et al., 2007. Acute first-time hamstring strains during high-speed running: a longitudinal study including clinical and magnetic resonance imaging findings. The American journal of sports medicine, 35, pp.197–206.

Askling, C.M. et al., 2008. Proximal hamstring strains of stretching type in different sports: injury situations, clinical and magnetic resonance imaging characteristics, and return to sport. The American journal of sports medicine, 36, pp.1799–1804.

Alqahtani Mahdi, 2010. Quantitative Ultrasound Image Analysis of the Gastrocnemius Muscle for Injury Evaluation. pp.173–174.

Barry, N.T. & Chris, K.E., 1997. No Title Guideline for Evaluating and Expressing the Uncertainty of NIST Measurement Results. NIST Technical Note, (1994 Edition).

Basset, O. et al., 1994. Charachterisation of MuscleTissue during an Effort by Texture Analysis of Ultrasound Images. In IEEE Ultrasonic Syposium Proceedings, 3, pp.1455–1458.

Beekman R, Visser L H., 2004. High-resolution sonography of the peripheral nervous system -- a review of the literature. Eur J Neurol. 11(5):305-14.

Beiner J. M. & Jokl, P., 2001. Muscle contusion injuries: current treatment options. J Am Acad Orthop Surg., 9(4), pp.227–237.

Beiner, J.M. & Jokl, P., 2002. Muscle contusion injury and myositis ossificans traumatica. Clinical orthopaedics and related research, pp.S110–S119.

Bharati S et al., 1998. Sonographic evaluation of tears of the gastrocnemius model head (tennis leg). J Ultrasound Med, 17(3), pp.157–162.

Bharati, M.H., Liu, J.J. & MacGregor, J.F., 2004. Image texture analysis: methods and comparisons. Chemometrics and Intellegent Laboratory Sysytems, 72(1), pp.57–71.

Bianchi, S. et al., 1998. Sonographic evaluation of tears of the gastrocnemius medial head ("tennis leg"). J Ultrasound Med, 17(3), pp.157–162.

Blankenbaker, D.G. & Tuite, M.J., 2010. Temporal changes of muscle injury. Semin Musculoskelet Radiol, 14(2), pp.176–193. Available at: https://www.thieme-connect.de/DOI/DOI?10.1055/s-0030-1253159.

Blankenbaker, D.G. & De Smet, A.A., 2004. MR imaging of muscle injuries. Applied Radiology, 33(4), pp.14–26.

Blew, R.M. et al., 2014. Standardizing evaluation of pQCT image quality in the presence of subject movement: qualitative versus quantitative assessment. Calcified tissue international, 94(2), pp.202–11. Available at: http://www.ncbi.nlm.nih.gov/pubmed/24077875 [Accessed November 2, 2014].

Bocchi, L. et al., 1997. Tissue characterization from X-ray images. Medical engineering & physics, 19(4), pp.336–342.

Bovik, a. C., Clark, M. & Geisler, W.S., 1990. Multichannel texture analysis using localized spatial filters. IEEE Transactions on Pattern Analysis and Machine Intelligence, 12(I).

Brancaccio, P., Maffulli, N. & Limongelli, F.M., 2007. Creatine kinase monitoring in sport medicine. British Medical Bulletin, 81–82(1), pp.209–230.

Brancaccio, P., Lippi, G. & Maffulli, N., 2010. Biochemical markers of muscular damage1. Clin.Chem.Lab Med., 48(6), pp.757–767.

Braun, M.J. et al., 1998. Clinical evaluation of a high-resolution new peripheral quantitative computerized tomography (pQCT) scanner for the bone densitometry at the lower limbs. Physics in medicine and biology, 43, pp.2279–2294.

Broek, R.W. Ten, Grefte, S. & Hoff, J. w. Den, 2010. Regulatory Factors and Cell Populations Involved in Skeletal Muscle Regeneration. J Cell Physiol, 224, pp.7–16.

Burns, E. et al., 2008. Skeletal Muscle Tissue Engineering. ????, ???(???), p.????

Bushberg, J. et al., 2012. The Essential Physics of Medical Imaging Third. C. W. Mitchel, ed., Lippincott Williams & Wilkins.

Caltech, 2005. Introduction to Matlab.

Campbell R S D and Wood, 2002. Ultrasound of muscle. Imaging, 14(3), pp.229–240.

Campbell, S.E., Adler, R. & Sofka, C.M., 2005. Ultrasound of muscle abnormalities. Ultrasound quarterly, 21, pp.87-94, 153–4. Available at: http://www.ncbi.nlm.nih.gov/pubmed/15905818.

Carlton, R.R. & Arlene M. Adler, 2013. Radiographic Imaging, Concepts and Principles 5th ed., New York: Delmar.

Carlson BM, Faulkner JA. The regeneration of skeletal muscle fibers following injury: A review. Med. Sci. Sports Exerc. 1983; 15:187–198

Castellano, G., Bonilha, L. & Cendes, L.M., 2004. Texture analysis of medical images. clinical Radiology, 59, pp.1061–1069.

Chabat François, PhD, Guang-Zhong Yang, PhD, and David M. Hansell, MD, FRCP, FRCR. 2003, Obstructive Lung Diseases: Texture Classification for Differentiation at CT, Volume 228, Issue 3

Chan, K.L. & Mccarty, K., Aspect of theE Statistical Texture Analysis of Medical Ultrasound Images. IEE Colloquium on Ultrasound Instrumentation, p.1/3-3/3.

Chaudhuri. B B. and Nirupam Sarkar, JANUARY 1995, Texture Segmentation Using Fractal Dimension., IEEE, Transactions on Pattern Analysis and Machine Intelligence, Vol. 17, NO. 1.

Cheung, A.M. et al., 2013. High-resolution peripheral quantitative computed tomography for the assessment of bone strength and structure: a review by the

Canadian Bone Strength Working Group. Current osteoporosis reports, 11(2), pp.136–46. Available at: http://www.pubmedcentral.nih.gov/articlerender.fcgi?artid=3641288&tool=pmcentrez&rendertype=abstract [Accessed November 8, 2013].

Christopher J Mann et al., 2011. Aberrant repair and fibrosis development in skeletal muscle. Skeletal Muscle, 1, pp.1–21.

Chung-Ming W., Yung-Chang Chen & Hsieh, K.-S., 1992. Texture features for classification of ultrasonic liver images. Medical Imaging, IEEE Transactions, 11(2), pp.141–152.

Claassen JAHR. The gold standard: not a golden standard. British Medical Journal 2005, 330(7500), 1121

Clague, J.E. et al., 1995. Muscle imaging in health and disease. Neuromuscul Disord, 5(3), pp.171–178.

Clausi, D.A. & Can., J., 2002. An analysis of co-occurrence texture statistics as a function of grey level quantization. Remote Sensing, 28(1), pp.45–62.

Cohen, L., 1989. Time-frequency distributions-a review. Proceedings of the IEEE, 77(7), pp.941–981.

Collewet, G., Strzelecki, M. & Mariette, F., 2004. Influence of MRI acquisition protocols and image intensity normalization methods on texture classification. Magnetic Resonance Imaging, 22, pp.81–91.

Connell David A., Michal E. Schneider-Kolsky, Jan Lucas Hoving, Frank Malara, Rachelle Buchbinder, George Koulouris, Frank Burke and Cheryl Bass., (2004) Longitudinal Study Comparing Sonographic and MRI Assessments of Acute and Healing Hamstring Injuries,American Journal of Roentgenology. 2004;183: 975-984. 10.2214/ajr.183.4.1830975

Connolly, D.A., Sayers, S.P. & McHugh, M.P., 2003. Treatment and prevention of delayed onset muscle soreness. J Strength Cond Res, 17(1), pp.197–2003.

Crema, M.D. et al., 2015. Imaging techniques for muscle injury in sports medicine and clinical relevance. Current Reviews in Musculoskeletal Medicine, 8(2), pp.154–161.

Dae-Cheol, K. et al., 2010. Assessment of the Effect of Bone Density and Soft Tissue Thickness on Phantom Measurements. Journal of the Korean Physical Society, 57(5), p.1263. Available at: http://www.kps.or.kr/jkps/abstract_view.asp?articleuid=BDDBEA00-405D-4626-B800- EF0DB8EBCA36.

Damilakis J, Adams JE, Guglielmi G, Link TM. 2010.Radiation exposure in X-ray based techniques used in osteoporosis. European Radiology, volume 20, number 11, pages 2707-2714

Da Ponte, Gelber, J.S. & Fox, J.., 1988. Effect of co-occurrence displacement vector on quantization of ultrasonic image texture. Bioengineering Conference, Proceedings of the Fourteenth Annual Northeast, pp.298–300.

Dae-Cheol, K. et al., 2010. Assessment of the Effect of Bone Density and Soft Tissue Thickness on Phantom Measurements. Journal of the Korean Physical Society, 57(5), p.1263. Available at: http://www.kps.or.kr/jkps/abstract_view.asp?articleuid=BDDBEA00-405D-4626-B800- EF0DB8EBCA36.

Daugman, J.G., 1988. Complete discrete 2-D gabor transforms by neural networks for image analysis and compression. IEEE Transactions on Acoustics, Speech, and Signal Processing, 36(7), pp.1169–1179.

Day M, Phil M, McCormack RA, Nayyar S, Jazrawi., 2016. Physician Training Ultrasound and Accuracy of Diagnosis in Rotator Cuff Tears. Bull Hosp Jt Dis. Sep;74(3):207-11

De Certaines JD, Larcher T, Duda D, Azzabou N, Eliat P-A, Escudero LM, Pinheiro AMG, Yang G, Coatrieux J-L, Snezkho E, Shulelovich A, Pereira M, Lerski RA. 2015. Application of texture analysis to mucle MRI: 1-What kind of information should be expected from texture analysis? EPJ Nonlinear Biomedical Physics, volume 3, number 3, DOI 10.1140/s40366-015-0017-1

Delgado, G.J. et al., 2002. Tennis leg: clinical US study of 141 patients and anatomic investigation of four cadavers with MR imaging and US. Radiology, 224(1), pp.112–119. Available at: http://radiology.rsna.org/content/224/1/112.full.pdf.

Dixon, J.B., 2009. Gastrocnemius vs. soleus strain: How to differentiate and deal with calf muscle injuries. Current Reviews in Musculoskeletal Medicine, 2(2), pp.74–77.

Doi, K., 2005. Current status and future potenial of computer-aided diagnosis in medical imaging. British J of Radiolgy, 78, pp.3–19.

Dost, K., 2013. Traumatic arteriovenous fistula. Der Chirurg; Zeitschrift fur alle Gebiete der operativen Medizen, 40, pp.506–510.

Ehman R L & Berquist, T.H., 1986. Magnetic resonance of musculoskeletal trauma. Radiol Clin North Am, 24(2), pp.291–319.

El-Khoury, G.Y. et al., 1996. Imaging of muscle injuries. Skeletal Radiol, 25(1), pp.3–11.

E. L. Hall, R. P. Kruger, S. J. Dwyer, D. L. Hall, R. W. McLaren, and G. S. Lodwick, 1971. A survey of preprocessing and feature extraction techniques for radiographic images. IEEE Transactions on Computers, vol. 20, no. 9, pp. 1032–1044.

Engelke, K. et al., 2008. Clinical Use of Quantitative Computed Tomography and Peripheral Quantitative Computed Tomography in the Management of Osteoporosis in Adults: The 2007 ISCD Official Positions. Journal of Clinical Densitometry, 11, pp.123–162.

Erik Burns, Kelsi Krier, Marc Lebel, Matt Peppel 2008.Skeletal Muscle Tissue Engineering Evans, J.D., 1996. Straightforward Statistics for the Behavioral Sciences., p.122.

Erlandson MC,Lorbergs AL, Mathur S, Cheung AM. 2016. Muscle analysis using pQCT, DXA and MRI. European Journal of Radiology, volume 85, number 5, pages 1505-1511.

Farr, J.N. et al., 2011. Skeletal muscle fat content is inversely associated with bone strength in young girls. Journal of bone and mineral research: the official journal of the American Society for Bone and Mineral Research, 26(9), pp.2217–25. Available at: http://www.ncbi.nlm.nih.gov/pubmed/21544865 [Accessed November 2, 2014].

Faul, J.L. et al., 1999. The reproducibility of repeat measures of airway inflammation in stable atopic asthma. American Journal of Respiratory and Critical Care Medicine, 160(11), pp.1457–1461.

Fleiss, J., 1986. Reliability of Measurement,

Fornage, B.D., 1995. Muscular trauma, New York, NY. Musculoskeletal ultrasound, (Cutchill Livingstone).

Fornage, B.D., 2000. The case for ultrasound of muscles and tendons. Seminars in Musculoskeletal Radiology, 4, pp.375–391.

Frank-Wilson, A.W. et al., 2015. Measurement of muscle and fat in postmenopausal women: precision of previously reported pQCT imaging methods. Bone, 75, pp.49–54. Available at: http://linkinghub.elsevier.com/retrieve/pii/S8756328215000307.

Froimson, A.I., 1969. Tennis Leg. Jama, 209(3), pp.415–416.

Fuller, C.W. et al., 2006. Consensus statement on injury definitions and data collection procedures in studies of football (soccer) injuries. Scandinavian Journal of Medicine and Science in Sports, 16, pp.83–92.

Galloway M M, 1975. Texture analysis using gray level run lengths. Computer Graphics and Image Processing, 4(2), pp.172–179.

Garra BS1, Insana MF, Shawker TH, Wagner RF, Bradford M, Russell M. 1989. Quantitative ultrasonic detection and classification of diffuse liver disease. Comparison with human observer performance. nvest Radiol. 1989 Mar;24(3):196-203.

Garrett Jr., W.E., 1990. Muscle strain injuries: clinical and basic aspects. Med Sci Sports Exerc, 22(4), pp.436–443.

Garrett WE Jr. 1993. Muscle strain injuries. Am J Sports Med. 24 (6 Suppl) S2-8.

Garrett Jr., W.E. et al., 1989. Computed tomography of hamstring muscle strains. Med Sci Sports Exerc, 21(5), pp.506–514.

Giger, M.L., Chan, H.-P. & Boone, J., 2008. Anniversary paper: History and status of CAD and quantitative image analysis: the role of Medical Physics and AAPM. Medical physics, 35(12), pp.5799–820. Available at: http://www.pubmedcentral.nih.gov/articlerender.fcgi?artid=2673617&tool=pmcentrez&rendertype=abstract [Accessed November 28, 2014].

Gokhin, D.S. et al., 2012. Thin-filament length correlates with fiber type in human skeletal muscle. Am J Physiol Cell Physiol, 302(3), pp.C555-65.

Goldman, L.W., 2007. Principles of CT: radiation dose and image quality. Journal of nuclear medicine technology, 35(4), pp.213-225-228.

Gordon, C.L. et al., 1996. In vivo assessment of trabecular bone structure at the distal radius from high-resolution computed tomography images. Phys Med Biol, 41, pp.495–508.

Grace Carvajal Mulatti, André Brito Queiroz and Erasmo Simão da Silva. Traumatic Arteriovenous Fistula.Ch 10, http://dx.doi.org/10.5772/56368

Guerrero M, Guiu-Comadevall, Cadefau J, Parra J, Balius R, Estruch, Rodas G, Bedini J L, Cusso R, 2008. Fast and slow myosin as markers of muscle injury. BR J Sport Med, August, 42(8): 695

Hajek, M. et al., 2006. Texture Analysis for Magnetic Resonance Imaging, med4 publishing.

Haralick R. M, 1979. Statistical and structural approaches to texture. Proceedings of the IEEE, 67(5), pp.786–804.

Haralick R. M, Shanmugam K & Dinstein Itshak, 1973. Textural Features for Image Classification. Man and Cybernetics: IEEE Transactions, 3(6), pp.610–621.

Hari Babu Nandpuru, Salankar S S, Bora V. R..2014. MRI Brain Cancer Classification Using Support Vector Machine. IEEE Students' Conference on Electrical, Electronics and Computer Science.

Harrison, L., 2011. Clinical Applicability of MRI Texture Analysis,

Hassner M, Sklansky J. 1981.The use of Markov random fields as model of texture.IN: Roseenfled A Image Modelling. Academic Press:185-198

Hayashi, N., et al., Accuracy of Abnormal Paraspinal Muscle Findings on Contrast-enhanced MR Images as Indirect Signs of Unilateral Cervical Root-Avulsion Injury. Radiology, 2002. 223(2): p. 397-402.

Herlidou S. Y. Rolland J. Y. Bansard E Le Rumeur J D de Certaines., 1999. Comparison of automated and visual texture analysis in MRI: characterization of normal and diseased skeletal muscle. Magn Reson Imaging, 17:1393-1397.

Magnetic resonance imaging, 1999, Vol.17(9), p.1393-1397.

Miles KA, Ganeshan B, Griffiths MR, Young RCD, Chatwin CR. 2009. Colorectal cancer: textural analysis of portal phase hepatic CT images as a potential marker of survival. Radiology, volume 250, number 2, pages 444-452.

Herzog, W., Leonard, T.R. & Guimaraes, A.C., 1993. Forces in gastrocnemius, soleus, and plantaris tendons of the freely moving cat. J Biomech, 26(8), pp.945–953. Available at: http://ac.els-cdn.com/002192909390056K/1-s2.0-002192909390056K-main.pdf?_tid=54d3d78a-154a-11e2-bae3-00000aab0f6c&acdnat=1350142157_2c43ed98f8e8174dca1c527a4007cdb9

Holli, K.K. et al., 2010. Texture analysis of MR images of patients with mild traumatic brain injury. BMC medical imaging, 10, p.8.

Holsbeeck M. V. & Introcaso, J., 2001. Sonography of musclr St Loius. Musculoskeletal ultrasound, 2nd Editio.

Huard, J., Li, Y. & Fu, F.H., 2002. Muscle injuries and repair: current trends in research. J Bone Joint Surg Am, 84–A (5), pp.822–832.

Huda, W. & Morin, R.L., 1996. Patient doses in bone mineral densitometry. British Journal of Radiology, 69, pp.422–425.

Hurme, T. et al., 1991. Healing of skeletal muscle injury: an ultrastructural and immunohistochemical study. Med Sci Sports Exerc, 23(7), pp.801–810.

Jarvinen T. A. Kaariainen M, Aarimaa V, Vaittinen S, Kalimo H and Jarvinen M, J.T.L., 2007. Muscle injuries: optimising ercovery. Best Practice & Research Clinical Rheumatology, 21(2), p.317–331.

Jarvinen T. A. Kaariainen M, Aarimaa V, Vaittinen S, Kalimo H and Jarvinen M, J.T.L., 2005. Muscle Injuries: Biology and Treatment. The Amarican Journal of Sports Medicine, 33((5)745-764).

Jean-Sébastien Roy, Caroline Braën, Jean Leblond, François Desmeules, Clermont E Dionne, Joy C MacDermid, Nathalie J Bureau, Pierre Frémont,2015,Diagnostic accuracy of ultrasonography, MRI and MR arthrography in the characterisation of rotator cuff disorders: a meta-analysis,Br J Sports Med doi:10.1136/bjsports-2014-094148

Ji, Q., Engel, J. & Craine, E., 2000. Texture analysis for classification of cervix lesions. IEEE Transactions on Medical Imaging, 19(11), pp.1144–1149.

Joe, G. & Derrickson, B., 2007. Introducton to the Human Body,the essential of anatomy and physiology. , (7th Edition), p.173.

Jungbluth H, Sewry CA, Counsell S, et al. Magnetic resonance imaging of muscle in nemaline myopathy. Neuromuscul Disord. 2004; 14:779–784. doi: 10.1016/j.nmd.2004.08.005

Kasemkijwattana C1, Menetrey J, Bosch P, Somogyi G, Moreland MS, Fu FH, Buranapanitkit B, Watkins SS, Huard J. 2000. Use of growth factors to improve muscle healing after strain injury. Clin Orthop Relat Res. Jan;(370):272-85.

Kary, J.M., 2010. Diagnosis and management of quadriceps strains and contusions. Current Reviews in Musculoskeletal Medicine, 3, pp.26–31.

Kawakami, Y., Ichinose, Y. & Fukunaga, T., 1998. Architectural and functional features of human triceps surae muscles during contraction. J Appl Physiol, 85(2), pp.398–404. Available at: http://jap.physiology.org/content/85/2/398.full.pdf.

Klein, J.H., 1990. MR imaging of muscle and tendon injury. Eur J Radiol, 25(3), pp.198–208.

Tae-Yun Kim, Jaebum Son, and Kwang-Gi Kim, .2011. The Recent Progress in Quantitative Medical Image Analysis for Computer Aided Diagnosis Systems. Healthc Inform Res. 17(3): 143–149.

König T, Steffen J, Rak M, Neumann G, von Rohden L, Töbnnies KD. 2015. Ultrasound texture-based CAD system for detecting neuromuscular diseases. International Journal of Computer Assisted Radiology and Surgey, volume 10, number 9, pages 1493-1503

Koulouris G, Connell, D. Hamstring muscle complex: an imaging review. Radiographics 2005; 25: 571-586.

Kneeland, J.P., 1997. MR imaging of muscle and tendon injury. Eur J Radiol, 25(3), pp.198–208.

Kubo, A. et al., 2012. Absence of mechanical hyperalgesia after exercise (delayed onset muscle soreness) in neonatally capsaicin-treated rats. Neuroscience Research, 73(1), pp.56–60.

Kyriacou, E. et al., 1998. Computer assisted characterization of diffused liver disease using image texture analysis techniques on B-scan images . Nuclear Science Symposium, IEEE, 2, pp.1479–1483.

Lala, D. et al., 2014. Measuring apparent trabecular structure with pQCT: A comparison with HR-pQCT. Journal of Clinical Densitometry, 17(1), pp.47–53. Available at: http://dx.doi.org/10.1016/j.jocd.2013.03.002.

Le Rumeur, E. et al., 1994. Multiparametric classification of muscle T1 and T2 relaxation times determined by magnetic resonance imaging. The effects of dynamic exercise in trained and untrained subjects. Br J Radiol, 67(794), pp.150–156.

Lee, J.C., Mitchell, A.W.M. & Healy, J.C., 2012. Imaging of muscle injury in the elite athlete. British Journal of Radiology, 85, pp.1173–1185.

Lee, J. & Healy, J., Imaing of lower limb injury. Aspetar, pp.142–147.

Lerski R A et al., 1993. Mr image texture analysis-an approch to tissue characterisation. Magn Reson Imaging, 11(6), pp.873–887.

Lerski, R.A. et al., 2015. Application of texture analysis to muscle MRI: 2 – technical recommendations. EPJ Nonlinear Biomedical Physics, 3(1), p.2. Available at: http://www.epjnonlinearbiomedphys.com/content/3/1/2.

Li p. s. et al., 2004. The reproducibility and short-term and long-term repeatability of sonographic measurement of splenic length. Ultrasound Med Biol, 30(7), pp.861–866.

Lin, Y.T. et al., 2008. Sonographic diagnosis of nontraumatic musculotendinous rupture of hamstring. Journal of Medical Ultrasound, 16(3), pp.233–236.

Lieber, R.L. & Friden, J., 1999. Mechanisms of muscle injury after eccentric contraction. J Sci Med Sport, 2(3), pp.253–265.

LLS, W., 2005. Imaging of Muscle Injuries. J Hong Kong Coll Radiol, (8)4, pp.191–201.

Longo, U.G. et al., 2012. Tissue Engineered Strategies for Skeletal Muscle Injury. Stem Cells International, 2012(Article ID 175038), p.13.

Costa Luciano da Fontaoura & Cesar Roberto Marcondes, J., 2009. Shape Classification and Analysis Theory and Practice Second Edi., CRC Press, Taylor & francis Group.

Macdonald, H.M. et al., 2005. Maturity- and sex-related changes in tibial bone geometry, strength and bone-muscle strength indices during growth: a 20-month pQCT study. Bone, 36(6), pp.1003–11. Available at: http://www.sciencedirect.com/science/article/pii/S8756328204004739 [Accessed November 14, 2014].

Masani K, Alizadeh-Meghrazi M, Sayenko DG, Zariffa J, Moore C, Giangregorio L, Popovic MR, C.C.B., 2014. Muscle activity, cross-sectional area, and density following passive standing and whole body vibration: A case series. Spinal Cord Med., 37(5), pp.575–581.

Mass, 1994. Statistical Methods in Ultrasonic Tissue Characterisatio. Massachusettes Institute of Technology (MIT).

Materka, A., 2004. Texture analysis methodologies for magnetic resonance imaging. Dialogues in clinical neuroscience, 6(2), pp.243–250. Available at: http://eutils.ncbi.nlm.nih.gov/entrez/eutils/elink.fcgi?dbfrom=pubmed&id=22033841&retmode=ref&cmd=prlinks%5Cnpapers2://publication/uuid/506F280F-E0D4-403F-B148-669FC085A339.

Materka. A, Strzelecki. M.,1998, Texture Analysis Methods – A Review, Technical. University of Lodz, Institute of Electronics, COST B11 report, Brussels– A Technical Review, Texture Analysis Methods. University of Lodz, Institute of Electronics, COST B11 report, Brussels

Mathias, J.M., Tofts, P.S. & Losseff, N.A., 1999. Texture analysis of spinal cord pathology in multiple sclerosis. Magnetic Resonance in Medicine, 42(5), pp.929–935.

Mohammed. M. Abdelsamea ., 2014. Unsupervised Parallel Extraction based Texture for Efficient Image Representation. Mathematics Department, Assiut University, Egypt.

Nandpuru, H.B., Salankar, S.S. & Bora, V.R., 2014. MRI Brain Cancer Classification Using Support Vector Machine. Electrical, Electronics and Computer Science (SCEECS), 2014 IEEE Students' Conference. IEEE., pp.1–6. Available at: http://ieeexplore.ieee.org/lpdocs/epic03/wrapper.htm?arnumber=6804439.

Malik Qaiser, MRI vs Ultrasound, posted on August 18, 2015, updated on August 24, 2015 by London Imaging Centre.

Megliola A1, Eutropi F, Scorzelli A, Gambacorta D, De Marchi A, De Filippo M, Faletti C, Ferrari FS., 2006. Ultrasound and magnetic resonance imaging in sports-related muscle injuries. Radiol Med. Sep;111(6):836-45.

Mihran, T. & Jain, A.K., 1998. Texture Analysis. The Handbook of Pattern Recognition and Computer Vision, 2nd Edition (World Scientific publishing), pp.207–248.

Miles, K.A. et al., 2009. Colorectal cancer: texture analysis of portal phase hepatic CT images as a potential marker of survival. Radiology, 250(2), pp.444–52. Available at: http://www.ncbi.nlm.nih.gov/pubmed/19164695.

Mir, A.H., Hanmandlu, M. & Tondon, S.N., 1995. Texture Analysis of CT Images. IEEE Engineering in Medicine and Biology, pp.781–786.

Mryka Hall-Beyer 2007 The GLCM Tutorial Home Page

Moreno, M.A. et al., 2012. Effects of Wheelchair Sports on Respiratory Muscle Strength and Thoracic Mobility of Individuals with Spinal Cord Injury. Am J Phys Med Rehabil.

Morris, D.T., An evaluation of the use of texture measurements for the tissue characterisation of ultrasonic images in vivo of human placentae. Ultrasound in Medicine & Biology, 14(5), pp.378–395.

Mueller-Wohlfahrt, H.-W. et al., 2012. Terminology and classification of muscle injuries in sport: The Munich consensus statement. British Journal of Sports Medicine, pp.342–350.

Naqvi, G.A. et al., 2002. Accuracy of ultrasonography and magnetic resonance imaging for detection of full thickness rotator cuff tears. Current Science, 3(4), pp.524–526.

Nielsen, P.K. et al., 2000. Quantitative ultrasound image analysis of the supraspinatus muscle. Clinical biomechanics (Bristol, Avon), 15 Suppl 1, pp. S13–S16.

Nielsen, P.K. et al., 2006. Quantitative ultrasound tissue characterization in shoulder and thigh muscles--a new approach. BMC musculoskeletal disorders, 7, p.2.

Nozaki, M. et al., 2008. Improved muscle healing after contusion injury by the inhibitory effect of suramin on myostatin, a negative regulator of muscle growth. Am J Sports Med, 36(12), pp.2354–2362.

Nsitem, V., 2013. Diagnosis and rehabilitation of gastrocnemius muscle tear: a case report. The Journal of the Canadian Chiropractic Association, 57(4), pp.327–33.

Oge Marques, 2011. Practeical Image and Video Processing Using MATLAB IEEE Press. R. W. T., ed., John Wiley & sons, Inc.

Ojala T & Pietikainen M, 2004. Texture Classification in Machine Vision and Media Processing Unit. University of Oulu, Finland.

Ota, S. et al., 2011. Intramuscular transplantation of muscle-derived stem cells accelerates skeletal muscle healing after contusion injury via enhancement of angiogenesis. Am J Sports Med, 39(9), pp.1912–1922.

Palmer, W.E., Kuongs, S.J. & Elmadadbouh, S.J.H.M., 1999. MR imaging of myotendinous strain. AJR Am J Roentgenol, 173(3), pp.703–709.

Patra, S., Raju, P. & Maruthuperumal, S., 2013. Texture Analysis Using Statistical and Structural Approaches. Ijltet.Org, 3(1), pp.267–274. Available at: http://ijltet.org/wp-content/uploads/2013/11/38.pdf.

Pavlopoulos, S. et al., 1996. Evaluation of texture analysis techniques for quantitative characterization of ultrasonic liver images. Engineering in Medicine and Biology Society, Bridging Disciplines for Biomedicine. Proceedings of the 18th Annual International Conference of the IEEE, 3, pp.1151–1152.

Peetrons, P., 2002. Ultrasound of muscles. Eur Radiol, 12(1), pp.35–43.

Peng, W. et al., 2015. A Novel Computational CT Image Analysis Method for Classifying Nodules from Normal.

Phillips & Dwayne, 2000. Image Processing in C Electronic., R & D Publications.

Pillen, 2011. Skeletal muscle ultrasound. Neurological Research.ISBN:1743-1328 (Electronic)\r0161-6412 ISSN: 01616412.

Pillen, S. et al., 2009. Quantitative gray-scale analysis in skeletal muscle ultrasound: A comparison study of two ultrasound devices. Muscle and Nerve, 39, pp.781–786.

Powell R W, 1883. Lawn tennis leg. Lancent, 2, p.44.

Prasad, B.G. & Krishna, a N., 2011. Statistical texture feature-based retrieval and performance evaluation of CT brain images. 2011 3rd International Conference on Electronics Computer Technology, pp.289–293. Available at: http://ieeexplore.ieee.org/lpdocs/epic03/wrapper.htm?arnumber=5941703.

Qiang.Ji, Engel, J. & Craine, E., 2000. Texture analysis for classification of cervix lesions. Medical Imaging, IEEE Transactions, 19(11), pp.1144–1149.

Rittweger, J. et al., 2000. Bone-muscle strength indices for the human lower leg. Bone, 27(2), pp.319–326.

Romijn R. L.1, Thijssen J. M, Oosterveld B J, Verbeek A M.1991. Ultrasonic differentiation of intraocular melanomas: parameters and estimation methods. Ultrasonic Imaging.13(1):27-55.

Rong-Sheng Lu et al., 2006. Grinding surface roughness measurement based on the co-occurrence matrix of speckle pattern texture. Applied Optics, 45(35), pp.8839–8847.

Rosner, B., 2010. Fundamentals of biostatistics - seventh edition, Available at: http://books.google.com/books?hl=en&lr=&id=-CQtWiJJL0cC&oi=fnd&pg=PR7&dq=Fundamentals+of+Biostatistics&ots=W1K4reTwct&sig=eVAhrOjm1iAJhMLlBJH9B_LvqSw.

Rosslyn, S., 2011. Digital Imaging and Communications in Medicine (DICOM) Part 1: Introduction and Overview. Medicine, pp.1–22.

Roy, J.-S. et al., 2015. Diagnostic accuracy of ultrasonography, MRI and MR arthrography in the characterisation of rotator cuff disorders: a systematic review and meta-analysis. British journal of sports medicine, 49(20), pp.1316–28. Available at: http://www.ncbi.nlm.nih.gov/pubmed/25677796%5Cnhttp://www.pubmedcentral.nih.gov/articlerender.fcgi?artid=PMC4621376.

Rybak, L.D. & Torriani, M., 2003. Magnetic resonance imaging of sports-related muscle injuries. Top Magn Reson Imaging, 14(2), pp.209–219.

Samira Saraya a, Rehab El Bakry Ultrasound: Can it replace MRI in the evaluation of the rotator cuff tears?The Egyptian Journal of Radiology and Nuclear Medicine (2016) 47, 193–201.

Saitoh H. CT findings of muscular dystrophy: limb girdle type (LG), myotonic type (MYD) and Duchenne type (DMD) (In Japanese). Nihon Igaku Hoshasen Gakkai Zasshi. (1991) 51(7): 790-8.

Schiaffino S, Reggiani C. 1996 Molecular diversity of myofibrillar proteins: gene regulation and functional significance. Physiol Rev. 76:371–423Sharma, M. & Singh, S., 2001. Evaluation of texture methods for image analysis. Intelligent Information Systems Conference, The Seventh Australian and New Zealand, pp.117–121.

Shelly, M.J. et al., 2009. MR imaging of muscle injury. Magn Reson Imaging Clin N Am, 17(4), p.757–73, vii.

Sheppard, M.A. & Shih, L., 2007. Image Texture Clustering for Prostate Ultrasound Diagnosis. Ultrasonics Symposium, IEEE, 28–31, pp.2473–2476.

Sikio, M. et al., 2015. The effect of region of interest size on textural parameters. 9th International Symposium on Image and Signal Processing and Analysis, ISPA 2015, (Ispa), pp.149–153.

Sipila S. & Suominen H., 1991. Ultrasound imaging of the quadriceps muscle in elderly athletes and untrained men. Muscle Nerve. 14(6) 527-533.

Skoch A, Jirák D, Vyhnanovská P, Dezortová M, Fendrych P, Rolencová E, H.M., 2004.Classification of calf muscle MR images by texture analysis. MAGMA, 16(6), pp.259–267.

Shu, Z. et al., 2010. Texture classification of tissues in computed tomogeraphy based on wavelet-based contourlet packet. Proceedings - 2010 3rd International Congress on Image and Signal Processing, CISP 2010, 4, pp.1966–1969.

Smet, D. & Best, T.M., 2000. MR imaging of the distribution and location of the acute hamstring injuries in atheletes. AJR Am J Roentgenol, 174(2), pp.393–399.

Smith T O, Hunt N J & Wood S J, 2006. The physiotherapy management of muscle haematomas. Physical Therapy in Sport, 7(4), pp.201–209.

Smith, N.B. & Webb, A., 2013. Introduction toMedical Imaging, Physics, Engineering and Clinical Applications 4th ed. M. B. Smith, ed., Cambridge: Cambridge, United Kingdom. Available at: www.cambridge.org/9780521190657.

Sogawa K, Nodera H, Takamatsu N, Mori A, Yamazaki H, Shimatani Y, Izumi Y, Kaji R. 2017. Neurogenic and myogenic diseases: quantitative texture analysis of muscle ultrasound data for differentiation. Radiology, volume 283, number 2, pages 492-498.

Speer, K.P., Lohnes, J. & Garrett Jr., W.E., 1993. Radiographic imaging of muscle strain injury. Am J Sports Med, 21(1), p.89–95; discussion 96.

Srinivasan G. N. and Shobha G, 2008. Statistical Texture Analysis. In proceedings of world academy of science, Engineering and Technology, 36, pp.1264–1269.

Staron, R.S., 1997. Human skeletal muscle fiber types: delineation, development, and distribution. Can J Appl Physiol, 22(4), pp.307–327.

Steinbach, Fleckenstein, J. & Mink, J., 1997. MR imaging of muscle injuries. Semin Musculoskelet Radiol, 1, pp.127–141.

Strang, J.G. & Dogra, V., 2007. Body CT Secrets, Questions you will be asked, Philadelphia: Elsevier Mosby.

Stratec Medizintechnic, 2007. XCT 2000 Manual,

Sttrzelecki, M., 1998. Texture Analysis Methods- A Review. Technical University of Lodz, Institute of Electronics, COST B11 Report, Brussles.

Stuart B. Porter 2013. Tidy's Physiotherapy,

Sun Y.N. et al., 1996. Ultrasonic image analysis for liver diagnosis. Engineering in Medicine and Biology Magazine, 15(6), p.I 93-101.

Srinivasan G. N. and Shobha G (2008) Statistical Texture Analysis. In Proceedings of World Academy of Science, Engineering and Technology.36, 1264-1269

Swash, M., Brown, M.M. & Thakkar, C., 1995. CT muscle imaging and the clinical assessment of neuromuscular disease. Muscle & Nerve, 18(7), pp.708–71

Szczypinski, P.M., Strzelecki, M. & Materka, A., 2007. Mazda - a software for texture analysis. In Information Technology Convergence, 2007. ISITC 2007. International Symposium on. pp. 245–249.

Szczypiński, P.M. et al., 2009. MaZda-A software package for image texture analysis. Computer Methods and Programs in Biomedicine, 94, pp.66–76.

Tae-Yun Kim, , Jaebum Son, P and Kwang-Gi Kim, PhD, 2011 Sep;17. The Recent Progress in Quantitative Medical Image Analysis for Computer Aided Diagnosis Systems, Biomedical Engineering Branch, National Cancer Center, Goyang, Korea.Biomedical Engineering Branch, National Cancer Center, Goyang, Korea.

Takahashi, H. et al., 1994. Changes in magnetic resonance images in human skeletal muscle after eccentric exercise. Eur J Appl Physiol Occup Physiol, 69(5), pp.408–413.

Takebayashi, S. et al., 1995. Sonographic findings in muscle strain injury: clinical and MR imaging correlation. J Ultrasound Med, 14(12), pp.899–905.

Ten Dam, L., et al., Reliability and accuracy of skeletal muscle imaging in limb-girdle muscular dystrophies. Neurology, 2012. 79(16): p. 1716-1723.

Thomas, E., 2005. An introduction to medical statistics for health care professionals: basic statistical tests. Musculoskeletal care, 3(4), pp.201–212.

Vapnik and A. Lerner. 1963. Pattern recognition using generalized portrait method. Automation and Remote Control, 24.

Van Schie, H.T.M. et al., 2001. Efficacy of computerized discrimination between structure-related and non-structure-related echoes in ultrasonographic images for the quantitative evaluation of the structural integrity of superficial digital flexor tendons in horses. American Journal of Veterinary Research, 62, pp.1159–1166.

Varela J. R. et al., 2000. Complete rupture of the distal semimembraosus tendon with secondary hamstrin muscle atrophy: MR finding in two cases. Skeletal Radiol, 29(6), pp.362–364.

Verrall, G.M. et al., 2006. Assessment of physical examination and magnetic resonance imaging findings of hamstring injury as predictors for recurrent injury. The Journal of orthopedic and sports physical therapy, 36(4), pp.215–224.

Wagner, 1999. Handbook of computer vision Academic P.,

Westbrook, C. & Carolyn kaut, 1998. MRI in Practice Second edition., Blackwell Science.

Wolfgang & Birkfellner, 2014. Applied Medical Image Processing: a basic course Second Edi., Taylor & Francis Group, LLC.

Worsley P. R., Kitsell , F ., Samuel , D ., Stokes, M.., 2014. Validity of measuring distal vastus medialis muscle using rehabilitative ultrasound imaging versus magnetic resonance imaging". , 19, pp.259–263.

Youssef A. M. and Sharawi A A,. 1990. KSODATA clustering analysis for diffuse liver diseases. In Proc. IEEE Symp. Ultrasound.

Zhi-Jun, H., et al., Accuracy of magnetic resonance imaging signal intensity ratio measurements in the evaluation of multifidus muscle injury and atrophy relative to that of histological examinations. Spine, 2014. 39(10): p. E623-E629.

Zauner, G. et al., 2006. Denoising of computed tomography images using multiresolution based methods. Proceedings of ECNDT, Berlin Sept, pp.1–9. Available at: http://citeseerx.ist.psu.edu/viewdoc/download?doi=10.1.1.151.6340&rep=rep1&type=pdf.

Internet websites

https://home.comcast.net/~pegglestoncbsd/muscular.htm

http://classes.midlandstech.edu).

http://media.omedix.com?healthwise/nr55552069.jpg

http://www.essentialoilspedia.com/wp-content/uploads/bruise.jpg).

www.metabolicimaging.org.

http://fas.org/irp/imint/docs/rst/Intro/Part2_26c.html

www.revisemri.com

www.keyres-technologies.com,www.maths.bris

www.socscistatistics.com

http://physioworks.com.au/injuries-conditions-1/calf-muscle-tears

Appendix A: Physics and Technology of Magnetic Resonance Imaging

A.1 Introduction

This section aims to briefly describe the basic principles of Magnetic Resonance Imaging (MRI) to understand the quantitative analysis of the acquired images.

Magnetic resonance imaging (MRI) is based on a physics phenomenon that is called nuclear magnetic resonance (NMR). It was first theorised in 1946 by Felix Bloch of Stanford University. NMR is the study of the magnetic properties of the atomic nucleus. Nuclei with an odd number of protons or neutrons have an electric charge and nuclear spin and therefore they produce an electromagnetic field. If such nuclei are placed in a strong magnetic field, they may interact by absorbing energy and subsequently releasing energy into the surrounding environment. Interacting between nuclei and applied magnetic field is called NMR. This interacting occurs at Larmor precessional frequency. In other words, NMR is a method that depends on the distribution and behaviour of the magnetic moments of nuclei. Hydrogen nuclei (protons) are more sensitive than any other nuclei (Hajek et al. 2006). About two third of the human body is composed of water, and this justifies why MRI has become widely implemented in medicine. Water content differs among tissues and organs (Joe & Derrickson 2007). Abnormalities (diseases) yield changes in tissue or organ water content.

In MRI the patient is placed in a strong static magnetic field (B_0). The body is then stimulated by a radio frequency (RF) field (B_1) and this results in a change in hydrogen proton orientation (excitation), as illustrated in Figure A.1. Relaxation causes RF energy to be released and thus detected in MRI scanner. Finally, the detected signal is used to construct in internal image of the exposed part of the body.

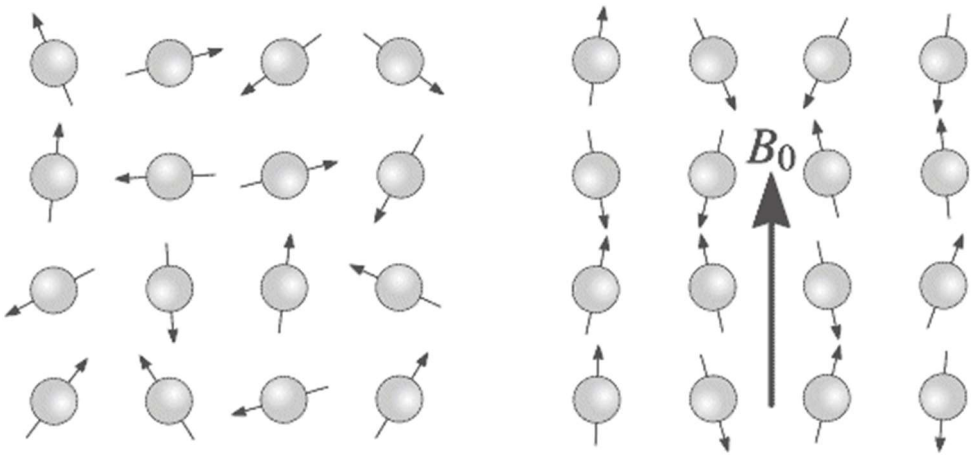

Figure A.1: Simplified distribution of free protons without and with an external magnetic field(B_0).Without an external magnetic field, protons in random orientation of magnetic moment (magnetic moment=0). With external magnetic field (B_0), protons oriented in two possible ways: parallel and antiparallel to the external magnetic field.

The first scanner was installed during the 1980s. Since then, MRI has become the major medical diagnostic technique for imaging anatomical structure and physiological functions of the human body (Carlton and. Adler 2013). It utilises the properties of hydrogen atoms to create an image of body organs and tissue.

A.2 MRI Instrumentation

A.2.1 Introduction

MRI equipment consists of a magnet, a radiofrequency (RF) subsystem, gradient coils and a computer, as shown in Figure A.2.

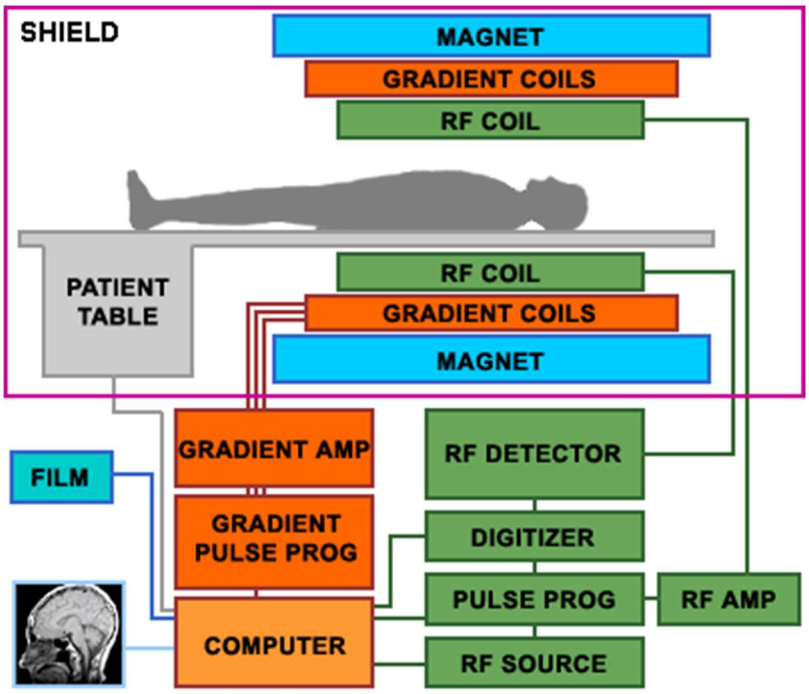

Figure A.2: MRI scanner main components (http://fas.org/irp/imint/docs/rst/Intro/Part2_26c.html).

A.2.1.1 MRI Magnet

The magnet is the heart of the MRI scanner. The performance criteria are the field strength and field homogeneity, which depends on the magnet's design. The magnet produces an extremely strong magnetic field to magnetize tissue. The strength of the magnet is rated using a unit of measurement called a tesla (T) and another older unit that is known as a gauss (1 tesla=10,000 gauss). Nowadays, MRI magnets creates a magnetic field strength of between 0.5 tesla and 3.0 tesla (Carlton and Adler 2013). The Earth's magnetic field is 0.5 gauss and this indicates how strong the MRI magnetic field is.

MRI magnets can be classified, in terms of their field strength, into 5 categories:

1. Ultrahigh field (4.0 to 7.0 T)
2. High field (1.5 to 3.0 T)
3. Midfield (0.5 to 1.4 T)
4. Low field (0.2 to 0.4 T)
5. Ultralow field (< 0.2 T)

In addition to the previous classification, MRI magnets can be classified into three main types according to their design:

1. Permanent magnet.
2. Resistive magnets.
3. Superconductive magnets.

In a permanent magnet, the magnetic field is always there. In other words, the magnetic field is on all of the time and cannot be switched off. This type has low cost and low maintenance but does not offer a sufficiently strong field (Westbrook and Kaut 1998).

The resistive magnet is based on a flowing current in a coil, which has electrical resistance and produces a magnetic field. The produced magnetic field can be switched on and off (Westbrook and Kaut 1998).

Most MRI scanners use a superconductor magnet to create high field strength (1.5T). Maintaining the produced magnetic field steady needs a good control of coil resistance. The magnetic field that is generated is produced by passing a current into magnet winding, and this generates heat. Superconductivity is temperature dependent; reducing the temperature will reduce the winding resistance (giving less heat) for the current. To produce a system with zero resistance, the magnet must therefore be cooled down by submerging it in a cryogenic liquid. The commonly used cryogenic liquid in superconducting MRI systems is liquid helium (He). The temperature of liquid helium is 269.1° below zero degrees Celsius. The resistance-free system is thus called a superconducting system, and this yields the highest-quality imaging (Carlton and Adler 2013).

A.2.1.2 Radiofrequency (RF) Subsystem

The radio frequency (RF) subsystem is the antenna (coil) of the MRI, which is composed of a transmitter and one or more receivers. The RF transmitter is used to generate the RF signal (pulse) which excites the hydrogen protons. It utilizes alternating current and hence generates a very weak oscillating magnetic field called the secondary magnetic field (B_1). The specific frequency required to excite protons is known as Larmor precessional frequency:

$\omega_1 = \gamma B_0$

where B_0 is the main magnetic field strength, and γ is a constant that is called the gyromagnetic ratio. The hydrogen gyromagnetic ratio is 42.6 megahertz/tesla (MHz/T) (Carlton and Adler 2013). The hydrogen proton Larmor frequency at 1.5 T magnetic field, can be calculated using above equation as follows:

$$\omega_1 = 42.6(\text{MHz/T}) * 1.5(\text{T}) = 63.9 \text{ MHz}$$

There are two methods of positioning the transmitter coil. Firstly, the transmitter coil is positioned within the scanner itself. In the second method, the transmitter coil is positioned on the patient during the scan.

The receiver coil is used for MR signals that are emitted by the patient's body. For all body parts there are specific coil designs which fit and which yield the best MR signal detection. MR coils have different shapes and sizes, as shown in Figure A.3.

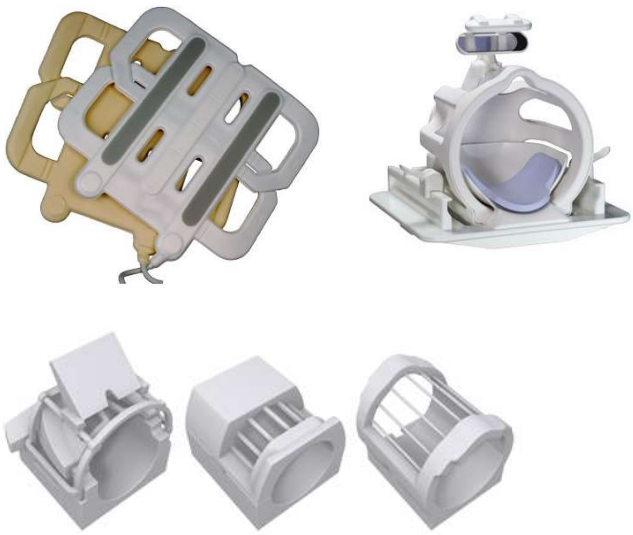

Figure A.3: MRI different patient coils (Carlton and Adler 2013).

A.2.1.3 Gradient Coils

A gradient indicates a rate of increase or decrease (a slope). In general, gradient coils function to produce deliberate variations in the total static magnetic field according to the location of MR slices (spatial information encoding). This is achieved by superimposing the gradient magnetic field that is produced by the gradient coils over the main magnetic field in 3 orthogonal directions that correspond to the axes x, y, and z. The labelling of these coils is based on the direction in which the gradient field is created, as illustrated in Figure A.4. The coil that creates a gradient field along the right-left direction of the magnet/patient is labelled as the x-gradient coil. The coil that creates a gradient field along the anterior-posterior direction of the magnet/patient is labelled as the y-gradient coil. The coil that creates a gradient field along the head-foot direction of the magnet/patient is labelled as the z-gradient coil. All 3 sets of gradient coil windings are situated within the bore of the magnet.

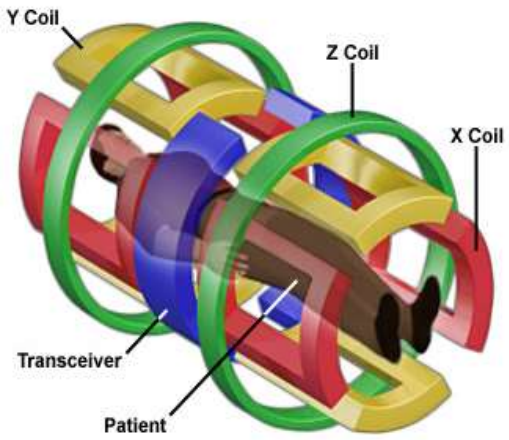

Figure A.4: Gradient coil configurations. (https://nationalmaglab.org/education/magnet-academy/learn-the-basics/stories/mri-a-guided-tour)

The total magnetic field is equal to B_0 at the isocentre, even when a gradient is utilised. The passage of current through one of the gradient coils induces a gradient magnetic field around it. The magnetic field that is generated either subtracts from, or adds to, the static magnetic field (B_0). This mechanism is performed in a linear fashion so that the precessional frequency that is experienced by the protons situated along the gradient coil axis can be predicted. In protons that are located at an increased magnetic field strength, the precessional frequency increases, whereas protons that are located

at a decreased magnetic field strength decrease their frequency. As a result of this, the positions of protons along the gradient can be identified according to their precessional frequency, and this process is therefore known as spatial encoding. Spatial encoding helps to locate a slice within the selected scan plane (axial, sagittal or coronal) (Westbrook and Kaut 1998).

A.3 MRI Physics

Nuclei which have an odd atomic mass number (the sum of the nuclear particles) are magnetically active, and property. They have nuclear spin and exhibit a magnetic property called a magnetic moment. In MRI this property of the hydrogen nucleus is utilised. Hydrogen has a single proton in its nucleus and it is almost 100 % abundant in the human body. Such hydrogen spin (proton) behaves as a tiny bar magnet with two poles, and this is referred to as a dipole (Carlton and Adler 2013).

The magnetic moments of hydrogen protons are randomly aligned, but when placed in a strong externally applied magnetic field (B_0) their magnetic moments align either with (parallel/low energy state) or against (anti-parallel/high energy state) the direction of the applied magnetic field. As a result of a slightly higher number of protons being in parallel alignment, the tissue will exhibit a bulk or a net magnetisation vector (M_0) that is aligned with the direction of the externally applied magnetic field ($B_{0)}$. This condition is known as thermal equilibrium. The net magnetisation vector is defined by 3 components (a three-dimensional Cartesian co-ordinate system). Longitudinal magnetisation (M_z) is along the z direction, which is parallel to the applied magnetic field (B_0). The remaining two components are called transverse (horizontal) magnetisation (M_x and M_y). The longitudinal magnetisation cannot be measured and therefore it must be tipped into the x-y transverse plane. To accomplish this, a secondary magnetic field is needed. This field is called the RF field and it is applied as a pulsed magnetic field (B_1), as described earlier (Carlton and Adler 2013).

The hydrogen protons precess about the direction of the applied magnetic field (B_0) in the same way as a top wobbles as it spins, as shown in Figure A.5. The rate of hydrogen precession (the Larmor frequency) is B_0 strength dependent. At thermal equilibrium,

the individual protons do not precess at exactly the same frequency (they are not in phase) and this is due to the magnetic field not being homogeneous (uniform), particularly after the patient is placed in the magnetic field. The other reason is that the hydrogen in water molecules precesses at a higher frequency than those in fat molecules. The difference in frequency is known as a chemical shift. The chemical shift is field strength (B_0) dependent. Increasing B_0 yields an increase in chemical shift (Carlton and Adler 2013).

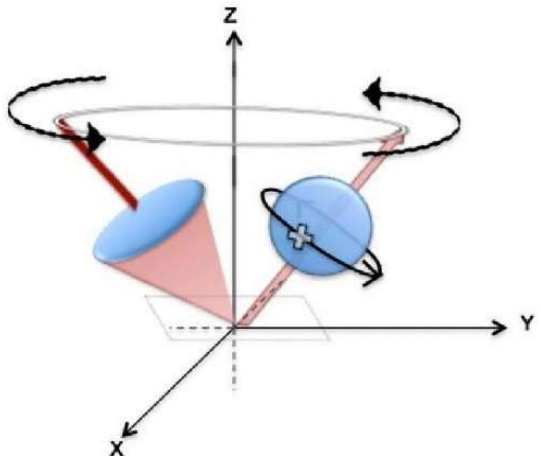

Figure A.5: Proton of Hydrogen precessing around the direction of the applied magnetic field in the way as a top wobbles when it spins (courtesy of www.medscape.com)

Longitudinal magnetisation recovery is caused by release of energy by the protons to the surrounding, or the lattice, and it is often called spin lattice relaxation. The rate of recovery is an exponential process with a recovery time constant known as T1. At T1, 63% of the longitudinal magnetisation (M_z) has recovered in the tissue as shown in Figure A.6(A). (Westbrook & Kaut 1998). T1 relaxation times vary with tissue type. For example, fat protons has a short T1 relaxation time of approximately 150 milliseconds at 1.5 T, and water-based protons have a relatively long T1 relaxation time of approximately 2000 milliseconds at 1.5 T (Carlton and Adler 2013).

Transverse magnetisation decay is caused by protons exchanging energy with neighbouring protons. The energy exchange is caused by the interaction of each of the protons with its neighbour, and it is often called spin spin relaxation. The rate of decay

is also an exponential process. At T2 63% of the transverse magnetisation (M_{xy}) has decayed (lost) in tissues, as shown in Figure A.6(B) (Westbrook and Kaut 1998). T2 relaxation times for all tissues are relatively short. For example, the fat proton T2 relaxation time is approximately 200 milliseconds at 1.5 T. In addition to spin spin relaxation, the chemical shift and inhomogeneities in the magnetic field immediately begin to affect the spin and cause faster decay of transverse magnetisation. This overall effect is characterised by $T2^*$ (pronounced T2 star) (Carlton and Adler 2013).

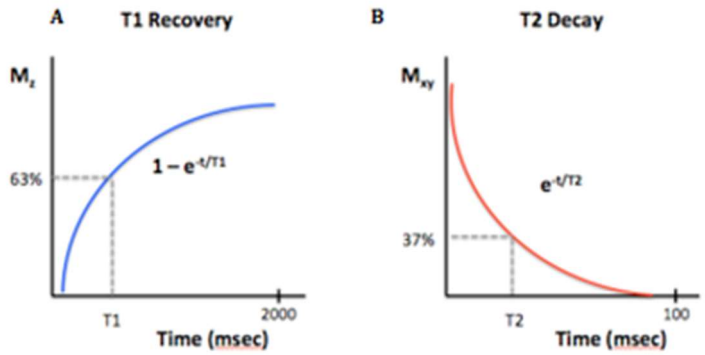

Figure A.6: T1 recovery (A) and T2 decay (B) signals.

To tip the tissue's net magnetisation (M) from the longitudinal (M_z) to the transverse plane (M_{xy}), the frequency of the RF pulse (B_1) must be centred at about the Larmor or resonant frequency for the protons (efficient energy transfer). If this condition is not achieved, the net magnetisation will not be affected. The protons (spins) begin to precess in phase, and some of the spins that are in parallel alignment (low energy state) absorb energy from the RF field and move to a high energy state (anti-parallel alignment). This process results in rotation and the tipping of the net magnetisation vector towards the transverse plane. The greater the amount of RF power, the further the net magnetisation vector tips away from the longitudinal alignment (M_z) into the transverse plane (M_{xy}). Flip angles are the result of the angular displacement of the longitudinal magnetisation moment vector (M_z) from the equilibrium position towards the transverse plane. The flip angle is dependent on the duration and amplitude of the RF pulse signal (B_1 field) in a linear fashion. For a fixed B_1 field amplitude, a 90° displacement takes half the time of 180° displacements and yields the largest possible transverse magnetisation moment vector (M_{xy}). Moreover, with angles less than 90°, less time is needed to displace the longitudinal magnetisation moment vector (M_z), and a larger transverse magnetisation per unit of excitation time is achieved.

Furthermore, if 90° RF pulses are used and followed before recording (sampling) the MR signal by an 180° RF Pulse, this is known as a spin echo (SE). The purpose of using the 180° is to correct the local in homogeneities and the slight resonance frequency difference between the water based protons and the fat based protons (chemical shift). There is a type of RF pulse sequence other than SE, and this is known as gradient recalled echo (GRE). It is used for very rapid acquisition techniques when patient holds his or her breath during examination of liver, kidney or cardiac studies. The flowing blood appears hyper intense (bright) relative to the surrounding tissue (Carlton and Adler 2013).

When the B_1 field is switched off, the net magnetisation now precesses in the transverse (xy) plane. The receiver coils are designed to make the net magnetisation vector precess through the loop of the coil material (copper). This will induce a current in the coil conductor which is known as the MR signal. The electronic equipment associated with the receiver coil (including analogue to digital convertor) will measure and sample the MR signal.

On switching off the RF pulse, the spins start to relax back to the start point and try to align with B_0 into longitudinal direction. During relaxation, the spins give up the absorbed RF energy and the induced current in the receiver coil decreases. The relaxation process is called free induction decay (FID). The amount of magnetisation in the longitudinal plane (M_z) gradually increases (Figure A.7) and this is called recovery and is caused by T1 recovery, whereas the amount of magnetisation in the transverse plane (M_{xy}) gradually decreases is called decay and (Westbrook & Kaut 1998).

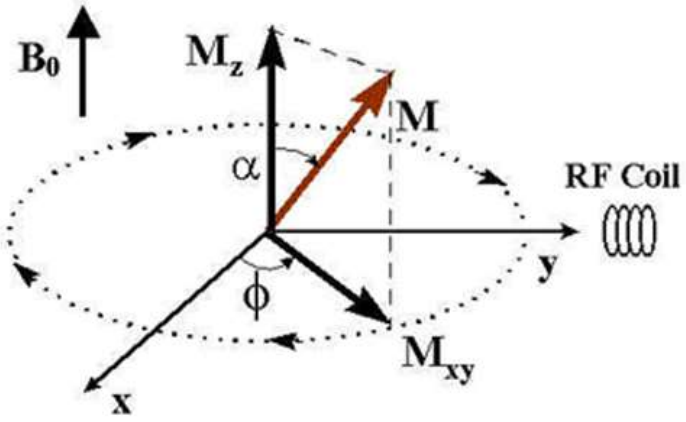

Figure A.7: Longitudinal magnetisation (Mz) is the vector component of the magnetic moment in the z-direction. Transverse magnetisation (Mxy) is the vector component of the magnetic moment in the xy-plane (Bushberg et al. 2012).

The RF pulse sequence consists of several parameters, and these are as follows:

1. The time of repetition (TR), which is the time from the application of one RF pulse to the application of the next. It is measured in milliseconds. The TR controls the amount of the protons' relaxation in between two successive RF pulses, as shown in Figure 3.30.
2. The time of echo (TE), which is the time from the application of the RF pulse signal to the peak of the signal being induced into the coil. It is measured in milliseconds. TE determines how much decay of the transverse magnetisation (M_{xy}) is allowed to occur before the signal record as shown in Figure A.8.

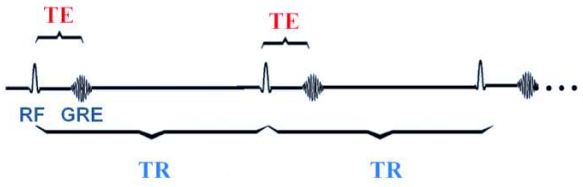

Figure A.8: Time of repetition (TR) and time of echo (TE) (Bushberg et al. 2012).

A.3.1 Image Weighting and Contrast

The main advantage of MRI, when compared with other imaging technology is the excellent soft tissue discrimination in the images. It is therefore important to discuss the factors that affect the image contrast.

A.3.1.1 MRI Image Contrast

Image contrast indicates signal variations within the image areas with a high signal appear white on the image and areas with a low signal appear dark on the image with areas of intermediate signal having different shades of grey. The magnetisation vector can be discriminated into individual vectors for each tissue that is present in the patient, for instance, muscle, fat, and cerebrospinal fluid (CSF).

If the transverse magnetisation (M_{xy}) component is high, then the tissue has a high signal. This results from the coil recording high signal amplitude, which yields bright areas in the image and vice versa.

Water (H_2O) is hydrogen linked to oxygen. The oxygen molecule tends to steal the electrons away from the hydrogen nucleus. This results in an effect on the main magnetic field. Fat is hydrogen linked to carbon and is composed of large molecules named lipids. The carbon does not take the electron from around the hydrogen nucleus, but it remains in an electron cloud that protects the nucleus from the effect of the main magnetic field. The Larmor frequency of hydrogen in water is thus higher than that of hydrogen in fat. Hydrogen in fat recovers faster along the longitudinal axis (M_z) than that in water and transverse magnetisation (M_{xy}) decays faster than in water. Water and fat thus appear differently in MR images (Westbrook and Kaut 1998; Carlton and Adler 2013).

In summary, fat regains longitudinal magnetisation (M_{xy}) rapidly (shorter T1 recovery time) and water regains longitudinal magnetisation (M_{xy}) slowly (longer T1 recovery time), as shown in Figure A.9 (Westbrook and Kaut 1998).

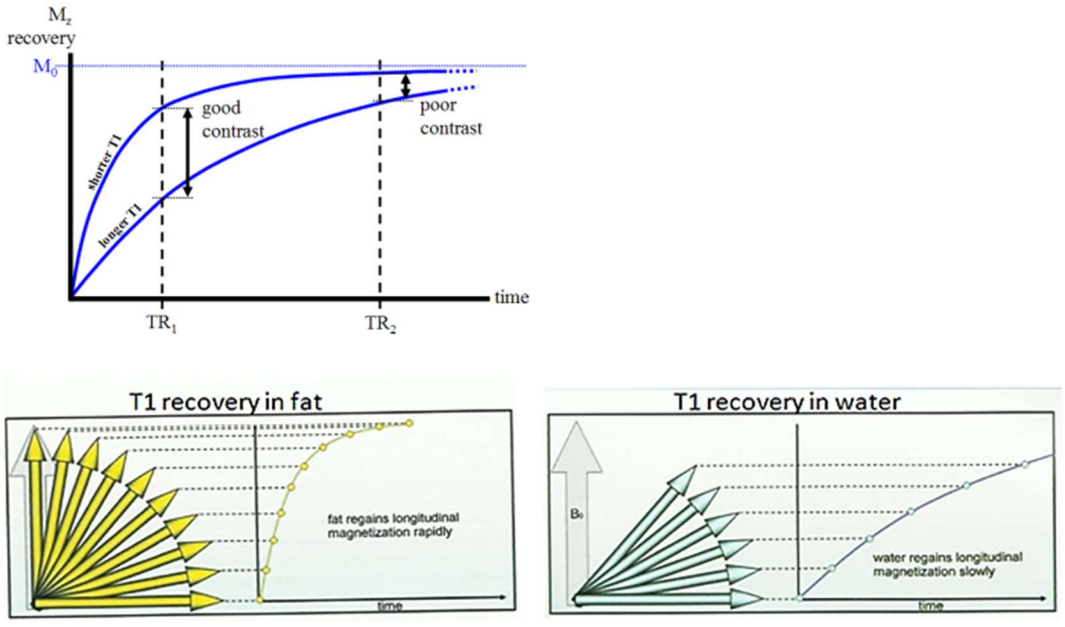

Figure A.9: T1 recovery in fat is faster than in water (www.revisemri.com).

Moreover, T2 decay in fat is more efficient than that in water, it is therefore short (200 ms), whereas in water it is less efficient and it is therefore long (2000 ms), as depicted in Figure A.10 (Westbrook and Kaut 1998).

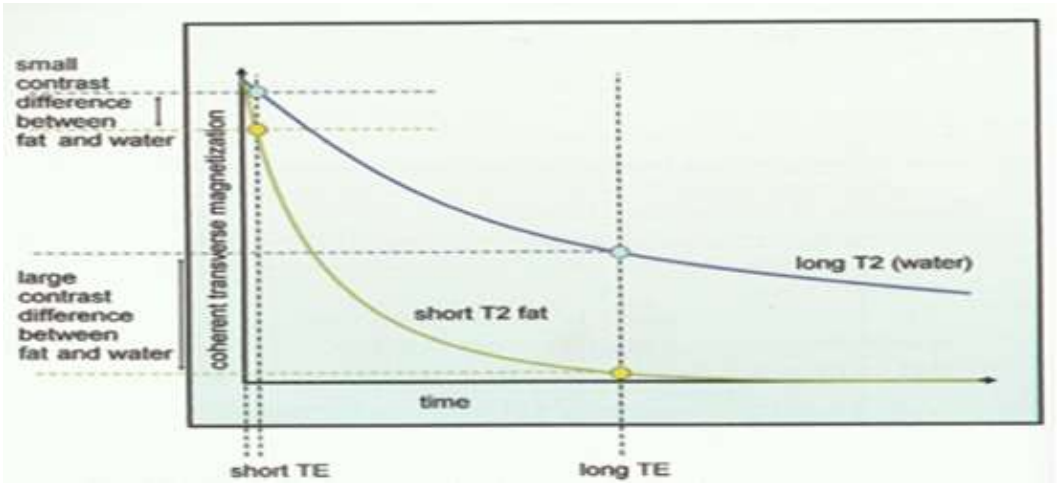

Figure A.10: The difference between fat and water decay(www.revisemri.com).

Proton density contrast reflects the variation in the proton densities between the tissues being imaged. The variations are related to transverse magnetisation. Tissues with a high proton density have a large transverse magnetisation component and so have a high signal, which appears as bright areas. Tissues with a low proton density have a small transverse magnetisation component and so appear as dark areas. Proton density depends on the tissue undergoing examination (Westbrook and Kaut 1998) .

A.3.1.2 MR Weighting Images

In spin echo imaging the specific values of TR and TE have an impact on T1, proton density or T2 contrast, and this weights an image such that one contrast mechanism predominates over the other two:

- Water has long T1 and relaxationT2 time.
- Fat has short T1 and relaxationT2 time.
- To produce a high signal (bright), there must be a large transverse magnetisation component (M_{xy}) to induce a large signal in the receiver coil.
- To produce a small signal (dark), there must be a small transverse magnetisation component (M_{xy}) to induce a small signal in the receiver coil.

- T1 weighted images are characterised by dark water and bright fat.
- T2 weighted images are characterised by bright water and dark fat.
- Proton density weighted images are characterised by areas with high proton density that are bright, and areas with low proton density that are dark.

In T1 weighted images, TR controls the amount of T1 weighting and it must be short. In T2 weighted images, the TE controls the amount of T2 weighting and it must be long. In proton density images:

- To diminish T2, TE must be short.
- To diminish T1, TR must be long.

Appendix B: The Stratec XCT2000 pQCT scanner

B.1 Description of the Scanner

The Stratec XCT 2000 pQCT device is a fully automated measuring system for the determination of bone density and soft tissue distribution and density. It consists of two main parts: a scanner (Figure B.1) and a control/analysis computer system. The scanner consists of an X-ray source and a translation-rotation multi-detector system. The X-ray tube has been specially developed with a very small focal spot. It operates at 56.7 kV and an anode current of less than 0.3 mA. The mean X-ray energy is 37 keV, after being filtered by 15mm metal (6 mm aluminum and 9 mm copper). The energy spectrum of the X-ray beam has a full width at half maximum (FWHM) of 22 keV. The number of projections is either 180 or 360. The size of the pixels is operator defined within a range of 0.2 to 2.0 mm with step increments of 0. 1 mm. The speed of the translational scan movement is adjustable from 3 to 40 mm/s in steps of 0.1 mm/s.

The detector system consists of 12 semi-conductor detectors, a highly charge-sensitive preamplifier, a shaping amplifier and a comparator; these rotate in a gantry which has an opening diameter of 140 mm.

During the CT-scan, the x-ray beam passes perpendicular to the axis of the scanned object. After each scan, the transverse scan gantry rotates 12°. The angular distance of the 12 detectors relative to the x-ray source is 1.0°. The gantry does 15 rotations, which results in 180 projections (15 times 12). Hence, it covers the necessary angular range of 180° (Stratec Medizintechnic 2007).

The control system consists of a DOS-compatible computer with a high resolution colour display monitor and a colour ink jet printer. The computer controls the complete scanning procedure and integrates all of the information obtained into the slice that is reconstructed. During acquisition, the operator makes a choice 1 or 2 blocks, where each block represents a combination of number of projections and angular step to cover an angular range of 180°. With 1 block, there are 180 projections with an angular step of 1° while for 2 blocks, there are 360 projections with an angular step of 0.5°.

One block yields 15 slices while two blocks yield 30 slices. Although the manufacturer does not explicitly state the type of reconstruction algorithm, it is most likely to be filtered back-projection. The tomographic slice is divided into pixels. As the slice has a predetermined constant thickness, the pixels represent volume units in tissue (voxels).

Figure B.1: *pQCT scanner.*

B.2 Measurement Principle

The pQCT scanner measures the attenuation of the X-ray beam passing through the tomographic slice. The attenuation along a particular X-ray path depends on the linear attenuation coefficient and the thickness of the tissues in that path. The linear attenuation coefficient depends on tissue density, average atomic number and electron density (number of electrons per unit mass). Mass attenuation coefficient is the linear coefficient divided by density. The estimation of bone mineral density (calcium hydroxyapatite) is the most usual procedure for which attenuation measurements can be used.

The linear attenuation coefficient (μ) is the fractional reduction in intensity of the X-ray beam per unit increase in thickness. This is usually expressed in units of inverse centimeters (cm^{-1}) (Bushberg et al. 2012). Monoenergetic X-rays are attenuated exponentially, i.e. their intensity is reduced by a fixed percentage for each fixed

increase in thickness of a given material. A polyenergetic X-ray beam with a narrow spectrum (small FWHM) behaves in a similar way to a monoenergetic beam.

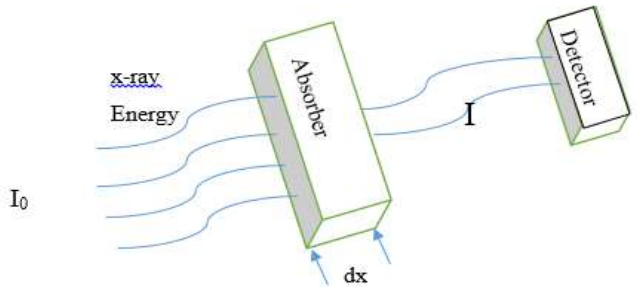

Figure B.2: *Linear attenuation principle.*

The X-ray beam transmitted intensity can be calculated according to the following equation:

$$I = I_0 e^{-\mu.dx}$$

where I_0 is the incident intensity, I is the transmitted intensity, μ is the linear attenuation coefficient, and dx is the absorber thickness (Figure B.2).

The reconstruction algorithm calculates the linear attenuation coefficient value that corresponds to each pixel. This is the average linear attenuation coefficient of the tissues in the corresponding voxel and this is proportional to tissue density. However, the scanner is unable to assess the density associated with each pixel directly. For bone mineral, a special hydroxyapatite phantom is used for the conversion of linear attenuation coefficient to density. In fact, each pixel value is transformed into an equivalent volumetric mineral density (mg/cm^3) irrespective of the actual type of tissue in the voxel. In this way, the scanner expresses cortical bone, water/soft tissue and fat pixel values as hydroxyapatite equivalent volumetric densities of 1200 mg/cm^3, 60 mg/cm^3 and 0 mg/cm^3, respectively (Frank-Wilson et al., 2015).

If the linear attenuation coefficient were equal for all tissues, there would be no image. The difference in x-ray penetration between different tissues represents the contrast in the image, and this relates to the ease with which different tissues can be distinguished.

As mentioned previously, the mean energy of the X-ray beam in the pQCT scanner is 37 keV. At this energy value, it is possible to distinguish muscle tissue from surrounding tissues (particularly adipose tissue) as depicted in Figure B.3. Adipose tissue consists mainly of fat.

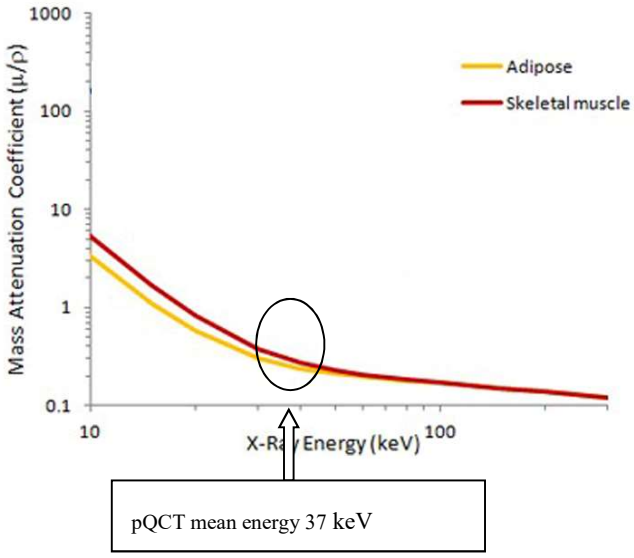

Figure B.3: Variation of attenuation coefficient with photon energy: the attenuation coefficient difference between adipose tissue and skeletal muscle at 37 keV highlights the ability of the pQCT scanner to distinguish muscle border.

B.3 Subject Radiation Dose

The radiation dose of the Stratec 2000 was measured by the scanner manufacturer using thermo-luminescent dosimetry (TLD). TLD chips were positioned at the centre of a 5 cm diameter acrylic cylinder in order to simulate the x-ray attenuation and the scatter of a human limb. The total skin dose is about 125 μSv and the resulting whole body effective dose is about 0.22 μSv (Stratec Medizintechnic 2007).

B.4 Operator Radiation Dose

The radiation dose to the scanner operator is negligible. During a scan procedure, at the scanner aperture, the total leakage plus scatter radiation dose rate is less than 10 μSv/hr. The leakage radiation dose at 5 cm from the gantry surface is equal to 0.9 μSv for a pQCT scan. The operator dose, measured at a distance of 40 cm, is 0.02 μSv, whereas, at a distance of 100 cm, it is less than 0.01 μSv (Stratec Medizintechnic 2007).

B.5 Safety Features

The XCT 2000 scanner has been designed to be safe for both operator and patient. The X-ray beam is highly filtered and highly collimated in order to yield a minimum subject dose. The X-ray beam is on only during patient or quality assurance scans. Furthermore, if the system is not gathering data, the X-ray tube voltage and current are automatically switched off. An amber warning light on top of the gantry body informs the operator that the X-ray tube is switched on and a highlighted text message is displayed on the monitor screen. (Stratec Medizintechnic 2007).

B.6 Quality Assurance of the pQCT Scanner

A quality assurance (QA) procedure is used to test that all the system components are working correctly. However, it is not a system calibration procedure, which fits the output to the expected QA result. The QA procedure must be performed every working day so as to detect any possible malfunctions. It is not possible to scan a patient without a new valid QA measurement taken within the last 24 hours. The QA is performed using two phantoms: a standard phantom and a cone phantom (Figure B.4). Both phantoms are built into one phantom body, which is called the European Forearm Phantom. It is made of 3 different plastic materials: polytetrafluorethylene (PTFE), polyoxymethylene (POM) and polyvinylfluoride (PVDF). Cortical bone is represented by a shell of polyvinylchloride (PVC), which has a thickness of 1 mm. The QA measurement is based on the difference between the measured density values of the 3 materials, so as to detect any changes in the energy spectrum or the photon flux (Braun et al., 1998; Stratec Medizintechnic 2007).

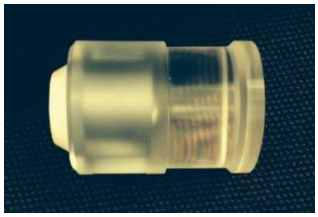

Figure B.4: pQCT phantom for quality control.

The QA procedure starts by placing the QA phantom in a clamp at the gantry opening, as shown in Figure B.5. The position of the standard phantom is detected automatically and the CT measurements begin. The software compares the measured values with the rated values. If the difference between the measured and the rated values is less than 1%, the software gives the message ‘QA successful’, otherwise it gives an error message.

Every 30 days, the cone phantom must be measured to confirm the linearity of the three different density ranges and the precision of repositioning the device, as indicated by the measured cross-sectional area of the cone. This procedure takes about 15 minutes.

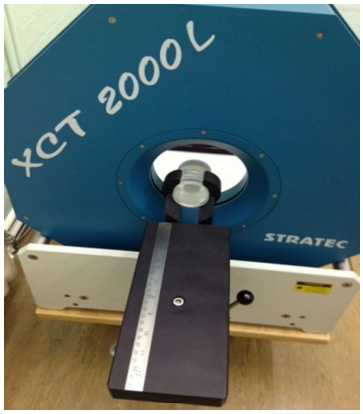

Figure B.5: Scan of phantom for quality control.

Appendix C: Participant Information Sheet and Consent Form

Comparison of peripheral quantitative computed tomography and magnetic resonance imaging for tissue characterisation in the gastrocnemius muscle

Participant information sheet

You are being invited to take part in a research study carried out by the Institute of Medical Engineering, Cardiff University as a part of a PhD Thesis. The purpose of this form is for you to decide whether or not you wish to participate. Information regarding why you have been asked to participate, what the study will involve and how the results to be used are included in this document.

It is important that you take time to read the following information and consider your decisions carefully as whether to participate - perhaps discuss it with friends or family if you think a second opinion would be useful.

Also, it is important that you do not feel pressured or obligated to take part in these procedures. If there is any part that you do not understand and would like more information regarding the procedure, please ask any member of the research team and we will be gladly give assistance and answer any question you have.

Finally, thank you for taking the time to read this information sheet and in taking an interest in our work.

- **What is the purpose of this study?**

This study aims to investigate whether peripheral quantitative computed tomography (pQCT) offers any advantages over magnetic resonance imaging (MRI) for tissue characterisation in the gastrocnemius muscle, and to reveal any association between them in order to improve the treatment of muscle injuries.

- **Why have I been chosen?**

As you are a healthy volunteer you are ideal for this study. Volunteers of between 18-40 years of age are being asked to volunteer and participate, as muscle injuries are common in this population.

- **Do I have to take part?**

No, you are not obligated to take part. It is important for you to take time to understand the information you have been given and to decide whether you wish to participate. If you do not wish to take part, for whatever reason, you can refuse or withdraw. You can do this anytime without giving any reason.

It is also important to understand that your current or future medical care will not be affected by your decisions.

Upon reading this form, you will be asked to keep it and consider your decision. If you choose to participate, you will then be asked to sign a consent form. Once this form has been signed you are still completely free to withdraw without giving reason.

- **What will happen to if I take part?**

Firstly, you will be asked to attend to the MRI centre for approximately of 1 hour. At this session, we will scan the gastrocnemius muscle within your body using a magnetic resonance imaging scanner. MRI is capable of producing highly detailed images of the interior of the body. Before scanning starts, the MRI operator will brief you about the whole procedure. You will be asked to remove any metal objects and all jewelry and put on a medical gown. During the procedure, the MRI machine generates a significant amount of noise, but you will still able to communicate with MRI operator.

Secondly, you will be asked to attend a different location for pQCT scanning. During this session, we will scan the same muscle using pQCT scanner, which is a transmission x-ray imaging modality with a negligible radiation dose.

- **Are there any side-effects?**

MRI does not use ionising radiation and so there are no radiation risks associated with the procedure. However, there might be other types of risk to those who have implanted metal objects in their bodies. For your safety, you will be given a pre-procedure questionnaire, on which you will need to answer all questions.

The effective radiation dose from pQCT is very small, equivalent to much less than one day's worth of natural background radiation.

- **What will happen to the results of the research study?**

The results that we obtain form your visits will be in the form of MRI images and pQCT images. These images will be analysed and should we find valuable new information, they will be presented at a scientific conference and/or published in a scientific journal. This will allow the wider academic community to access these findings. Should you wish to know the results of our findings, contact Professor Len Nokes and Professor Wil Evans using the contact details at the end of this form.

- **Will my participation in this study be kept confidential?**

Members of the research team are drawn from Medical Physics and Clinical Engineering at the University Hospital of Wales (Professor Wil Evans, Dr. Declan Colman), and the Cardiff University School of Engineering (Professor Len Nokes, Mr. Fahad AlGohani). Funding for this project is not required, as all staff involved are able to spend research time as part of their contract of employment.

- **Who has reviewed the study?**

To safeguard the welfare of volunteers, any study that requires voluntary participation has to be approved by a Research Ethics Committee. This study has been reviewed and its conduct approved by the Cardiff University School of Engineering Ethics Committee.

For further information please contact:

- Professor Len Nokes, Academic Supervisor, Cardiff University
- Professor Wil Evans, Academic Co-Supervisor, University Hospital of Wales

Date: **……**

Participant Questionnaire

Sex: **Male** ☐

Female ☐

Age: **……**

Q1: Do you have any pain in the lower leg?

Yes ☐

No ☐

Q2: Do you or have had any injury to your calf muscle? If yes when?

Yes ☐

……

……..

No ☐

Q3: Do you have any muscular weakness, spasticity, rigidity or loss of muscular control?

Yes ☐

No ☐

Q4: Do you do any sport activities?

Yes ☐

No ☐

If yes, which type of sport? And how frequently?

……

……..

Q5: Do you do any exercise to increase the calf muscle strength?

Yes ☐

No ☐

Q6: Have had any operation or surgery to the lower leg? If yes, when?

Yes ☐

No ☐

……

……..

Comparison of peripheral quantitative computed tomography and magnetic resonance imaging for tissue characterisation in the gastrocnemius muscle

CONSENT FORM

Participants Name: ……..

Please read the statements below and, if you agree to them, please tick the appropriate box. On completion, please sign the form to state your consent.

If there are any statements that you do not understand or require clarification on, then please ask one of the research team who will be more than happy to assist.

If you disagree with any of these statements, then feel free not to complete this form and opt out of the study.

1. I confirm that I have read and understood the information sheet entitled 'Comparison of peripheral quantitative computed tomography and magnetic resonance imaging for tissue characterisation in the gastrocnemius muscle', that I have had the opportunity to ask questions and I accept the ans ☐ received.

2. I understand that my participation is entirely voluntary and that I am free to withdraw at any time without giving any reason, and that neither my right to present or future medical care will not be affected, nor my legal rights. ☐

3. I agree to take part in the above study. ☐

Name of Subject	Date	Signature
Name of Researcher	Date	Signature